RADAR IMAGING FOR AIRCRAFT IDENTIFICATION AND PLANETARY ASTRONOMY

Thesis by

Raymond Scott Hudson

In Partial Fulfillment of the Requirements

for the Degree of

Doctor Of Philosophy

California Institute of Technology

Pasadena, California

1991

(Submitted November 15, 1990)

To Laurie, Taylor, and Haley,

who put up with a lot!

Acknowledgements

What makes graduate school more than just reading books, writing computer programs, and turning oscilloscope knobs is the spirited interaction with others who are willing to share their knowledge, ideas, and experiences. It is this intangible part of my time at Caltech that has been of most value to me, and I would like to explicitly thank several people.

Professor Demetri Psaltis, as my advisor, played the key role in my development as a scientist. I am particularly indebted to him for the broad exposure to so many aspects of science (even the political) that I have gained over the last five years. He provided generous support while at the same time allowing me the freedom to follow my research wherever it led. I am sure I will never have such a good deal again.

Dr. Steven Ostro of the Jet Propulsion Laboratory has gone to great effort to thoroughly expose me to the world of radar astronomy. Chapter 5, and the Ganymede and Callisto sections of Chapter 6, are the results of collaborations between Steve and myself.

Dr. Martin Slade of the Jet Propulsion Laboratory, and Dr. John Harmon of the Arecibo Observatory have both been very generous in making data available from the Goldstone and Arecibo radars. The Mars section of Chapter 6 grew out of a collaborative effort between myself, John, and Marty.

The technical staff at Litton Data Systems Division, especially Ken Snapp, Bill

Ross, John Lucas, and Lou Kelly, made the research presented in Chapter 2 possible through their initiative and support.

Professor Ward Whaling of Caltech provided me with my first exposure to a real research environment when I worked in his laboratory as a SURF student. I am very thankful that he convinced me to go on to graduate school.

Ninety percent of a graduate student's interactions are with other graduate students. Past and present members of Professor Psaltis's research group have provided lots of help, advice, and good times. They are, in alphabetical order (sorry Jeff), Dr. Dave Brady, Dr. Claire Gu, Francis Ho, Dr. John Hong, Dr. Ken Hsu, Chuanyi Ji, Dr. David Kagan, Seiji Kobayashi, Sidney Li, Steve Lin, Dave Marx, Dr. Fai Mok, Mark Neifeld, Dr. Eung Paek, Dr. Chool Hoon Park, Yong Qiao, Subrata Rakshit, Dr. Nabeel Riza, Dr. Robert Snapp, Charlie Stirk, Dr. Kelvin Wagner, Alan Yamamura, and Dr. Jeff Yu (spelled Y U). Special thanks to John, for being a mentor my first year, to Kelvin, for popularizing the term "bogus," to Robert, whose plotting program is responsible for dozens of the following pages, to Charlie and Subrata, for picking up the system-administration torch (such as it was), and to Mark, for his agreement on the bogusness of many things.

Also, day-to-day survival would not have been possible without the "nuts-and-bolts" know how of Helen Carrier and Su McKinley.

Abstract

The potential for identifying aircraft using one-dimensional radar range profiles in conjunction with a bank of correlation filters is investigated. Filters which maximize the expected value of the correlation with a target's profiles are derived, and an algorithm for computing them is presented. The algorithm is used on an extensive set of real aircraft profiles, and target identification experiments are performed. It is found that an averaging of identifications of several profiles is required to achieve reliable identification.

The use of multiple radar range profiles to form two-dimensional images through the techniques of inverse synthetic aperture radar (ISAR) is explored. Particular attention is given to the blurring which can arise when the target aspect does not vary linearly with time. An iterative algorithm for estimating target motion is developed which allows well-focused images to be formed in these cases. It is applied to simulated data and to an acoustic imaging experiment.

A technique for forming two-dimensional radar images of a spherical planetary surface using one-dimensional Doppler spectra is developed. Simulations are used to explore the technique's effectiveness and robustness. It is then applied to real data from Jupiter's moons Ganymede and Callisto, and to Mars.

Contents

Acknowledgements iii

Abstract v

1 Introduction 1

1.1 The Radar Equation 3

1.2 Radar Cross Section 6

1.3 Far-Field Backscatter from a 3D Object 8

2 Aircraft Identification Using Radar Range Profiles 12

2.1 Introduction 12

2.2 High Range Resolution Techniques 16

2.3 Radar Range Profiles 24

2.4 Range Profile Fluctuations 26

2.5 Optimal Correlation Filters 29

2.6 The Data Set 33

2.7 Correlation Experiments 35

2.8 Factors Affecting Identification 37

2.9 Identification Using Multiple Profiles 40

2.10 Optical Correlator Implementation 42

2.11 Conclusion 44

3 Inverse Synthetic Aperture Radar 72

3.1 Introduction 72

3.2 Range Compensation 78

3.3 Aspect Compensation 80

3.4 Applications 88

3.5 Optical Processor Implementation 94

3.6 Conclusion 96

4 Fundamentals of Planetary Radar Astronomy 106

4.1 Objectives 108

4.2 Surface Scattering 110

4.3 Coordinate Systems 116

4.4 Radar Resolution of Rotating Spheres 119

4.5 Noise 127

5 Doppler-Radar Imaging of Spherical Planetary Surfaces 140

5.1 The Forward Problem 143

5.2 The Inverse Problem 150

5.3 Simulations 156

5.4 Conclusion 165

6 Applications of Doppler-Radar Imaging 183

6.1 Ganymede 185

6.2 Callisto 194

6.3 Mars 197

6.4 Conclusion 203

Chapter 1

Introduction

This thesis is concerned with the use of *radar* systems to discern physical properties of objects, either because these properties are of interest directly or because they can be put to use for other purposes, e.g., for identification. Radar is an acronym for *ra*dio *d*etection *a*nd *r*anging. As the name implies, it was originally developed to detect the presence of, and measure the range (distance) to, military targets using radio waves. Its effectiveness was clearly demonstrated early in World War II during the Battle of Britain where the early warning provided by their "Chain Home" radar system was a crucial factor in the British victory. A great attraction of radar is that it can operate under virtually all weather conditions, and it is equally effective night and day. Moreover, its ranging capabilities complement the angular resolution of optical detection and tracking systems.

Although military systems have always been, and continue to be, the primary focus of radar research and development, over the last five decades several spin-offs have utilized radar technology for civilian purposes. Among the most visible of these are the air traffic control systems present at every major airport; among

the most ubiquitous are the radar guns used by police officers to enforce highway speed limits. Weather radars play an important role in the prediction and tracking of storms [49]. Imaging radars placed aboard aircraft and spacecraft have provided important geological information about the surface of the Earth [8], and huge Earth-based radars have been built to study the other bodies in the solar system [34].

In this thesis we will apply some basic radar concepts to two very different situations. The first is to study methods for spatially resolving radar echoes from aircraft for the purpose of aircraft identification. The motivation is to extend the detection and ranging capabilities of radar so that it is also possible to determine *what* has been detected. The most straight-forward approach is to use one-dimensional, range-resolved images called *range profiles.* The potential for performing identification based on range profiles is explored in Chapter 2. The original contribution of this chapter is a method for calculating optimal correlation filters from sets of range profiles, and the investigation of its effectiveness by applying it to an extensive set of real data.

The limitations which arise in using one-dimensional range profiles as a basis for identification motivate us to explore techniques for obtaining an extra dimension of spatial resolution, and this leads to the concept of *inverse synthetic aperture radar* (ISAR) in Chapter 3. A major difficulty of ISAR processing is that it requires knowledge of target motion, and this is generally unavailable to us *a priori.* The typical response to this problem has been to *assume* the target moved in a particular manner, but this results in a poorly focused image if the assumption is incorrect. The original contribution of Chapter 3 is the development of a technique for estimating target motion iteratively, thereby allowing well-focused ISAR images to be formed for more general types of target motion.

The final chapters deal with radar astronomy. We give an overview of this field

in Chapter 4, and we describe the problem of *overspreading* of planetary targets which precludes the use of delay-Doppler techniques for providing fully resolved images of many planetary surfaces. Overspread targets have generally been studied by observing their *Doppler spectra*, which are one-dimensional projections of the target's two-dimensional distribution of surface reflectivity. The original contribution of Chapter 5 is the development of a technique for using a set of one-dimensional Doppler spectra of a spherical planet, moon, or asteroid to form a two-dimensional image of the distribution of radar reflectivity over its surface. Then in Chapter 6 we apply the technique to Ganymede and Callisto (moons of Jupiter), and to Mars.

An excellent introduction to radar concepts and systems can be found in [49]. For the remainder of this chapter we will briefly touch on those concepts that are of importance to us in this thesis.

1.1 The Radar Equation

A radar observation consists of the transmission of a radio signal, propagation of that signal to a target as an electromagnetic field, scattering of that field by the target, propagation of the scattered field back to the radar, and reception of this backscattered field at the radar. The received field is always much less intense than the transmitted field. Just how much less depends on the distance to, and nature of, the target and the characteristics of the radar system. It is important to know quantitatively how these factors affect the strength of the received signal for several reasons.

One is the fact that all observations are corrupted by noise, and if the received signal is not of sufficient strength it will be hopelessly obscured. Therefore, in designing a radar system, or in planning a radar observation, the strength of the received

signal must be predicted beforehand to ensure that useful information can be obtained. This is particularly true in the field of radar astronomy where observations are planned months in advance and require large commitments of time and personnel. The expression that gives the received signal strength in terms of radar system and target parameters is called the *radar equation*, and we will derive it now.

Assume a radar transmits with power P_t. If this power is transmitted equally in all directions, i.e., isotropically, then after a time t it will be uniformly spread out over a sphere of radius $R = ct$, with c the speed of light. The surface area of this sphere is $4\pi R^2$, so the intensity with which this field illuminates a target at the distance R is

$$I_i = P_t \frac{1}{4\pi R^2}. \tag{1.1}$$

However, in practice, radars do not radiate isotropically. Instead they utilize antennas to achieve *antenna gain*, or directivity, and thereby increase the intensity of the radiated field in a particular direction. Therefore, the target is actually illuminated with an intensity

$$I_i = P_t \frac{G}{4\pi R^2}, \tag{1.2}$$

where the dimensionless quantity G is the antenna gain. For a well-designed system $G \gg 1$.

Intuitively we expect that if the target presents a projected area (along the radar line of sight) of σ, it will intercept an amount of power $I_i\sigma$. If this power is scattered isotropically, the intensity of the backscattered field at the radar is

$$I_r = \frac{I_i\sigma}{4\pi R^2}. \tag{1.3}$$

If the radar intercepts some of this backscattered field with an antenna of area A then the total received power is

$$P_r = \frac{I_i\sigma}{4\pi R^2} A. \tag{1.4}$$

Using (1.2) we write this as

$$P_r = P_t \frac{GA\sigma}{(4\pi)^2 R^4}. \tag{1.5}$$

This is the radar equation. From basic antenna theory [49] we have that for an ideal antenna of aperture A the gain is

$$G = \frac{4\pi}{\lambda^2} A, \tag{1.6}$$

with λ the radar wavelength, so we can also write the radar equation in either of the forms:

$$P_r = P_t \frac{A^2 \sigma}{4\pi \lambda^2 R^4}, \tag{1.7}$$

$$P_r = P_t \frac{\lambda^2 G^2 \sigma}{(4\pi)^3 R^4}. \tag{1.8}$$

Equation (1.7) is instructive because it shows clearly the physical parameters that determine received signal strength. The factors that are more or less under our control are the transmitted power P_t, the antenna aperture area A, and the radar wavelength λ. Clearly we want as large a transmitter power as possible, but there are practical limitations to the power a radar can transmit. It quickly becomes prohibitively expensive to increase P_t past a certain level. Received power goes as A^2 so we would like to have large antenna apertures. Indeed, large apertures are probably the single most important factor in the design of a highly sensitive radar. However, here too there are practical limitations; it is difficult to build very large apertures that maintain their structural integrity. Equation (1.7) implies that an easy way to increase P_r would be to decrease λ, but this increases the cost of the antenna since its surface must be accurate to within a fraction of the radar wavelength, and this becomes increasingly difficult to achieve for small λ. The factors that we cannot control are R and σ. The fact that P_r falls off as R^{-4} is one of the most serious limitations of radar. Effective radar design requires that all these factors be taken

into account and resources devoted to the most cost-effective approach(s) of achieving high sensitivity.

Although (1.7) may be useful for design purposes, real radar systems have losses and other imperfections that limit the validity of the assumptions under which (1.7) was derived. In practice, equation (1.8) is used and G is *measured*, for example, by placing a known target at a known distance from the radar and measuring the received power relative to the power fed into the transmitter. This empirical value of G then takes into account losses in the transmitter and receiver, imperfections in the shape of the antenna, and so on.

1.2 Radar Cross Section

The only parameter in the radar equation that depends on the properties of the target is the *radar cross section* σ. This is the equivalent area such that if all the power falling on it were scattered isotropically it would produce the observed backscattered power at the radar. A target's radar cross section need not be equal to its projected area, however. It *is* for the important special case of a perfectly conducting sphere, provided the sphere is much larger than the radar wavelength. Accordingly, the radar cross section of a target can be defined as the projected area of a perfectly conducting sphere which, if placed at the same distance as the target, would produce the same backscattered intensity.

For more complex targets, radar cross section and projected area will generally not be the same. First of all, no real target is perfectly reflective but rather absorbs some of the incident power resulting in less backscattered power and a correspondingly smaller radar cross section. For example, a sphere with projected area A_{proj}, but

with a reflectivity of $\rho < 1$, will have a radar cross section of

$$\sigma = \rho A_{proj}, \tag{1.9}$$

which is less than its projected area. Additional complexities arise for nonspherical targets which, in general, do not scatter isotropically. For example, a flat plate will backscatter very strongly when oriented normal to the incident field, but for modestly oblique orientations it will barely backscatter at all since most of the reflected power travels off in the direction that satisfies Snell's Law. Yet the plate's projected area differs little for these two cases. To take this effect into account we would have to write

$$\sigma = \rho\, g(\theta, \phi)\, A_{proj}, \tag{1.10}$$

where $g(\theta, \phi)$ is a "target gain" factor that depends on the angles (θ, ϕ) describing the target's orientation with respect to the radar. This gain factor describes how the anisotropic scattering of the target affects its radar cross section.

We see that a measurement of radar cross section does not uniquely determine the physical properties of a target but rather provides a mutual constraint on its size, reflectivity, and shape or structure. In using radar backscatter measurements to make unambiguous statements about the physical properties of a target, therefore, we need to make many independent measurements and/or interpret them in terms of some model of the target into which we have placed all our *a priori* knowledge of the target and of radar scattering in general. We will make use of two models in this thesis. In the chapters on radar astronomy we will discuss various *scattering laws* that have been developed on both theoretical and empirical grounds to account for the function $g(\theta, \phi)$. These will be described in Chapter 4. In Chapters 2 and 3, where we are concerned with scatter from aircraft, we will use the *physical optics approximation* [28] that has been found to give a reasonably accurate representation

of backscatter from such objects [56]. We describe this model in more detail below.

1.3 Far-Field Backscatter from a 3D Object

Consider the geometry shown in Figure 1.1. The radar is located at the point $\mathbf{R}$ while location on the target is denoted by $\mathbf{r}$. The radar transmits a signal $s(t)$. This travels out, strikes the various points on the target, is reflected from these points, and these reflected fields travel back to the radar where their sum is received. The physical optics approximation assumes the target can be characterized by a *reflectivity distribution* $f(\mathbf{r})$ such that the field backscattered from a small volume dV about the point $\mathbf{r}$ has an amplitude at the radar of $af(\mathbf{r})\,dV$, where a contains the factors from the radar equation and is (essentially) constant for all points on the target. The round trip delay from the radar to the point $\mathbf{r}$ and back is $\Delta t = 2|\mathbf{R}-\mathbf{r}|/c$, so the component of the received field due to this small volume is

$$dE(t) = af(\mathbf{r})s(t - 2|\mathbf{R}-\mathbf{r}|/c)\,dV. \tag{1.11}$$

The total received field is just the sum of all such components:

$$E(t) = a\int f(\mathbf{r})s(t - 2|\mathbf{R}-\mathbf{r}|/c)\,dV, \tag{1.12}$$

where the integration is over all parts of the target.

The distance $|\mathbf{R}-\mathbf{r}|$ can be written

$$\begin{aligned} |\mathbf{R}-\mathbf{r}| &= \sqrt{|\mathbf{R}-\mathbf{r}|^2} \\ &= \sqrt{|\mathbf{R}|^2 + |\mathbf{r}|^2 - 2\mathbf{R}\cdot\mathbf{r}} \\ &= |\mathbf{R}| - \frac{\mathbf{R}}{|\mathbf{R}|}\cdot\mathbf{r} + \frac{|\mathbf{r}|^2}{2|\mathbf{R}|} + O\left(\frac{(|\mathbf{r}|^2 - 2\mathbf{R}\cdot\mathbf{r})^2}{|\mathbf{R}|^3}\right). \end{aligned} \tag{1.13}$$

If $|\mathbf{R}|$ is very large then we can ignore all but the first two terms of expression (1.13) and write

$$|\mathbf{R}-\mathbf{r}| \approx R - \mathbf{e}_R\cdot\mathbf{r}, \tag{1.14}$$

where $R = |\mathbf{R}|$ and $\mathbf{e}_R = \mathbf{R}/R$ is the unit vector in the radar's direction. This approximation is valid if the neglected terms are much smaller than the radar wavelength λ [17]. This will generally be so provided

$$\frac{|\mathbf{r}|^2}{|\mathbf{R}|} \ll \lambda \quad \Rightarrow \quad R \gg \frac{|\mathbf{r}|^2}{\lambda} \tag{1.15}$$

for all points $\mathbf{r}$ on the target. This is the *far-field* condition, and (1.14) is the *far-field approximation* that we will assume is valid in all discussions henceforth. Using this in (1.12) results in

$$E(t) = a \int f(\mathbf{r}) s\left(t - \frac{2R}{c} + \frac{2\mathbf{e}_R \cdot \mathbf{r}}{c}\right) dV \tag{1.16}$$

as our expression for the total backscattered field.

In this thesis we will be concerned with situations in which the radar position $\mathbf{R}$ is assumed to be restricted to a single plane. By appropriate orientation of our coordinate system we can make this the x, y plane. Then we can write

$$\mathbf{e}_R = (\cos\theta, \sin\theta, 0) \tag{1.17}$$

$$\mathbf{e}_R \cdot \mathbf{r} = x\cos\theta + y\sin\theta, \tag{1.18}$$

where θ is the angle $\mathbf{e}_R$ makes with the x axis, and (1.16) becomes

$$E(t) = a \int\int\int f(x,y,z) s\left(t - \frac{2R}{c} + \frac{2}{c}(x\cos\theta + y\sin\theta)\right) dx\, dy\, dz. \tag{1.19}$$

The argument of $s()$ does not depend on z. We can therefore define the target's equivalent two-dimensional reflectivity distribution as

$$f(x,y) = \int f(x,y,z)\, dz, \tag{1.20}$$

and we can then write

$$E(t) = a \int\int f(x,y) s\left(t - \frac{2R}{c} + \frac{2}{c}(x\cos\theta + y\sin\theta)\right) dx\, dy \tag{1.21}$$

as the expression for the backscattered field. If we are not concerned with changes in θ then it is often convenient to orient the coordinate system so that the radar lies on the x axis resulting in

$$E(t) = a \int \left[\int f(x,y)\, dy \right] s\left(t - \frac{2R}{c} + \frac{2x}{c} \right) dx. \tag{1.22}$$

In this case the x coordinate measures range on the target. The argument of $s()$ does not depend on y, so we can define an equivalent one-dimensional distribution of reflectivity in range:

$$f(x) \equiv \int f(x,y)\, dy, \tag{1.23}$$

and we can write

$$E(t) = a \int f(x) s\left(t - \frac{2R}{c} + \frac{2x}{c} \right) dx. \tag{1.24}$$

We will use these expressions in the next two chapters, with an appropriate choice of $s(t)$, to describe techniques to resolve radar echoes from aircraft.

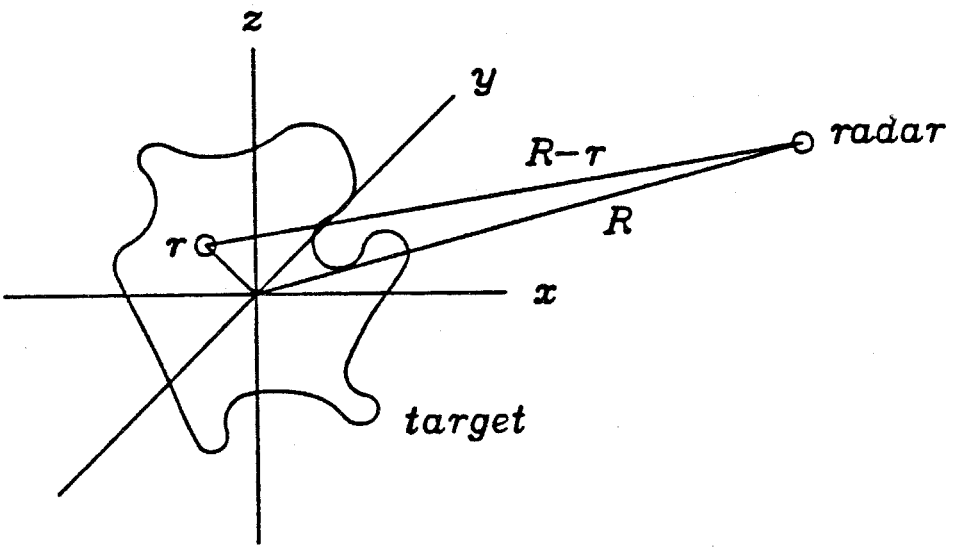

Figure 1.1: Geometry of radar observations.

Chapter 2

Aircraft Identification Using Radar Range Profiles

2.1 Introduction

Over the last half century radar has proven to be a very powerful tool for the detection, ranging, and tracking of aircraft. However, these capabilities leave a key question unanswered: What has been detected? This is the crucial piece of information in a military scenario as it determines the degree of threat and the appropriate response. The possible consequences of not knowning what a blip moving on a radar scope represents were made horribly clear on July 2, 1988 when the U.S.S. Vincenes, finding itself in a hostile situation in the Persian Gulf during the Iran/Iraq war, destroyed a commercial aircraft, killing the crew and passengers because the jet was mistaken for a fighter on a hostile approach. While it is sometimes possible to augment radar detections with other sensors, e.g., visual sightings, one of the great attractions of radar is its ability to operate under virtually all weather and lighting conditions.

Situations will arise where radar detections are possible but other sensors are useless, for example, cloud cover in the case of visual sightings. Ideally, radar systems should have the ability to provide their own reliable identification for every detection they make. The need for this additional capability has motivated considerable research into techniques for automatic radar target identification over the past few decades [49].

Techniques for identifying targets from their radar echoes fall into the general field of *inverse scattering*. If we had a complete electromagnetic description of a target, i.e., its precise shape and composition, and we knew its orientation with respect to the radar, then we could, in principle, solve Maxwell's equations with the appropriate boundary conditions to exactly predict the backscattered field for any incident field we use to illuminate the target. We can represent this solution symbolically as

$$\mathbf{y} = \mathbf{h}[\mathbf{x}; \theta], \tag{2.1}$$

with $\mathbf{x}$ the incident field, $\mathbf{y}$ the backscattered field, $\mathbf{h}$ the electromagnetic description of the target, and θ the (possibly time-varying) orientation or *aspect* of the target. This is known as the *forward* scattering problem: Given the description of the target, find the backscattered field for a given incident field. For target identification, on the other hand, we *measure* the backscattered field, so we know both $\mathbf{x}$ and $\mathbf{y}$. We may, or may not, know the target's orientation θ. It is the description of the target, $\mathbf{h}$, that we do not know and that we need to determine from the fields. This is the inverse scattering problem. Solving this is a difficult task in general. In fact, there may not even be a unique solution to the inverse problem, that is, there may be many possible targets that produce the same backscatter from a given incident field. Generally the target is better constrained when the diversity of the illumination is greater, so we would like to be able to illuminate targets with many frequencies and over a wide range of angles. Unfortunately, this diversity is usually accompanied

by increased cost in system complexity, processing requirements, and/or observation time. This motivates us to seek the least costly approach that still provides reliable identification.

For target identification purposes it is usually not necessary to fully solve the inverse scattering problem and to determine **h** completely. It is often the case that we know *a priori* that the target cannot be an arbitrary object but rather must be one of a set of possible targets. For example, we may know that only two types of aircraft could be present in a particular situation. In such cases a limited amount of observational data may suffice to place enough constraints on **h** that we can answer questions such as: Is it target A or target B that is producing this backscatter? This is the situation we will examine in this chapter using a data set of radar signatures of several aircraft in flight. To place our work in context, however, we first give an overview of another area of active radar target identification research that is, in a sense, explained below, complementary to the approach we take in this chapter.

Identification based on Scattering Resonances

If a target is made of materials with linear electromagnetic characteristics, such as dielectrics and metals, then the electromagnetic scattering from the target is a linear process. Moreover, if, as is usually the case, these properties do not change with time then it is a time-invariant linear process. As such it can be fully characterized by its impulse response, or equivalently, by its transfer function. If $x(t)$ represents the signal that the radar transmits, and $y(t)$ represents the received backscattered signal, then we can express the relation between them as

$$y(t) = \int_0^\infty h_\theta(t-\tau)x(\tau)\,d\tau, \tag{2.2}$$

where $h_\theta(t)$ is the *impulse response* of the target at aspect θ. Using the convolution theorem we have

$$Y(s) = H_\theta(s)X(s), \tag{2.3}$$

with $X(s)$, $Y(s)$, and $H_\theta(s)$ the Laplace transforms of $x(t)$, $y(t)$, and $h_\theta(t)$.

Marin [30] has shown that for a perfectly conducting body $H(s)$ is a meromorphic function, that is, it is analytic in the entire complex plane except for isolated poles:

$$H_\theta(s) = \Phi_\theta(s) + \sum_k \frac{a_k(\theta)}{s - s_k}, \tag{2.4}$$

where $\Phi_\theta(s)$ is analytic in the entire s plane and satisfies the conditions required for the Paley-Wiener theorem [46] to apply. Thus

$$h_\theta(t) = \phi_\theta(t) + \sum_{k=1}^{\infty} a_k(\theta)e^{s_k t} \tag{2.5}$$

where $\phi_\theta(t)$ is a *time-limited* function and $\{s_k\}$ are the poles of $H_\theta(s)$. These poles are the complex resonant frequencies of the target, analogous to the resonant frequencies of a cavity or an electric circuit. The period during which $\phi_\theta(t)$ is nonzero is termed the "early-time" response; the period after that, when only the resonant terms are present, is termed the "late-time" response. While the function $\phi_\theta(t)$ and the amplitudes $a_k(\theta)$ depend on the nature of the illuminating waveform and the orientation of the target, the poles are determined only by the structure of the target. Hence, if it should prove possible to determine the poles from a backscattered field they would provide a set of aspect-invariant features for target recognition purposes.

The practical difficultly with this approach is that $Re(s_k) < 0$, i.e., the resonant oscillations are radiation damped (if they were not radiating energy we would not be able to observe them), and so they very quickly fall off into the noise that is present in all real measurements. Yet if the poles are to be measured precisely the functions $e^{s_k t}$ must remain above the noise for a significant length of time. For certain simple

bodies, such as the sphere, exact solutions to the electromagnetic scattering problem are available. In this case it is found that the scattered field consists of a reflection followed by a series of exponentially decaying "creeping waves." These creeping waves are just the superposition of the resonant "ringing" terms $a_k^{(\theta)} e^{s_k t}$. In order to identify the resonant frequencies it has been found that second and higher order creeping waves must be above the noise [5]. Since each successive creeping wave is much attenuated with respect to the previous one, this is a severe requirement, and this approach to radar target identification has had limited success to date. Nonetheless, because of the promise of aspect invariance, considerable research continues in this area.

An interesting variation on this theme is the k-pulse (kill-pulse) concept [27]. If we choose the transmitted waveform so that its Laplace transform is zero at the complex resonant frequencies of a particular target, i.e.,

$$X(s_k) = 0 \qquad \text{for all } k, \tag{2.6}$$

then the reflected field from that target will be free of late-time resonant "ringing." Such a waveform "kills" the resonances. Other targets that presumably have different complex resonant frequencies *will* produce resonant scatter when illuminated with this same waveform. Therefore, based on the presence or absence of ringing, such a waveform has the potential to answer the question: Is this target A or another target? However, the need to detect the presence of the exponentially decaying ringing leads to the same problems with noise we discussed above.

2.2 High Range Resolution Techniques

In light of the difficulties with the resonant frequencies approach to radar target identification, it is natural to ask if components of a target's impulse response other than late-time resonances can provide useful information for identification purposes.

Specifically, we are interested in using the entire impulse response $h_\theta(t)$. While this presents the disadvantage that it is aspect dependent, it has the advantage that the early-time component of the impulse response is generally much stronger than the ringing, and so should prove more useful in the noisy environments that characterize most real-world radar observations.

In principle, the impulse response of a target could be measured by transmitting an impulse $s(t) = \delta(t)$ and observing the backscattered field. From (1.24) this would be

$$E(t) = a \int f(x)\delta(t - \frac{2R}{c} + \frac{2x}{c})\, dx, \tag{2.7}$$

with $f(x)$ the equivalent one-dimensional reflectivity distribution of the target in range. At a given time t this field contains contributions only from those points on the target for which

$$x = R - \frac{ct}{2}, \tag{2.8}$$

and we say that the target has been resolved in range.

In practice it is not possible to transmit a true impulse, for two reasons. First, the bandwidth of $\delta(t)$ is infinite while all real systems operate with finite bandwidths. Second, the instantaneous power of $\delta(t)$ is infinite at $t = 0$, but real systems are always limited in the level of instantaneous power they can produce. Therefore $|s(t)|^2$ must necessarily be limited and we will assume for simplicity that $|s(t)|^2 \leq 1$. Within the limitations of finite bandwidth and finite power there are waveforms that can provide reasonable approximations to a target's impulse response. We investigate some of these below.

Pulsed-CW Waveform

Conceptually, the simplest way to achieve range resolution is to pulse a continuous-wave (cw) transmitter thereby producing a transmitted waveform

$$s(t) = \text{rect}\left(\frac{t}{T_p}\right) e^{-i2\pi\nu_0 t}, \tag{2.9}$$

where T_p is the pulse duration, ν_0 is the transmitter frequency, and

$$\text{rect}(x) = \begin{cases} 1 & \text{if } |x| \leq 1/2 \\ 0 & \text{otherwise.} \end{cases} \tag{2.10}$$

If this signal is scattered from a target consisting of two point scatterers at distances $r_1 = R - x_1$ and $r_2 = R - x_2$ then the received backscatter will be

$$E(t) = a\,\text{rect}\left(\frac{t - 2r_1/c}{T_p}\right) e^{-i2\pi\nu_0(t-2r_1/c)} + a\,\text{rect}\left(\frac{t - 2r_2/c}{T_p}\right) e^{-i2\pi\nu_0(t-2r_2/c)}, \tag{2.11}$$

or with the carrier $e^{-i2\pi\nu_0 t}$ mixed out,

$$E(t) = a\,\text{rect}\left(\frac{t - 2r_1/c}{T_p}\right) e^{i2\pi\nu_0 2r_1/c} + a\,\text{rect}\left(\frac{t - 2r_2/c}{T_p}\right) e^{i2\pi\nu_0 2r_2/c}. \tag{2.12}$$

Here c is the speed of light, and $2r_1/c$ and $2r_2/c$ are the round-trip propagation times from the radar to the point scatterers and back. As illustrated in Figure 2.1, these returned pulses are resolved if $|r_1 - r_2| > cT_p/2$, hence we refer to

$$\delta r = \frac{cT_p}{2} \tag{2.13}$$

as the *range resolution* of the pulsed-cw waveform. Alternately we can write

$$\delta r = \frac{c}{2B_p} \tag{2.14}$$

where $B_p = 1/T_p$ is the (effective) bandwidth of the pulse.

In principle we can keep reducing the pulse duration, hence increasing the pulse bandwidth, without limit, to achieve arbitrarily fine range resolution and get closer to

the ideal impulse response. However, in practice we must contend with the presence of noise. Thermal noise at microwave frequencies is white with a spectral power density in Watts per Hertz of $S_n = k_B T_n$, where k_B is Boltzmann's constant, and T_n is the *system noise temperature* [49]. In order to receive a pulse of bandwidth B_p our radar receiver must have a bandwidth at least this broad, so the noise power will be

$$P_n = k_B T_n B_p. \tag{2.15}$$

From the radar equation

$$P_r = P_t \frac{GA\sigma}{(4\pi)^2 R^4}, \tag{2.16}$$

so the *signal-to-noise ratio* (SNR) is

$$\begin{aligned} \text{SNR} &= \frac{P_r}{P_n} && (2.17)\\ &= P_t \frac{GA\sigma}{(4\pi)^2 R^4 k_B T_n B_p} && (2.18)\\ &= P_t \frac{GA\sigma}{8\pi^2 R^4 k_B T_n c} \delta r, && (2.19) \end{aligned}$$

where we have used (2.14). Since SNR is proportional to δr, we see that the fidelity of the received signal decreases as range resolution is made finer. This significant limitation of the pulsed-cw waveform can be overcome using the technique of pulse compression that we now describe.

Pulse Compression

Assume a radar transmits a signal $s(t)$, $|s(t)| \leq 1$, which has a duration T_p, and assume it is backscattered from a point target at range r. The result is a received signal $as(t - 2r/c)$ where a contains all the relevant factors from the radar equation:

$$|a|^2 = P_t \frac{GA\sigma}{(4\pi)^2 R^4}. \tag{2.20}$$

If we correlate the received signal with the transmitted signal we get (limits of integration are $-\infty$ to ∞ unless otherwise shown)

$$u(\tau) = \int as(t-2r/c)s^*(t-\tau)dt \tag{2.21}$$

$$= a\int s(t')s^*(t'-(\tau-2r/c))dt'. \tag{2.22}$$

Using the convolution theorem [17] we can write this as

$$u(\tau) \approx a\int |S(\nu)|^2 e^{i2\pi\nu(\tau-2r/c)}d\nu. \tag{2.23}$$

If we choose the spectrum of $s(t)$ to be essentially flat over the range $|\nu| < B_p/2$, and essentially zero for $|\nu| > B_p/2$, then

$$u(\tau) = a|S(0)|^2 \int_{-B_p/2}^{B_p/2} e^{i2\pi\nu(\tau-2r/c)}d\nu$$

$$= a|S(0)|^2 B_p \,\mathrm{sinc}B_p(\tau-2r/c), \tag{2.24}$$

where

$$\mathrm{sinc}(x) = \frac{\sin\pi x}{\pi x}. \tag{2.25}$$

We will assume that $|s(t)| = 1$ over the pulse duration T_p. This is usually the case in practice since it results in maximum possible transmitted power. Parseval's theorem [17] then requires that

$$\int_{-B_p/2}^{B_p/2} |S(\nu)|^2\, d\nu = \int_{-T_p/2}^{T_p/2} |s(t)|^2\, dt \tag{2.26}$$

and hence that

$$B_p|S(0)|^2 = T_p. \tag{2.27}$$

Therefore we have

$$u(\tau) = aT_p\ \mathrm{sinc}B_p(\tau-2r/c). \tag{2.28}$$

The effective width of the sinc function is $\delta\tau = 1/B_p$, and since $\delta r = c\delta\tau/2$ we have

$$\delta r = \frac{c}{2B_p} \tag{2.29}$$

just as for the pulsed-cw waveform. Notice, however, we need not have $B_p = 1/T_p$. In fact the range resolution is independent of the duration of the transmitted signal, and, provided we keep the bandwidth constant, we are free to make T_p as large as we like.

Now consider the presence of noise. Putting a received signal corrupted by additive noise $n(t)$ through the correlation process results in

$$\begin{aligned} u(2r/c) &= \int [as(t) + n(t)]s^*(t)\,dt \\ &= aT_p + \int n(t)s^*(t)\,dt \end{aligned} \tag{2.30}$$

as the value of the processed signal at the peak of the output of the uncorrupted correlation, i.e., at $\tau = 2r/c$. The term aT_p is the correlation signal and the integral is the correlation noise. The correlation signal "power" is

$$P_s = |a|^2 T_p^2 \tag{2.31}$$

and the correlation noise "power" is

$$P_n = E\left[\left|\int_{-T_p/2}^{T_p/2} n(t)s^*(t)\,dt\right|^2\right] \tag{2.32}$$

$$= \int_{-T_p/2}^{T_p/2}\int_{T_p/2}^{T_p/2} E[n(t)n^*(t')]s^*(t)s(t')\,dt\,dt', \tag{2.33}$$

where E denotes the expected value. We can evaluate this expression (approximately) by using the sampling theorem [17] to convert the integrals to discrete sums:

$$P_n = \sum_k \sum_{k'} E\left[n(\frac{k}{B_p})n(\frac{k'}{B_p})\right] s^*(\frac{k}{B_p})s(\frac{k'}{B_p})\frac{1}{B_p^2}, \tag{2.34}$$

where $dt = 1/B_p$ is the Nyquist sampling period for $s(t)$ and $n(t)$. If $n(t)$ is white noise with variance $\sigma_n^2 = k_B T_n B_p$, this becomes

$$\begin{aligned} P_n &= \frac{k_B T_n B_p}{B_p^2} \sum_k |s(\frac{k}{B_p})|^2 \\ &= k_B T_n T_p. \end{aligned} \tag{2.35}$$

To evaluate the sum we have used the fact that $|s(t)|^2 = 1$, and the number of terms in the sum is $T_p/(1/B_p) = T_pB_p$. The signal-to-noise ratio is thus

$$\begin{aligned} \text{SNR} &= \frac{|a|^2 T_p^2}{k_B T_n T_p} \\ &= \frac{|a|^2 T_p}{k_B T_n} \\ &= P_t \frac{GA\sigma}{8\pi^2 R^4 k_B T_n c} \delta r T_p B_p, \end{aligned} \tag{2.36}$$

where (2.20) has been used. This is the same as the result for the pulsed-cw waveform except here there is an additional factor of T_pB_p, the *time-bandwidth product* of the transmitted signal. SNR still decreases as the range resolution gets finer, but this can be overcome by merely increasing the duration of the pulse in inverse proportion.

Waveforms for Pulse Compression

The most commonly used waveform for pulse compression is the *chirp*, which has the form

$$s(t) = \text{rect}\left(\frac{t}{T_p}\right) e^{-i\pi\beta t^2} \tag{2.37}$$

and satisfies $|s(t)| = 1$ for $|t| < T_p/2$ as we assumed above. Instead of showing that the spectrum of the chirp is approximately flat over some bandwidth it is easier to compute the autocorrelation directly as

$$\begin{aligned} u(\tau) &= \int_{T_p/2}^{T_p/2} e^{-i\pi\beta t^2} e^{-i\pi\beta(t-\tau)^2}\, dt \\ &= e^{-i\pi\beta\tau^2} \int_{T_p/2}^{T_p/2} e^{-i2\pi\beta\tau t}\, dt \\ &= e^{-i\pi\beta\tau^2} T_p \,\text{sinc}(T_p\beta\tau). \end{aligned} \tag{2.38}$$

Comparing this with (2.24) we see that the effective bandwidth of the chirp is $B_p = T_p\beta$. This makes sense if we consider that the instantaneous frequency of the

chirp is the time derivative of its phase:

$$\nu_{inst} = \frac{1}{2\pi}\frac{d}{dt}\pi\beta t^2 = \beta t, \tag{2.39}$$

and that this varies over $[-\beta T_p/2, \beta T_p/2]$ for a total bandwidth of βT_p. Because of the linear dependence of instantaneous frequency on time, the chirp is also referred to as a *linear FM* (frequency modulation) waveform.

Instead of continuously varying the frequency we can increase it in discrete steps as in

$$s(t) = \sum_{n=-N/2}^{N/2} \text{rect}\left(\frac{t - n\delta t}{\delta t}\right) e^{-i2\pi n\delta f t}, \tag{2.40}$$

which has a time duration of $T_p = (N+1)\delta t$ and a bandwidth of $B_p = N\delta f$. This is called a *frequency stepped* waveform. It has found applications in military and astronomical radar systems. A nice feature of this waveform is that the time steps δt and the frequency steps δf can be generated by a computer controlled frequency synthesizer that affords complete programmability as opposed to the continuous chirp which is usually generated by analog hardware.

The chirp and stepped frequency waveforms both have the form

$$s(t) = e^{i\phi(t)}, \tag{2.41}$$

and we can think of $\phi(t)$ as a *phase code.* If we restrict $\phi(t)$ to the values $\{0, \pi\}$, hence $s(t)$ to $\{-1, +1\}$, then we have a *binary phase coded waveform.* Allowing the phase to change with a period δt results in a waveform

$$s(t) = \sum_{n=0}^{N-1} q_n \text{rect}\left(\frac{t - n\delta t}{\delta t}\right) \tag{2.42}$$

where $q_n \in \{+1, -1\}$ and δt is called the *baud.* Sequences $\{q_n\}$ can be found that produce a waveform providing an impulse-like autocorrelation. The class of *shift-register sequences* has found particular application in radar astronomy [43].

2.3 Radar Range Profiles

The radar impulse response of a target is called its *radar range profile.* A radar range profile is a one-dimensional "image" or projection of the target onto the radar's line-of-sight. This is illustrated in Figure 2.2. At a given time (e.g., t_2) the pulse illuminates only a single strip, or *range bin*, of the target consisting of all points at a certain range (and within the radar's range resolution) from the radar. Thus the backscattered field received at the radar at a given time consists of the sum of scatter from only the points of the target in the corresponding range bin. The resulting range profile thus resolves the points of the target in range, to within the range resolution δr of the radar.

If the aspect of the target (the angle at which the radar views the target) changes, then the relative ranges of points may change with the result that two points that were once in the same range bin are no longer. For example, consider the case shown in Figure 2.3. If the wingtips are originally at the same range and are a distance W apart, a small aspect change of $\Delta\theta$ will cause the wingtips to differ in range by approximately $W\Delta\theta$. If this is larger than the radar's range resolution, i.e., if

$$W\Delta\theta > \delta r, \tag{2.43}$$

then the wingtips will no longer fall into the same range bin, and the range profile at the new aspect will provide a different projection of the target. This places a limit

$$\Delta\theta < \frac{\delta r}{W} \tag{2.44}$$

on the change in aspect for which the radar profile can still be considered the same projection of the target. As an example, if $\delta r = 0.5$ m and $W \approx 5$ m then

$$\Delta\theta < 0.1 \text{ rad} = 6^\circ. \tag{2.45}$$

In this case if the target's aspect changed by more than about 6° the radar would effectively see a different projection of the target.

Even if the aspect does not change enough to cause the radar to see a different projection of the target, changes in the relative ranges to different scatterers of a fraction of the radar wavelength can cause the radar profile to fluctuate significantly due to interference effects. For example, if in Figure 2.3

$$W\Delta\theta \approx \frac{\lambda}{4}, \tag{2.46}$$

where λ is the radar wavelength, then the scatter from the wingtips will change from constructively interfering to destructively interfering, or *vice versa*, even though they are still in the same range bin, and the range profile will fluctuate significantly. To avoid this the aspect would have to stay constant to within

$$\Delta\theta \ll \frac{\lambda}{4W}. \tag{2.47}$$

For some typical numbers, $\lambda = 3$ cm, $W = 10$ m, we would require

$$\Delta\theta \ll 1.5 \text{ mrad} = 0.04° \tag{2.48}$$

which is a very small angle. The aspect of a flying aircraft will not stay constant to within this limit for any significant length of time. Therefore we expect aircraft profiles in real-world situations to fluctuate in time. (An example is given in Figure 2.5.) Moreover, it is not practical to measure a target's aspect to within the accuracy required by (2.48). For these reasons it is more appropriate to think of a target's aspect from observation to observation as a *random variable* rather than a well-defined quantity. We will use this fact below to investigate the statistics of range profile fluctuations.

We now derive an explicit expression for a target's finite-resolution range profile.

If we set

$$s(t) = \text{rect}\left(\frac{t}{T_p}\right) e^{-i2\pi\nu_0 t} \tag{2.49}$$

in (1.21) and assume $\theta \ll 1$, so $\cos\theta \approx 1$ and $\sin\theta \approx \theta$, we get

$$\begin{aligned} E(t) &= a\int\int f(x,y)\,\text{rect}\left(\frac{t-2R/c+2x/c+2y\theta/c}{T_p}\right) \\ &\quad \times e^{-i2\pi\nu_0(t-2R/c+2x/c+2y\theta/c)}\,dx\,dy. \end{aligned} \tag{2.50}$$

If $2y\theta/c \ll T_p$, that is $y\theta \ll cT_p/2 \equiv \delta r$, we can neglect this term in the argument of the rect function (this is just the requirement that the aspect not change enough to alter the target's projection). If the radar carrier $e^{-i2\pi\nu_0 t}$ is mixed out we then have

$$E(t) = ae^{i2\pi\frac{R}{\lambda/2}}\int\int f(x,y)\text{rect}\left(\frac{t-2R/c+2x/c}{T_p}\right) e^{-i2\pi\frac{x}{\lambda/2}} e^{-i2\pi\frac{\theta}{\lambda/2}y}\,dx\,dy. \tag{2.51}$$

We will refer to $E(t)$ as the "complex range profile." The received power,

$$p(t) = |E(t)|^2, \tag{2.52}$$

will be called simply the "range profile." We use this below to examine the statistics of profile fluctuations.

2.4 Range Profile Fluctuations

Because the field scattered from a range bin consists of the interference of scatter from (possibly) several distinct scattering centers, we expect that the intensity of the scattered field will change with target aspect. This is because the relative ranges to the scattering centers change, resulting in different relative phases between them. Here we will compute some first-order statistics of range bin intensity assuming a simple N-point-scatterers model.

Assume a range bin, at $x = 0$ say, consists of N scattering centers with cross range locations y_n, $1 \le n \le N$, and scattering amplitudes a_n. Then the reflectivity

distribution is

$$f(x,y) = \sum_{n=1}^{N} a_n \delta(x)\delta(y - y_n). \tag{2.53}$$

Using this in (2.51) results in a range profile which has the value

$$p(2R/c) = \left| \sum_{n=1}^{N} a_n e^{-i2\pi \frac{\theta}{\lambda/2} y} \right|^2 \tag{2.54}$$

for the backscatter from this range bin. Let's call this $I(\theta) \equiv p(2R/c)$. Expanding 2.54 gives

$$I(\theta) = \sum_{n=1}^{N} |a_n|^2 + 2 \sum_{n=1}^{N} \sum_{m=n+1}^{N} |a_n a_m| \cos\left(2\pi \frac{\Delta y_{nm}}{\lambda/2}\theta + \Delta\phi_{nm}\right), \tag{2.55}$$

where $\Delta y_{nm} = y_n - y_m$ and $\Delta\phi_{nm}$ is the phase difference between the scattering amplitudes a_n and a_m. For scatterers separated by about 1 m and illuminated by a radar of wavelength 3 cm, the cosine term will flip sign if θ changes by as little as 0.5°. In practice it is very difficult to estimate θ even to within ten times this. In fact the stated aspects for the profiles that we will use later have a resolution of 20°. Therefore, as we mentioned above, θ needs to be considered a random variable.

With θ treated as a uniformly-distributed random variable, we can compute the expected value

$$E[I(\theta)] = \sum_{n=1}^{N} |a_n|^2 \equiv I_0. \tag{2.56}$$

The variance of $I(\theta)$ is

$$\begin{aligned}
\sigma_I^2 &= E[(I(\theta) - I_0)^2] \\
&= E\left[\left(2 \sum_{n=1}^{N} \sum_{m=n+1}^{N} |a_n a_m| \cos\left(2\pi \frac{\Delta y_{nm}}{\lambda/2}\theta + \Delta\phi_{nm}\right)\right)^2\right] \\
&= 4 \sum_{n=1}^{N} \sum_{m=n+1}^{N} \sum_{n'=1}^{N} \sum_{m'=n'+1}^{N} |a_n a_m a_{n'} a_{m'}| \times \\
&\quad E\left[\cos\left(2\pi \frac{\Delta y_{nm}}{\lambda/2}\theta + \Delta\phi_{nm}\right) \cos\left(2\pi \frac{\Delta y_{n'm'}}{\lambda/2}\theta + \Delta\phi_{n'm'}\right)\right].
\end{aligned} \tag{2.57}$$

The expected value of each of these terms is zero unless $\Delta y_{nm} = \Delta y_{n'm'}$. This can happen in two ways. One is when $n = n'$ and $m = m'$. The other is when the same distance separates one set of scatterers as separates another set in the same range bin. This would be the case when the range bin contains some periodic structure. However, in this case the phase differences $\Delta\phi_{nm}$ and $\Delta\phi_{n'm'}$ introduce a phase shift between the cosines, and the product is as likely to be negative as to be positive, and on average will be zero. This leaves only the $n = n'$, $m = m'$ cases. Since

$$E\left[\cos^2\left(2\pi\frac{\Delta y_{nm}}{\lambda/2}\theta + \Delta\phi_{nm}\right)\right] = \frac{1}{2} \tag{2.58}$$

we have

$$\sigma_I^2 = 2\sum_{n=1}^{N}\sum_{m=n+1}^{N}|a_n a_m|^2. \tag{2.59}$$

Now consider some special cases. If all the scatterers have equal scattering strengths, $|a_n| = a$, then

$$I_0 = Na^2 \tag{2.60}$$

$$\sigma_I = \sqrt{2a^4\sum_{n=1}^{N}\sum_{m=n+1}^{N}1} = a^2\sqrt{N^2 - N}. \tag{2.61}$$

If $N > 2$ then

$$\sigma_I \approx Na^2 = I_0, \tag{2.62}$$

and the deviations of the range bin intensity are as large as its mean value. Another case of interest is when one of the scatterers is much stronger than the rest, say $|a_1| = a$, $|a_n| = \epsilon a$ for $n \neq 1$, and $\epsilon \ll 1$. In this case equations (2.56) and (2.59) can be evaluated to give

$$I_0 = a^2(1 + (N-1)\epsilon^2) \tag{2.63}$$

$$\sigma_I = a^2\epsilon^2\sqrt{2(N-1) + \epsilon^2(N-1)(N-2)} \tag{2.64}$$

as the range bin mean and standard deviation. For very small ϵ, $\epsilon \ll 1/\sqrt{N}$, these become

$$I_0 \approx a^2 \tag{2.65}$$

$$\sigma_I \approx a^2\epsilon^2\sqrt{2(N-1)}. \tag{2.66}$$

The factor $\epsilon^2\sqrt{2(N-1)}$ will be less than one, so the fluctuations are not as large as the mean a^2, but, as in the previous case, they are still proportional to the mean.

This result, that the fluctuations within a range bin are proportional to the mean value of the range bin, is bad news as far as target identification is concerned. To identify aircraft from their range profiles we want those profiles to contain strong, distinctive features. But the stronger the features, the more they will fluctuate, thereby limiting their usefulness. Note that the fluctuations discussed above are due strictly to aspect variations. For aircraft that have exposed moving parts, like propellers, there may be additional profile fluctuations due to the motion of these parts.

2.5 Optimal Correlation Filters

Despite the limitation imposed by fluctuations on the usefulness of range profiles for target identification, we expect that *on average* the profiles of one aircraft look more like one another than they look like those of another aircraft. If this is true then it should be possible to construct a *filter* for each target such that it correlates more strongly, on average, with the profiles of that target than with the profiles of other targets. This situation is depicted in Figure 2.4. A future profile from an unknown target could then be correlated against a library of filters for different known target types. The target type corresponding to the filter that produced the greatest

correlation would then serve as the identification for the unknown target.

Referring to (2.51), we see that a change in R causes the profile $p(t)$ to shift along the time axis an amount $2R/c$. For a moving aircraft R is usually continuously changing, and it is never known with great precision (i.e., to withing δr) *a priori*. This means that every radar profile contains some unknown shift along the time axis. Any target identification system using range profiles must therefore be shift invariant. A correlator satisfies this requirement since the correlation

$$(f \star p)(\tau) \equiv \int f(t)p(t+\tau)\,dt \tag{2.67}$$

is shift invariant. That is, if $p(t)$ is replaced by a shifted version of itself, say $\hat{p}(t) = p(t - t_0)$, the correlation is merely shifted by the same amount:

$$\begin{aligned}(f \star \hat{p})(\tau) &= \int f(t)\hat{p}(t+\tau)\,dt \\ &= \int f(t)p(t - t_0 + \tau)\,dt \\ &= (f \star p)(\tau - t_0).\end{aligned} \tag{2.68}$$

The peak of the correlation, which is what we will be interested in, remains the same. To simplify the notation, we will denote the functions $f(t)$ and $p(t)$ by the vectors $\mathbf{f}$ and $\mathbf{p}$. This is particularly appropriate since range profiles are typically sampled and manipulated as discrete vectors.

For a correlator to serve as an effective target recognition system, we need to produce filters that are as specific to a given target as possible. By specific we mean highly correlated with the radar profiles of that target. We want to find a filter $\mathbf{f}$ that maximizes $E[\max(\mathbf{f} \star \mathbf{p})]$, the expected or average value of the correlation peak between it and $\mathbf{p}$, where $\mathbf{p}$ is any randomly chosen profile of the target. The goal, as stated previously, is to create a bank of such filters

$$\mathbf{f}^{(1)}, \mathbf{f}^{(2)}, \ldots, \mathbf{f}^{(C)}, \tag{2.69}$$

one for each target, against which profiles from unknown targets can be correlated to produce numbers

$$\alpha^{(k)} = \max(\mathbf{f}^{(k)} \star \mathbf{p}) \tag{2.70}$$

(correlation peaks) with the hope that

$$\alpha^{(j)} > \alpha^{(k)} \quad \text{for all } k \neq j, \tag{2.71}$$

where the j^{th} filter is the "correct" one, i.e., the one that was produced to be specific to the unknown target.

In practice we have N profiles recorded for a given target sometime in the past, and the task is to use these profiles to estimate the optimal filter that will maximize the correlation peak with all future profiles from the same target. Towards this end we form the estimate

$$E[\max(\mathbf{f} \star \mathbf{p})] \approx \frac{1}{N} \sum_{n=1}^{N} \max(\mathbf{f} \star \mathbf{p}_n) \tag{2.72}$$

where $\{\mathbf{p}_1, \mathbf{p}_2, \ldots, \mathbf{p}_N\}$ is the set of previously recorded radar profiles for one particular target. *If we knew what* $\mathbf{f}$ *was* then we could shift each profile $\mathbf{p}_n$ into a new profile $\hat{\mathbf{p}}_n$ such that

$$\max(\mathbf{f} \star \mathbf{p}_n) = \mathbf{f} \cdot \hat{\mathbf{p}}_n, \tag{2.73}$$

where

$$\mathbf{f} \cdot \hat{\mathbf{p}}_n = \int f(t) p_n(t)\, dt \tag{2.74}$$

is the inner product of $\mathbf{f}$ and $\hat{\mathbf{p}}_n$. In other words, we could shift the profiles to be "aligned" with the filter. Then we would have

$$\begin{aligned} E[\max(\mathbf{f} \star \mathbf{p})] &\approx \frac{1}{N} \sum_{n=1}^{N} \mathbf{f} \cdot \hat{\mathbf{p}}_n \\ &= \mathbf{f} \cdot \frac{1}{N} \sum_{n=1}^{N} \hat{\mathbf{p}}_n. \end{aligned} \tag{2.75}$$

We want to maximize this inner product by choosing $\mathbf{f}$ properly. Note that we can always increase this by simply increasing the absolute scale of $\mathbf{f}$, but this will proportionally increase $\mathbf{f}$'s correlation with *all* other vectors. Therefore we constrain $\mathbf{f}$ to be a unit vector. The unit vector $\mathbf{f}$ which maximizes (2.75) is simply

$$\mathbf{f} = \frac{\sum_{n=1}^{N} \hat{\mathbf{p}}_n}{\| \sum_{n=1}^{N} \hat{\mathbf{p}}_n \|}, \tag{2.76}$$

with the result that

$$\begin{aligned} E[\max(\mathbf{f} \star \mathbf{p})] &\approx \frac{1}{N} \frac{\sum_{n=1}^{N} \hat{\mathbf{p}}_n \cdot \sum_{n=1}^{N} \hat{\mathbf{p}}_n}{\| \sum_{n=1}^{N} \hat{\mathbf{p}}_n \|} \\ &= \frac{1}{N} \| \sum_{n=1}^{N} \hat{\mathbf{p}}_n \|. \end{aligned} \tag{2.77}$$

While we don't known $\mathbf{f}$ *a priori*, the above analysis makes it clear that the largest $E[\max(\mathbf{f} \star \mathbf{p})]$ can be is $\frac{1}{N} \| \sum_{n=1}^{N} \hat{\mathbf{p}}_n \|$ and that the filter that achieves this is given by (2.76). Therefore we need only find the shifts that maximize $\frac{1}{N} \| \sum_{n=1}^{N} \hat{\mathbf{p}}_n \|$ and then evaluate (2.76) and we have computed the desired optimal correlation filter.

The practical difficulty is how to find the shifts that take $\{\mathbf{p}_1, \mathbf{p}_2, \ldots, \mathbf{p}_N\}$ into the set $\{\hat{\mathbf{p}}_1, \hat{\mathbf{p}}_2, \ldots, \hat{\mathbf{p}}_N\}$ which gives the optimal filter via (2.76). A global search over all possible shifts is out of the question. For example, suppose $N = 100$ and we need to consider 10 possible shifted versions of each profile. Then there are 10^{100} different configurations $\{\hat{\mathbf{p}}_1, \hat{\mathbf{p}}_2, \ldots, \hat{\mathbf{p}}_N\}$ possible and there is no hope of being able to examine each of these.

One possibility is an iterative procedure where a global search is performed over only the possible shifts of one profile at a time. To see how this can be carried out we write

$$\begin{aligned} \| \sum_{n=1}^{N} \hat{\mathbf{p}}_n \|^2 &= \| \hat{\mathbf{p}}_j + \sum_{k \neq j} \hat{\mathbf{p}}_k \|^2 \\ &= \| \hat{\mathbf{p}}_j \|^2 + \| \sum_{k \neq j} \hat{\mathbf{p}}_k \|^2 + 2 \hat{\mathbf{p}}_j \cdot \sum_{k \neq j} \hat{\mathbf{p}}_k \end{aligned} \tag{2.78}$$

where $\hat{\mathbf{p}}_j$ is any one of the profiles. The only term that will change when we shift $\hat{\mathbf{p}}_j$ is

$$2\hat{\mathbf{p}}_j \cdot \sum_{k \neq j} \hat{\mathbf{p}}_k \tag{2.79}$$

and increasing this will increase the quantity we are trying to maximize. Therefore, with respect to shifts of $\hat{\mathbf{p}}_j$, we are doing the best we can do if we make

$$\hat{\mathbf{p}}_j \cdot \sum_{k \neq j} \hat{\mathbf{p}}_k \tag{2.80}$$

as big as possible. Having done this for one profile we can go on to do it for the others and then start the process over. Each shift increases $\| \sum_{k=1}^{N} \hat{\mathbf{p}}_k \|$. Since there are a finite number of configurations $\{\hat{\mathbf{p}}_1, \hat{\mathbf{p}}_2, \ldots, \hat{\mathbf{p}}_N\}$ (assuming discrete profiles) we cannot go on increasing indefinitely. Eventually we will reach a maximum. Note that this is not guaranteed to be a global maximum. The technique is analogous to iterative line maximization techniques used to find extrema of functions of several variables [44], and it may potentially suffer the same problems of local maxima. However, in the applications described below, we investigated this problem by starting with many different initial profile configurations, and we found that the algorithm always converged to the same filter.

Below, we use this algorithm to form correlation filters from observed aircraft radar range profiles, and we then use these filters to attempt to identify the various aircraft. We begin with a description of the data set employed.

2.6 The Data Set

The data set used in this chapter consists of 11,968 radar profiles obtained by an experimental radar at the Air Force's Rome Air Development Center (RADC). The profiles consist of 200 range bins with a range resolution of approximately 0.5 meters.

They are grouped in sets of about 100 profiles each called an *encounter*. Each encounter arose from a several-second series of observations of a single aircraft in flight. There are 119 encounters in all. Within each encounter the profiles are grouped into *frames* of eight profiles each. The profiles within a frame were collected 2.5 milliseconds apart. An average of 12 frames were collected during each encounter. In between frames a few seconds were devoted to tracking the target and to storing the previous frame of data. The tracking data allowed the (nominally constant) aspect of the target to be estimated to within approximately 20°. The target type was known from an identifying code that each target transmitted. The actual target identities are classified, but for use in unclassified situations they are assigned arbitrary numbers, e.g., 01, 15, 23. Thus each encounter consists of roughly 100 profiles of a given target type at a given (estimated) aspect. Twenty-four distinct targets are represented in the data set. Not all are represented with equal frequency, for example, there was only a single encounter with target 15 but ten with target 05.

We had little technical information available to us concerning the absolute calibration of the radar. Without precise calibration data the absolute scale of the profiles is meaningless. Therefore we have removed all scale considerations from the profiles by normalizing each of them to have unit amplitude. That is, if $p(k)$, $1 \leq k \leq 200$, is a radar profile with k indexing the different range bins, we scaled the profile so that

$$\sum_{k=1}^{200} p^2(k) = 1. \tag{2.81}$$

The result is that we will only be concerned with a profile's shape and not with its overall relative amplitude. As far as the targets are concerned, this means that we are only concerned with the relative distribution of radar cross section over the different range bins and not with the absolute cross section.

While it is not practical to present all 11,968 profiles to the reader, the 119 plots in

Figures 2.6 through 2.20 present *mean* profiles for each encounter (solid curves) and its standard deviation (dotted curves). Note that the standard deviation generally follows the mean as we would expect from the analysis of section 2.4. The means were calculated by using the algorithm of section 2.5. Above each plot are five expressions separated by commas. The first is the designation of the target for that encounter, e.g., 01, 15. The second gives the estimated aspect in degrees, e.g., 0-20, 20-40, ..., 160-180. The third is a numerical designation of the encounter used for cataloging, e.g., 13.02 (this corresponds to the RADC tape file CONT13_ENC02.DAT). The fourth is a measure of the degree of *clustering* of the profiles in the encounter. It is the average value of the correlation between the profiles and their means in percent and is described in more detail in section 2.8. If all the profiles in an encounter were identical then this would have a value of 100; if they were completely unrelated this would have a value of 0. The fifth is the rate of correct identification (in percent) for the profiles of the encounter's test set obtained in the correlation experiment described below.

2.7 Correlation Experiments

The goal of this chapter is to investigate the degree to which a bank of correlation filters can identify aircraft from their radar range profiles. We have seen how a series of profiles can be used to estimate the filter that maximizes the expected value of the correlation peak with future profiles from the same target. We now want to see how well these filters perform in practice.

The 11,968 profiles in the data set were divided into a *training set* of 6,256 profiles and a *test set* of 5712 profiles. This was done by assigning the 8 profiles of each odd numbered frame of an encounter to that encounter's training set and the even

numbered frames to its test set. Profiles within a frame were not split between the training and test sets as this would create an unrealistically optimistic scenario; in practice it is very unlikely that we will see a target from exactly the same aspect as we have in the past. The relatively long time between frames allows the aspect to change enough to give us distinct aspects in the training and test sets.

With the profiles from each encounter suitably divided into training and test sets, the training profiles (roughly 50) of each encounter were used with the algorithm of section 2.5 to produce a correlation filter for that encounter. The result was a bank of 119 filters. Although there were instances where a given target at a given aspect was represented in more than one encounter, e.g., the first five average profiles of Figure 2.6, these encounters were not grouped together to form a single filter due to the crude nature of the aspect estimates. From the previous discussion of the geometric distortion of a profile due to range migration we known that we want to limit our aspect window to $\sim 5°$ or less; the $20°$ resolution of the aspect estimates is much coarser than this.

Having produced a filter bank, we then attempted to use it to identify the profiles of the test set. Each profile of the test set was correlated against each of the 119 filters. The profile was identified as belonging to the target whose filter produced the greatest correlation peak. If this was the actual target that produced the test profile then the identification was judged correct, otherwise it was incorrect. The percentage correct for each encounter is given by the last number above the mean profiles plots of Figures 2.6 through 2.20. The cumulative result for the entire test set was 3262 correctly identified out of 5712 profiles tested for a correct-identification rate of 57%. Note that random guessing would give a correct-identification rate of $1/24 = 4\%$, since there are 24 distinct targets represented in the data set.

2.8 Factors Affecting Identification

While the overall correct-identification rate was 57%, examination of the rates for individual encounters (Figures 2.6 through 2.20) shows rates from a low of 0% to a high of 100%. What accounts for this wide variation? An obvious statement is that profiles that are very distinctive can be easily identified while profiles that are not distinctive cannot be. This is essentially analogous to saying that profiles that can be easily identified can be easily identified, and those that cannot cannot. This does not provide much insight into the problem. We would like to see if there are any simple properties of profiles that give an indication of how well they can be identified. This could be useful in practice as it could serve as a guide to how much faith to put into the identification of any particular profile that might be observed.

The most obvious factor that would seem likely to affect the rate at which we can correctly identify profiles is the degree to which they fluctuate. If the profile of a target fluctuates significantly then it will be difficult for a filter to capture its essential features. The amount of fluctuation is quantitatively described by the standard deviation curves of Figures 2.6 through 2.20 (the dotted curves). To describe the overall fluctuations of the profiles of an encounter we can measure the average correlation of the profiles with their mean. This describes the degree to which the profiles are *clustered.* If all the profiles were identical then the average correlation would be 100%; the profiles would be highly clustered. If they were completely unrelated, the average correlation would drop to 0%; the profiles would be poorly clustered. This average correlation is given as the next-to-the-last number above each of the mean profile plots of Figures 2.6 through 2.20. They vary from 79% to 93%. The most poorly clustered encounter had a correct-identification rate of 0% while the encounter with the highest degree of clustering had a rate of 100%, indicating that the degree of

clustering is a factor in determining how well a target may be identified. Figure 2.21 is a plot of the correct-identification rate versus the degree of clustering for all 119 encounters (the open squares). Also plotted is a linear regression to these data. The data are so scattered that the regression is not very meaningful, however, it does suggest a trend towards more reliable identification with increasing clustering.

Unfortunately, the data set was not collected under controlled conditions, i.e., with precise knowledge of target aspects, nor do we know which, if any, of the targets had exposed moving parts (because we don't know what the target really were). Therefore, we cannot be certain of the causes of the fluctuations and if they are indicative of target structure. As we described in section 2.4, targets with range bins dominated by single scatterers tend to have lower fluctuations than targets with several strong scatterers per range bin. At the same time it is conceivable, although not likely, that some of the aircraft maintained very stable aspects over the several seconds of their encounter, and this would also result in small fluctuations.

Another important factor affecting the correct-identification rate comes to light if we examine some of the cases in Figure 2.21 where a high degree of clustering does not lead to reliable identification. The most notable of these are labeled with their encounter designation: 21.02, 16.03, 19.01. Examining the mean profiles of these encounters in Figures 2.20, 2.18, and 2.19, respectively, we see that they are all dominated by a single strong peak with little other significant structure. Effectively these targets appear as little more than point scatterers. Since their profiles have very little distinctive structure they are very difficult to correctly identify; they all look pretty much the same. A relatively small fluctuation in any of these profiles can destroy whatever distinctiveness it may have had. We can quantify the degree to which the profiles of an encounter are dominated by a single peak by measuring the peak of the encounter's filter. Since the filter, $f(n)$, $1 \leq n \leq 200$, is normalized we

have

$$\sum_{n=1}^{200} f^2(n) = 1, \tag{2.82}$$

and so

$$f(k) = \sqrt{1 - \sum_{n \neq k} f^2(n)}. \tag{2.83}$$

Assume $f(k)$ is the peak value of the filter. If the filter has lots of structure, i.e., significant amplitudes in several range bins, then $\sum_{n \neq k} f^2(n)$ will be large and $f(k)$ will be small. On the other hand, if the profile consists of a single range bin then $\sum_{n \neq k} f^2(n) = 0$ and $f(k)$ will be as large as possible, namely $f(k) = 1$. Therefore, the value of the strongest profile peak gives a measure of the "peakedness" of the profile. In Figure 2.22 the correct-identification rate is plotted versus the filter peak for each of the 119 encounters together with a linear regression to the data. Again the data are quite scattered but the regression suggests a trend towards less reliable identification with increasing filter peak, hence more reliable identification with greater filter structure.

The mutual dependence of the correct-identification rate on both of these factors is displayed in Figure 2.23. Here different correct-identification rates are shown as different symbols, each symbol corresponds to a single encounter, and the location of the symbol in the plot gives both the filter peak and the degree of clustering of the profiles of the encounter. This plot shows that, generally, encounters with a high correct-identification rate are either well clustered (large within encounter correlation) or have a small filter peak (hence lots of structure) or some combination of the two.

An interesting question is: Does the correct-identification rate depend on target aspect? We might expect that it would since profiles from aircraft at broadside incidence (aspect of 90°) are likely to be dominated by the point-like scatter from their fuselage (since the entire fuselage will be at essentially the same range) and so

we would have the problems associated with highly peaked profiles discussed above. On the other hand, we would expect profiles from aircraft at nose-on or tail-on aspects (aspects of 0° or 90°, respectively) to have more structure since the fuselage is now stretched out along the line-of-sight. Figure 2.24 shows the dependence of the correct-identification rate on target aspect. There is considerable scatter as in the previous plots but the quadratic regression to the data show the trend towards more reliable identification near nose-on and tail-on aspects.

2.9 Identification Using Multiple Profiles

When the profiles of a target are impulse-like there is little that can be done to increase their usefulness for identification since they simply do not contain enough information. However, if the difficulty arises from profile fluctuations then the possibility exists to use the identification of more than one profile to improve the probability of correctly identifying the target. While the profiles of a particular target may be so poorly clustered that several of them, even the majority of them, get incorrectly identified, if the incorrect identifications are spread out over several targets it may well be that more profiles are identified as belonging to the correct target than are identified as belonging to any *single* incorrect target. For example, suppose profiles from target A are so poorly clustered that of 10 only 3 are correctly identified as belonging to target A while 2 are identified as belonging to target B, 2 to target C, and one each to targets D, E, and F. While only 30% of the profiles are correctly identified, more are identified as belonging to target A than are identified as belonging to any other single target, i.e., A has gotten more identification "votes" than any other target. Alternately, we can think of this as a *decision integration* process where we base our final identification on the average identification over many profiles.

We applied this reasoning to the RADC profiles. A correlation was run in which not only individual profiles were identified but frames and entire encounters were also using decision integration. The 57% correct-identification rate for individual profiles rose to 65% for frames and to 86% for encounters. In several cases encounters with less than 50% profile rates were correctly identified based on the entire encounter test set. For example, encounter 16.08 (target 11) and encounter 02.06 (target 04) both had 23% correct-identification rates for individual profiles but were correctly identified using decision integration at the encounter level.

In order to record a series of profiles, a radar must dwell on the target for a period of time. During this time the target will have moved, and the changes in range, bearing, and altitude that the radar must make to track the target will provide information about the target's flight path and hence about its aspect. It will be possible in practice, therefore, to utilize an estimate of target aspect when attempting to perform identification based on a series of profiles. Accordingly, we performed an identification experiment in which each profile was correlated against only those filters that shared its estimated aspect. Again, we applied decision integration to both frames and entire encounters.

The results are given in Table 2.1. We see that decision integration significantly improves the rates of correct identification, especially when combined with aspect information. Of particular interest is the 100% rate for nose-on aspects (near 0°) using decision integration at the encounter level, especially since there are enough encounters and targets at this aspect (33 and 13, respectively) to suggest that this result is meaningful. This aspect is, for obvious reasons, the most critical for military scenarios.

2.10 Optical Correlator Implementation

The ability of a simple converging lens to compute a Fourier transform, and the ability of a spatial light modulator to perform many analog multiplications in parallel, give optical correlators potential advantages in speed and power requirements over digital systems. Digital systems, however, can be configured to have an arbitrarily large dynamic range while the dynamic range of optical spatial light modulators is necessarily limited by device characteristics. If a spatial light modulator's dynamic range is less than the dynamic range of the data put into it then information present in the data is lost. The more information that is lost the less likely it is that the optical correlation will accurately represent an ideal correlation. Advantages in speed and power requirements are irrelevant if the obtainable accuracy is less than that needed to provide discrimination.

A binary spatial light modulator (BSLM) imposes the most extreme limit on dynamic range of all, and so would not seem to have a place in systems that process analog signals. However, if the functions to be correlated are one-dimensional and the BSLM is two-dimensional, we can use the extra degree of freedom in the BSLM to encode amplitude and thereby gain the ability to perform analog correlations. Figure 2.25 shows a simple system that uses two-dimensional BSLMs to perform one-dimensional analog correlations. The correlations are performed in the x dimension; the y dimension is used to encode amplitude information.

Suppose we wish to correlate a real-valued function $p(x)$ against a real-valued function $f(x)$. We proceed as follows. We form a two-dimensional, binary function $g(x,y)$ such that

$$p(x) = \int g(x,y)dy.$$

(For example, we could form $g(x,y)$ by turning on (setting equal to 1) strips in the

y direction of length $p(x)$.) In the same manner we also form a function $h(x,y)$ such that

$$F^*(x) = \int h(x,y)dy,$$

where F is the Fourier transform of f. Since F will, in general, be complex, h will also be complex. Therefore we need to put h on the BSLM in holographic form. We simply form a real, binary function $\hat{h}(x,y)$ such that

$$Re\left(F^*(x)e^{i2\pi u_c x}\right) = \int \hat{h}(x,y)dy,$$

where u_c is the highest spatial frequency in $F(x)$, and put this on the BSLM . The carrier ensures that the diffracted orders will be spatially separated at the detector D. The system then behaves as if the complex function $h(x,y)$ were present.

The system operates as follows. Lens $L1$ Fourier transforms g. Spatial filter SF allows only the d.c. component in y to pass. Lenses $L2$ and $L3$ (essentially) inverse Fourier transform this in y and image it in x. The result is to produce a field in the plane of $h(x,y)$ which is

$$\int\int g(x',y')e^{i2\pi xx'}dx'dy'.$$

Since

$$\int g(x',y')dy' = p(x')$$

this field is just

$$\int p(x')e^{i2\pi xx'}dx' = P(x).$$

The second BSLM multiplies this by $h(x,y)$. Lens $L4$ (essentially) inverse Fourier transforms this product producing a field

$$\int\int P(x')h(x',y')e^{i2\pi(xx'+yy')}dx'dy'.$$

Detector D samples the intensity of this field along the line $y = 0$. Hence the output is

$$\left| \int \int P(x')h(x', y')e^{i2\pi xx'} dx'dy' \right|^2 .$$

But

$$\int h(x', y')dy' = F^*(x'),$$

so the detected field is

$$\left| intP(x')F^*(x')e^{i2\pi xx'} dx' \right|^2 .$$

By the convolution theorem, this is just

$$|p(x) \star f(x)|^2.$$

Therefore we have performed an analog correlation using BSLMs.

Actual BSLMs are not continuous in x and y but rather composed of discrete pixels. If N is the number of pixels in one dimension then the BSLM can hold N samples of a function with $N + 1$ gray levels (from 0 to N in steps of 1 or from $-N$ to N in steps of 2 for bipolar modulation). Hence, if the space bandwidth product of the functions $p(x)$ and $f(x)$ are no more than N, and if their dynamic range (as determined by the signal to noise level) is no more than N, then a correlator of the type just described implemented with discrete N by N BSLMs can accurately compute the correlation between $p(x)$ and $f(x)$. The RADC data require $N \approx 256$. BSLMs with this resolution are commercially available.

2.11 Conclusion

In this chapter we have examined the feasibility of identifying aircraft using their radar range profiles. It was shown that very small aspect changes can result in large

profile fluctuations. A technique was developed for using a set of radar range profiles to compute a correlation filter that is optimal in the sense that it produces the maximum average correlation peak with those profiles. This technique was applied to the RADC data set. Individual profiles were correctly identified at an overall rate of 57%, although rates varied from 0% to 100% for specific targets. Some of the factors affecting the correct-identification rate were examined. A trend towards more reliable identification near noise-on or tail-on aspects was found. By "averaging" the identifications over the eight profiles of a frame a correct-identification rate of 65% was achieved while averaging identifications over entire encounters (roughly 48 profiles) resulted in a correct-identification rate of 86%. If, in addition, aspect estimates were employed, correct-identification rates of 100% were achieved in most cases. It seems clear that a *single* radar profile does *not* contain enough information to reliably identify aircraft due to the fluctuation problem discussed above. However, we have shown that by averaging identifications and using aspect estimates, reliable identification may be possible. Finally, an optical correlator architecture was developed that utilizes two-dimensional, binary spatial light modulators, and that can be used to implement the identification process at high speeds.

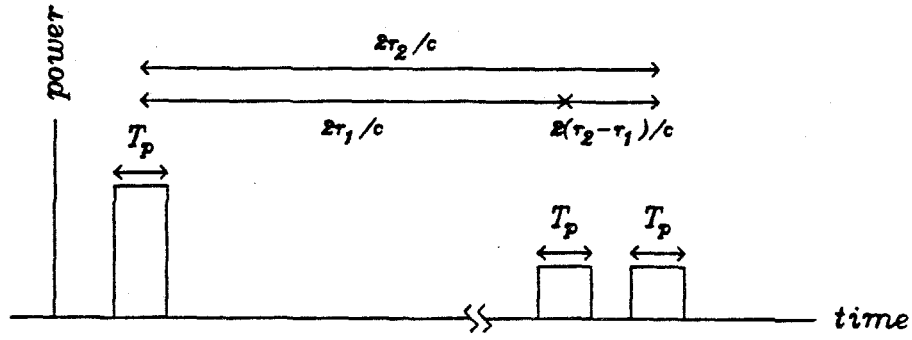

Figure 2.1: Resolution of two point scatterers using pulsed-cw waveform.

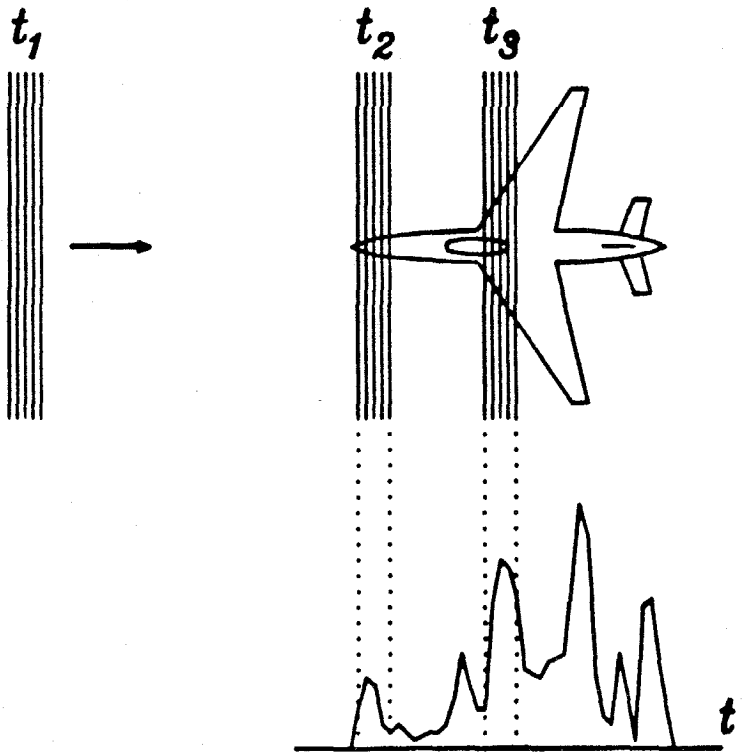

Figure 2.2: Relation of a radar range profile to a target. The radar (off to the left of the illustration) illuminates the target with a short pulse (if pulse compression is used the same effect is achieved after some signal processing). At different times (e.g., t_2, t_3) the pulse illuminates different strips, or range bins, on the target. The result is that the received range profile, i.e., the received backscattered power as a function of time, is a one-dimensionally resolved image of the target.

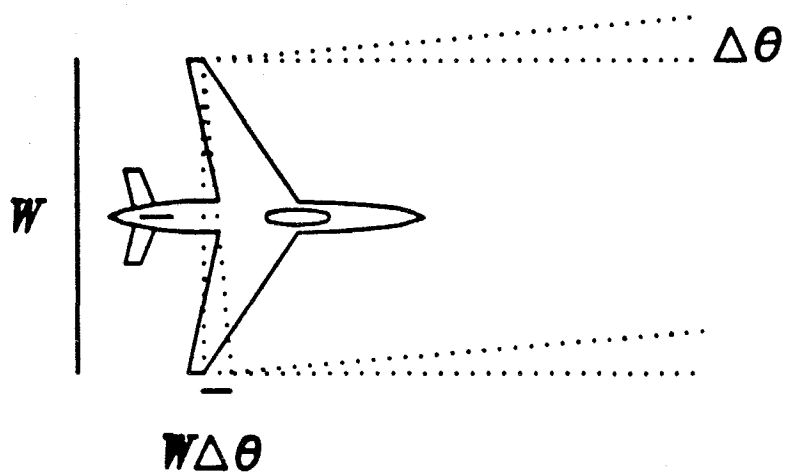

Figure 2.3: A change in target aspect causes relative changes in the ranges to different scattering centers within a given range bin. If this relative change is as little as a quarter of the radar wavelength then the range profile may fluctuate considerably as constructive interference becomes destructive interference and *vice versa.*

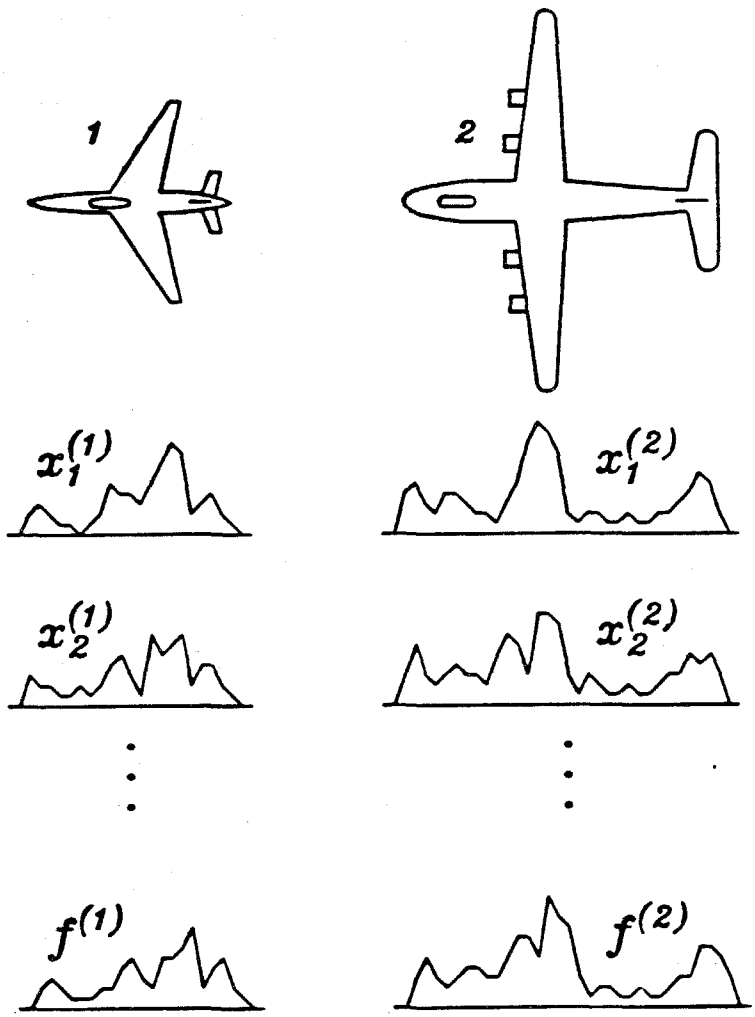

Figure 2.4: Producing filters from a series of range profiles. The profiles of a given target, e.g., target 1 or 2 above, fluctuate in time and so no two look alike. However, they may look more like one another than they look like those of another target. The profiles $\mathbf{x}_1^{(1)}, \mathbf{x}_2^{(1)}, \ldots$ of target 1 are all different, but hopefully they look more like one another than they look like any of the profiles of target 2, $\mathbf{x}_1^{(2)}, \mathbf{x}_2^{(2)}, \ldots$. If so, then filters $\mathbf{f}^{(1)}$ and $\mathbf{f}^{(2)}$ can be produced to identify the profiles of target 1 and 2 via correlation.

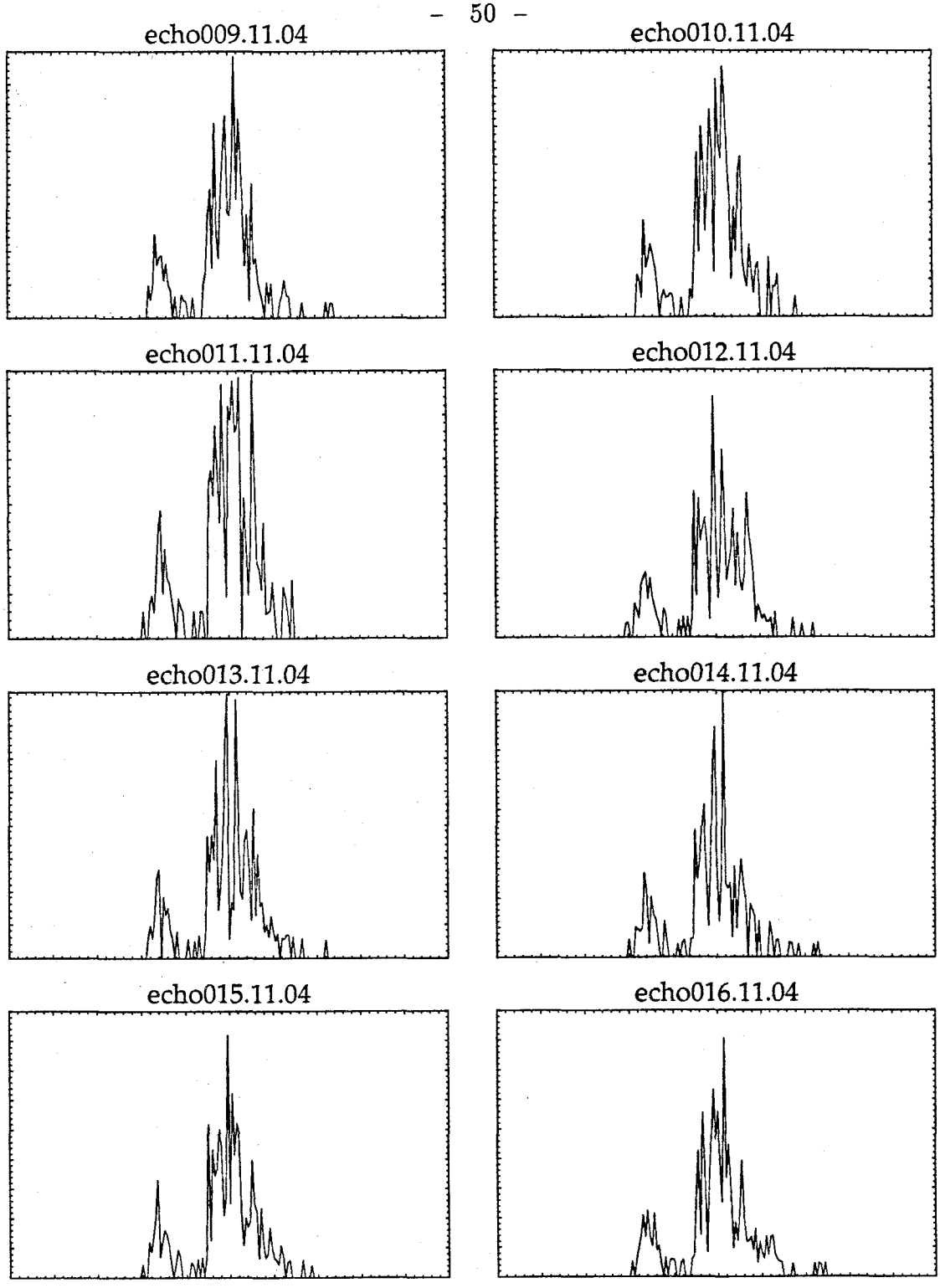

Figure 2.5: Example of range profile fluctuations. These eight range profiles of a flying aircraft were collected only 2.5 msec apart, yet their shapes differ significantly.

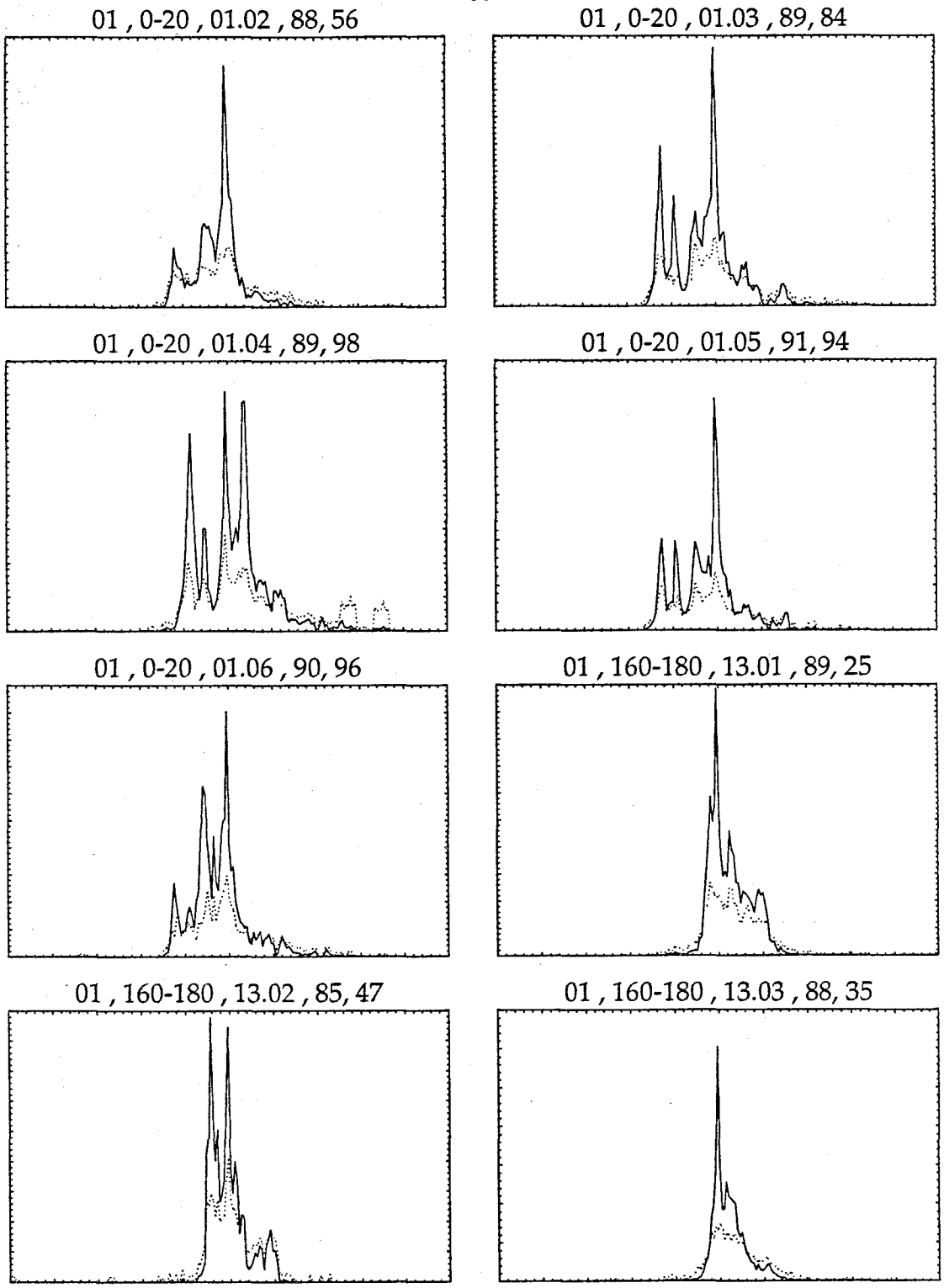

Figure 2.6: Average profile of RADC encounters (solid curve) and RMS fluctuation (dotted curve). Numbers at top are: target type, aspect (degrees), encounter designation, degree of clustering (percent), rate of correct identification (percent).

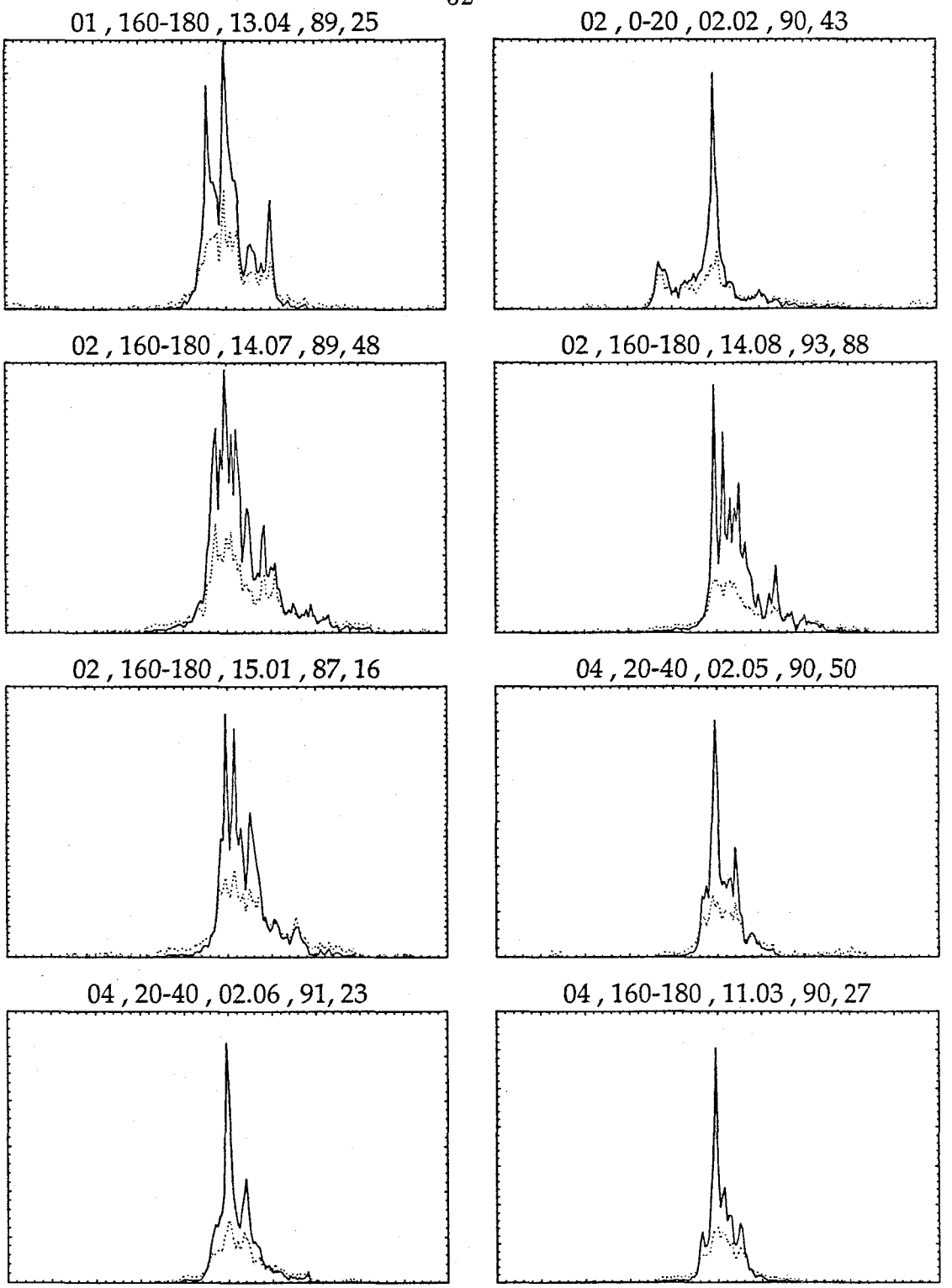

Figure 2.7: Average profile of RADC encounters (solid curve) and RMS fluctuation (dotted curve). Numbers at top are: target type, aspect (degrees), encounter designation, degree of clustering (percent), rate of correct identification (percent).

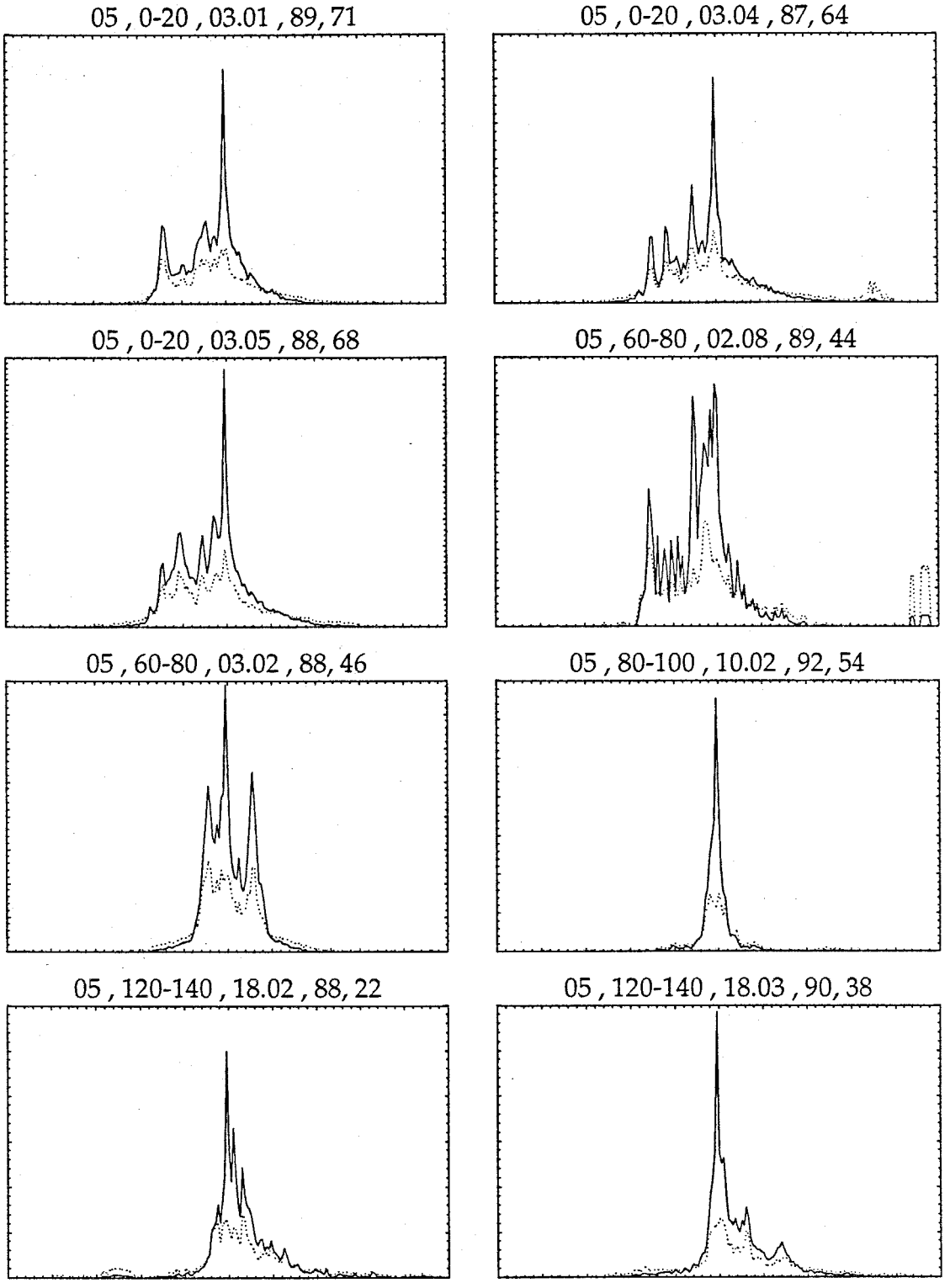

Figure 2.8: Average profile of RADC encounters (solid curve) and RMS fluctuation (dotted curve). Numbers at top are: target type, aspect (degrees), encounter designation, degree of clustering (percent), rate of correct identification (percent).

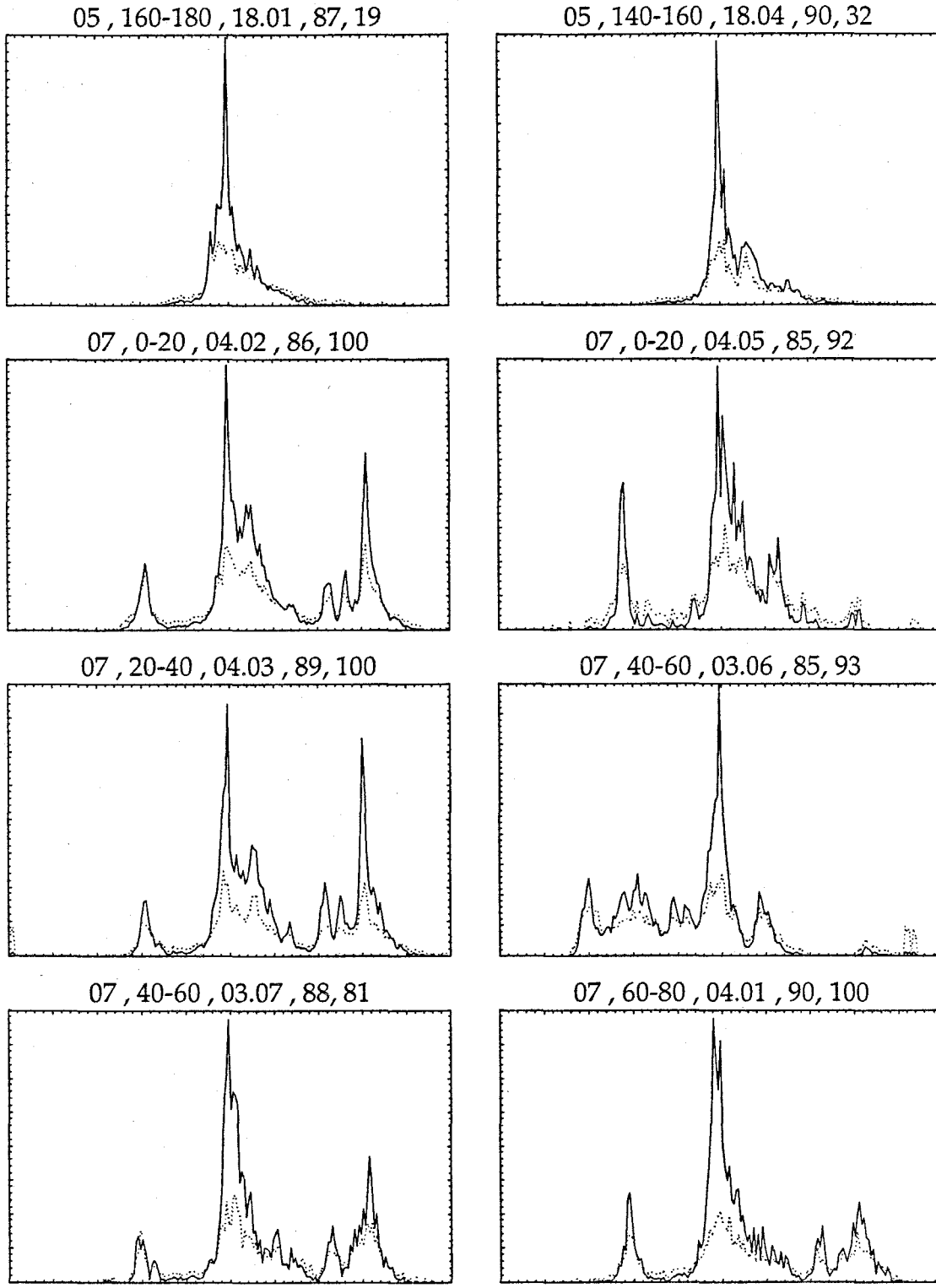

Figure 2.9: Average profile of RADC encounters (solid curve) and RMS fluctuation (dotted curve). Numbers at top are: target type, aspect (degrees), encounter designation, degree of clustering (percent), rate of correct identification (percent).

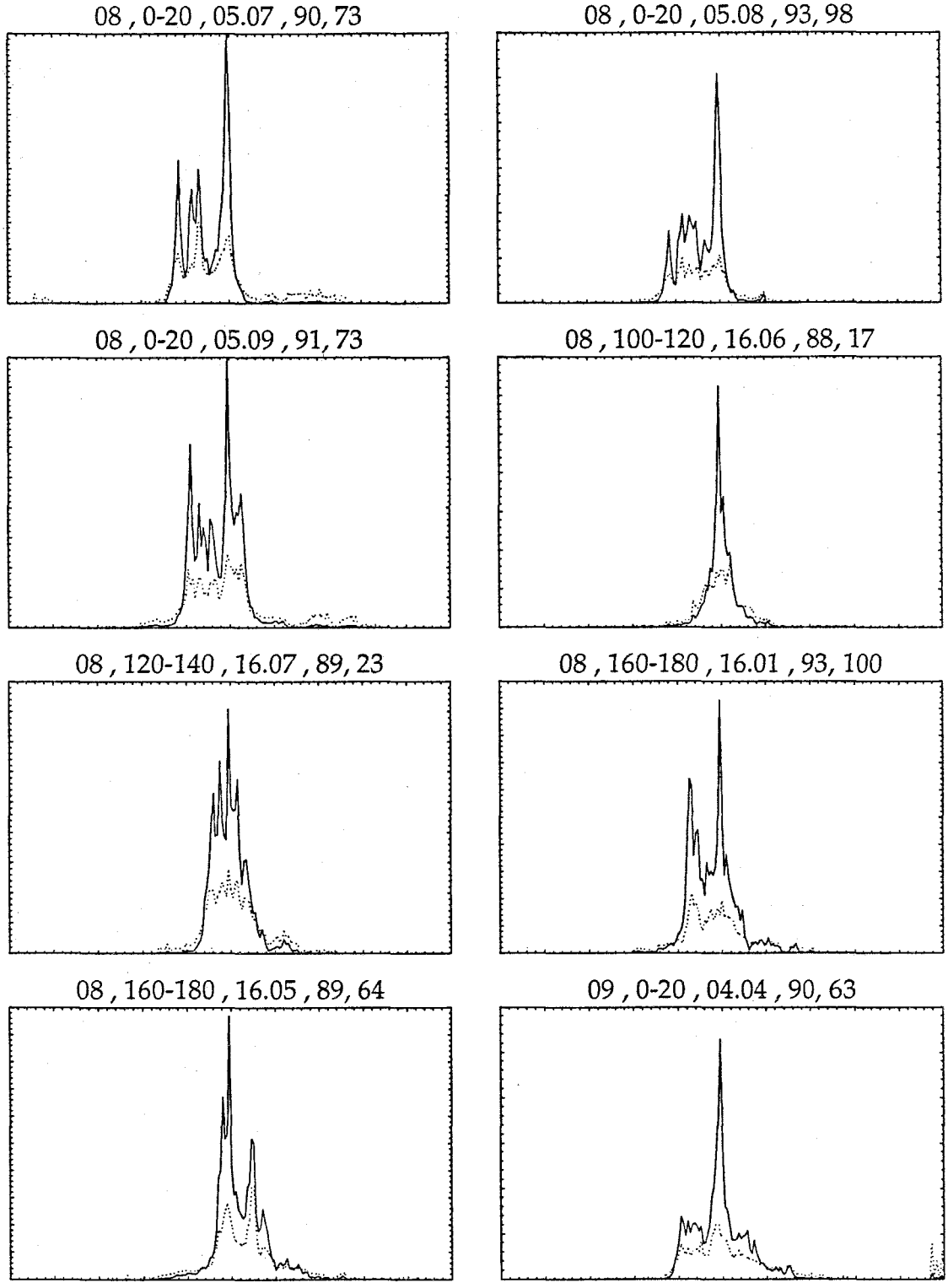

Figure 2.10: Average profile of RADC encounters (solid curve) and RMS fluctuation (dotted curve). Numbers at top are: target type, aspect (degrees), encounter designation, degree of clustering (percent), rate of correct identification (percent).

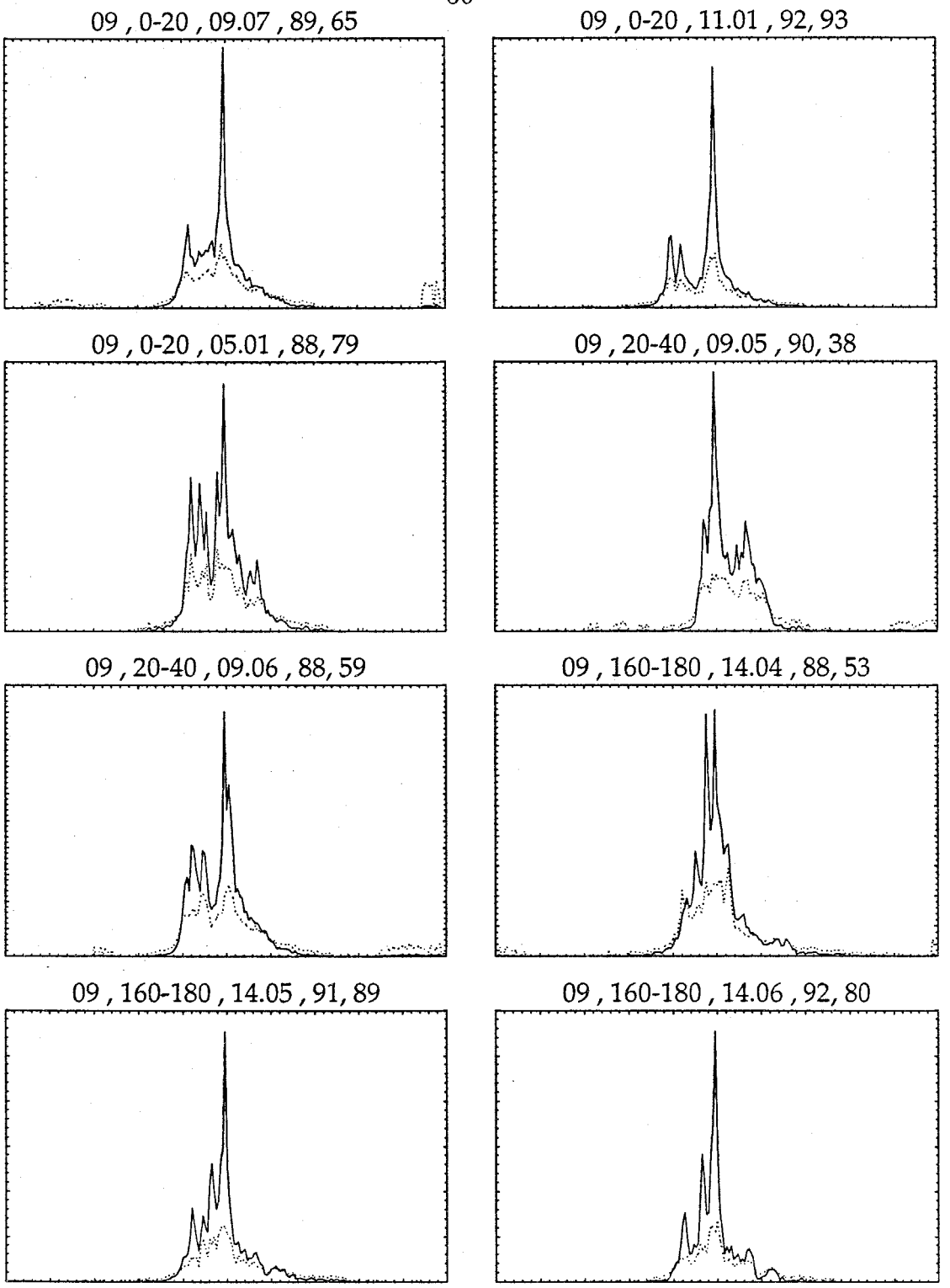

Figure 2.11: Average profile of RADC encounters (solid curve) and RMS fluctuation (dotted curve). Numbers at top are: target type, aspect (degrees), encounter designation, degree of clustering (percent), rate of correct identification (percent).

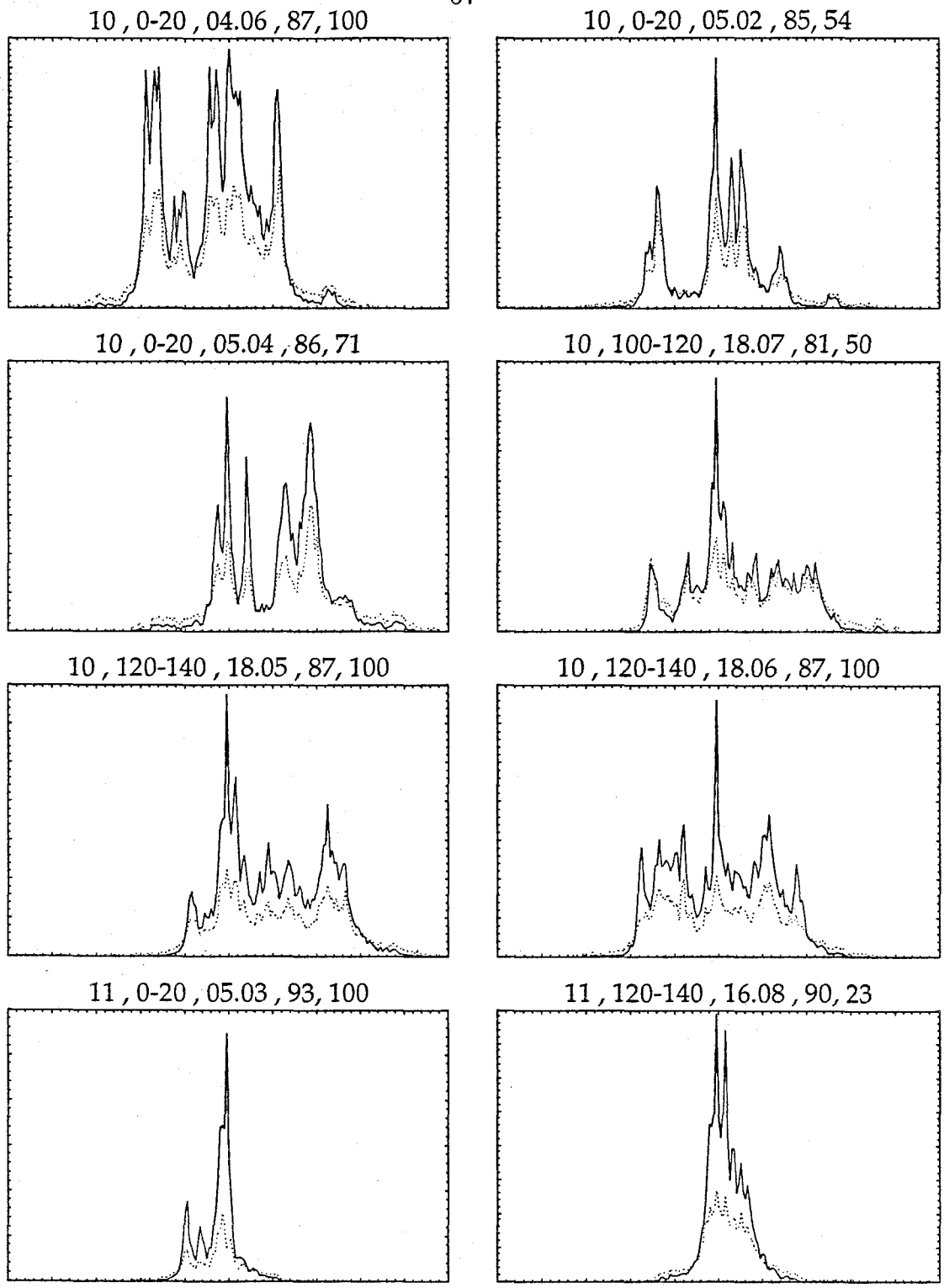

Figure 2.12: Average profile of RADC encounters (solid curve) and RMS fluctuation (dotted curve). Numbers at top are: target type, aspect (degrees), encounter designation, degree of clustering (percent), rate of correct identification (percent).

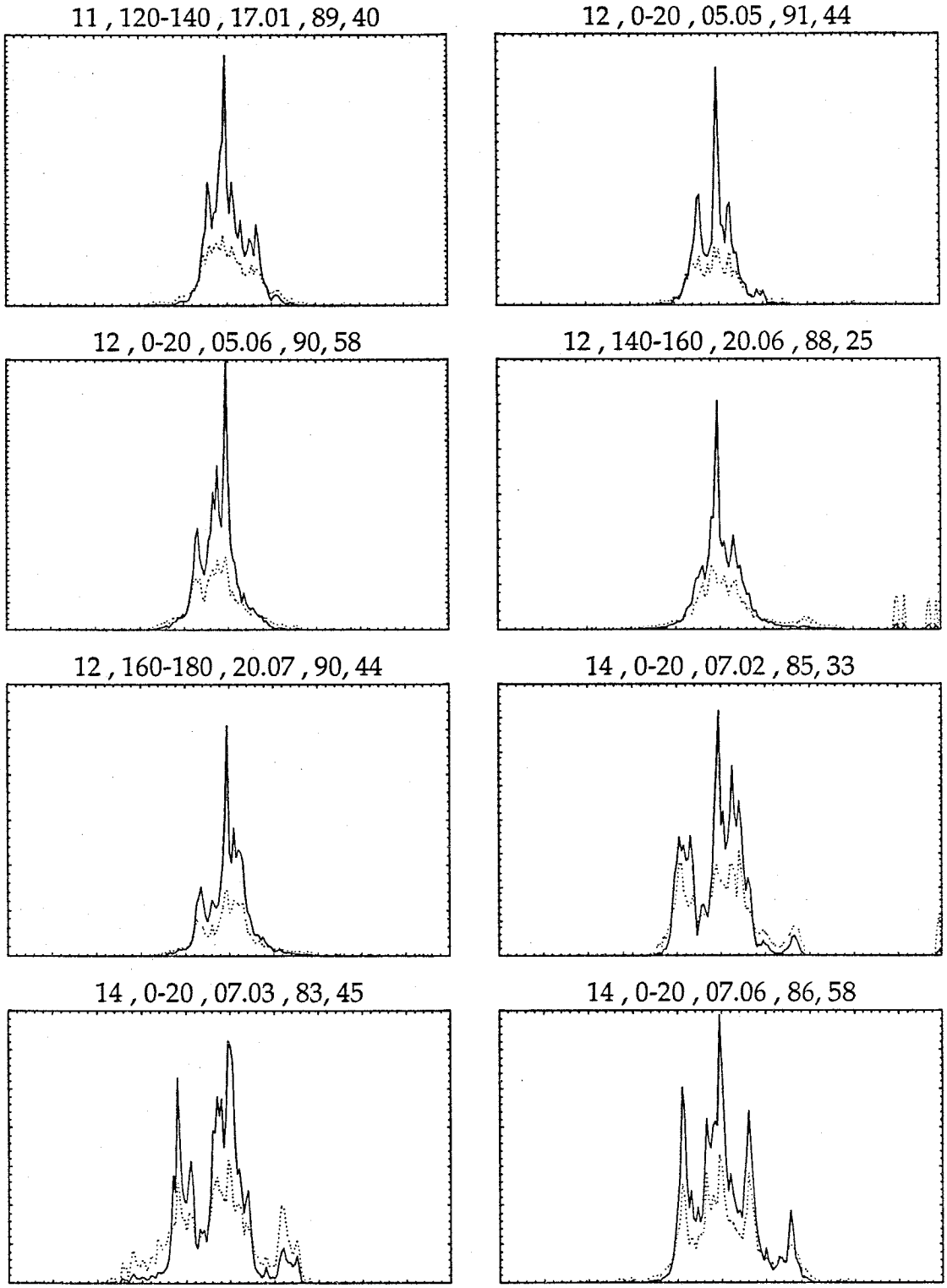

Figure 2.13: Average profile of RADC encounters (solid curve) and RMS fluctuation (dotted curve). Numbers at top are: target type, aspect (degrees), encounter designation, degree of clustering (percent), rate of correct identification (percent).

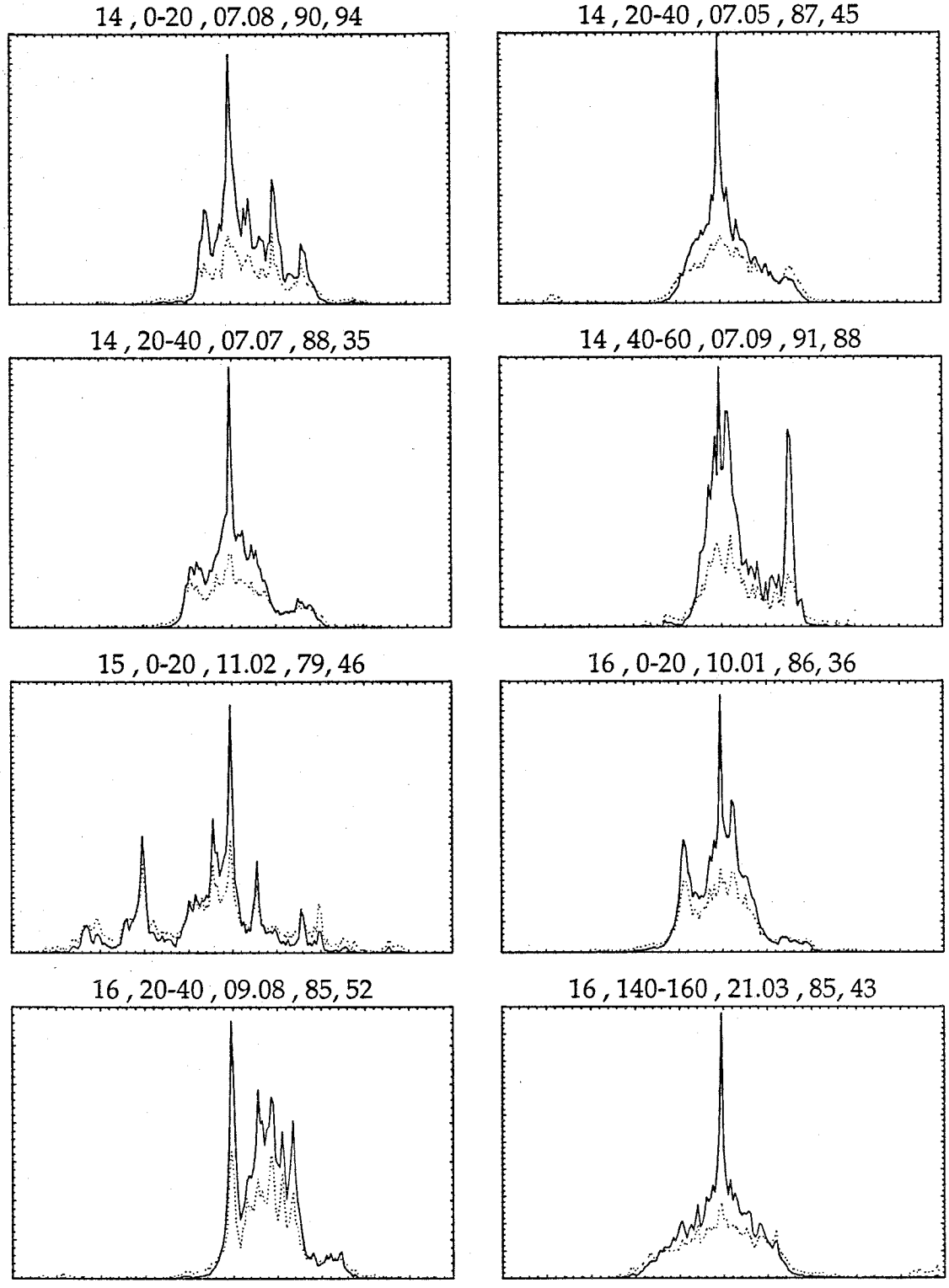

Figure 2.14: Average profile of RADC encounters (solid curve) and RMS fluctuation (dotted curve). Numbers at top are: target type, aspect (degrees), encounter designation, degree of clustering (percent), rate of correct identification (percent).

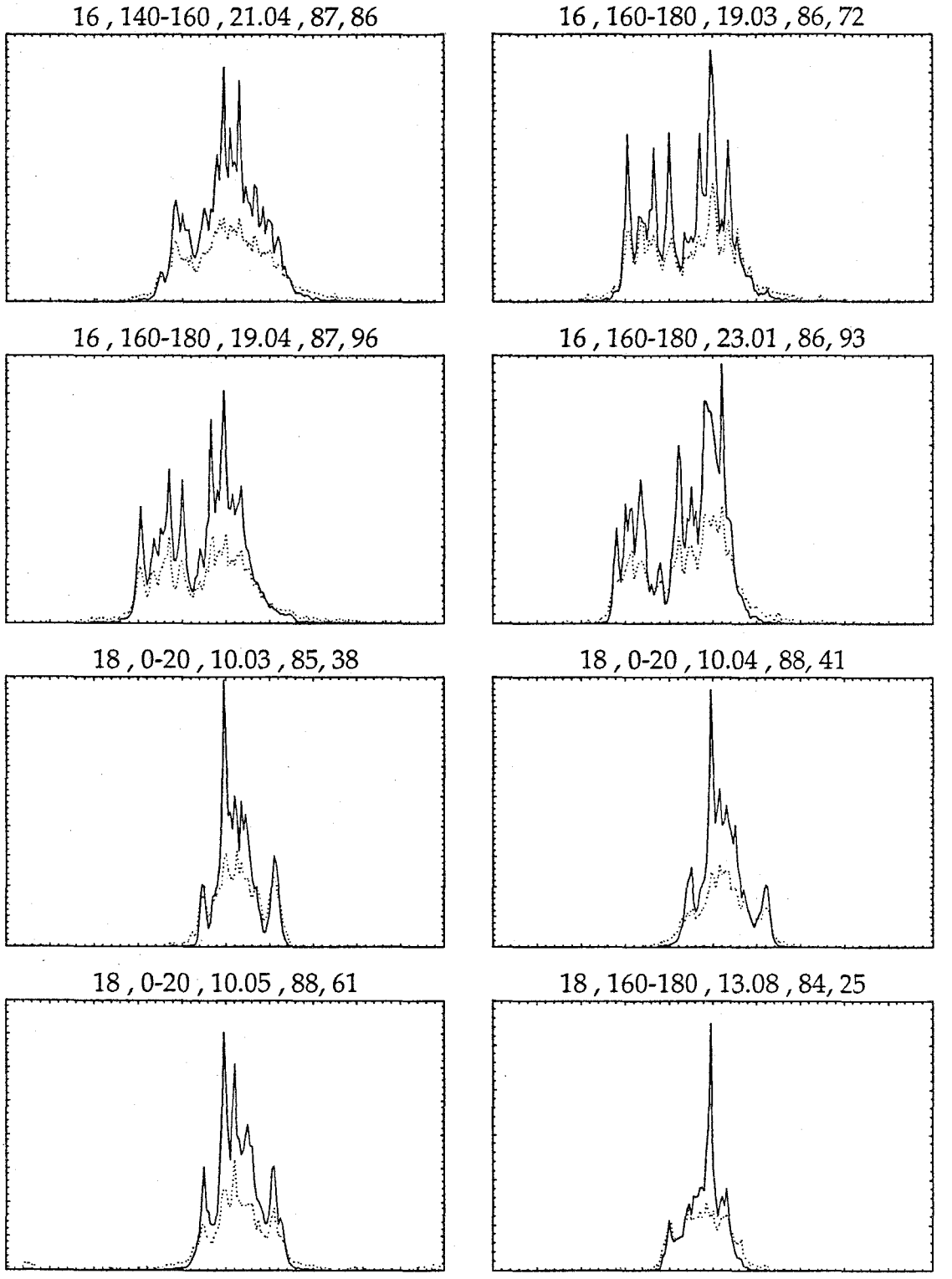

Figure 2.15: Average profile of RADC encounters (solid curve) and RMS fluctuation (dotted curve). Numbers at top are: target type, aspect (degrees), encounter designation, degree of clustering (percent), rate of correct identification (percent).

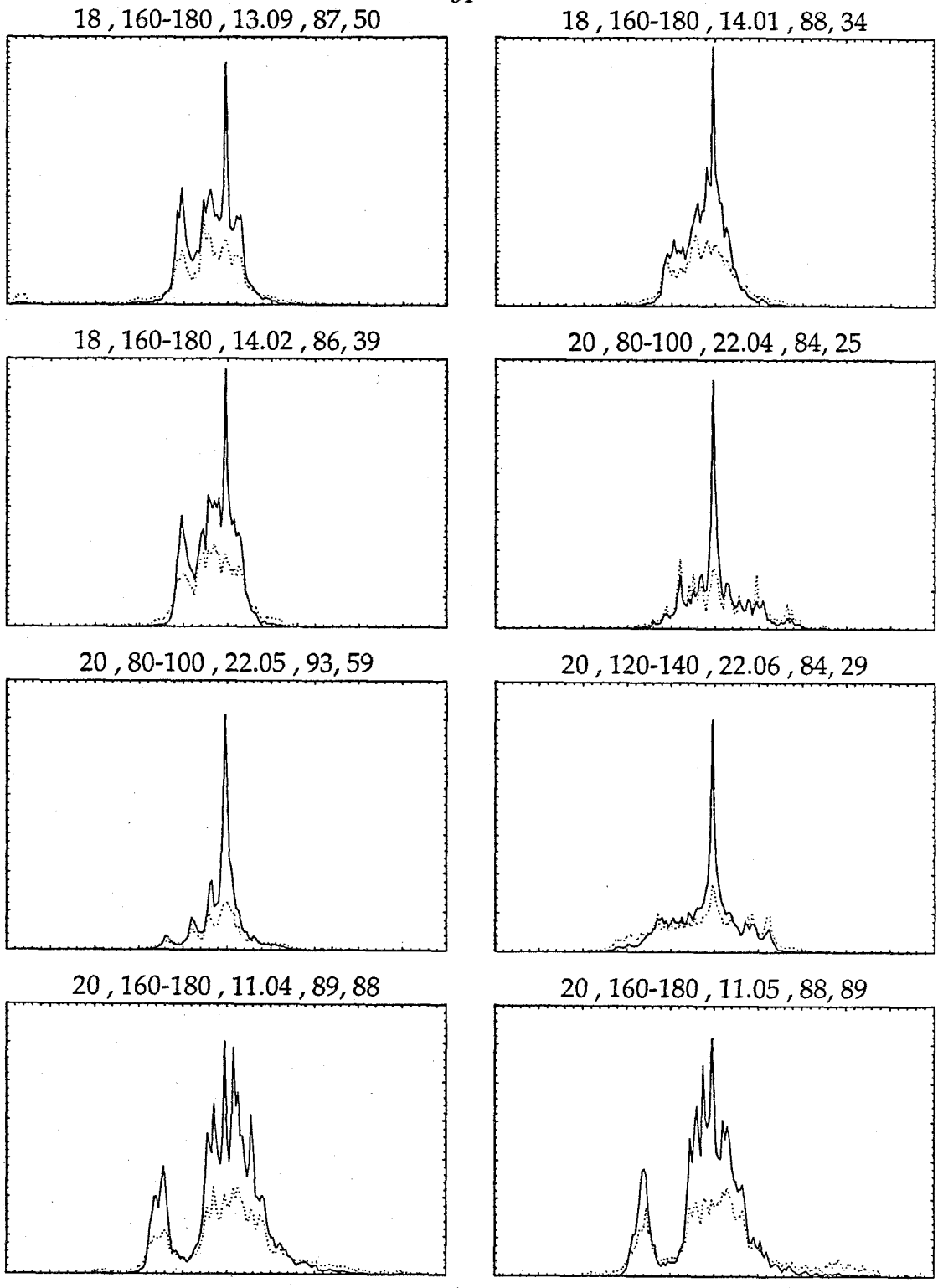

Figure 2.16: Average profile of RADC encounters (solid curve) and RMS fluctuation (dotted curve). Numbers at top are: target type, aspect (degrees), encounter designation, degree of clustering (percent), rate of correct identification (percent).

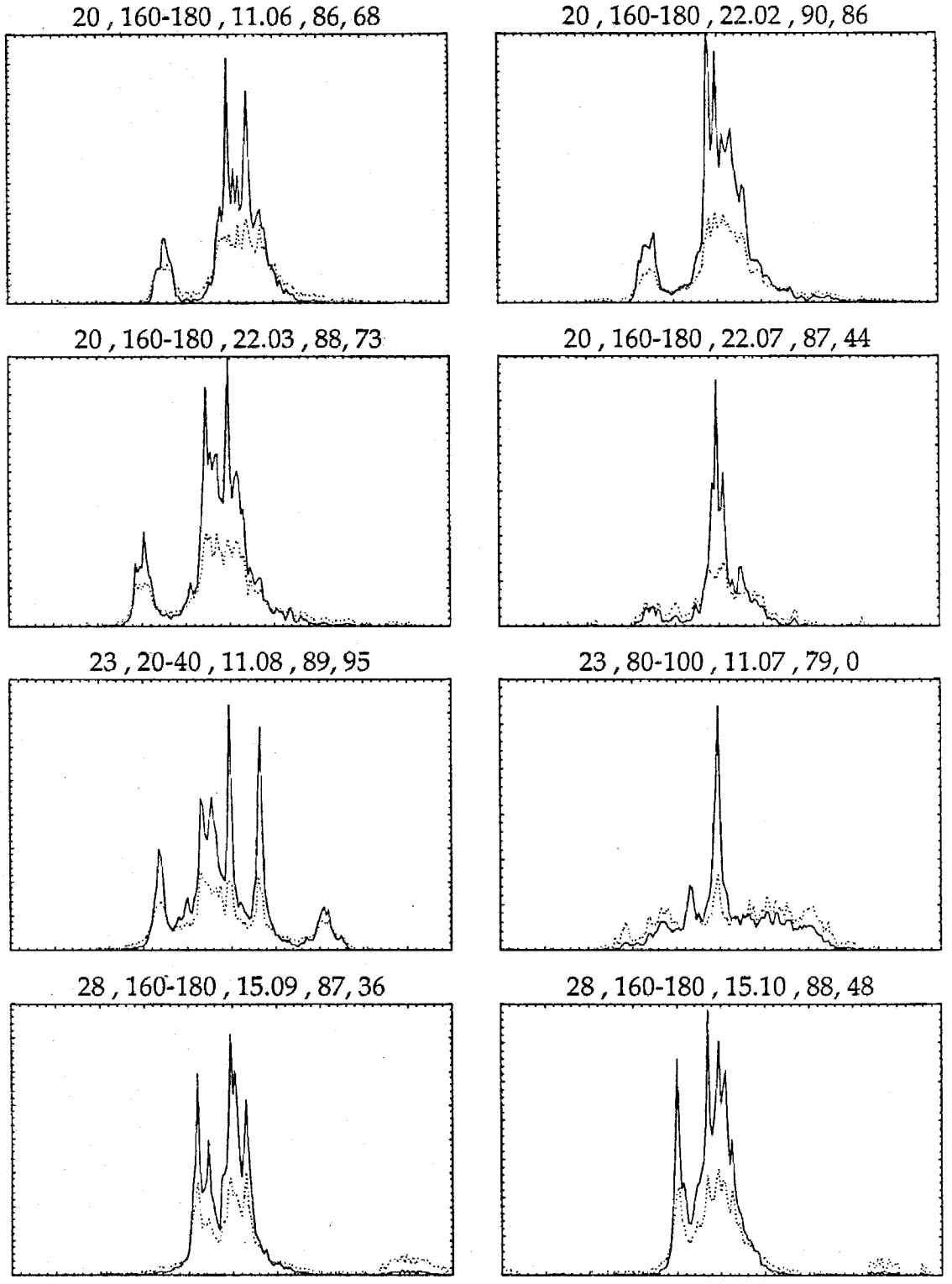

Figure 2.17: Average profile of RADC encounters (solid curve) and RMS fluctuation (dotted curve). Numbers at top are: target type, aspect (degrees), encounter designation, degree of clustering (percent), rate of correct identification (percent).

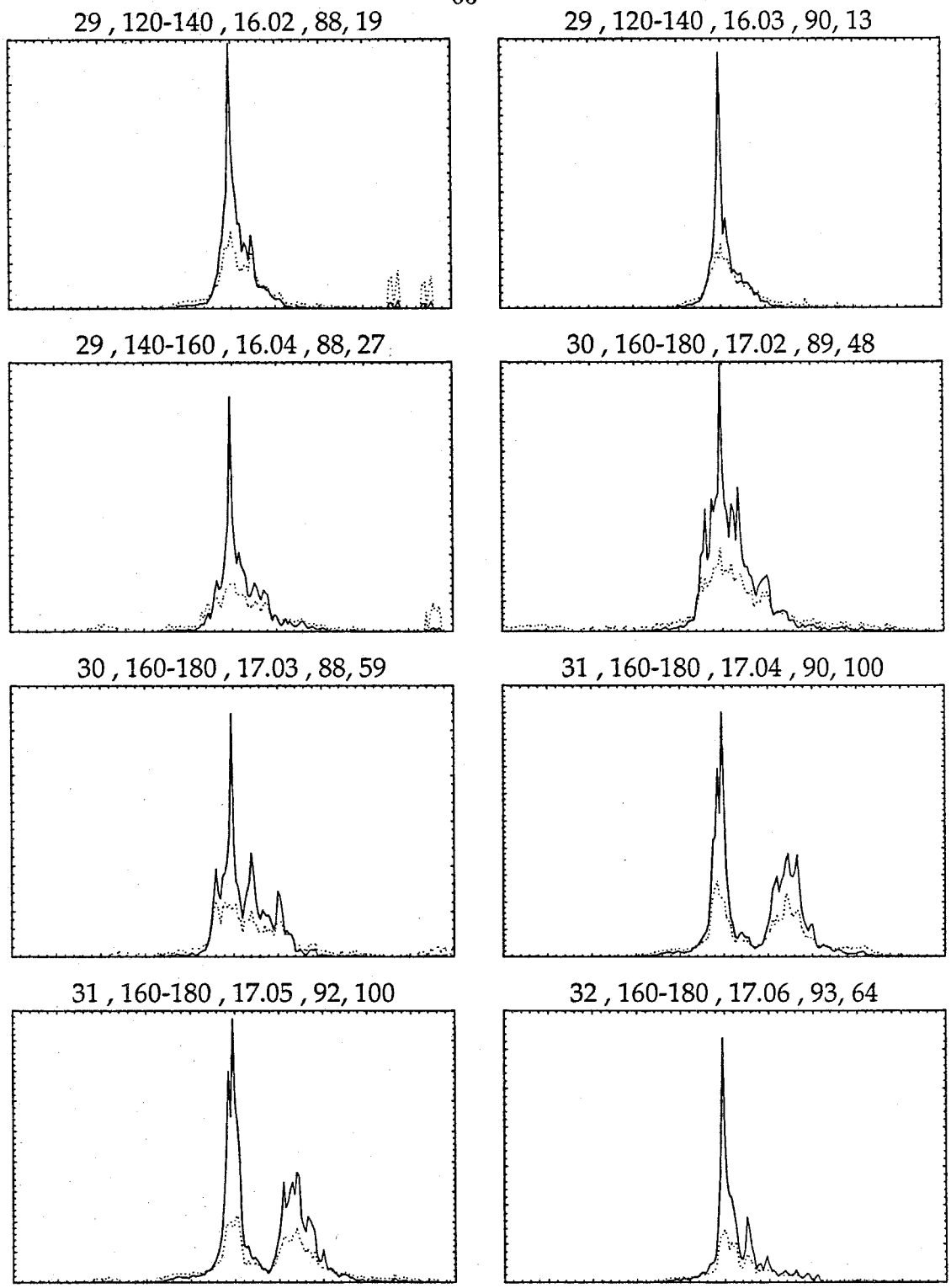

Figure 2.18: Average profile of RADC encounters (solid curve) and RMS fluctuation (dotted curve). Numbers at top are: target type, aspect (degrees), encounter designation, degree of clustering (percent), rate of correct identification (percent).

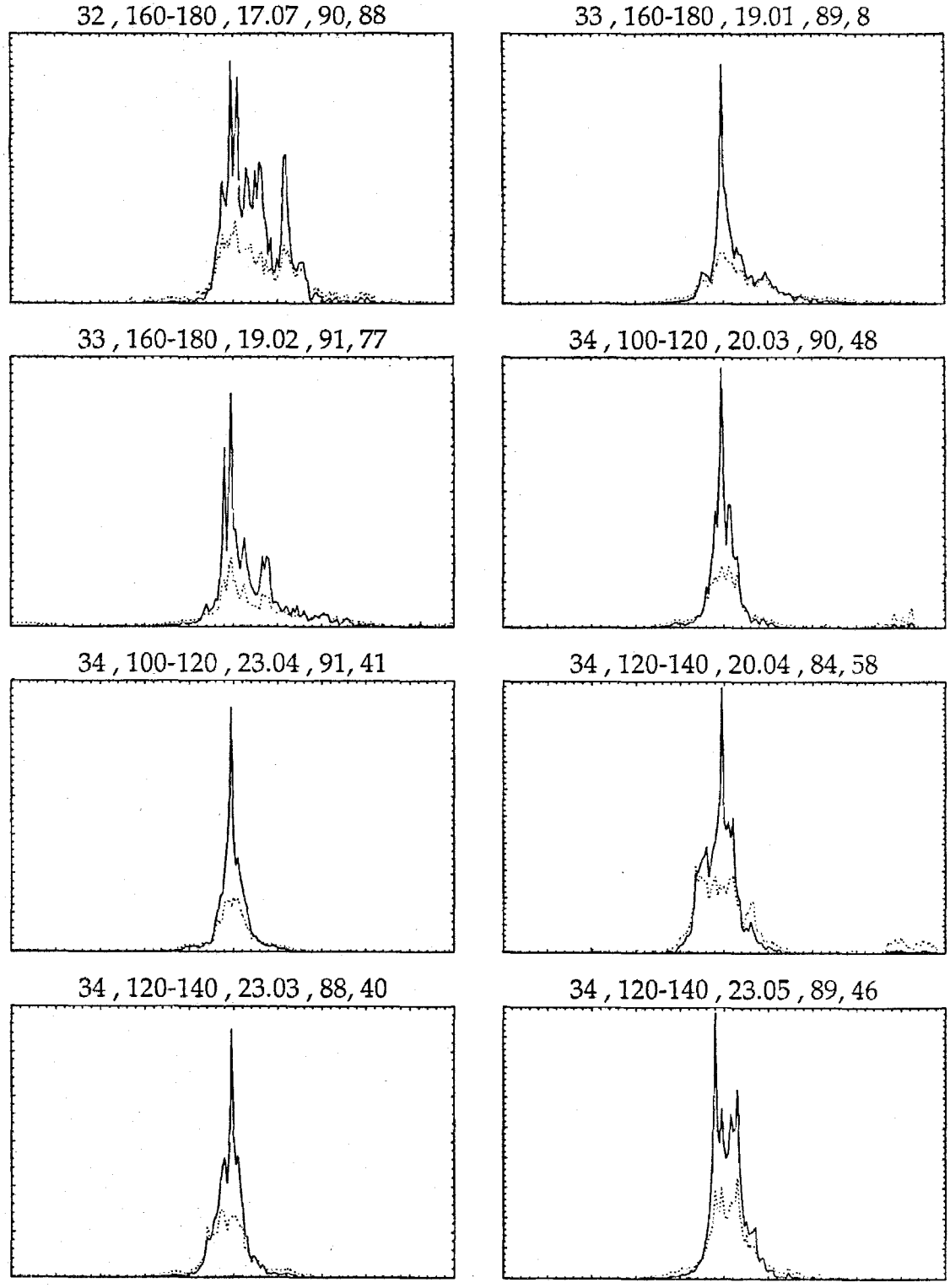

Figure 2.19: Average profile of RADC encounters (solid curve) and RMS fluctuation (dotted curve). Numbers at top are: target type, aspect (degrees), encounter designation, degree of clustering (percent), rate of correct identification (percent).

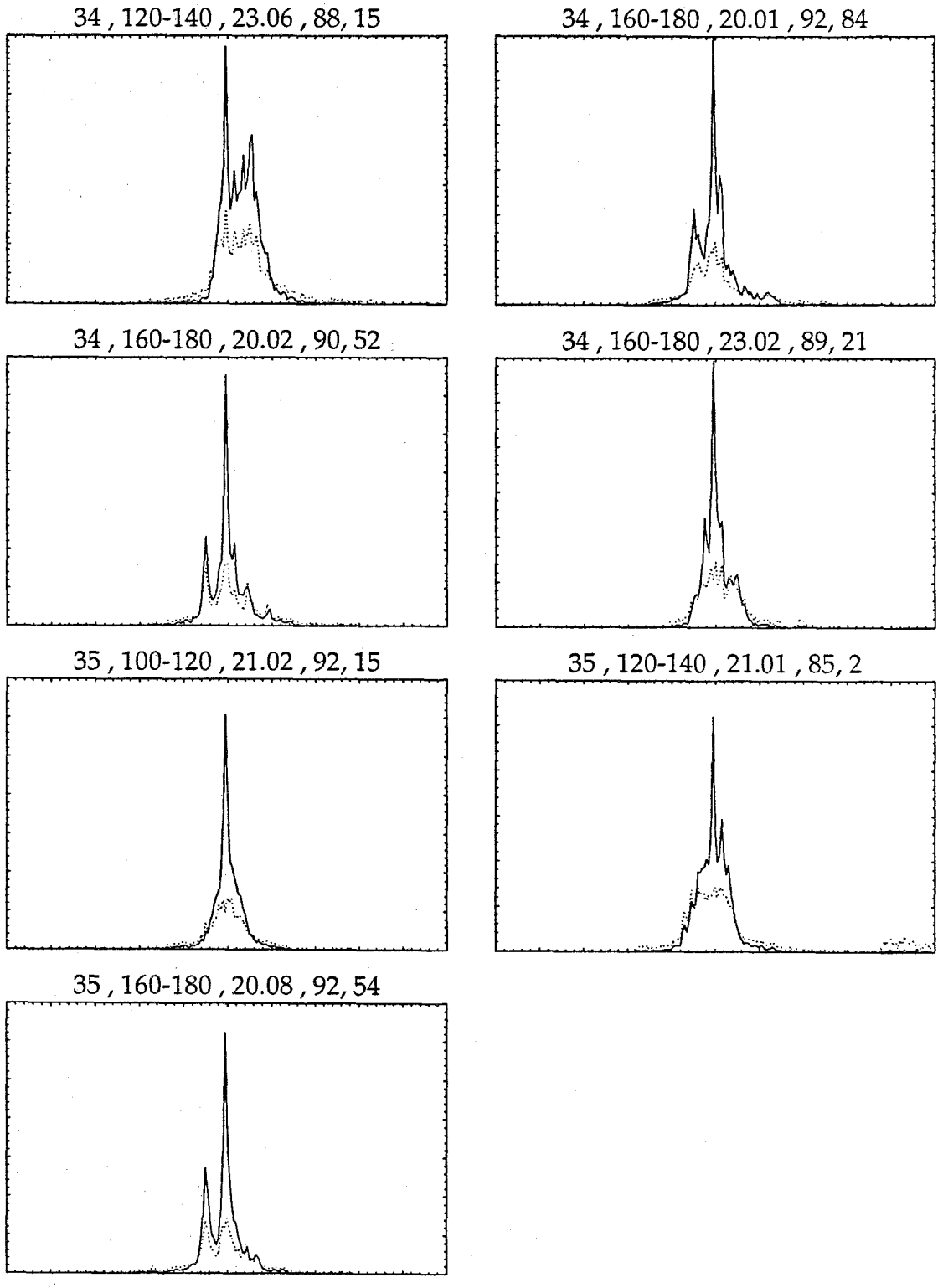

Figure 2.20: Average profile of RADC encounters (solid curve) and RMS fluctuation (dotted curve). Numbers at top are: target type, aspect (degrees), encounter designation, degree of clustering (percent), rate of correct identification (percent).

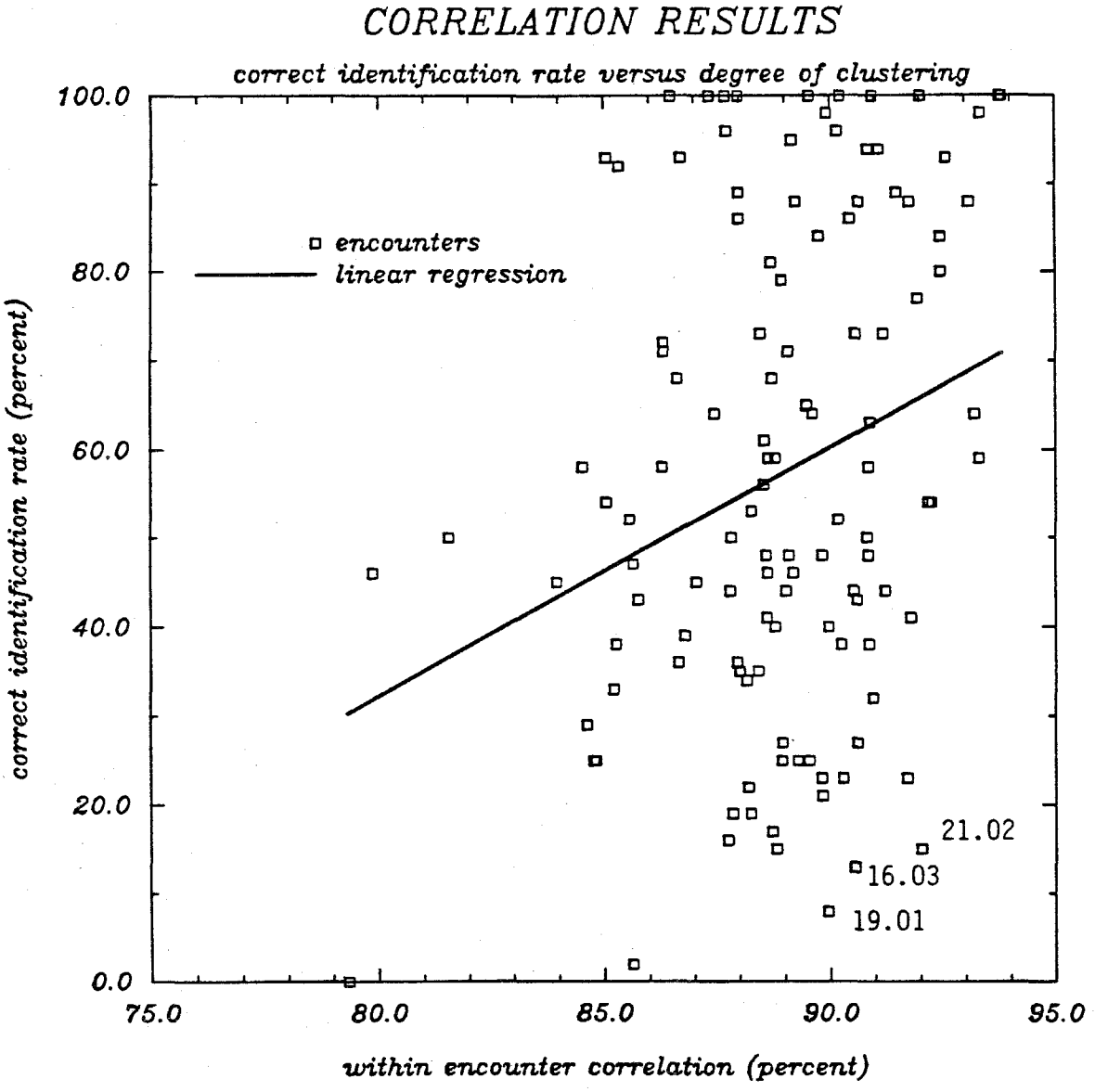

Figure 2.21: Correct identification rate versus degree of clustering. Uncertainty in regression slope $\sim 25\%$.

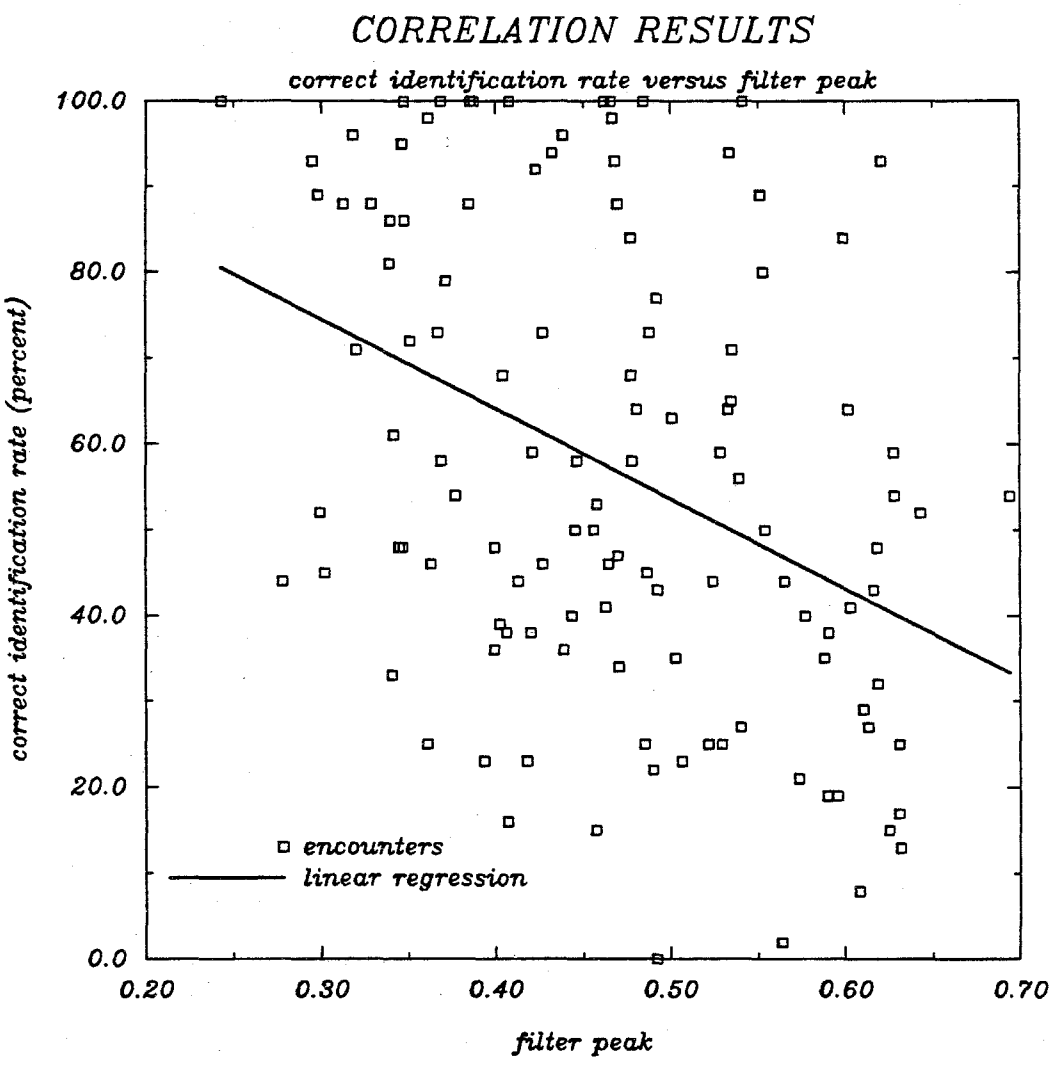

Figure 2.22: Correct identification rate versus filter peak. Uncertainty in regression slope $\sim 25\%$.

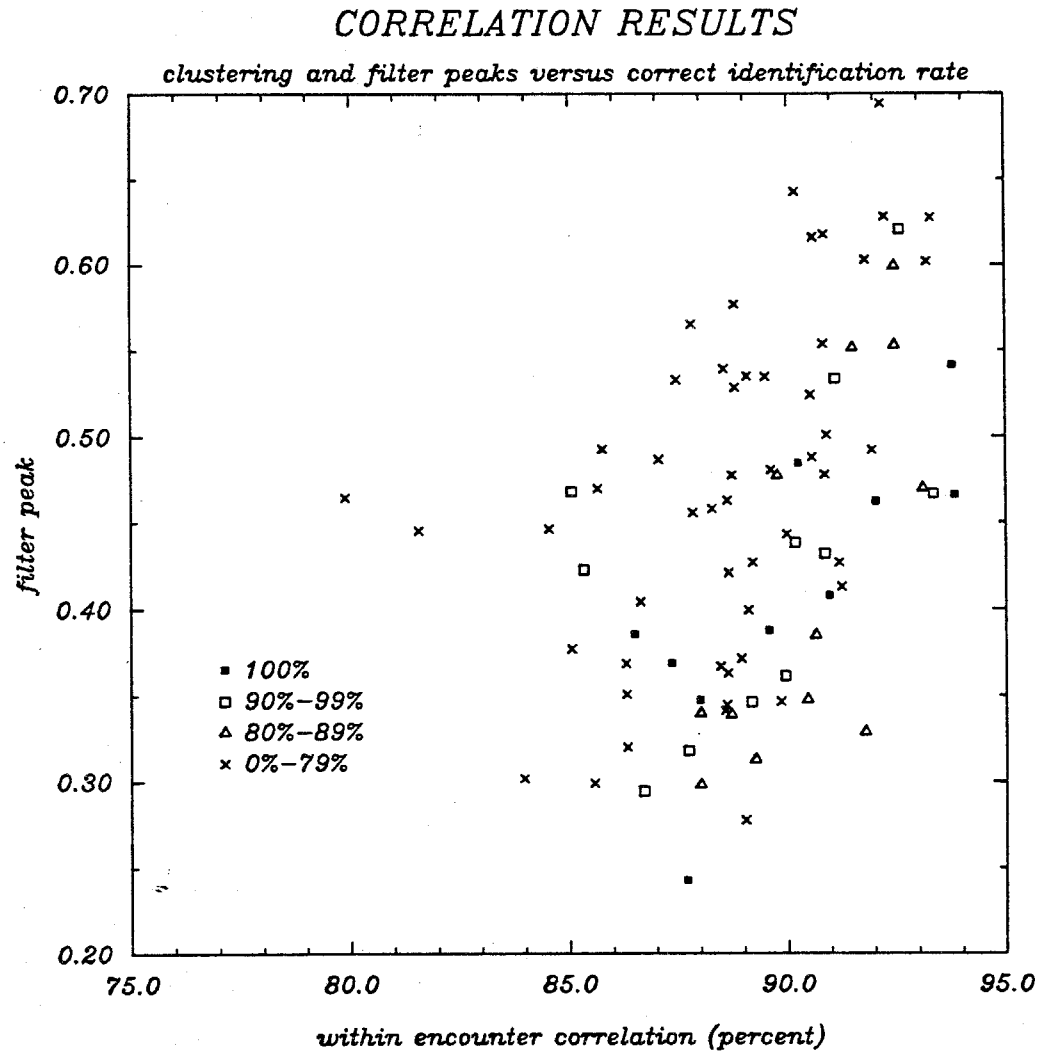

Figure 2.23: Degree of clustering and filter peak versus correct-identification rate.

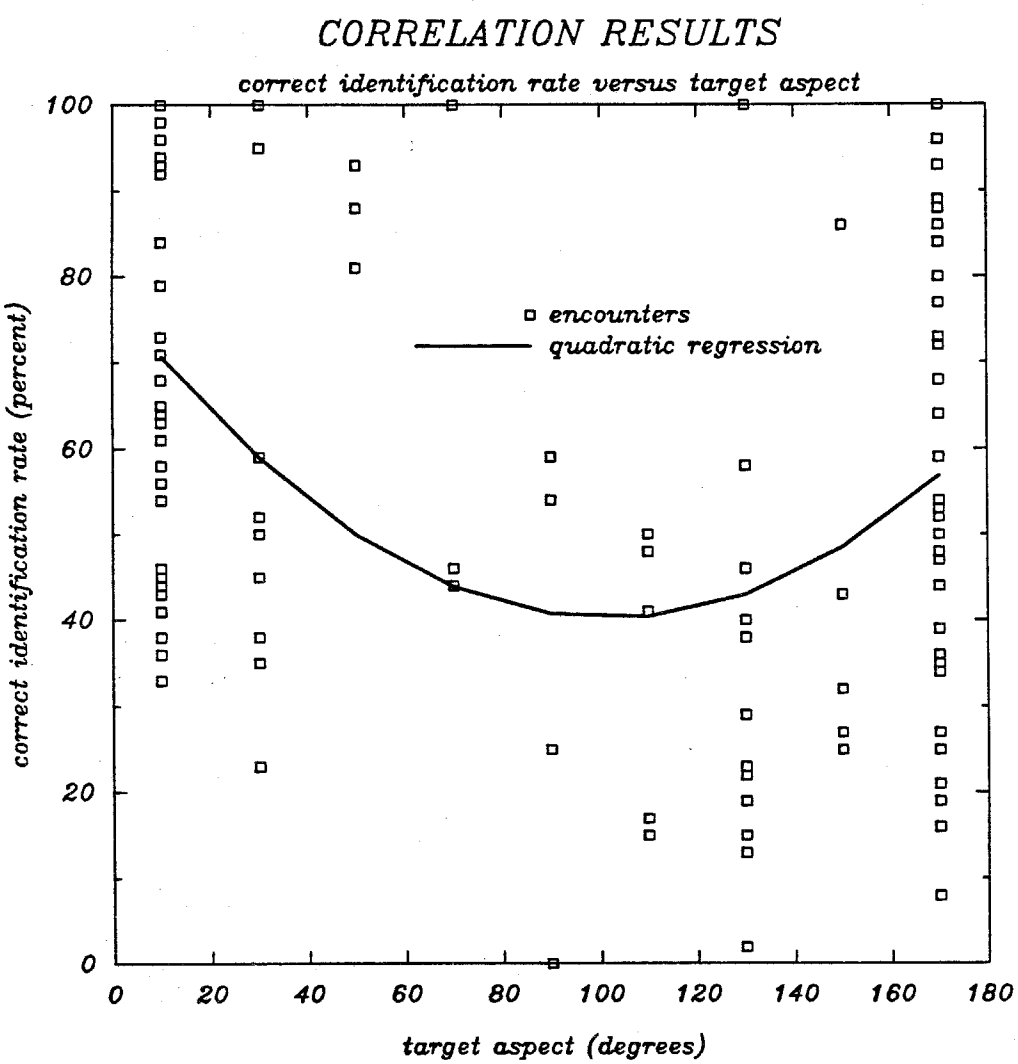

Figure 2.24: Correct-identification rate versus target aspect.

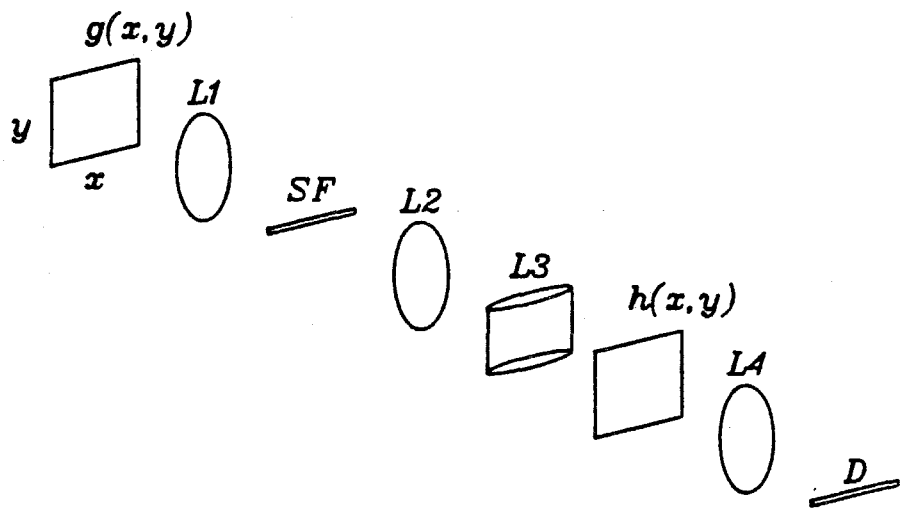

Figure 2.25: A system for performing one-dimensional, analog correlations using two-dimensional, binary spatial light modulators.

	identification rates			
aspect	random	profile	frame	encounter
0° - 20°	$\frac{1}{13} = 8\%$	$\frac{1256}{1584} = 79\%$	$\frac{167}{198} = 84\%$	$\frac{33}{33} = 100\%$
20° - 40°	$\frac{1}{6} = 17\%$	$\frac{354}{424} = 83\%$	$\frac{50}{53} = 94\%$	$\frac{9}{9} = 100\%$
40° - 60°	$\frac{1}{2} = 50\%$	$\frac{88}{88} = 100\%$	$\frac{11}{11} = 100\%$	$\frac{3}{3} = 100\%$
60° - 80°	$\frac{1}{2} = 50\%$	$\frac{96}{96} = 100\%$	$\frac{12}{12} = 100\%$	$\frac{3}{3} = 100\%$
80° - 100°	$\frac{1}{3} = 33\%$	$\frac{183}{216} = 85\%$	$\frac{22}{27} = 81\%$	$\frac{4}{4} = 100\%$
100° - 120°	$\frac{1}{4} = 25\%$	$\frac{109}{248} = 44\%$	$\frac{15}{31} = 48\%$	$\frac{4}{5} = 80\%$
120° - 140°	$\frac{1}{8} = 13\%$	$\frac{423}{704} = 60\%$	$\frac{55}{88} = 63\%$	$\frac{12}{15} = 80\%$
140° - 160°	$\frac{1}{4} = 25\%$	$\frac{212}{280} = 76\%$	$\frac{28}{35} = 80\%$	$\frac{5}{5} = 100\%$
160° - 180°	$\frac{1}{17} = 6\%$	$\frac{1466}{2072} = 71\%$	$\frac{204}{259} = 79\%$	$\frac{40}{42} = 95\%$
all	$\frac{1}{24} = 4\%$	$\frac{3262}{5712} = 57\%$	$\frac{465}{714} = 65\%$	$\frac{102}{119} = 86\%$

Table 2.1: Summary of results of correlation identification experiments. Rows correspond to different target aspects; columns correspond to different decision bases. The row labeled "all" gives results of the correlation in which no aspect information was used. Other rows give results, for particular aspects, of correlations in which aspect information was used. The random identification rate is what would be achieved by random guessing. It is equal to one over the number of targets in the corresponding test set. It varies from row to row because some aspects occurred more often than others. The rate of identification of single profiles is given in the "profile" column. Identification rates using decision integration at frame and encounter levels are given in following columns.

Chapter 3

Inverse Synthetic Aperture Radar

3.1 Introduction

In the previous chapter we saw that the radar range profile of a moving aircraft fluctuates considerably as the aspect changes. We had to consider these fluctuations as noise for the purpose of identifying aircraft from their range profiles. To combat this noise we resorted to averaging schemes using multiple profiles. In this chapter we will see that these fluctuations contain information about the target's structure. We will describe a technique, *inverse synthetic aperture radar* (ISAR), for using multiple complex profiles to extract an extra dimension of target resolution. The resulting two-dimensional images contain more information than a one-dimensional range profile, and should be less sensitive to aspect changes. Consequently they should provide a more reliable basis for aircraft identification. In this chapter we will concentrate on the issues involved in producing such images. We will not, however, discuss their use for identification purposes, which would involve an application of well-developed, two-dimensional image correlation techniques.

The main difficulty to be overcome is that range profile fluctuations depend not only on the structure of the target but also on the target's motion, since target motion determines how the target's aspect changes in time. Target motion is generally unknown to the radar *a priori*, so it must be estimated somehow if well-focused images are to be formed. Techniques for doing this are termed *motion compensation.* Two types of motion compensation may be required: range compensation and aspect compensation. Range compensation has received considerable attention as it is often a necessary step in the formation of *synthetic aperture radar* (SAR) images [56]. Aspect compensation has not received as much attention, and it is the topic with which this chapter is primarily concerned. The original contribution made in this chapter is an iterative technique for performing aspect compensation [25] which does not depend on the presence of isolated point scatterers as in other techniques proposed [57].

A fundamental result in the theory of imaging is that an aperture of linear extent D can provide at best an angular resolution λ/D when operating at a wavelength λ [17]. Since radar wavelengths are typically 10^5 to 10^6 times as large as optical wavelengths it follows that a radar system requires an aperture of 10^5 to 10^6 times the size of an optical system to achieve the same resolution. While the construction of a 10 cm optical aperture is entirely practical, the construction of a 10 or 100 km radar aperture is not. The solution is to *synthesize* an aperture of this extent using a much smaller physical aperture.

The principle behind SAR can be understood by returning to expression (2.51) for a target's complex range profile:

$$E(t) = a e^{i2\pi \frac{R}{\lambda/2}} \int\int f(x,y)\,\mathrm{rect}\left(\frac{t - 2R/c + 2x/c}{T_p}\right) e^{-i2\pi \frac{x}{\lambda/2}} e^{-i2\pi \frac{\theta}{\lambda/2} y}\, dx\, dy. \qquad (3.1)$$

R and θ are the gross-range and aspect between target and radar, and the amplitude factor a contains all the pertinent factors from the radar equation. We have

already discussed the range-resolved nature of $E(t)$. At a given time t, $E(t)$ contains contributions from only those points of the target for which

$$\left|\frac{t-2R/c+2x/c}{T_p}\right| \leq \frac{1}{2}, \tag{3.2}$$

that is, for points within $\pm\delta x/2$ of

$$x = R - \frac{ct}{2}, \tag{3.3}$$

where $\delta x = cT_p/2$. In practice, range profiles are recorded in sampled form, possibly after some signal processing, e.g., range compression. Assuming samples are taken at times

$$t_k = kT_p \tag{3.4}$$

the complex range profile samples

$$E_k \equiv E(kT_p) \tag{3.5}$$

give the total field scattered from the range bins centered on

$$\begin{aligned} x_k &= R - k\frac{cT_p}{2} \\ &= R - k\delta x. \end{aligned} \tag{3.6}$$

If we define

$$\begin{aligned} f_k(y) &= \int f(x,y)\,\mathrm{rect}\left(\frac{kT_p - 2R/c + 2x/c}{T_p}\right) e^{-i2\pi\frac{x}{\lambda/2}}\,dx \\ &= e^{-i2\pi\frac{x_k}{\lambda/2}} \int_{-\delta x/2}^{\delta x/2} f(x_k+\xi,y) e^{-i2\pi\frac{\xi}{\lambda/2}}\,d\xi, \end{aligned} \tag{3.7}$$

and use this in (3.1) then we can express E_k as

$$E_k = a e^{i2\pi\frac{R}{\lambda/2}} \int f_k(y) e^{-i2\pi\frac{\theta}{\lambda/2}}\,dy. \tag{3.8}$$

We refer to $f_k(y)$ as the cross-range reflectivity distribution of the k^{th} range bin. Let's consider this in more detail. The phase factor $e^{-i2\pi\frac{x_k}{\lambda/2}}$ is a multiplicative constant

which will not concern us as we will ultimately be working with image intensities (we could also absorb it into the definition of $f(x,y)$). The integration in (3.7) means that $f_k(y)$ is a blurred, i.e., finite resolution, image of the region of the target around the point (x_k, y). However, the blurring is not a simple averaging, as occurs in incoherent optical systems such as cameras or our eyes, but is accompanied by the spatially varying phase $e^{-i2\pi\frac{\xi}{\lambda/2}}$. Typically $\delta x \gg \lambda$, so this phase factor goes through several periods within each range bin. If there are multiple scatterers within a resolution cell, the presence of these phases can lead to constructive/destructive interference effects known as *speckle* [54]. Indeed, this is the same effect described in the previous chapter which produced range profile fluctuations. Speckle is a problem in all coherent imaging systems, but it typically becomes less severe as the size of resolution cells shrink [54]. If resolution cells become small enough so that at most only a single scattering center is present in each then speckle will not occur. This is often the case for aircraft ISAR images with the fine resolutions (as small as 10 cm) that are possible with state-of-the-art radars.

Using the definition of the Fourier transform,

$$F_k(v) = \int f_k(y) e^{-i2\pi vy}\, dy, \tag{3.9}$$

where v denotes spatial frequency, we can write (3.8) as

$$E_k = a e^{i2\pi\frac{R}{\lambda/2}} F_k\left(\frac{\theta}{\lambda/2}\right). \tag{3.10}$$

We see that each sample of the complex range profile in effect provides a sample of the Fourier transform of a particular range bin's cross-range reflectivity distribution at the spatial frequency

$$v = \frac{\theta}{\lambda/2}. \tag{3.11}$$

We will show the dependence of E_k on θ explicitly by writing $E_k(\theta)$ from now on.

Since functions are uniquely determined by their Fourier transforms, equation (3.10) makes it clear that $f_k(y)$ can be determined, to within some finite resolution, if complex range profiles are obtained over a sufficiently large range of aspects. More specifically, if $\Delta\theta$ denotes the range of aspects that are recorded, then $f_k(y)$ can be reconstructed to within a resolution

$$\delta y = \frac{1}{\Delta v} = \frac{\lambda}{2\Delta\theta}, \tag{3.12}$$

where (3.11) has been used. Conceptually, we could achieve this resolution by flying a radar along a path that subtends this range of target aspects while continuously recording complex range profiles. In practice, however, each profile requires a discrete transmit/receive cycle so we are taking discrete samples of F_k with every complex range profile we record. If $f_k(y)$ has an extent W in y then the Nyquist sampling period [42] for $F_k(v)$ is $\delta v = 1/W$. Therefore the maximum allowable aspect change between profiles is

$$\delta\theta = \frac{\lambda}{2W}. \tag{3.13}$$

If the radar moves through an aspect change greater than this then aliasing will occur, and it will not be possible to reconstruct $f_k(y)$. Figure 3.1 illustrates the concepts we have described so far.

The sequential recording of different components of a target's far-field scatter is what synthesizing an aperture refers to, in contrast to real aperture systems which collect all such components in parallel, e.g., a lens aperture. While aperture synthesis can be effected by the motion of a radar past a stationary target, it can also be effected by the motion of a target past a radar since all that is required is that different aspects of the target be observed. That is, there need only be *relative* motion between radar and target, and this can come about through any combination of radar and/or target motion. SAR refers to the situation in which the target is stationary and only the

radar moves. ISAR refers to any scenario in which there is target motion. The two cases are illustrated in Figure 3.2.

This overview of the SAR/ISAR principle has, for simplicity, neglected an important consideration which we now address. The k^{th} profile sample, E_k, corresponds to the position

$$x_k = R - k\delta x \tag{3.14}$$

on the target. However, if we are ignorant of R then we are ignorant of x_k. More specifically, if R varies from profile to profile by more than δx then corresponding samples in different profiles do not correspond to the same range bin. Yet, if we are to make a correspondence between profile samples and samples of the Fourier transforms of range bin reflectivities, we must know which samples correspond to a given range bin. This *profile alignment* problem must be overcome before any further processing can be accomplished.

Profile alignment is usually not an issue for SAR since the aircraft and spacecraft platforms that carry radars can maintain stable enough paths that changes in R are less than δx. Even if this is not possible, accelerometers can be used to measure these changes, allowing them to be compensated for. In the case of ISAR, on the other hand, changes in R are due, at least in part, to target motion, and there is no reason to expect target motion to cooperate with the needs of radar imaging. Moreover, placing accelerometers on the target is (usually) out of the question, so we generally do not have any *a priori* knowledge of how the target moved. Thus ISAR processing must begin with a profile alignment procedure. Typically this is done by noting the location of a strong spike in the range profiles and shifting the profiles so that these spikes align [56]. Alternately, a clustering technique like that presented in Chapter 2 could be used. Much more stringent requirements on our knowledge of variations in R arise because of the phase factor $e^{i2\pi\frac{R}{\lambda/2}}$ in (3.10). We consider this now.

3.2 Range Compensation

Provided the radar has recorded profiles at no less than the Nyquist rate (3.13), we can reconstruct the continuous functions $F_k\left(\frac{\theta}{\lambda/2}\right)$ from their samples, and we will take advantage of this fact to describe all subsequent signal processing in continuous terms.

We will assume for the moment a linear variation of aspect with time, $\theta(t) = \Omega t$. Then the field recorded for the k^{th} range bin is $e^{i2\pi\frac{R(t)}{\lambda/2}} F_k\left(\frac{\Omega t}{\lambda/2}\right)$, and we have already discussed how information about the cross-range structure of the range bin is contained in $F_k\left(\frac{\Omega t}{\lambda/2}\right)$. The phase factor $e^{i2\pi\frac{R(t)}{\lambda/2}}$ arises from the time-varying gross-range of the target, and it contains no information about target structure. We must remove this factor if we are to be able to determine the phase of $F_k\left(\frac{\Omega t}{\lambda/2}\right)$. If we do not, the result will be a blurred image of $f_k(y)$. To see this note that we want to compute

$$\begin{aligned} f_k(y) &= \int F_k(v) e^{i2\pi vy}\, dv \\ &= \frac{\Omega}{\lambda/2} \int F_k\left(\frac{\Omega t}{\lambda/2}\right) e^{i2\pi\frac{\Omega t}{\lambda/2}}\, dt, \end{aligned} \tag{3.15}$$

but if the gross-range phase factor is present we get

$$\begin{aligned} \hat{f}_k(y) &= \frac{\Omega}{\lambda/2} \int e^{i2\pi\frac{R(t)}{\lambda/2}} F_k\left(\frac{\Omega t}{\lambda/2}\right) e^{i2\pi\frac{\Omega t}{\lambda/2}}\, dt \\ &= \int e^{i2\pi\frac{2}{\lambda}R(\frac{\lambda v}{2\Omega})} F_k(v) e^{i2\pi vy}\, dv \\ &= f_k(y) * \mathcal{F}^{-1}\left[e^{i2\pi\frac{2}{\lambda}R(\frac{\lambda v}{2\Omega})}\right], \end{aligned} \tag{3.16}$$

where $\mathcal{F}^{-1}$ denotes the inverse Fourier transform, $*$ denotes convolution, and we have used the convolution theorem. This will be a blurred version of $f_k(y)$ unless the function $\mathcal{F}^{-1}\left[e^{i2\pi\frac{2}{\lambda}R(\frac{\lambda v}{2\Omega})}\right]$ is a δ-function. This will be the case only if $R(t)$ is linear in time (only linear phase functions have δ-function Fourier transforms), and this is most often not the case in real situations [56]. Therefore we must remove the phase factor $e^{i2\pi\frac{R(t)}{\lambda/2}}$ through some range-compensation technique.

The most widely used method for performing range compensation [50, 56, 57] requires the presence of a strong, isolated, point-like scatterer in at least one range bin. If this occurs then for that range bin

$$f_r(y) = \delta(y - y_r) \tag{3.17}$$

where y_r is the cross-range location of the point scatterer. From (3.10), the field recorded for this range bin will be

$$E_r = e^{i2\pi\frac{R(t)}{\lambda/2}} e^{-i2\pi y_r \frac{\Omega t}{\lambda/2}}, \tag{3.18}$$

which is a pure phase function. Range compensation is performed by multiplying the recorded fields of all range bins by the conjugate of this reference phase. For the k^{th} range bin this produces

$$e^{-i2\pi\frac{R(t)}{\lambda/2}} e^{i2\pi y_r \frac{\Omega t}{\lambda/2}} \times e^{i2\pi\frac{R(t)}{\lambda/2}} F_k\left(\frac{\Omega t}{\lambda/2}\right) = e^{i2\pi y_r \frac{\Omega t}{\lambda/2}} F_k\left(\frac{\Omega t}{\lambda/2}\right), \tag{3.19}$$

and the gross-range phase factor has been removed. Following this with an inverse Fourier transform results in

$$\begin{aligned} \hat{f}_k(y) &= f_k(y) * \delta(y + y_r) \\ &= f_k(y + y_r) \end{aligned} \tag{3.20}$$

Thus a well-focused image is produced which has simply been shifted by a distance y_r in cross-range. An analogous, but messier, calculation shows that this technique works, not just for linear $\theta(t)$, but for arbitrarily varying aspects.

Empirically it has been found that, for commercial aircraft, the required isolated point scatterers can often be found provided the range resolution δx is sufficiently fine. In an experiment on approximately thirty aircraft it was found that a resolution of 1 m isolated such a scatterer 80% of the time while a resolution of 3 m was successful only 25% of the time [50]. Other techniques have been proposed which do not depend on the presence of isolated point scatterers [56, 7].

3.3 Aspect Compensation

Assuming range compensation has been successful, we now turn our attention to complexities that can arise due to nonlinear variations in target aspect. We will show that, in these situations, aspect compensation is required before a well-focused image can be formed. Although all ISAR images of real aircraft presented in the literature to date were made under the assumption of a linear variation of target aspect, i.e., $\theta(t) = \Omega t$, this does not imply that this will always be the case in practice. Typically these images have been made of aircraft flying uniform paths at constant velocity [3, 50]. Ideally, though, an operational ISAR imaging system should be able to produce well-focused images for more complicated target motion, e.g., rapidly maneuvering targets. This is what motivates us to investigate the aspect compensation problem.

The aspect compensation problem can be stated as follows. Some range bin reflectivity distribution $f(y)$ exists which has the Fourier transform

$$F(\theta) = \int f(y) e^{-i2\pi v y}\, dy, \tag{3.21}$$

and we have recorded the field

$$G(t) = F(\theta(t)) \tag{3.22}$$

(for notational economy, we drop the subscripts on f and F and absorb the factor of $2/\lambda$ into $\theta(t)$). Can we recover $f(y)$ from $G(t)$ without *a priori* knowledge of $\theta(t)$?

The answer is no if this is all the information we are given, because for *any* guess we make at $\theta(t)$, say $\hat{\theta}(t)$, we can compute the function $\hat{f}(y)$ such that

$$G(t) = \hat{F}(\hat{\theta}(t)), \tag{3.23}$$

where $\hat{F}$ is the Fourier transform of $\hat{f}$. We can do this by forming $\hat{\theta}^{-1}(t)$, the inverse of $\hat{\theta}(t)$, and then calculating

$$\hat{f}(y) \;=\; \mathcal{F}^{-1}\left[G(\hat{\theta}^{-1}(t))\right]$$

$$= \int G(\hat{\theta}^{-1}(t))e^{i2\pi yt}\,dt. \tag{3.24}$$

There are an infinite number of functions $\hat{\theta}(t)$, and so there are an infinite number of possible solutions to our problem. Recovering $f(y)$ is underdetermined because we lack a key piece of information, namely $\theta(t)$, that determined how $G(t)$ was derived from $f(y)$.

To obtain a unique solution to an underdetermined problem we need to impose additional constraints which allow us to identify one of the infinite number of possible solutions of the unconstrained problem as the "true" solution. Obviously our choice of constraints is critical to the success of such a scheme. We can impose arbitrary constraints and get an arbitrary unique solution, but if we want the solution to well approximate $f(y)$ then the constraints need to be related to the problem in a relevant way. For example, a common "regularization" technique for underdetermined problems is to choose from the infinite number of possible solutions the one that is "smoothest" according to some quantitative criterion. This results in a solution that is smooth but not necessarily related to the true solution (unless the true solution is fortuitously the smoothest possible). In the aspect compensation problem we can impose constraints on the image $\hat{f}(y)$, or on the *aspect history estimate* $\hat{\theta}(t)$, or on both. Ideally these constraints should be related to conditions that are expected to arise in real imaging scenarios.

Common practice in ISAR imaging is to assume that the target undertakes no significant accelerations, so an aspect history estimate that is linear in time, $\hat{\theta}(t) = t$, is justified. This is reasonable for most "cruising" scenarios as these typically involve straight-line flight at constant velocity. However, ISAR imaging for identification purposes is very desirable in many situations in which the target will be maneuvering and *will* have nonlinear components in its aspect history. In these cases the no-

accelerations assumption will result in a blurred image. In effect the assumption $\hat{\theta}(t) = t$ circumvents the underdetermined nature of the aspect compensation problem by placing constraints on target motion. This is not really valid since target motion is not under the radar's control.

An analogy can be drawn to the problem of focusing a camera. If we wish to take a well-focused picture of an object at a distance d_o using a lens of focal length f then we must place the film a distance d_i behind the lens such that the imaging condition

$$\frac{1}{f} = \frac{1}{d_o} + \frac{1}{d_i} \tag{3.25}$$

is satisfied [17]. However, we generally are ignorant of d_o so this focusing problem is underdetermined. One solution is to assume that d_o will always have some "reasonable" value and to fix d_i to correspond to this. This is the idea behind "fixed-focus" cameras. This "solves" the focusing problem by attempting to constrain the object's distance, something that we do not really have control over. Obviously this solution fails in any situation where d_o is not the assumed value. Another solution is "adaptive" focusing. Here we admit ignorance of d_o and instead place constraints on the image, i.e., adopt some focusing criterion. We then iteratively adjust d_i (e.g., by turning a focusing ring) until we obtain a well-focused image. Making the assumption $\hat{\theta}(t) = t$ in ISAR imaging is analogous to the fixed-focus camera, and we will refer to it as "fixed-focus ISAR." Below we will propose an iterative focusing approach to ISAR. However, we begin by examining the effects of a nonlinear aspect history on fixed-focus ISAR.

If a target's aspect history is given by

$$\theta(t) = t + \epsilon(t), \tag{3.26}$$

where $\epsilon(t)$ includes all the nonlinear contributions due to accelerations, then the

recorded field will be

$$\begin{aligned} G(t) &= F(t+\epsilon(t)) \\ &= \int f(\eta) e^{-i2\pi\eta(t+\epsilon(t))}\, d\eta. \end{aligned} \tag{3.27}$$

The fixed-focus ISAR image will be

$$\begin{aligned} \hat{f}(y) &= \int G(t) e^{i2\pi y t}\, dt \\ &= \int \left(\int f(\eta) e^{-i2\pi\eta(t+\epsilon(t))}\, d\eta \right) e^{i2\pi y t}\, dt \\ &= \int f(\eta) \left(\int e^{-i2\pi\eta\epsilon(t)} e^{i2\pi(y-\eta)t}\, dt \right) d\eta \\ &= \int f(\eta) b_\eta(y-\eta)\, d\eta. \end{aligned} \tag{3.28}$$

This shows that $\hat{f}(y)$ is a blurred version of $f(y)$ where the blurring function, or imaging system impulse response, is the inverse Fourier transform of $e^{-i2\pi\eta\epsilon(t)}$. Although we cannot find a closed-form expression for this for arbitrary $\epsilon(t)$, it is illuminating to examine some limits. If the nonlinearities are small enough then

$$e^{-i2\pi\eta\epsilon(t)} \approx 1 - i2\pi\eta\epsilon(t), \tag{3.29}$$

and the blurring function is

$$b_\eta(y) \approx \delta(y) - i2\pi\eta \mathcal{F}^{-1}[\epsilon(t)]. \tag{3.30}$$

The δ-function alone would produce a well-focused image. The addition of the second term produces blurring. The shape of this blurring is determined by the spectrum of $\epsilon(t)$; the width of the blurring is wider the higher the frequencies that $\epsilon(t)$ contains. If we use β_1 to denote the bandwidth of $\epsilon(t)$ then this represents the width, in y, of the blurring term. We also see that the relative strength of the blurring term increases with increasing $|\eta|$, that is, towards the cross-range extremities of the target.

Another limit is that in which $\epsilon(t)$ is large and oscillates rapidly. The instantaneous frequency of $e^{-i2\pi\eta\epsilon(t)}$ is $\eta d\epsilon(t)/dt$. The bandwidth of $e^{-i2\pi\eta\epsilon(t)}$ is therefore

approximately

$$\beta_2 = 2|\eta| \max \left| \frac{d\epsilon(t)}{dt} \right|, \tag{3.31}$$

so this is approximately the width of $b_\eta(y)$. Note that this increases with $|\eta|$. Using Carson's rule [59] we can approximate the width of $b_\eta(y)$, for any $\epsilon(t)$, by $\beta_1 + \beta_2$.

We see that nonlinear components of the aspect history will result in a blurred image under the assumption $\theta(t) = t$, and that the blurring produced by $\epsilon(t)$ increases with increasing $|\eta|$, i.e., towards the edges of the target. To produce a well-focused image requires that these nonlinearities, if present, be compensated for. Aspect compensation essentially involves subjecting the recorded field to a coordinate transformation so that it represents the (undistorted) Fourier transform of the range bin reflectivity. At this point an inverse Fourier transform will produce a well-focused image of the range bin. That is, we want to start with $G(t)$ and go through the transformations:

$$G(t) \quad \Rightarrow \quad F(v) \quad \Rightarrow \quad f(y).$$

Since $G(t) = F(\theta(t))$, the first transformation can be achieved, assuming $\theta(t)$ is single valued, via

$$\begin{aligned} F(v) &= \int F(\theta(t))\delta(\theta(t) - v)\frac{d\theta}{dt}\, dt \\ &= \int G(t)\delta(\theta(t) - v)\frac{d\theta}{dt}\, dt, \end{aligned} \tag{3.32}$$

and the second via

$$f(y) = \int F(v) e^{i2\pi vy}\, dv. \tag{3.33}$$

Putting these together we have

$$f(y) = \int \left[\int G(t)\delta(\theta(t) - v)\frac{d\theta}{dt}\, dt \right] e^{i2\pi vy}\, dv, \tag{3.34}$$

and performing the integration over v results in

$$f(y) = \int G(t) e^{i2\pi\theta(t)y}\frac{d\theta}{dt}\, dt. \tag{3.35}$$

Thus, if the aspect history is known, the above linear transformation of the recorded field will produce a well-focused image.

The problem, of course, is that we do not know $\theta(t)$ *a priori*. If we use some estimate $\hat{\theta}(t)$, the result is

$$\hat{f}(y) = \int G(t) e^{i2\pi\hat{\theta}(t)y} \frac{d\hat{\theta}}{dt}\, dt. \tag{3.36}$$

How is this related to $f(y)$? If into this expression we substitute

$$G(t) = F(\theta(t)) = \int f(\eta) e^{-i2\pi\theta(t)\eta}\, d\eta, \tag{3.37}$$

and change the order of integrations, we arrive at

$$\begin{aligned} \hat{f}(y) &= \int f(\eta) \left[\int e^{i2\pi(\hat{\theta}(t)y - \theta(t)\eta)} \frac{d\hat{\theta}}{dt}\, dt \right] d\eta \\ &= \int f(\eta) b_\eta(y-\eta)\, d\eta, \end{aligned} \tag{3.38}$$

where the function $b_\eta(y)$ is the impulse response of this imaging process. We want this to be a δ-function so that $\hat{f}(y) = f(y)$. If we write

$$\hat{\theta}(t) = \theta(t) + \epsilon(t), \tag{3.39}$$

where $\epsilon(t)$ is the error (if any) in our aspect history estimate, then the impulse response can be written

$$\begin{aligned} b_\eta(y-\eta) &= \int e^{-i2\pi[\hat{\theta}(t)-\epsilon(t)]\eta} e^{i2\pi\hat{\theta}(t)y} \frac{d\hat{\theta}(t)}{dt}\, dt \\ &= \int e^{i2\pi\epsilon\eta} e^{i2\pi(y-\eta)\hat{\theta}}\, d\hat{\theta}, \end{aligned} \tag{3.40}$$

where in the last integral ϵ is considered to be a function of $\hat{\theta}$. This shows that the impulse response is the inverse Fourier transform of $e^{i2\pi\epsilon\eta}$. When $\epsilon \equiv 0$ this is $\delta(y-\eta)$, and $\hat{f}(y) = f(y)$. When ϵ is nonzero, however, b_η has finite width and this causes $\hat{f}(y)$ to be a blurred version of $f(y)$. By an analysis similar to that used previously it is

easy to show that this blurring increases with $|\eta|$, so the extremities of the target are the most blurred. Aspect compensation involves forcing ϵ to be identically zero, thus resulting in a well-focused image.

We can perform aspect compensation by allowing the aspect history estimate to take into account accelerations and higher order motion through the use of a polynomial representation,

$$\hat{\theta}(t) = c_1 t + c_2 t^2 + \cdots, \tag{3.41}$$

of whatever order we estimate is required to accurately model the true $\theta(t)$. The coefficients c_i are determined by the target's motion and are unknown to us *a priori*. To obtain a unique solution, constraints must then be placed on the image. Our criterion when focusing a camera is the amount of high spatial frequency components present in the image, i.e., its sharpness. This works for incoherent imaging systems in which misfocusing always causes a loss of these components. The well-focused image is guaranteed to have the highest bandwidth of all possible images. For coherent imaging systems, however, misfocusing does not necessarily lead to a loss of high spatial frequencies in the image intensity, it may even increase them. Thus we require a different focusing criterion for ISAR. Since the scattering characteristics of aircraft often seem to be dominated by point-like scattering centers [56], a possible constraint is to require the focused image to contain multiple, isolated point features [57]. However, it may not always be the case that an aircraft will consist of such features.

The technique that we propose is based on the fact that *all* aircraft are spatially limited, i.e., of finite extent. When attempting to image an aircraft flying against a nonreflective background (air), it follows that a well-focused ISAR image should be spatially limited. Moreover we have seen that errors in the aspect history estimate cause blurring which is most severe at the edges of the image. Since the width of

a blurred image is equal to the width of a well-focused image plus the width of the blurring at the edges, it follows that image width provides a measure of the error in our aspect history estimate. By iteratively adjusting this estimate to minimize image width we can arrive at a well-focused image.

More specifically, let

$$I = \int_{-\infty}^{\infty} |\hat{f}(y)|^2 \, dy \tag{3.42}$$

denote the total energy in the image of a range bin. Then we propose to choose as the best estimate to the true aspect history that $\hat{\theta}(t)$ which results in the image $\hat{f}(y)$ which minimizes α, where

$$\int_{-\alpha}^{\alpha} |\hat{f}(y)|^2 \, dy = \beta I, \tag{3.43}$$

and β is some number less than unity, 0.95 say. In other words we try to force "most" of the image energy into the smallest possible area. We do not take $\beta = 1$ because no real image will ever be truly spatially limited, due to finite resolution effects (sidelobes) and noise. In practice the parameter β is determined empirically to give the best results.

An important point to be made is that if we replace $\hat{\theta}(t)$ in (3.36) by $b\hat{\theta}(t)$, where b is any positive constant, we obtain

$$\begin{aligned} \hat{f}_b(y) &= \int G(t) e^{i2\pi b\hat{\theta}(t)y} b \frac{d\hat{\theta}}{dt} \, dt \\ &= b\hat{f}(by). \end{aligned} \tag{3.44}$$

The effect is to scale the image by a factor of $1/b$, yet this will not affect the degree of blurring in the image. We have to avoid mere scalings of $\hat{\theta}(t)$ because one possibility is $b \to \infty$ in which case the image would shrink to a point at $y = 0$. While a point always looks well focused by almost any criterion, this obviously is not the result that we seek.

A solution to this is to note that real data will be collected only over some finite time, say $0 \leq t \leq T_o$. Hence, in practice (3.36) will read

$$\hat{f}(y) = \int_0^{T_o} G(t) e^{i2\pi\hat{\theta}(t)y} \frac{d\hat{\theta}}{dt}\, dt. \tag{3.45}$$

If $\hat{\theta}(t)$ covers a range of aspects $\Delta\hat{\theta}$ during this time then the resulting spatial resolution in the image will be

$$\delta y = \frac{1}{\Delta\hat{\theta}}. \tag{3.46}$$

(Recall that we have absorbed $\lambda/2$ into θ, so this is the same as (3.12).) If we do not want different aspect estimates to change the resolution of the image then we need to require that each covers the same range of aspects. For example, we can require that all aspect estimates satisfy

$$\hat{\theta}(0) = 0 \quad , \quad \hat{\theta}(T_o) = \Delta\theta. \tag{3.47}$$

Since we do not know the range of aspects the target actually moved through, we typically do not know the *absolute* cross-range scale of the image [56]; we can only ensure that all images we produce while searching over different aspect history estimates will have the same (unknown) scaling in cross range.

3.4 Applications

In this section we will apply our iterative technique to an ISAR simulation and an "acoustic ISAR" imaging experiment to explore its potential. We will also describe an attempt to perform ISAR imaging with the RADC data set used in the previous chapter.

Simulation

Here we present the results of a simulation designed to test the effectiveness of our ISAR focusing technique. A target in the form of a V-shaped collection of point scatterers was simulated (Figure 3.3). Its far-field scatter was computed for an aspect history $\theta(t) = t^2$, for $0 \leq t \leq 1$, with the vertex of the V being the center of rotation, and assuming a pulsed-cw waveform with sufficient range resolution so that only two point scatterers fell into each range bin (except the first which had only one).

We used a second degree model for the aspect history estimate:

$$\hat{\theta}(t) = c_1 t + c_2 t^2. \tag{3.48}$$

As discussed above, we need to ensure that all allowable estimates cover the same range of aspects. We did so by imposing the constraints

$$\hat{\theta}(0) = 0 \quad , \quad \hat{\theta}(1) = 1. \tag{3.49}$$

This requires

$$c_1 + c_2 = 1, \tag{3.50}$$

so we can write all permissible estimates in the form

$$\hat{\theta}(t) = (1 - c)t + ct^2, \tag{3.51}$$

with c our free parameter.

The focusing algorithm began with the aspect history estimate $\hat{\theta}(t) = t$, i.e., $c = 1$, thus producing the fixed-focus ISAR image. The resulting image intensity is displayed in the top of Figure 3.4. Although this can be seen to be poorly focused away from the vertex, with the fixed-focus approach we would stop at this point and accept this result. The iterative approach begins with this image and attempts to perform aspect compensation. The first step is to search the range bins and find the bin in which the

image intensity is the most spread out in cross-range, since, as we mentioned above, this is the range bin that will provide the most sensitive measure of error in the aspect history. The data in this range bin is then used in the iterative-focusing algorithm described above, its aspect history estimate (the parameter c) being adjusted until it arrives at the minimum-width image. The resulting aspect history estimate is then used to focus the other range bins, resulting in the two-dimensional image intensity shown in the bottom of Figure 3.4. This is seen to be well focused at all points on the target. Clearly this image would be much more useful for identifying the target than the fixed-focus image would be.

Acoustic Imaging Experiment

Simulations have the drawback that the simulator is in such complete control of every aspect of the simulation that there is always the suspicion that the model used was not realistic enough, or that something was "tweeked" to get a desired result, or for some other reason that the simulation results do not accurately depict how the proposed technique will perform in practice. Ideally, simulations should always be followed up with studies using real data. Unfortunately, radar data for testing our iterative ISAR technique was not readily available. We therefore have sought to remedy the situation somewhat by building an acoustic imaging system analogous to a radar.

The system was built around a Polaroid ultrasonic transducer designed for use in automatic-focus cameras. We built transmitting/receiving drivers and an interface card for use with an IBM PC that allowed the transducer to transmit a pulsed-cw waveform and to receive the echoes from it. Received echoes were digitized in real time and recorded on diskette for later processing. The center frequency of the acoustic transmitter was 50 kHz, and the pulsed-cw waveform had a duration of 16 cycles. Taking the speed of sound to be 330 m s^{-1}, the range resolution of the acoustic

imaging system was thus

$$\delta x = \frac{330 \text{ m s}^{-1}}{2(50 \text{ kHz}/16)} = 5.3 \text{ cm}. \tag{3.52}$$

A V-shaped target, analogous to the simulated target used above, was constructed by attaching ping-pong balls along two plastic rods connected at the vertex of the V. The target was approximately 0.5 m in length. It was attached to the top of a vertical bar, the bottom of which was attached to a rotational micrometer, and the entire target assembly was placed approximately 5 m from the acoustic transducer. By adjusting the rotational micrometer, the aspect of the target relative to the acoustic imaging system could be controlled.

The target was rotated in 64 discrete steps with nonlinearly varying aspects

$$\theta(k) = 5^\circ \left(\frac{k}{63}\right)^2 \qquad 0 \le k \le 63. \tag{3.53}$$

With each rotational step the target was illuminated with a single acoustic pulse, and the acoustic backscatter was recorded. The total aspect change of 5° was enough to allow a cross-range resolution of

$$\delta y = \frac{\lambda}{2\Delta\theta} = \frac{330 \text{ m s}^{-1}/50 \text{ kHz}}{2(0.0873 \text{ rad})} = 3.8 \text{ cm}. \tag{3.54}$$

After all 64 pulses had been recorded, range compensation was performed using the point-scatter reference technique. This was necessary because the analog oscillator that produced the 50 kHz carrier was not coherent, i.e., phase locked, with the circuitry which produced the 16 cycle rectangular pulse. Therefore, an unknown and random phase was introduced into each complex profile.

After range compensation, the backscattered data was put through the same processing steps used in the simulation described above. Figure 3.5 shows the resulting images. One can see that the fixed-focus image (top) is only able to focus the part of the target near the vertex of the V (small $|\eta|$), and that parts of the target with large

cross-range coordinates (the arms of the V) are not present in this image. On the other hand, our iterative technique, by starting with the fixed-focus image and adjusting its aspect history estimate until the minimum-width condition is met, is able to focus essentially the entire V. Notice that, although sharply focused, the image intensity falls off away from the vertex of the V. This is not due to the way the data was processed but to the fact that the ping-pong balls did not scatter as independent point targets but rather cast acoustic shadows on one another. Those parts of the target that appear weak in the bottom image of Figure 3.5 do so because they *were* weak acoustic scatterers, being shadowed by the parts of the target nearer to the acoustic transducer.

Experiment with RADC Data Set

As mentioned, we would ideally like to explore the effectiveness of the technique presented in this chapter using real radar data collected from aircraft in flight. One might think that the RADC data set used in the previous chapter has the potential to produce crude ISAR images in that it is grouped in frames of eight consecutive complex profiles. If these eight profiles were to sample enough aspect change it would be possible to form ISAR images with eight pixels of cross-range resolution on the target. Unfortunately, since each frame of data was taken over only 7×2.5 ms $= 17.5$ ms we do not expect any accelerations to have had enough time to significantly alter the apparent angular velocity of the target, and so the aspect compensation technique of this chapter will probably not be applicable. If there are any significant aspect changes, an assumption of linear time dependence should be sufficient to describe them. For completeness, we here examine the possibility of producing ISAR images from this data set.

Recall that if the width of an aircraft is W then an aspect change of

$$\Delta\theta \geq \frac{\lambda}{2W} \tag{3.55}$$

is required to begin to resolve the target (from equation (3.12)). Assume $W = 10$ m, then for $\lambda = 12$ cm (approximate wavelength of the RADC data) we require an apparent target rotation rate of

$$\begin{aligned} \Omega &\geq \frac{\Delta\theta}{17.5 \text{ ms}} \\ &= \frac{0.12 \text{ m}}{2(10 \text{ m})} \frac{1}{17.5 \text{ ms}} \\ &= 0.34 \text{ rad s}^{-1} \\ &= 20^\circ \text{ s}^{-1} \end{aligned} \tag{3.56}$$

to begin to resolve the target in cross-range. To put a full eight pixels on the target would require eight times as fast of an apparent rotation rate, i.e., 160° s$^(-1)$.

We subjected each frame of eight complex profiles to a fixed-focus ISAR algorithm. To begin we performed profile alignment. Then range compensation was done by setting the phase of the strongest range bin to be identically zero for each profile. Finally the eight samples within each range bin were put through a discrete Fourier transform and the modulus squared of the resulting complex amplitudes then yielded an ISAR image for the frame.

We put all 1,496 frames of RADC data through this procedure and examined the images using a false-color representation designed to emphasize any cross-range structure. We found no consistent evidence of such image structure for any of the 24 aircraft. Figure 3.6 shows typical examples. We conclude that the 17.5 ms observation time was not enough to capture a sufficient range of target aspects to allow any of the targets to be resolved.

3.5 Optical Processor Implementation

The cross-range focusing operation,

$$\begin{aligned} f(y) &= \int G(t) \left[e^{i2\pi y \hat{\theta}(t)} \frac{d\hat{\theta}}{dt} \right] dt \\ &= \int G(t) h(y,t)\, dt, \end{aligned} \tag{3.57}$$

is a linear transformation of the recorded data $G(t)$ into the image $f(y)$. This operation needs to be done repeatedly in our iterative algorithm as it searches over possible aspect histories looking for that which produces a well-focused image. It is therefore very desirable that the required processing be implemented in a manner that allows each iteration to be performed very fast. Optical processing has proven to be a very effective method for performing linear transformations at high speeds and with modest power requirements. In this section we present an implementation of the iterative ISAR technique in optical hardware, and we present an experiment that demonstrates the feasibility of constructing such a system.

Figure 3.7 shows the optical processor for performing the linear transformation (3.57). The input $G(t)$ is fed into a one-dimensional, analog spatial light modulator, e.g., an acousto-optics device. Alternately, a two-dimensional, binary spatial light modulator could be used with appropriate spatial filtering, as in the system described in the previous chapter, to reconstuct the analog signal $G(t)$. This is followed by a combination of spherical and cylindrical lenses that images this field in t, and spreads it uniformly in y. This field then passes through the the two-dimensional modulator having transmittance $h(y,t)$. The field immediately after the modulator is then the product $G(t)h(y,t)$. Another comination of cylindrical and spherical lenses images this field in y and integrates it in t. The resulting output is thus

$$\hat{f}(y) = \int G(t)h(y,t)\, dt, \tag{3.58}$$

which is the desired result. This output could then be passed through a feed-back loop which would evaluate the width criterion of $\hat{f}(y)$, and vary $\hat{t}heta(t)$, and hence $h(y,t)$ to drive the image width to a minimum. However, it would probably be simplier to merely do a global search over $\hat{\theta}(t)$ and keep track of that which resulted in the minimum-width image. For example, hundreds, even thousands of transparencies $h(y,t)$ could be written onto an optical disk, and the disk could be spun to successively bring each into the system, and hence calculate images for all of them, in a time on the order of a second. These issues should be explored more thoroughly after experience with real ISAR data makes it clear how varied theactual aircraft motions are in practice, hence how many potential transformations $h(y,t)$ need to be considered.

We performed a preliminary feasibility study of this system using a magneto-optical device (MOD) as the programmable transparency $h(y,t)$. We did not implement the first half of the processor but rather formed the product $G(t)h(y,t)$ digitally and then fed a binarized version of the result into the MOD. For $G(t)$ we used data from the simulation described above, that is, $G(t)$ was taken to be the recorded field of a range bin consisting of two point scatterers when the target aspect varied as $\theta(t) = t^2$. Again, aspect history estimates based on

$$\hat{\theta}(t) = (1-c)t + ct^2 \tag{3.59}$$

were used, and c was varied steps of 0.1 from -1 to 1. Figures 3.8 and 3.9 show oscilloscope traces of the output of detector D for various values of c. These are the images $|\hat{f}(y)|^2$ of this particular range bin. The two point scatterers are seen to come into focus as the system moves from $c = 0$ (the fixed-focus image) to $c = 1$ (the "true image").

3.6 Conclusion

In the previous chapter we found that the use of multiple range profiles were required to achieve reliable aircraft identification. In this chapter we have described how, alternately, the same profiles can be used to form a two-dimensional image of the target. The cost of this additional image dimension is that we must precisely estimate target motion. The technique we have developed above shows promise of being able to do this for fairly general target motion. While we have not yet been able to apply it to a radar data set, we have demonstrated its potential through simulation and an acoustic imaging experiment. We have also demonstrated the feasibility of performing the required processing with an optical computing system.

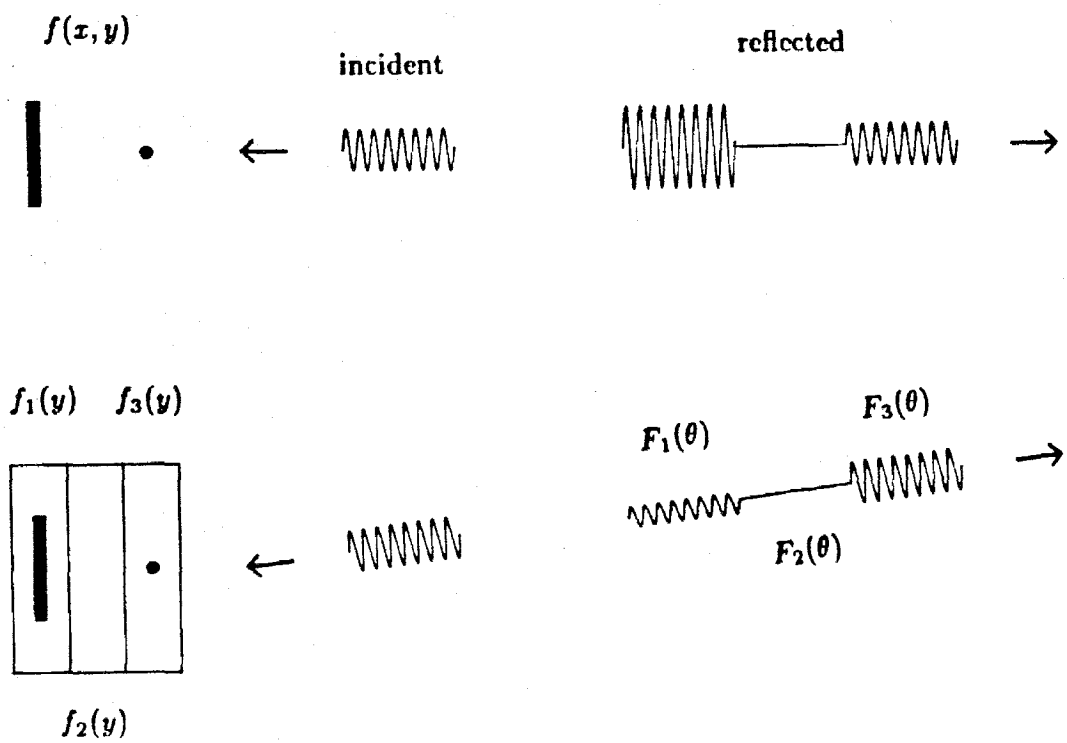

Figure 3.1: Under the physical optics approximation, a target can be characterized by a reflectivity distribution $f(x, y)$. In the case shown it is 1 in the bar and dot and 0 elsewhere. An incident pulse travels farther in being reflected from the bar, so the scatter from the ball and bar are spatially separated in the scattered field which returns to the radar. Thus the target is resolved into range bins (outlined in the bottom illustration). Each range bin can be characterized by a one-dimensional reflectivity distribution $f_k(y)$. When a pulse is incident from a different aspect the amplitude of the scatter from the different range bins may change. This change gives an indication of the cross-range (y) structure of the range bin. In fact each is a sample of the Fourier transform of the range bin reflectivity distribution. The argument of the Fourier transform being proportional to the aspect θ.

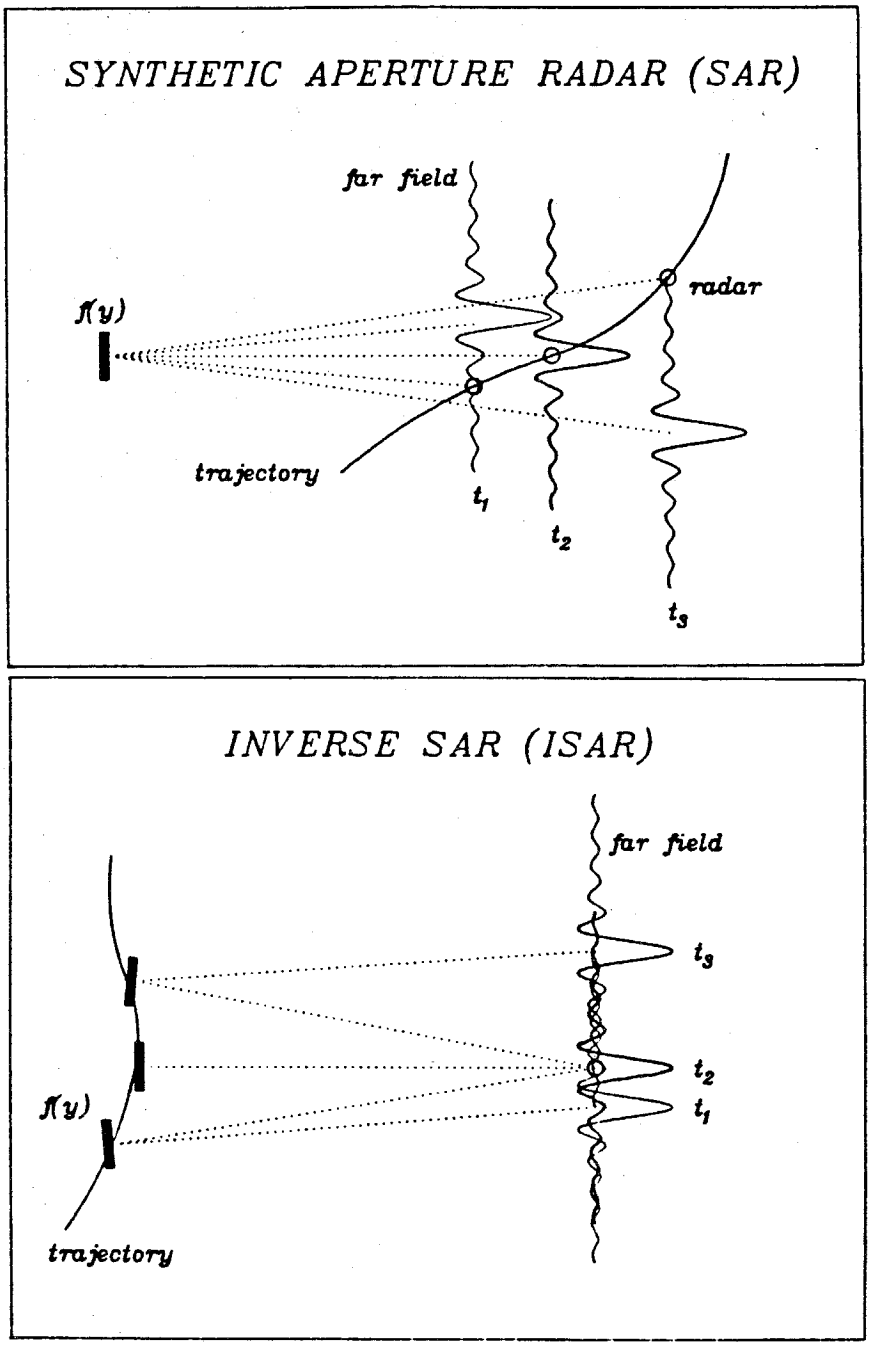

Figure 3.2: Different sources of relative motion for SAR and ISAR. In the SAR case, the *radar* moves along a trajectory, and as it does it sees different target aspects. When it illuminates the target at different times, e.g., t_1, t_2, t_3, it thus samples different components of each range bin's far-field scatter. In the ISAR case the same effect arises by motion of the *target* along a trajectory.

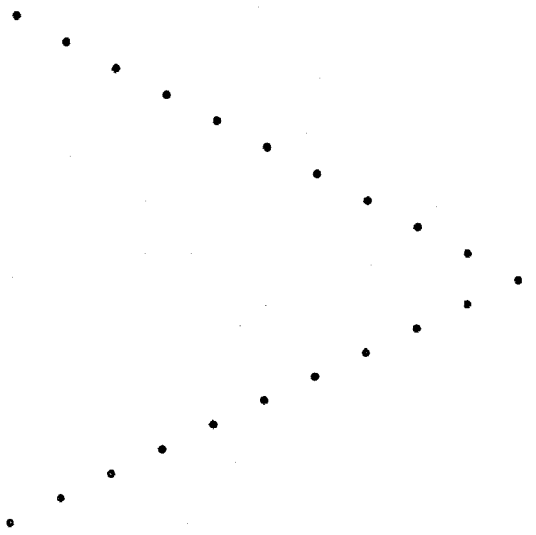

Figure 3.3: Simulated target for testing iterative ISAR algorithm. Radar is off to the right.

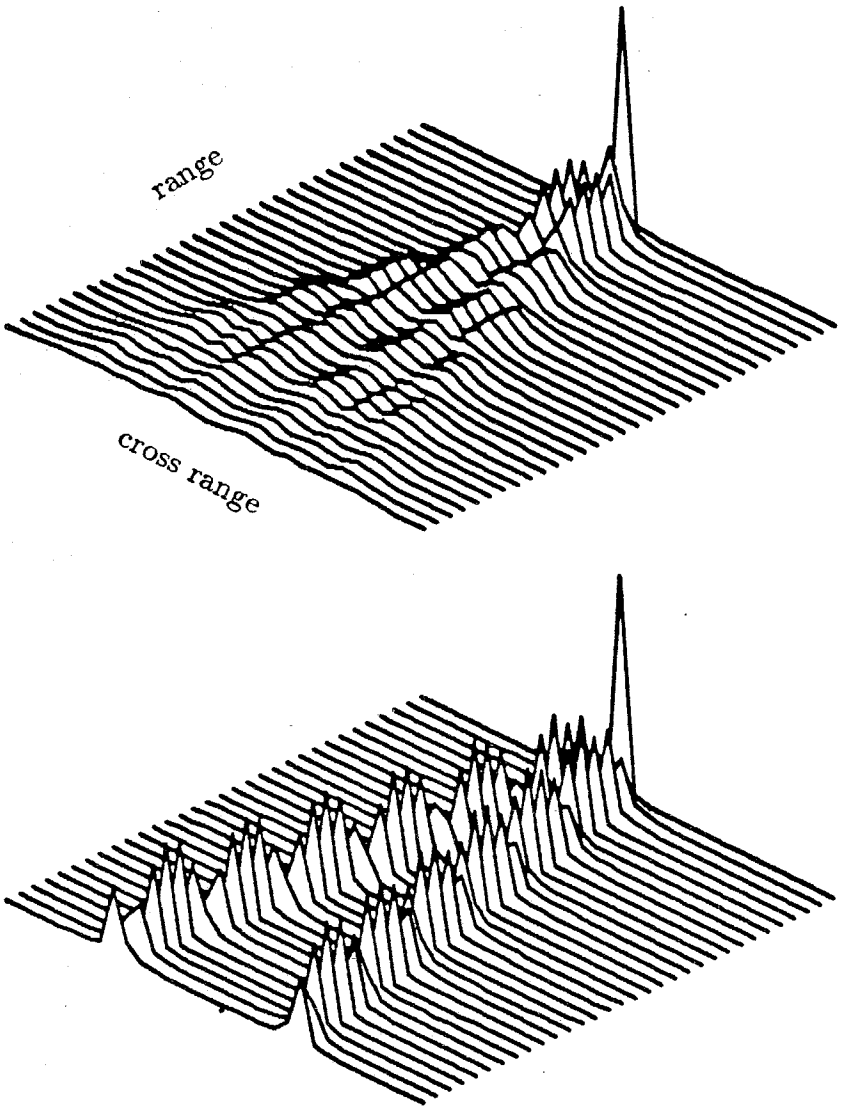

Figure 3.4: Simulated ISAR images. Top is result of fixed-focus processing while bottom is result of iterative approach. Each of the 32 lines is the image of a single range bin.

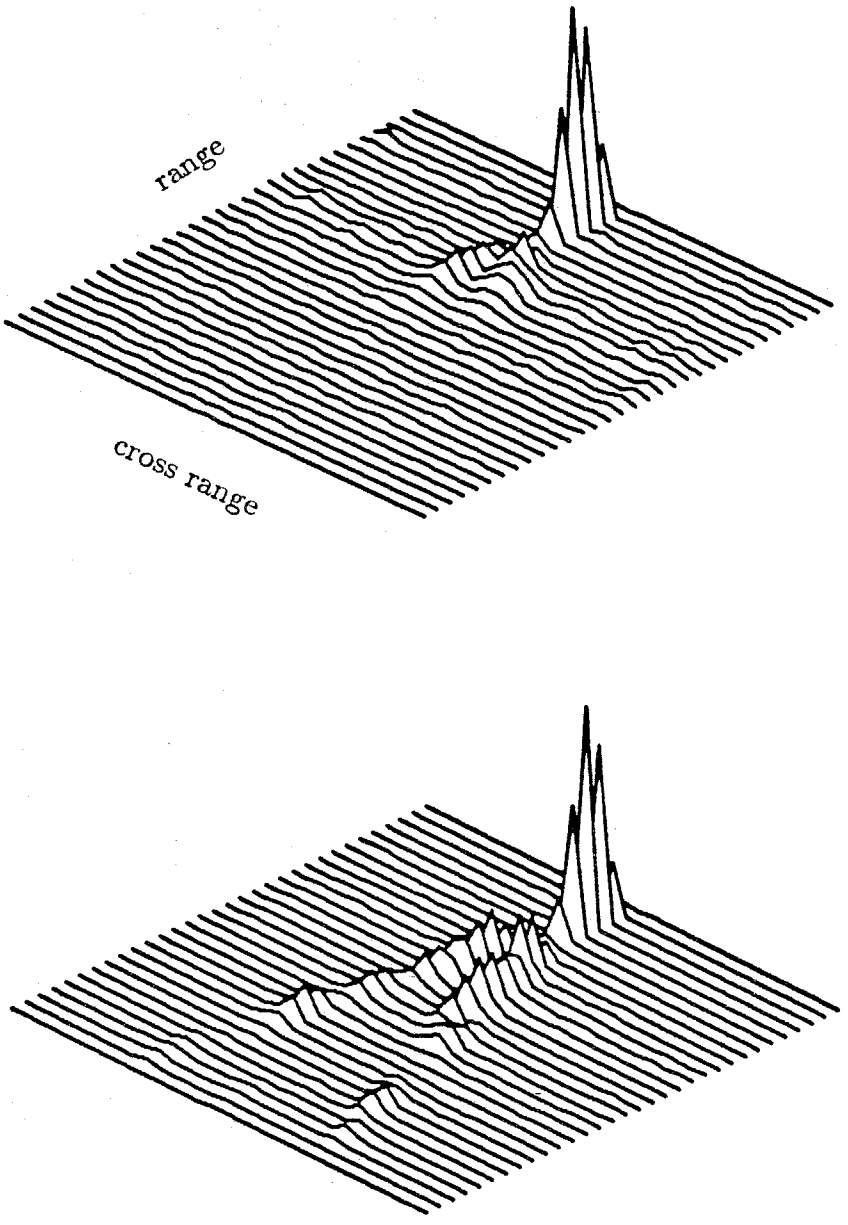

Figure 3.5: Acoustic "ISAR" images. Top is result of fixed-focus processing. Bottom is result of iterative technique described in text.

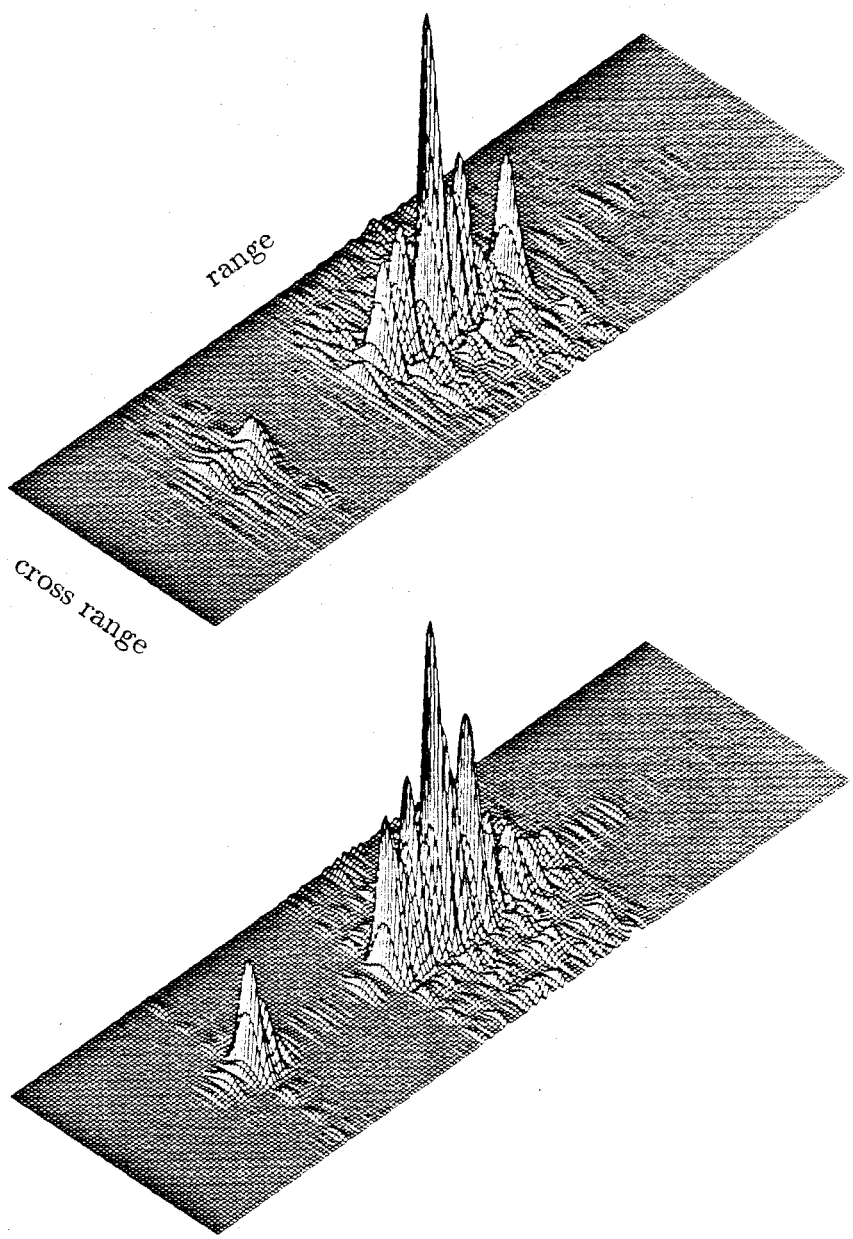

Figure 3.6: ISAR images derived from RADC data set. Both images are of the same aircraft at (nominally) the same aspect. There are only eight resolution cells in cross range, but these have been interpolated to thirty-two for visualization purposes. Essentially all image energy falls into the zero cross-range cell.

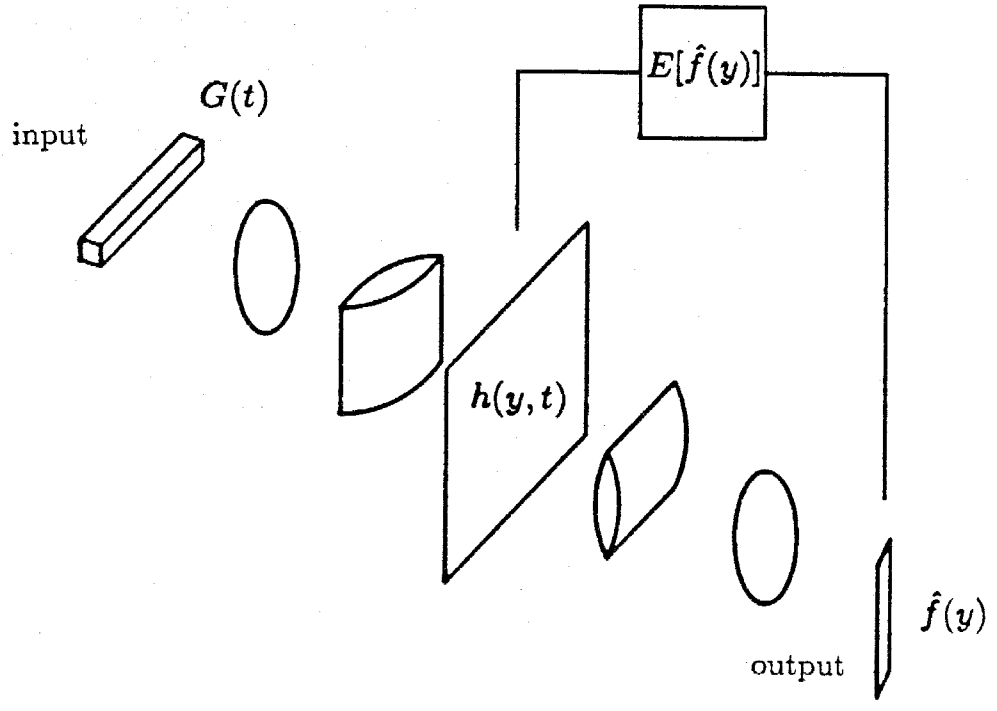

Figure 3.7: Optical system for performing linear transformations required by ISAR processor.

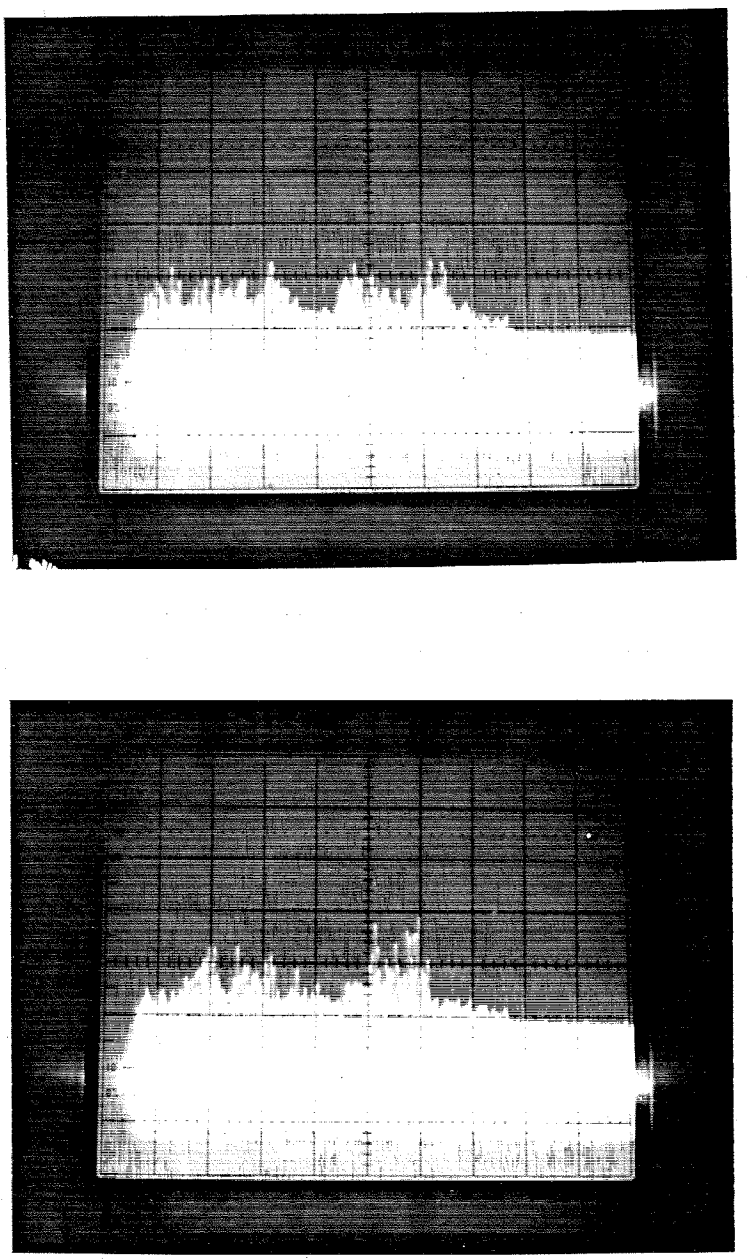

Figure 3.8: Output of optical ISAR processor attempting to focus range bin consisting of two point scatterers. Top $c = 0$, bottom $c = 0.5$.

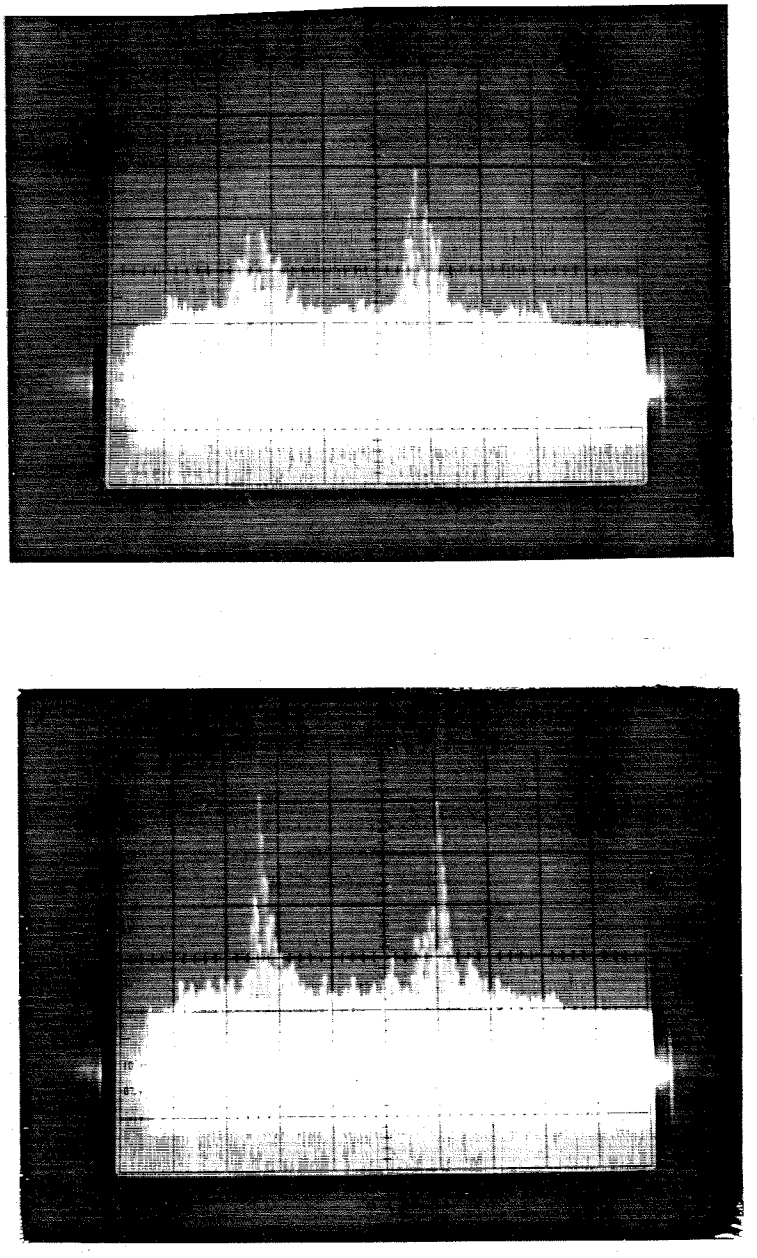

Figure 3.9: Output of optical ISAR processor attempting to focus range bin consisting of two point scatterers. Top $c = 0.8$, bottom $c = 1$.

Chapter 4

Fundamentals of Planetary Radar Astronomy

Radar astronomers use radar systems to investigate solar system bodies other than Earth: the Sun, planets, moons, asteroids, comets, and planetary rings. The Sun's unique environment makes it a special case, and the techniques and goals of solar radar astronomy differ sufficiently from those of planetary radar astronomy that the two are considered separate fields with their own distinct practitioners and literature. In this and the following chapters we will be concerned with planetary radar astronomy using Earth-based systems exclusively, however, spacecraft-based radars are playing an increasing role in the field. Earth-based astronomical radars do not differ in basic design from other radars except that they must employ huge apertures, extremely high power transmitters, and very low noise receivers in order to compensate for the tremendous R^{-4} losses encountered when observing objects at great distances (on the order of 1 AU = 150,000,000 km). Consequently they are expensive to build and maintain, and currently there are only two such instruments devoted to

planetary radar astronomy. The Goldstone Solar System Radar, which has a primary wavelength of 3.5 cm, is located in the Mojave desert of California and is operated by the Jet Propulsion Laboratory as part of the National Aeronautics and Space Administration's Deep Space Network. The 300 m Arecibo Observatory, which has a primary wavelength of 12.6 cm, is located in Arecibo, Puerto Rico, and is operated by the National Astronomy and Ionosphere Center. Both instruments are scheduled for upgrades in the near future that will increase their capabilities. The nominal system parameters for both upgraded instruments will be approximately: antenna gain of $10^{7.4}$, transmitter power of 1 MW, and system noise temperature of 20 K. However Arecibo, operating at 3.7 times the wavelength of Goldstone, will be roughly a factor of $3.7^2 = 14$ more sensitive.

In 1946 researchers in both Hungary and the United States obtained radar echoes from the Moon [34]. Although their objectives were to study radio wave propagation through the ionosphere and to investigate the possibility of using the Moon as a communications relay, this was the first detection of a planetary body by radar and can be considered as the beginning of planetary radar astronomy. However, it was not until the beginning of the space age that there was sufficient interest to motivate the construction of radar systems with enough sensitivity to study planetary structure in some detail. In the early 1960's the radar properties of the Moon were extensively studied [52, and references therein], and much of our understanding of radar scattering from rocky surfaces stems from these investigations [48].

During the 1960's and 1970's, improvements in the sensitivities of Earth-based radars allowed researchers to undertake increasingly detailed studies of other solar system entities [6, 16, 14, 39]. For example, before 1972 it had been thought that the rings of Saturn were composed of sub-millimeter-size particles. Radar detections of the rings proved that a significant fraction of the particles must have sizes on the

order of 10 cm [39, and references therein]. This was later verified by the voyager spacecraft during their encounters with Saturn. Shortly after that, radar echoes were obtained from Jupiter's moons Europa, Ganymede, and Callisto. These echoes had bizarre polarization properties unlike anything that had been observed for the inner planets [33], spurring investigations into the possible radar scattering mechanisms of icy bodies [38, 15, 18, 9, 10, 41]. During the last decade radar observations have provided information on the surface structure and composition of members of the huge, but poorly understood, population of mainbelt asteroids [36], and provided the only practical methods to date for constraining the shape of near-Earth asteroids [37, 40, 35].

4.1 Objectives

The goals of planetary radar astronomy generally fall into two categories. The first concerns the determination of a target's motion. Radar observations are important in refining, often dramatically, our knowledge of orbits. The utility of radar for this purpose stems from its ability to measure distance via time delay, and radial velocity through the Doppler effect. These quantities complement optical observations that can only provide angular plane-of-sky position. Moreover, the precision of radar observations is very high, typically on the order of 1 part in 10^6 to 10^8. Augmenting optical sightings of a newly discovered object with precise radar measurements can refine our knowledge of its orbit to such an extent as to make the difference between it being lost and it being recovered at its next apparition. This has been particularly true in the case of near-Earth asteroids which are so small that they can be observed only for the short time when they pass by the Earth [58]. Because it can directly measure distance, and due to its high precision, radar has also been among the most

powerful tools for the determination of the astronomical unit (AU), the mean distance from the Earth to the Sun, thus fixing the scale of the solar system, and for testing the predictions of the General Theory of Relativity regarding planetary motion. Apart from its orbit, planetary motion also involves rotation of a body about its polar axis. The field scattered from a rotating body contains a Doppler broadening that is proportional to its rotation rate, and this was used in the 1960's to accurately determine for the first time the rotation periods of Mercury and Venus [39]. This Doppler broadening also depends on the orientation of the target's pole with respect to the radar. This effect makes radar a potentially powerful tool for the determination of pole directions [29].

The second category of radar astronomy objectives is concerned with investigating the nature of the target itself, the composition and structure of its surface. The success of these investigations relies on our ability to physically interpret the origin of the field backscattered from a target. The most common radar experiments involve transmitting a circularly polarized field and receiving both orthogonal circular polarizations. Two observable properties of great importance in the backscattered field are its intensity and its polarization state. For rocky surfaces such as those of the inner planets, the Moon, and the asteroids, these provide constraints on the reflectivity of the surface material and its degree of wavelength-scale roughness. These, in turn, can provide constraints on such things as the surface bulk density, metal content, and rock population [34, 20]. For icy bodies such as the large moons of Jupiter, it is not yet clear what the corresponding physical properties are, and ongoing research seeks to better understand the processes responsible for the radar properties of such objects [41].

For observations that do not spatially resolve the object, the results are global averages of these quantities. If the radar echoes from different regions of the target can

be spatially resolved, then one can observe the variations of these physical quantities over the surface, thereby helping to increase our understanding of the geology of the object. Accordingly, a primary goal of radar astronomical work has always been to develop and apply techniques for obtaining spatial resolution. The last two chapters of this thesis are concerned with the development and application of a technique for spatially resolving the radar echoes from bodies for which the standard method of delay-Doppler resolution, described in section 4.4, is not applicable.

4.2 Surface Scattering

In order to interpret the radar echoes of an object we need to understand, at least at a simple level, how the interaction of the incident field with the surface gives rise to a backscattered field. At a rigorous level, i.e., a full solution of Maxwell's equations with the appropriate boundary conditions, this is an intractable problem for any real surface. We will therefore be content with simple, intuitive models of surface scattering which, nonetheless, seem to provide a reasonably accurate description of experimental data.

If a patch of the surface is smooth, flat, and homogeneous at all scales within a few orders of magnitude of the radar wavelength, then the scattering of an incident plane wave is well approximated by the classical result for a plane wave incident on a flat dielectric interface [45, chapter 6]. If the angle of incidence is zero (the plane wave is normally incident) then the reflected field will be a plane wave traveling directly back towards the radar. The intensity of this backscattered wave will be reduced relative to the intensity of the incident field by the reflection coefficient

$$R = \left| \frac{n-1}{n+1} \right|^2 , \tag{4.1}$$

where n is the index of refraction of the surface material and we assume the atmo-

sphere (if any) of the object has an index very close to 1. If the angle of incidence is non-zero (non-normal incidence) then the reflected plane wave will not be backscattered but instead will travel off in a direction determined by Snell's Law. If we use γ to denote the angle of incidence then the backscattered power dP from a surface patch of area dS is given by

$$dP \propto \sigma_0(\gamma)\, dS, \tag{4.2}$$

where

$$\sigma_0(\gamma) \propto \begin{cases} R & \text{if } \gamma = 0 \\ 0 & \text{otherwise} \end{cases} \tag{4.3}$$

is called the surface's *scattering law.* A surface with a scattering law of this form is called a *specular* surface. We generally use the radar equation to express the received power in terms of the target's radar cross section. The scattering law is then defined by

$$d\sigma = \sigma_0(\gamma)\, dS, \tag{4.4}$$

where $d\sigma$ is the radar cross section of the surface patch of area dS for an angle of incidence γ. We assume the scattering law depends only the angle of incidence, that is, that the scattering from the surface is azimuthally isotropic.

The method of *facets* treats a more general surface as being composed of a collection of planar surface patches each of which has specular scattering characteristics. This is depicted in Figure 4.1. At a particular angle of incidence only those facets that are oriented normal to the incident field will contribute to the backscatter. Note that for a single observation these scattering contributions will add up coherently, i.e., with definite phase relations among themselves. This results in the phenomenon of *speckle* or *self noise* in the total scattered field. In practice it is *always* necessary to incoherently average the power from many observations in order reduce the effects of thermal noise as well as speckle. Each of these observations will be from a slightly

different orientation, because the object is moving, and hence will involve different phase relations between the various facets. Coherent interference between the facets will be averaged out, and the averaged backscattered power then consists of the sum of the scattered power from each of the facets. This is what allows us in all that follows, to write the total backscattered power as the sum of backscattered power from each surface patch.

We define the slope of a facet as the angle it makes with the mean surface. For a random surface, the distribution of slopes will have zero mean (by definition) and some rms (root mean square) value. As long as the angle of incidence is less than the rms slope there will be a significant number of facets oriented normal to the incident field and hence significant backscatter. When the angle of incidence exceeds the rms slope then the backscattered power will begin to decrease as there will be fewer and fewer facets with large enough slopes to produce backscatter. Thus, the scattering law $\sigma_0(\gamma)$ will be largest at $\gamma = 0$ and will fall off with increasing γ. The width of $\sigma_0(\gamma)$ gives an indication of the rms surface slope.

Various models for scattering laws have been proposed based on, among other things, theoretical considerations and analytic simplicity. One of the most widely used models is the *Hagfors law*,

$$\sigma_0(\gamma) = \frac{\rho}{\left(\cos^4\gamma + s_0^{-2}\sin^2\gamma\right)^{3/2}} \tag{4.5}$$

where s_0 is the rms slope in radians and ρ is a constant depending on the electrical properties of the surface. For analytical simplicity a *cosine scattering law* is very attractive. They have the form

$$\sigma_0(\gamma) = \rho\cos^n\gamma \tag{4.6}$$

where n is some real number and ρ is a constant. The value of n determines the width of this scattering law and hence gives an indication of the rms slope. If we take the

half-power angle as indicative of "effective" slope then

$$\text{"effective" slope} \approx \cos^{-1} \sqrt[n]{0.5} \, . \tag{4.7}$$

Both the Hagfors and cosine scattering laws are plotted in Figure 4.2 for the case of an rms slope of 10°.

When a circularly polarized plane wave is normally incident on a planar dielectric interface, the reflected field it gives rise to is also circularly polarized but in the opposite sense, i.e., a right-handed incident wave gives rise to a left-handed reflected wave and vice versa. We say that the reflected field is in the *OC polarization*, i.e., the opposite circular polarization from the transmitted field. Scattering of this type is sometimes called *polarized scattering.* If the facet model gave a complete description of planetary surfaces then all backscattered power would be in the OC polarization. While most of the power in radar echoes from rocky bodies (as opposed to icy bodies) is in the OC polarization, this is generally accompanied by varying amounts of power in the SC polarization (same circular polarization as the transmitted wave).

Backscattered power in the SC polarization can arise from multiple scattering and/or from scattering from structures with significant variations at scales on the order of the radar wavelength. As an extreme example consider the scattering of a circularly polarized wave from a straight wire. The structure of the wire allows the incident field to induce current only along the length of the wire, hence the scattered field will necessarily be linearly polarized. A linearly polarized field is the superposition of equal amounts of both orthogonal circular polarizations. In this manner a circularly polarized wave scattered from a linear structure produces a field that contains equal amounts of power in both the OC and SC polarizations. This idealized case might be approximated in practice by scattering from the jagged edges of rocks. Scattering from an ellipsoidal rock of wavelength-order dimensions would produce a

similar effect. Its electrical susceptibility will be greater along its longer dimension, so the linear components of the incident circular wave will be backscattered with different amplitudes resulting in a non-circularly polarized reflection. Therefore the scattered field it produces will in general contain power in both circular polarizations. This kind of scattering is sometimes referred to as *depolarized scattering.*

A wavelength-scale structure will generally be a fairly isotropic scatterer. The total backscattered power from a surface containing many such scatterers, randomly oriented and positioned (for example, a planetary surface strewn with rocks as the surface of Mars appears in Viking lander images) will be the sum of all their individually scattered powers (assuming an averaging of many observations as described above). We therefore expect that scattering laws for depolarized scatter will not have the specular characteristics of polarized scatter but instead a more broad, or *diffuse*, dependence on the angle of incidence. If a surface patch scatters isotropically for any angle of incidence, then the backscattered power is simply proportional to the incident intensity. As γ increases, the incident intensity on the surface decreases, as illustrated in Figure 4.3, because the radar maintains a constant intensity over the projected area $dA = \cos\gamma\, dS$ but this is spread out over a surface area dS which increases with γ. This spreading results in an intensity on the surface which is proportional to $\cos\gamma$. Therefore in this case

$$\sigma_0(\gamma) = \rho \cos\gamma, \tag{4.8}$$

where ρ is a constant that describes the depolarized "brightness" of the surface.

An object that scatters in this manner is said to be *uniformly bright* because each element of projected area produces the same amount of backscatter (provided ρ is the same, of course). At optical wavelengths the full Moon is such an object. When we look at the full Moon we are observing backscattered sunlight. In such cases the Moon appears as a uniformly bright disk (except for the markings due to ρ variations)

with no falling off of the brightness near the edges, i.e., at points of large incidence angle.

The uniformly-bright scattering model is sometimes an over-idealization, and in many cases depolarized scatter from a surface will not be perfectly diffuse as in (4.8) but will be slightly more specular ($\sigma_0(\gamma)$ slightly more peaked near $\gamma = 0$). For many objects

$$\sigma_0(\gamma) = \rho \cos^2 \gamma \tag{4.9}$$

gives a more accurate description. Objects that backscatter in this fashion are said to be *Lambertian*. We can describe either of these cases, or something in between, with a general cosine scattering law

$$\sigma_0(\gamma) = \rho \cos^n \gamma, \tag{4.10}$$

where for a given situation we can choose n to be the real number that leads to the best description of the observed backscattering. The cosine scattering law is plotted in Figure 4.4 for $n = 1$ and $n = 2$. This scattering law is ubiquitous in models of depolarized radar scatter and has proven to provide a reasonably accurate description of observed backscatter [20, 53].

We have seen that smooth surfaces give rise to only OC backscatter while surfaces with wavelength-scale roughness produce both OC and SC backscatter. If σ_{OC} and σ_{SC} are the target's radar cross sections in the OC and SC polarizations, then the *circular polarization ratio*,

$$\mu_c = \frac{\sigma_{SC}}{\sigma_{OC}}, \tag{4.11}$$

is a dimensionless quantity that provides a measure of the amount of wavelength-scale roughness of the surface. A surface composed of smooth facets would produce only polarized backscatter and would have $\mu_c = 0$. With increasing surface roughness, the depolarized component of the backscatter would account for an increasing portion

of the total backscattered power and μ_c would increase. In the limit of a "perfectly rough" surface we might expect $\mu_c \rightarrow 1$. However, this line of reasoning applies only to rocky surfaces such as those of the inner planets and asteroids. The icy Galilean satellites, for example, are characterized by $\mu_c > 1$. The reason for these polarization inversions is not well understood, but the much greater depth of penetration of radio waves into ice, as opposed to rock, so that icy targets are dominated much more by volume scattering, is probably a key factor [41].

4.3 Coordinate Systems

The question of what astronomical coordinate system to use is now a matter of convenience, but it was once considered a heresy to advocate the use of any but an Earth-centered system, even though as early as the third century B.C., Aristarchius had pointed out that the motions of the planets and the stars are much simpler to describe in a Sun-centered coordinate system than in an Earth-centered system [22]. Fortunately man's desire for a simple explanation of nature proved more powerful than his need for dogma, and by the eighteenth century A.D. the Sun-centered picture of the solar system, with the combined weight of Copernicus, Galileo, Kepler, and Newton on its side, gained general acceptance as the most appropriate in which to describe planetary motion. Now all educated people take it for granted that the Sun is the center of the solar system, that the Earth is just one of several planets, that the planets orbit around the Sun, and that the apparent daily motions of the Sun and stars through the sky are due to the rotation of the Earth.

Figure 4.5 shows the relation between Sun-based, Earth-based, and target-based coordinate systems. We consider the Sun at rest. The Earth and the target have two motions. First, each follows an elliptical orbit around the Sun, and second, each spins

about its polar, i.e., z, axis. (If the target is a moon then its motion has three parts: it shares the orbital motion of its host planet around the Sun, it follows an elliptical orbit around its planet, and it rotates.) For a given problem the appropriate coordinate system is that which leads to the most useful description. For observational purposes an Earth-based system, or more precisely a telescope-based system, is appropriate because it gives the positions of objects relative to the observer and tells us in what direction to point our telescope. When we are interested in describing the interaction of a radar signal with the surface of an object, target-based coordinates are the most appropriate.

The systems we will make use of in the following chapter are shown in Figure 4.6. All systems have their origin at the spherical target's center of mass. The (x, y, z) system, "target coordinates," rotates with the target. The z axis coincides with the target's axis of rotation, and the target's equator lies in the $x - y$ plane. The orientation of this system at time $t = 0$ (e.g., the start of observations) will be denoted by the (x_0, y_0, z_0) system. The effect of the target's rotation is to cause the x and x_0 (and the y and y_0) axes to separate by an angle

$$\psi = \frac{2\pi t}{P}, \tag{4.12}$$

called the *rotational phase*, with P the target's rotation period. This results in the following relations:

$$x_0 = x\cos\psi - y\sin\psi \tag{4.13}$$

$$y_0 = x\sin\psi + y\cos\psi \tag{4.14}$$

$$z_0 = z. \tag{4.15}$$

Rotating the (x_0, y_0, z_0) system through an angle δ about the y_0 axis in a left-handed

sense we obtain the (x_r, y_r, z_r) system:

$$x_r = (x\cos\psi - y\sin\psi)\cos\delta + z\sin\delta \tag{4.16}$$

$$y_r = x\sin\psi + y\cos\psi \tag{4.17}$$

$$z_r = -(x\cos\psi - y\sin\psi)\sin\delta + z\cos\delta. \tag{4.18}$$

We will refer to these as "radar coordinates." The orientation of these systems is chosen so that the radar lies on the x_r axis; the angle δ is then called the *subradar latitude*, and ψ may also be called the *subradar longitude*. At the point on the sphere with latitude δ and longitude ψ, the radar appears to be directly overhead. These two angles, together with the radar's x_r coordinate, completely specify the orientation between the target and the radar.

Corresponding to the (x, y, z) and (x_0, y_0, z_0) systems are the spherical coordinates (θ, ϕ) and (θ_0, ϕ_0):

$$x_0 = a\sin\theta_0\cos\phi_0 \tag{4.19}$$

$$y_0 = a\sin\theta_0\sin\phi_0 \tag{4.20}$$

$$z_0 = a\cos\theta_0, \tag{4.21}$$

with a the radius of the sphere, and an identical relation holds between the (x, y, z) and (θ, ϕ) systems. Because these angles are measured with respect to the sphere's axis of rotation, the transformation between these systems is very simple:

$$\theta_0 = \theta \tag{4.22}$$

$$\phi_0 = \phi + \psi. \tag{4.23}$$

In radar coordinates, the sphere's surface unit normal at a point (x_r, y_r, z_r) is simply $(x_r, y_r, z_r)/a$, where $a = \sqrt{x_r^2 + y_r^2 + z_r^2}$ is the sphere's radius. In radar coordinates the unit vector $(1, 0, 0)$ points in the radar's direction. The inner product of

these two vectors is the cosine of the angle of incidence at the point (x_r, y_r, z_r), hence

$$\gamma = \cos^{-1} \frac{x_r}{a}. \tag{4.24}$$

4.4 Radar Resolution of Rotating Spheres

In radar coordinates, let the radar be at $(R, 0, 0)$, with R very large, and consider a small surface patch dS on the sphere at (x_r, y_r, z_r). The patch's distance from the radar is

$$R_{dS} = \sqrt{(R - x_r)^2 + y_r^2 + z_r^2} \tag{4.25}$$

which can be expanded

$$R_{dS} = (R - x_r)[1 + \frac{1}{2}\frac{y_r^2 + z_r^2}{(R - x_r)^2} + \cdots]. \tag{4.26}$$

Since $R \gg x_r$ and $x_r^2 + y_r^2 \leq a^2$, we can write

$$\frac{y_r^2 + z_r^2}{(R - x_r)^2} \approx \frac{y_r^2 + z_r^2}{R^2} \leq \left(\frac{a}{R}\right)^2. \tag{4.27}$$

The quantity a/R is half the (maximum) angular size of the target as seen from the radar. Except for the Sun and the Moon, all solar system bodies look like points, i.e., a/R is less than the arc-minute resolution limit of our eyes, and so $(a/R)^2 \leq 10^{-7}$. This justifies the *far-field approximation* in which we neglect all but the first term of (4.26) and write

$$R_{dS} = R - x_r. \tag{4.28}$$

The distance from the radar to the target's center of mass, R, is called the *gross range*. We have already remarked how measurement of this quantity can provide powerful constraints for orbit determination. However, when we are concerned with measuring properties of the target's surface, as opposed to its orbit, this is a useless

constant, and we can remove it from (4.28) leaving

$$R_{dS} = -x_r. \tag{4.29}$$

(In practice this is done by adjusting the radar's *delay window*, the time interval over which we record backscatter.) This shows that range-resolved observations of the target will separate the backscatter from points with different x_r coordinates. The radar can only illuminate the half of the sphere that faces it; the other half is shadowed. The illuminated half is $x_r \geq 0$. The maximum value of x_r for an illuminated point is a and the minimum value is 0. These differ in range by a so their round trip delay difference will be

$$T = \frac{D}{c} \tag{4.30}$$

where $D = 2a$ is the diameter of the target and c is the speed of light. This is the *delay dispersion* of the target.

Neglecting relativistic effects, the *Doppler frequency* of a moving scatterer is given by $-2v_r/\lambda$, where λ is the radar wavelength and v_r is the scatterer's radial velocity with respect to the radar [49, section 3.1]. Therefore the Doppler frequency of the surface patch dS is

$$\nu_{dS} = -\frac{2\dot{R}_{dS}}{\lambda}, \tag{4.31}$$

and using (4.28) we can write this as

$$\nu_{dS} = -\frac{2}{\lambda}\dot{R} + \frac{2}{\lambda}\dot{x}_r. \tag{4.32}$$

The first term is the Doppler frequency of the object's center of mass, called the target's *Doppler centroid.* Like the gross range it is useful in orbit determination but of no value for studying the object's surface as it is common to all points on the sphere. Removing it we have

$$\nu_{dS} = \frac{2}{\lambda}\dot{x}_r. \tag{4.33}$$

Making use of (4.12), (4.16), and (4.17) we find

$$\frac{2}{\lambda}\dot{x}_r = -\frac{2}{\lambda}(x\sin\psi + y\cos\psi)\dot{\psi}\cos\delta \tag{4.34}$$

$$= -\frac{4\pi\cos\delta}{\lambda P}y_r, \tag{4.35}$$

and so

$$\nu_{dS} = -\frac{4\pi\cos\delta}{\lambda P}y_r. \tag{4.36}$$

(The Doppler centroid is removed in practice by tuning the center frequency of the radar receiver to the Doppler centroid.) This shows that Doppler-resolved observations separate backscatter from points with different y_r coordinates. The extreme values of y_r are $-a$ and a, so the Doppler bandwidth, or *Doppler dispersion*, of the target is

$$B = \frac{4\pi D\cos\delta}{\lambda P}. \tag{4.37}$$

A measurement of B provides a mutual constraint on D, $|\delta|$, and P. If any two of these are known then the third can be determined. This is the principle by which rotational periods, diameters, and pole directions are determined from radar observations.

Doppler Spectra

If we illuminate a target with a sinusoidal signal, each patch on the target's surface will contribute to the radar echo a sinusoidal signal shifted by the patch's Doppler frequency. The power in this contribution will be proportional to the patch's cross section. If the echo is recorded for a time Δt, then the power spectrum of this recording will resolve the echo power at different Doppler frequencies with a resolution $\Delta\nu = 1/\Delta t$. This *echo power spectrum*, or *Doppler spectrum*, is a one-dimensional radar image of the target's surface where each Doppler "pixel," or resolution bin, contains power contributions from only those points on the target's surface with the

corresponding Doppler frequency. In this section we will explore the dependence of a Doppler spectrum on the target's surface characteristics.

Assume a spherical target had the known scattering law $\sigma_0(\gamma;\theta,\phi)$ at each point (θ,ϕ) on the surface. Then a surface patch dS at (θ,ϕ) will contribute an amount of radar cross section

$$d\sigma = \sigma_0(\gamma;\theta,\phi)\,dS \tag{4.38}$$

to the Doppler bin with frequency given by (4.36). If we add up all the contributions to the Doppler bin with Doppler frequency ν, we arrive at the following expression:

$$\sigma(\nu)\,\Delta\nu = \int_{\mathcal{C}} \sigma_0(\gamma;\theta,\phi)\,dS, \tag{4.39}$$

where the region $\mathcal{C}$ contains all illuminated points on the sphere having a Doppler frequency within the Doppler resolution $\Delta\nu/2$ of ν. The function $\sigma(\nu)$ gives the density of radar cross section with respect to Doppler frequency and is typically expressed in units of $\mathrm{km}^2\,\mathrm{Hz}^{-1}$. The illuminated region of the sphere is $x_r \geq 0$, and the Doppler frequency is ν if

$$y_r = -\frac{\lambda P}{4\pi\cos\delta}\,\nu, \tag{4.40}$$

so in the limit of infinitesimal Doppler resolution, i.e., $\Delta\nu \to d\nu$, $\mathcal{C}$ is a semicircle as illustrated in Figure 4.7. Since the angle of incidence γ is the angle between the radar's direction and the surface normal, the surface patch of area dS has a projected area

$$\begin{aligned} dA &= dz_r\,dy_r = \cos\gamma\,dS \\ &= \frac{x_r}{a}\,dS \end{aligned} \tag{4.41}$$

as shown in Figure 4.8. Therefore

$$\sigma(\nu)\,d\nu = a\int_{\mathcal{C}} \frac{\sigma_0(\gamma;\theta,\phi)}{x_r}\,dz_r\,dy_r \tag{4.42}$$

or, using (4.36),

$$\sigma(\nu) = \frac{a\lambda P}{4\pi \cos\delta} \int_{-b}^{b} \frac{\sigma_0(\gamma;\theta,\phi)}{x_r}\, dz_r \tag{4.43}$$

where b is the maximum extent of z_r on the constant-Doppler contour. The contour of integration starts and ends on the boundary of the illuminated region defined by $x_r = 0$, which is also $y_r^2 + z_r^2 = a^2$, so $b = \sqrt{a^2 - y_r^2}$.

For the special case of a uniform sphere, i.e., $\sigma_0(\gamma)$ independent of θ, ϕ, and for a cosine scattering law,

$$\sigma_0(\gamma) = \rho \cos^n \gamma = \rho \left(\frac{x_r}{a}\right)^n, \tag{4.44}$$

we have

$$\sigma(\nu) \propto \rho \int_{-b}^{b} x_r^{n-1}\, dz_r. \tag{4.45}$$

For simplicity we scale things so that $a = 1$ and $y_r = -\nu$, then

$$\begin{aligned} \sigma(\nu) &\propto \rho \int_{-\sqrt{1-\nu^2}}^{\sqrt{1-\nu^2}} (1 - \nu^2 - z_r^2)^{\frac{n-1}{2}}\, dz_r \\ &= \rho(1-\nu^2)^{\frac{n}{2}} \int_{-1}^{1} (1 - w^2)^{\frac{n-1}{2}}\, dw, \end{aligned} \tag{4.46}$$

with

$$w = \frac{z_r}{\sqrt{1-\nu^2}}. \tag{4.47}$$

The integral is independent of ν, so

$$\sigma(\nu) \propto \rho(1-\nu^2)^{n/2}. \tag{4.48}$$

The amplitude and shape of the spectrum are determined by ρ and n respectively. For a real planet, variations in the scattering law over the surface will affect the shape of the spectrum. However, by summing spectra taken from different perspectives of the planet we can average out these effects, and the strength and shape of the resulting average spectrum gives us an indication of the average scattering law of the planet. Doing this for both OC and SC polarizations allows us to determine the average polarization ratio. Figure 4.9 shows examples of averaged spectra from Mars.

For a non-uniform sphere with scattering law variations over its surface, the Doppler spectrum will change with rotational phase as the target rotates different regions into the radar's view. We will denote the Doppler spectrum at rotational phase ψ as $\sigma(\nu;\psi)$ and refer to this as the target's *phase-Doppler distribution.* In the next chapter we will investigate how this function can be used to image the target's surface.

Delay-Doppler Resolution

A rotating spherical target can be resolved in both time delay and Doppler frequency using a pulsed cw waveform or a repetitive phase-coded waveform with pulse compression [34]. As shown above, this resolves the target in x_r and y_r. In general there are two distinct points on a sphere with given x_r and y_r coordinates, namely $(x_r, y_r, \pm\sqrt{a^2 - x_r^2 - y_r^2})$. Therefore a delay-Doppler image of a sphere suffers from a two-fold "North-South" ambiguity. To resolve these two ambiguous points requires either an additional receiving antenna to form an interferometer [2, 26], or the geometric leverage provided by multiple delay-Doppler images from different orientations of the target [14]. We leave aside the problem of the North-South ambiguity and consider the issues involved in obtaining delay-Doppler resolution.

Each pulse provides a delay profile of the target. We noted above that the length of these profiles, the target's delay dispersion, is

$$T = \frac{D}{c}. \tag{4.49}$$

The inter-pulse period (IPP), the time between cw pulses, must be longer than the target's delay dispersion or else profiles will overlap in time and we will suffer a delay ambiguity. So we require

$$\text{IPP} \geq T. \tag{4.50}$$

Each delay bin of a profile samples the Doppler frequencies of the points of the target within that delay bin. The sampling theorem requires that the time between these samples, which is IPP, be no bigger than the reciprocal of the Doppler bandwidth or else aliasing, i.e., Doppler ambiguities, will appear. For no ambiguities to appear in any delay bin, this requires that

$$\text{IPP} \leq \frac{1}{B}. \tag{4.51}$$

Together these conditions require

$$T \leq \text{IPP} \leq \frac{1}{B} \tag{4.52}$$

which can be satisfied only if

$$TB \leq 1. \tag{4.53}$$

The product of the target's delay and Doppler dispersions, TB, is called the target's *overspread factor.* If it exceeds unity the target is said to be *overspread* and a pulsed cw waveform, or an equivalent pulse compression approach, cannot unambiguously resolve it in delay and Doppler. The inner planets, Jupiter's Galilean Satellites, Titan, and the largest asteroids are all overspread at the principal wavelengths of the most powerful radar telescopes as show in Table 4.1.

More generally, consider *any* transmitted waveform having time duration T_t and bandwidth B_t. The bandwidth B_t will provide a delay resolution of $1/B_t$. The number of delay bins on the target is therefore

$$N_\tau = \frac{T}{1/B_t} = TB_t. \tag{4.54}$$

The time duration of T_t will provide a Doppler resolution of $1/T_t$. The number of Doppler bins on the target is therefore

$$N_\nu = \frac{B}{1/T_t} = T_t B, \tag{4.55}$$

and the total number of delay-Doppler resolution pixels is $N_\tau N_\nu$.

The time duration of the received signal is the time duration of the transmitted signal plus the delay dispersion of the target:

$$T_r = T_t + T. \tag{4.56}$$

Likewise, the bandwidth of the received signal is the bandwidth of the transmitted signal plus the Doppler dispersion of the target:

$$B_r = B_t + B. \tag{4.57}$$

Therefore, the time-bandwidth product of the received signal is

$$\begin{aligned} T_r B_r &= (T_t + T)(B_t + B) \\ &= T_t B_t + TB + T_t B + TB_t \\ &= \frac{N_\nu N_\tau}{TB} + TB + N_\nu + N_\tau, \end{aligned} \tag{4.58}$$

where we have used (4.54) and (4.55). Now $T_r B_r$ is the number of samples it takes to represent the received signal, and so it is also the maximum number of independent constraints that the received signal can place on the delay-Doppler distribution. We must have

$$N_\tau N_\nu \leq T_r B_r \tag{4.59}$$

or else there are more unknowns ($N_\tau N_\nu$) than constraints ($T_r B_r$), and the delay-Doppler distribution cannot be determined unambiguously. But this requires

$$N_\tau N_\nu \leq \frac{N_\nu N_\tau}{TB} + TB + N_\nu + N_\tau. \tag{4.60}$$

If the target is not overspread (i.e., if $TB \leq 1$) this will be true, as it must be, since we showed above that a pulsed cw waveform works in this case. If the target is overspread then it may or may not be true depending on N_τ, N_ν, and TB. If N_τ

or N_ν is zero then (4.60) is true regardless of the overspread factor. This just means that we may obtain a delay profile *or* a Doppler spectrum from any target no matter how overspread. Condition (4.60) is also satisfied if

$$N_\tau N_\nu = TB, \tag{4.61}$$

that is, the total number of resolution cells is the same as the target's overspread factor. This can be achieved by transmitting a *single* cw pulse of duration T_t. The bandwidth of this pulse is $B_t = 1/T_t$ so

$$N_\tau = \frac{T}{T_t} \tag{4.62}$$

$$N_\nu = \frac{B}{1/T_t} = T_t B, \tag{4.63}$$

and

$$N_\tau N_\nu = TB. \tag{4.64}$$

Obviously this technique can provide significant resolution only if the target is very overspread ($TB \gg 1$). No waveforms have yet been found that can circumvent (4.60) and provide unambiguous delay-Doppler resolution of an overspread target, although waveforms have been developed for use in ionospheric work for the purpose of spreading the ambiguities out into pseudo-uniform background clutter [51].

4.5 Noise

Previously we derived the radar equation:

$$P_r = \frac{P_t G^2 \lambda^2 \sigma}{(4\pi)^3 R^4}, \tag{4.65}$$

with P_r, P_t the received and transmitted powers, G the gain of the radar antenna, σ the radar cross section of the target, λ the radar wavelength, and R the distance

to the target. Dividing P_r by the noise power gives us an expression for the signal-to-noise ratio (SNR). At microwave frequencies thermal noise has a uniform spectral density equal to $k_B T_N$ where k_B is Boltzmann's constant and T_N is the system noise temperature. If the radar receiver is sensitive over a bandwidth B then the total noise power is $k_B T_N B$. Generally signals are so weak that it is necessary to perform incoherent averaging to increase the SNR. If we average N_a spectra then the SNR increases by a factor of $\sqrt{N_a}$, so

$$\text{SNR} = \frac{P_r \sqrt{N_a}}{k_B T_N B} \tag{4.66}$$

$$= \frac{P_t G^2 \lambda^2 \sigma \sqrt{N_a}}{(4\pi)^3 R^4 k_B T_N B}. \tag{4.67}$$

To capture the sum of all backscattered power we set the receiver bandwidth to equal the Doppler bandwidth of the target:

$$B = \frac{4\pi D \cos\delta}{\lambda P}. \tag{4.68}$$

We can write the sphere's radar cross section as $\sigma = \hat{\sigma}\pi D^2/4$, where $\hat{\sigma}$ is the *albedo* of the target, its radar cross section per unit projected area, and $\pi D^2/4$ is the target's total projected area. Substituting these into (4.67) gives us

$$\text{SNR} = \frac{P_t G^2 \lambda^3}{2^{10}\pi^3 k_B T_N} \frac{D P \hat{\sigma}}{R^4 \cos\delta} \sqrt{N_a} \tag{4.69}$$

where the first factor on the right contains the radar system parameters and the second the parameters of the target. The time required to obtain a frequency resolution of B is $1/B$. For a single observing session, or integration time, of duration T_i, the number of spectra with this resolution that can be obtained and averaged is

$$N_a = B T_i. \tag{4.70}$$

Using this and (4.68), equation (4.69) becomes

$$\text{SNR} = \frac{P_t G^2 \lambda^{5/2}}{2^9 \pi^{5/2} k_B T_N} \frac{D^{3/2} P^{1/2} \hat{\sigma}}{R^4 \cos^{1/2}\delta} \sqrt{T_i}. \tag{4.71}$$

A cw radar observation usually consists of turning on the transmitter and transmitting until backscatter begins to reach the radar, then shutting off the transmitter and receiving until no backscatter remains to be received. A single transmit/receive cycle of this sort is called a *run*. The length of the single run receive time is limited to the round trip delay to the target and back, $2R/c$, and this represents the maximum single-run integration time. Using this in (4.71) gives

$$\mathrm{SNR} = \frac{P_t G^2 \lambda^{5/2}}{2^{17/2} \pi^{5/2} c^{1/2} k_B T_N} \frac{D^{3/2} P^{1/2} \hat{\sigma}}{R^{7/2} \cos^{1/2} \delta}. \tag{4.72}$$

as the expression for a target's single-run SNR.

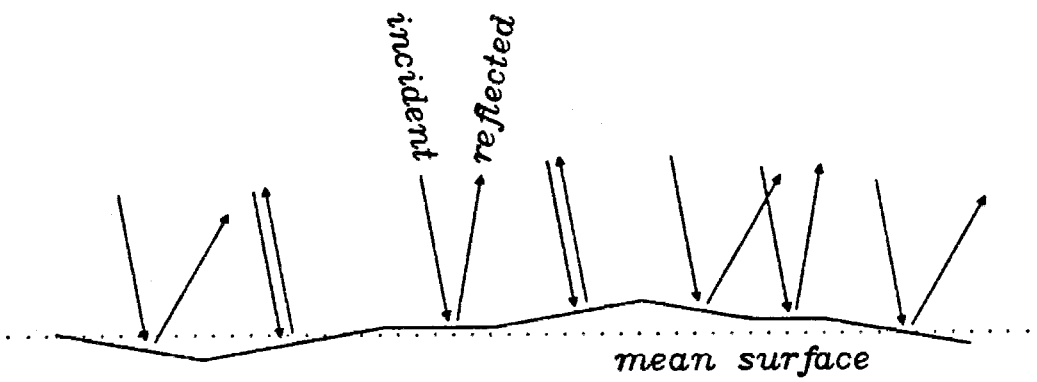

Figure 4.1: The facet model of surface scattering. The surface is modeled as piecewise planar with each facet assumed to scatter specularly. Only those facets that are normal to the incident field contribute to the backscatter (reflected field traveling in opposite direction of incident field). The facet slopes are defined relative to the mean surface (dotted line).

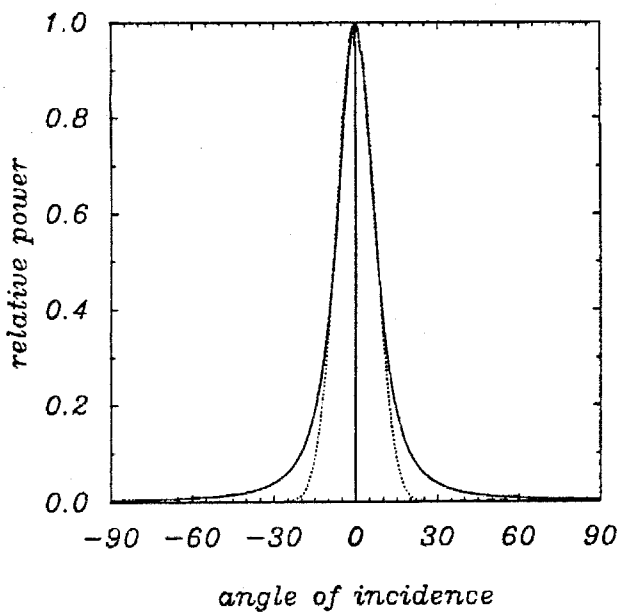

Figure 4.2: Angular scattering laws $\sigma_0(\gamma)$ for a facet model. The value of $\sigma_0(\gamma)$ is proportional to the total area of all the surface patches with slopes of γ. The characteristic width of the scattering law is related to the rms value of surface slope. The solid curve is the Hagfor's law, the dotted curve a cosine law. Both assume an rms slope of 10°.

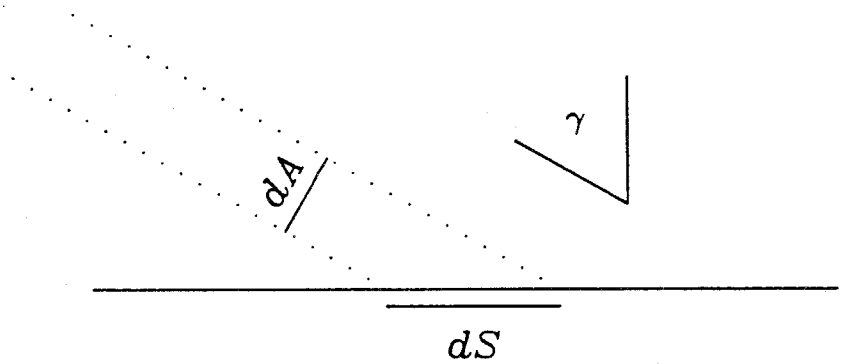

Figure 4.3: Illumination intensity as a function of angle of incidence. The radar transmits a fixed amount of power through the projected area $dA = \cos\gamma\, dS$, but this is spread out over the surface area dS resulting in an illumination intensity on the surface proportional to $\cos\gamma$.

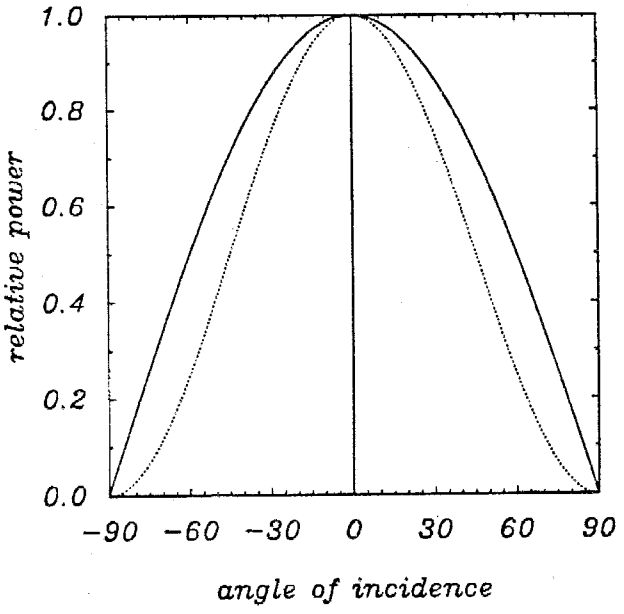

Figure 4.4: Cosine scattering laws of the form $\cos^n \gamma$. Solid curve has $n = 1$, dotted curve has $n = 2$. Depolarized scattering from rough surfaces is generally well characterized by a scattering law somewhere in between.

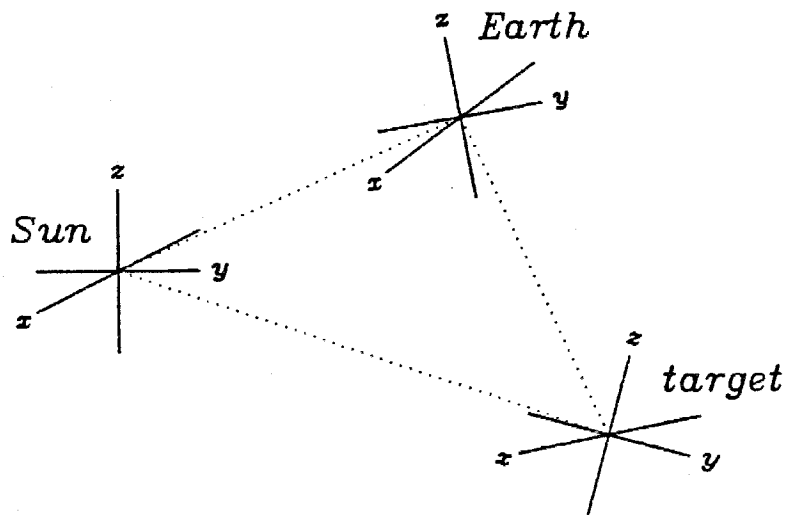

Figure 4.5: Sun, Earth, and target coordinate systems.

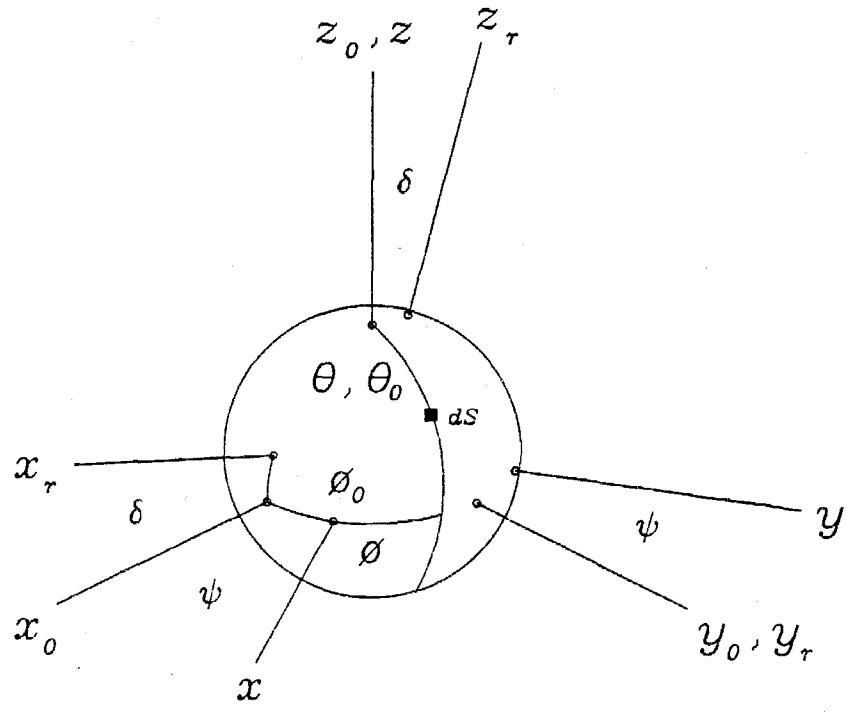

Figure 4.6: Radar and target coordinates.

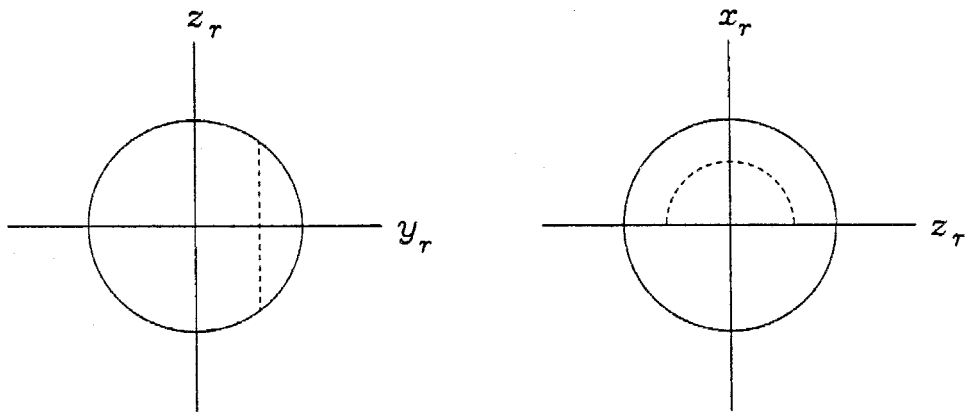

Figure 4.7: Two views of the illuminated region of the sphere with a given Doppler frequency. This is the contour of integration $\mathcal{C}$ in (4.39) for the case of infinitely fine Doppler resolution. The left figure shows the sphere as seen by the radar. The right figure is a side view in which the radar would be towards the top of the page.

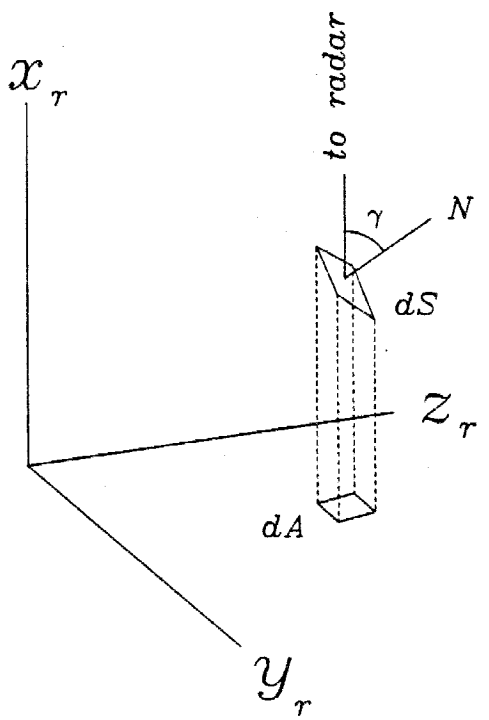

Figure 4.8: Projected area of a surface patch. The surface patch of area dS has a surface normal $N = (x_r, y_r, z_r)/a$ which makes an angle $\gamma = \cos^{-1}(x_r/a)$ with the incident illumination. The radar sees the projected area $dA = \cos\gamma\, dS$.

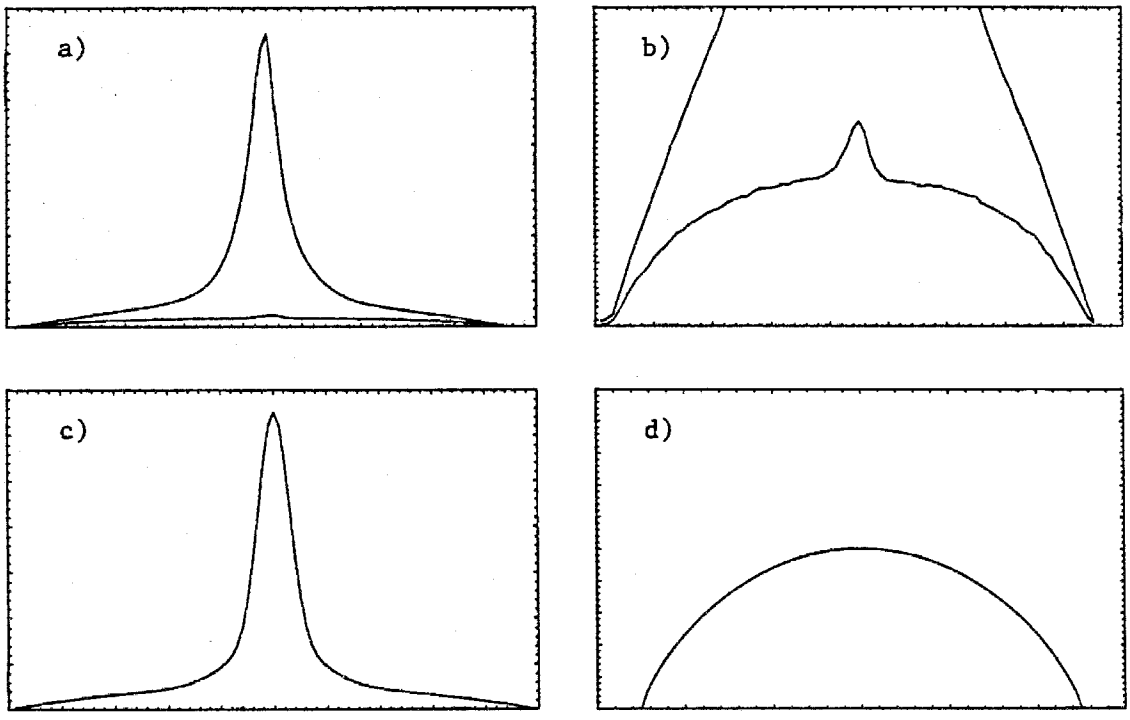

Figure 4.9: Averaged Martian Doppler spectra and modeled spectra. Figures a) and b) show both OC, the stronger signal, and SC, the weaker signal, polarizations. The vertical scale of Figure b) is magnified to better show the shape of the SC spectrum. (The anomalous bump in the center could be cross talk from the OC channel but there is strong evidence that it is in fact SC scatter from Mar's south pole.) Figures c) and d) are plots of spectra derived from cosine scattering law models of the form (4.48). Figure c) is a composite model containing both quasi-specular (large n) and diffuse (small n) components to model the polarized and depolarized contributions to the OC spectrum. Figure d) is a single-n diffuse model of the SC spectrum.

Target	$\|\delta\|_{max}$	Arecibo OSF	Goldstone OSF
Mercury	11°	1.8	6.2
Venus	8°	4.4	16
Mars	25°	170	620
Io	3°	29	100
Europa	3°	11	38
Ganymede	3°	15	53
Callisto	3°	5.3	19
Titan	27°	6.4	23
1 Ceres	?	9.4	33
2 Pallas	?	3.7	13
4 Vesta	?	5.9	21

Table 4.1: Maximum subradar latitudes (δ) and overspread factors (OSF) for selected solar system targets. Principle wavelengths are: Arecibo $\lambda = 13$ cm, Goldstone $\lambda = 3.5$ cm.

Chapter 5

Doppler-Radar Imaging of Spherical Planetary Surfaces

What information do Doppler spectra contain concerning regional variations in radar scattering properties? If some anomalously bright region produces a prominent spike in a spectrum, then the source of this spectral feature must lie along a particular constant-Doppler contour on the surface, i.e., we know the source's y_r coordinate for that particular rotational phase ψ (Figure 4.7). Much tighter constraints on source location follow if several spectra showing the feature are available at different rotational phases, because we can then use relation (4.17) to determine the source's x and y coordinates. Thus the potential exists to use the target's phase-Doppler distribution $\sigma(\nu;\psi)$ to localize reflectivity features to within a North-South ambiguity (the source's z coordinate could be either $\pm\sqrt{a^2-x^2-y^2}$). This idea has been applied, with various degrees of success, to Venus [13], Mercury [16, 60], and Mars [19, 20] to locate the sources of strong, spiked spectral features. However, this technique cannot resolve the North-South ambiguity, nor can it be used to explain the non-

spiked part of a spectrum, i.e., to estimate a continuous reflectivity map.

One way to estimate a continuous reflectivity map from Doppler spectra is simply to use trial and error — change the map and use it to generate model Doppler spectra until a reasonable match to the observed spectra is obtained [53]. More sophisticated approaches treat this inversion as an optimization problem: the reflectivity map is parameterized and search techniques are applied to the parameter space until some measure of the difference between the observed and the modeled spectra is minimized. Vogt et al. [55] used this strategy to form images of rapidly-rotating, spotted stars from stellar line profiles, and they coined the term "Doppler imaging" to describe it. They divided the star's surface into patches, treated the brightness of each patch as a free parameter, and used a numerical optimization technique to maximize a criterion function consisting of two terms. The first term measured the goodness-of-fit between observed and modeled Doppler spectra while the second measured the map's entropy. Inclusion of the entropy term guaranteed a unique solution to the inversion, but at the expense of replacing a linear system (linear least-squares) with a nonlinear one (linear least-squares plus maximum entropy).

Another approach is to expand the relevant surface characteristic in a spherical harmonic series and then construct a system of equations relating the coefficients of this series to the observed data set. Russell [47] set a precedent for this approach as early as 1906. He explored the problem of mapping the reflectivity of a spherical planetary surface using disk-integrated observations and showed that the problem is underdetermined, even if observations are available from all aspects. Deutsch [4] explored essentially the same problem with respect to spotted stars. However, by incorporating additional data unique to stellar observations, he was able to derive a system of equations from which the spherical-harmonic coefficients up to the second degree could be found analytically. Falk and Wehlau [12, 11] extended this approach

to take into account Doppler-resolved observations. They presented an equation relating the spherical-harmonic coefficients up to second degree to stellar Doppler spectra. Unfortunately, they did not present a derivation of their equation, so it is not clear how to go about extending their technique to higher degree, and hence higher resolution.

In this chapter we develop the Doppler imaging concept into a technique for using phase-Doppler distributions to make radar images of spherical planetary targets. A spherical harmonic series of arbitrary degree is used to provide a continuous representation of the surface reflectivity. Then a system of linear equations is constructed which expresses the echo spectra as analytic functions of the series coefficients. These equations contain the radar scattering law, which is assumed to have a $\rho(\theta, \phi) \cos^n \gamma$ form where ρ is the unknown surface reflectivity. The scattering law exponent n is arbitrary but assumed uniform over the target's surface. It is then possible to formulate the inverse problem of estimating the series coefficients from a given phase-Doppler distribution. The spherical harmonic series representation of the reflectivity gives the inverse problem a special structure that allows it to be separated into a number of much smaller least-squares inversions. It is practical to perform these inversions directly, as opposed to iteratively, even for very high resolution imaging, i.e., a large number of series coefficients.

The accuracy of a Doppler-radar image derived from a real phase-Doppler distribution will depend on the signal-to-noise ratio and the rotational-phase and subradar-latitude coverage. Some systematic error will probably be introduced by the assumption of a uniform scattering law exponent. However, the nature and severity of the various kinds of uncertainty and ambiguity in the estimated image can be calibrated by suitable simulations.

In Section 5.1 the forward problem of calculating a sphere's phase-Doppler distri-

bution as a function of its reflectivity distribution, (global) scattering law exponent, and subradar latitude is solved. The strategy is to compute the contribution of each term in the spherical harmonic expansion of the reflectivity distribution, and then to sum all such contributions. In Section 5.2 this result is used to formulate a least-squares solution to the inverse problem of computing the reflectivity distribution from an observed phase-Doppler distribution.

Section 5.3 is devoted to simulations designed to explore the effectiveness of Doppler-radar imaging. Since, as will be shown, the inversion equations constitute an imaging system that is linear in the distribution of reflectivity and shift invariant in longitude, it can be fully characterized by its impulse response as a function of latitude. Therefore the first set of simulations calculates the impulse response of the imaging system as a function of such parameters as subradar latitude and scattering law exponent. This is followed by a test of the ability of the imaging system to recover extended reflectivity features at various latitudes, and the sensitivity of the results to noise in the data. Special attention is given to the role of assumptions about the target's radar scattering law. These simulations are not exhaustive, but they are adequate to establish the technique's capabilities.

5.1 The Forward Problem

If a sphere is characterized by a scattering law

$$\sigma_0(\theta, \phi; \gamma) = \rho(\theta, \phi) \cos^n \gamma, \tag{5.1}$$

with γ the angle of incidence and n a constant, what phase-Doppler distribution $\sigma(\nu; \psi)$ will be observed for a given subradar latitude δ? A formal expression for

$\sigma(\nu;\psi)$ was derived in the previous chapter:

$$\begin{aligned}\sigma(\nu;\psi) &= \frac{a\lambda P}{4\pi\cos\delta}\int_{-b}^{b}\frac{\sigma_0(\gamma;\theta,\phi)}{x_r}\,dz_r \\ &= \frac{\lambda P}{4\pi a^{n-1}\cos\delta}\int_{-b}^{b}\rho(\theta,\phi)x_r^{n-1}\,dz_r,\end{aligned} \tag{5.2}$$

with

$$b=\sqrt{a^2-y_r^2}, \tag{5.3}$$

and where we have used $\cos\gamma = x_r/a$. For simplicity, in all that follows we will measure distances in units of the radius of the sphere, so that the target becomes a unit sphere, and we will measure Doppler frequencies in units of half the Doppler bandwidth of the target, so that $-1 \le \nu \le 1$ and $\nu = -y_r$. Then

$$\sigma(\nu;\psi)=\int_{-\sqrt{1-y_r^2}}^{\sqrt{1-y_r^2}}\rho(\theta,\phi)x_r^{n-1}\,dz_r. \tag{5.4}$$

Being in integral form this is not of much practical use. What is more desirable is a solution in which $\sigma(\nu;\psi)$ is given in terms of discrete parameters and functions that will allow an efficient computer implementation of the inverse problem.

The most natural way to express a continuous function on the surface of a sphere in terms of discrete parameters is to express it as a spherical harmonic series [23]:

$$\begin{aligned}\rho(\theta,\phi) &= \sum_{l=0}^{\infty}\sum_{m=0}^{l}(a_{lm}\cos m\phi + b_{lm}\sin m\phi)P_l^m(\cos\theta) \\ &= Re\left(\sum_{l=0}^{\infty}\sum_{m=0}^{l}(a_{lm}-ib_{lm})e^{im\phi}P_l^m(\cos\theta)\right)\end{aligned} \tag{5.5}$$

where the associated Legendre functions $P_l^m(z)$ are given by

$$P_l^m(z)=\frac{(-1)^m}{2^l l!}(1-z^2)^{m/2}\frac{d^{l+m}}{dz^{l+m}}(z^2-1)^l. \tag{5.6}$$

The function $(z^2-1)^l$ is even in z, and it is differentiated an even/odd number of times as $l+m$ is even/odd. Therefore $P_l^m(z)$ is even/odd in z as $l+m$ is even/odd. For each point in the northern hemisphere with spherical coordinates (θ,ϕ) there

is a conjugate point in the southern hemisphere with coordinates $(\pi - \theta, \phi)$. Since $\cos(\pi - \theta) = -\cos(\theta)$, the function $P_l^m(\cos\theta)$ is even/odd with respect to reflection about the equatorial plane as $l+m$ is even/odd, and these situations will be referred to as NS-even and NS-odd, respectively. The NS-odd terms of (5.5) allow north to be distinguished from south. If they are removed from (5.5) then the series representation will be symmetric about the equatorial plane. Consequently $\rho(\theta, \phi)$ will be replaced by $[\rho(\theta, \phi) + \rho(\pi - \theta, \phi)]/2$. This situation is referred to as being NS-ambiguous.

Since the Doppler spectra are linear in the reflectivity, the superposition principle can be applied. The strategy will be to compute the contribution of a single term of (5.5) and then to sum up all such contributions to get the complete spectra. In other words, substitute (5.5) into (5.4) and integrate term by term.

In (5.5) the reflectivity is expressed in the (θ, ϕ) system. However, the integral in (5.4) is most conveniently computed in the (x_r, y_r, z_r) system. We therefore want to express a spherical harmonic in terms of the (x_r, y_r, z_r) coordinates. We do this by transforming to these coordinates in a series of steps.

Relations (4.23) and (4.23) produce

$$e^{im\phi} P_l^m(\cos\theta) = e^{-im\psi} e^{im\phi_0} P_l^m(\cos\theta_0). \tag{5.7}$$

Thus the dependence on rotational phase is through a simple phase factor. Relations (4.20) through (4.21) give

$$\begin{aligned} e^{im\phi_0} &= (\cos\phi_0 + i\sin\phi_0)^m \\ &= \frac{(\sin\theta_0\cos\phi_0 + i\sin\theta_0\sin\phi_0)^m}{\sin^m\theta_0} \\ &= \frac{(x_0 + iy_0)^m}{(1 - z_0^2)^{m/2}}. \end{aligned} \tag{5.8}$$

Using (5.8) and (5.6) in (5.7) produces

$$e^{im\phi} P_l^m(\cos\theta) = \frac{(-1)^m e^{-im\psi}}{2^l l!} (x_0 + iy_0)^m \frac{d^{l+m}}{dz_0^{l+m}} (z_0^2 - 1)^l. \tag{5.9}$$

Application of the binomial expansion to the terms $(x_0+iy_0)^m$ and $(z_0^2-1)^l$ put this in the form

$$e^{im\phi}P_l^m(\cos\theta)=\frac{(-1)^m e^{-im\psi}}{2^l l!}\sum_{p=0}^{m}\binom{m}{p}i^p y_0^p x_0^{m-p}\sum_{q=0}^{l}\binom{l}{q}(-1)^q\frac{d^{l+m}}{dz_0^{l+m}}z_0^{2(l-q)}. \tag{5.10}$$

Consider the derivatives in the above equation. If $l+m\le 2(l-q)$ and hence $q\le(l-m)/2$, then

$$\frac{d^{l+m}}{dz_0^{l+m}}z_0^{2(l-q)}=\frac{(2l-2q)!}{(l-m-2q)!}z_0^{l-m-2q} \tag{5.11}$$

while for $q>(l-m)/2$ the differentiation "kills off" the term, so

$$\begin{aligned}e^{im\phi}P_l^m(\cos\theta) &= \frac{(-1)^m e^{-im\psi}}{2^l l!}\sum_{p=0}^{m}\binom{m}{p}i^p y_0^p x_0^{m-p}\\ &\times \sum_{q=0}^{\lfloor\frac{l-m}{2}\rfloor}\binom{l}{q}(-1)^q\frac{(2l-2q)!}{(l-m-2q)!}z_0^{l-m-2q}\end{aligned} \tag{5.12}$$

is the expression for a spherical harmonic in the (x_0,y_0,z_0) system when the sphere is at rotational phase ψ. (The symbol $\lfloor x\rfloor$ denotes the integer part of x.) Using (4.16) through (4.18) and the binomial expansion

$$\begin{aligned}x_0^{m-p} &=\\ &= \sum_{j=0}^{m-p}\binom{m-p}{j}(-1)^j(\sin\delta)^j(\cos\delta)^{m-p-j}x_r^{m-p-j}z_r^j,\end{aligned} \tag{5.13}$$

and

$$z_0^{l-m-2q}=\sum_{k=0}^{l-m-2q}\binom{l-m-2q}{k}(\sin\delta)^k(\cos\delta)^{l-m-2q-k}x_r^k z_r^{l-m-2q-k}. \tag{5.14}$$

Plugging these expressions into (5.12) yields

$$e^{im\phi}P_l^m(\cos\theta)=e^{-im\psi}\sum_{p=0}^{m}\sum_{q=0}^{\lfloor\frac{l-m}{2}\rfloor}\sum_{j=0}^{m-p}\sum_{k=0}^{l-m-2q}i^p\alpha_{pqjk}^{lm}y_r^p x_r^{m-p-j+k}z_r^{l-m-2q-k+j}, \tag{5.15}$$

where

$$\alpha_{pqjk}^{lm} = \frac{(-1)^{m+q+j}}{2^l l!}\frac{(2l-2q)!}{(l-m-2q)!}\binom{m}{p}\binom{l}{q}\binom{m-p}{j}\binom{l-m-2q}{k} \times (\cos\delta)^{l-2q-p}(\tan\delta)^{j+k} \quad . \tag{5.16}$$

Substituting (5.15) in place of $\rho(\theta,\phi)$ in (5.4) gives the contribution of a single harmonic to the cross sectional distribution,

$$e^{-im\psi}\sum_{p=0}^{m}\sum_{q=0}^{\lfloor\frac{l-m}{2}\rfloor}\sum_{j=0}^{m-p}\sum_{k=0}^{l-m-2q} i^p \alpha_{pqjk}^{lm} y_r^p \int_{-\sqrt{1-y_r^2}}^{\sqrt{1-y_r^2}} x_r^{m-p-j+k+n-1} z_r^{l-m-2q-k+j}\, dz_r \tag{5.17}$$

which will be denoted by

$$e^{-im\psi}(C_{lm}(\nu) + iS_{lm}(\nu)), \tag{5.18}$$

$C_{lm}(\nu)$ being the real part of the summation and $S_{lm}(\nu)$ the imaginary part. Since the integration is over the illuminated region ($x_r \geq 0$) of the surface of a unit sphere, the substitution

$$x_r = \sqrt{1-y_r^2-z_r^2} \tag{5.19}$$

can be used, and with the definition

$$w = \frac{z_r}{\sqrt{1-y_r^2}} \tag{5.20}$$

this yields

$$z_r = w\sqrt{1-y_r^2} \tag{5.21}$$

$$x_r = \sqrt{1-w^2}\sqrt{1-y_r^2}. \tag{5.22}$$

Using these and the fact that $y_r = -\nu$ we have

$$C_{lm}(\nu) + iS_{lm}(\nu) = \sum_{p=0}^{m}\sum_{q=0}^{\lfloor\frac{l-m}{2}\rfloor}\sum_{j=0}^{m-p}\sum_{k=0}^{l-m-2q} (-i)^p \alpha_{pqjk}^{lm}\nu^p(1-\nu^2)^{\frac{n+l-p-2q}{2}} \times \int_{-1}^{+1}(1-w^2)^{\frac{n-1+m-p-j+k}{2}} w^{l-m-2q-k+j}\, dw. \tag{5.23}$$

When $l-m-k+j$ is odd the above integral is zero. When $l-m-k+j$ is even the substitution $t=w^2$ allows it to be evaluated in terms of the *beta function* (Carrier et al. 1983), defined by

$$B(p,q)=\int_0^1 t^{p-1}(1-t)^{q-1}\,dt, \tag{5.24}$$

and which can be evaluated in terms of the *gamma function* via

$$B(p,q)=\frac{\Gamma(p)\Gamma(q)}{\Gamma(p+q)}. \tag{5.25}$$

Therefore new constants

$$\begin{aligned}\mu_{pq}^{lm} &= \sum_{j=0}^{m-p}\sum_{k=0}^{l-m-2q}\alpha_{pqjk}^{lm}\,\epsilon(l-m-k+j)\\ &\times\ B\left(\frac{l-m-k+j+1}{2}-q,\frac{n+m-p-j+k+1}{2}\right)\end{aligned} \tag{5.26}$$

can be defined, where

$$\epsilon(k)=\begin{cases}1, & k \text{ is even;}\\ 0, & k \text{ is odd}\end{cases}, \tag{5.27}$$

to arrive at

$$C_{lm}(\nu)+iS_{lm}(\nu)=\sum_{p=0}^{m}\sum_{q=0}^{\lfloor\frac{l-m}{2}\rfloor}(-i)^p\mu_{pq}^{lm}\nu^p(1-\nu^2)^{\frac{n+l-p-2q}{2}}. \tag{5.28}$$

The value of p determines whether a term in the above sum is real or imaginary. When p is even, i.e., $p=2r$, then the term will be real; when p is odd, i.e., $p=2r+1$, then the term will be imaginary. Therefore breaking equation (5.28) into its real and imaginary parts leads to

$$C_{lm}(\nu) = \sum_{r=0}^{\lfloor\frac{m}{2}\rfloor}\sum_{q=0}^{\lfloor\frac{l-m}{2}\rfloor}\beta_{2r,q}^{lm}\nu^{2r}(1-\nu^2)^{\frac{n+l}{2}-r-q} \tag{5.29}$$

$$S_{lm}(\nu) = \sum_{r=0}^{\lfloor\frac{m-1}{2}\rfloor}\sum_{q=0}^{\lfloor\frac{l-m}{2}\rfloor}\beta_{2r+1,q}^{lm}\nu^{2r+1}(1-\nu^2)^{\frac{n+l-1}{2}-r-q}, \tag{5.30}$$

where the coefficients are given by

$$\beta_{pq}^{lm} = \frac{(-1)^{m+q+\lfloor\frac{p+1}{2}\rfloor}}{2^l l!}\frac{(2l-2q)!}{(l-m-2q)!}\binom{m}{p}\binom{l}{q}\cos^{l-p-2q}\delta$$

$$\times \sum_{j=0}^{m-p}(-1)^j \sum_{k=0}^{l-m-2q} \epsilon(l-m+j-k) \binom{m-p}{j} \binom{l-m-2q}{k} \tan^{j+k}\delta$$
$$\times B(\frac{l-m+j-k+1}{2} - q, \frac{n+m-p-j+k+1}{2}). \qquad (5.31)$$

Consider the properties of these functions. From the dependence on ν of the terms in (5.29) and (5.30) it is clear that $C_{lm}(\nu)$ is even in ν while $S_{lm}(\nu)$ is odd. The dependence of these functions on the subradar latitude δ is through the coefficients β_{pq}^{lm}. These, in turn, depend on δ through integral powers of $\cos\delta$, which is even in δ, and $\tan\delta$, which is odd in δ. When $l-m$ is even/odd, the factor $\epsilon(l-m+j-k)$ in equation (5.31) allows only terms with $j-k$ even/odd (and hence even/odd powers of $\tan\delta$) to contribute to the summations. It follows that $C_{lm}(\nu)$ and $S_{lm}(\nu)$ are even/odd in δ as $l-m$ is even/odd. Thus when $\delta = 0$ and $l-m$ is odd, we have $C_{lm}(\nu) \equiv S_{lm}(\nu) \equiv 0$. In other words, when $\delta = 0$, the NS-odd terms of the spherical harmonic series are "invisible." In the special case of uniform reflectivity, a_{00} is the only non-zero coefficient and the phase-Doppler distribution will be

$$\sigma(\nu;\psi) = a_{00}C_{00}(\nu) \qquad (5.32)$$
$$\propto (1-\nu^2)^{n/2} \qquad (5.33)$$

which is the Doppler spectrum of a uniform sphere that we derived in the previous chapter.

Now that the contribution of a single spherical harmonic to the distribution of cross section has been calculated, the principle of superposition can be used to write the distribution of cross section due to an arbitrary reflectivity (5.5) as

$$\sigma(\nu;\psi) = Re\left(\sum_{l=0}^{\infty}\sum_{m=0}^{l}(a_{lm}-ib_{lm})e^{-im\psi}(C_{lm}(\nu)+iS_{lm}(\nu))\right)$$
$$= \sum_{l=0}^{\infty}\sum_{m=0}^{l}\Big[(a_{lm}C_{lm}(\nu)+b_{lm}S_{lm}(\nu))\cos m\psi$$
$$+ (a_{lm}S_{lm}(\nu)-b_{lm}C_{lm}(\nu))\sin m\psi\Big]. \qquad (5.34)$$

This is the solution to the forward problem.

We tested these analytical results extensively by comparing them to numerical integrations of (5.4) for various values of l, m and n.

5.2 The Inverse Problem

The problem of practical interest in radar astronomy is to use a measurement of $\sigma(\nu;\psi)$ to find $\rho(\theta,\phi)$. Given the left-hand side of (5.34) we want to invert this system to determine a_{lm} and b_{lm} for all l and m. The first step in solving this inverse problem is to put equation (5.34) in the form of a Fourier series in ψ, by changing the order of summation. The summation region in the l,m plane is $l \geq 0, 0 \leq m \leq l$. We can also express this region as $m \geq 0, l \geq m$. Therefore equation (5.34) can be written

$$\begin{aligned}
\sigma(\nu;\psi) &= \sum_{m=0}^{\infty}\sum_{l=m}^{\infty}\Big[(a_{lm}C_{lm}(\nu)+b_{lm}S_{lm}(\nu))\cos m\psi \\
&\qquad + \ (a_{lm}S_{lm}(\nu)-b_{lm}C_{lm}(\nu))\sin m\psi\Big] \\
&= \sum_{m=0}^{\infty}\Big[\cos m\psi\sum_{l=m}^{\infty}(a_{lm}C_{lm}(\nu)+b_{lm}S_{lm}(\nu)) \\
&\qquad + \ \sin m\psi\sum_{l=m}^{\infty}(a_{lm}S_{lm}(\nu)-b_{lm}C_{lm}(\nu))\Big] \qquad (5.35)
\end{aligned}$$

which expresses $\sigma(\nu;\psi)$ as a Fourier series in ψ. We call the coefficients

$$f_m(\nu) = \sum_{l=m}^{\infty}(a_{lm}C_{lm}(\nu)+b_{lm}S_{lm}(\nu)) \qquad (5.36)$$

$$g_m(\nu) = \sum_{l=m}^{\infty}(a_{lm}S_{lm}(\nu)-b_{lm}C_{lm}(\nu)) \qquad (5.37)$$

Since the $C's$ are even functions of ν and the $S's$ are odd, we can break f_m and g_m into their even and odd parts:

$$f_m^{(e)}(\nu) = \sum_{l=m}^{\infty}a_{lm}C_{lm}(\nu) \qquad (5.38)$$

$$g_m^{(o)}(\nu) = \sum_{l=m}^{\infty} a_{lm} S_{lm}(\nu) \tag{5.39}$$

$$-g_m^{(e)}(\nu) = \sum_{l=m}^{\infty} b_{lm} C_{lm}(\nu) \tag{5.40}$$

$$f_m^{(o)}(\nu) = \sum_{l=m}^{\infty} b_{lm} S_{lm}(\nu) \tag{5.41}$$

Here $C_{lm}(\nu)$ and $S_{lm}(\nu)$ are known functions, the left-hand sides are found from the echo spectra, and we want to calculate values for the unknown coefficients a_{lm} and b_{lm}. At this point we are stuck. There is no way, in general, to invert a linear combination of an infinite number of continuous functions. However, if we model the reflectivity as a finite spherical harmonic series

$$\rho(\theta,\phi) = \sum_{l=0}^{L} \sum_{m=0}^{l} (a_{lm} \cos m\phi + b_{lm} \sin m\phi) P_l^m(\cos\theta) \tag{5.42}$$

then in place of equations (5.38) through (5.41) we obtain

$$f_m^{(e)}(\nu) = \sum_{l=m}^{L} a_{lm} C_{lm}(\nu), \tag{5.43}$$

$$g_m^{(o)}(\nu) = \sum_{l=m}^{L} a_{lm} S_{lm}(\nu), \tag{5.44}$$

$$-g_m^{(e)}(\nu) = \sum_{l=m}^{L} b_{lm} C_{lm}(\nu), \tag{5.45}$$

$$f_m^{(o)}(\nu) = \sum_{l=m}^{L} b_{lm} S_{lm}(\nu) \tag{5.46}$$

Let us define the vectors

$$\mathbf{a}_m = (\, a_{mm} \quad a_{m+1,m} \quad \dots \quad a_{Lm} \,)^T \tag{5.47}$$

$$\mathbf{b}_m = (\, b_{mm} \quad b_{m+1,m} \quad \dots \quad b_{Lm} \,)^T \tag{5.48}$$

$$\mathbf{y}_m = (\, f_m^{(e)}(\nu) \quad g_m^{(o)}(\nu) \,)^T \tag{5.49}$$

$$\mathbf{z}_m = (\, -g_m^{(e)}(\nu) \quad f_m^{(o)}(\nu) \,)^T \tag{5.50}$$

and the matrix

$$\mathbf{W}_m = \begin{pmatrix} C_{mm}(\nu) & C_{m+1,m}(\nu) & \dots & C_{Lm}(\nu) \\ S_{mm}(\nu) & S_{m+1,m}(\nu) & \dots & S_{Lm}(\nu) \end{pmatrix} \tag{5.51}$$

so equations (5.43) through (5.46) can be written compactly as

$$\mathbf{y}_m = \mathbf{W}_m \mathbf{a}_m \tag{5.52}$$

$$\mathbf{z}_m = \mathbf{W}_m \mathbf{b}_m \tag{5.53}$$

Note that $\mathbf{y}_m$ and $\mathbf{z}_m$ are infinite dimensional (continuous) vectors, as are the $L-m+1$ columns of $\mathbf{W}_m$, while we have only $L-m+1$ parameters, $\mathbf{a}_m$ or $\mathbf{b}_m$, in each equation. These systems are overdetermined and, in general, can only be solved in a least-squares sense. The least-squares solutions are found by solving the normal equations

$$\mathbf{W}_m^T \mathbf{y}_m = \mathbf{W}_m^T \mathbf{W}_m \mathbf{a}_m \tag{5.54}$$

$$\mathbf{W}_m^T \mathbf{z}_m = \mathbf{W}_m^T \mathbf{W}_m \mathbf{b}_m \tag{5.55}$$

where $\mathbf{W}_m^T$ denotes the transpose of the matrix $\mathbf{W}_m$. We adopt the notation

$$\mathbf{R}_m = \mathbf{W}_m^T \mathbf{W}_m \tag{5.56}$$

$$\mathbf{u}_m = \mathbf{W}_m^T \mathbf{y}_m \tag{5.57}$$

$$\mathbf{v}_m = \mathbf{W}_m^T \mathbf{z}_m \tag{5.58}$$

and write the normal equations as

$$\mathbf{u}_m = \mathbf{R}_m \mathbf{a}_m \tag{5.59}$$

$$\mathbf{v}_m = \mathbf{R}_m \mathbf{b}_m \tag{5.60}$$

These equations are discrete and finite; $\mathbf{u}_m$ and $\mathbf{v}_m$ are of dimension $L-m+1$ while $\mathbf{R}_m$ has dimensions $L-m+1$ by $L-m+1$. The elements of $\mathbf{R}_m$ are given by

$$R_{m,kj} = \int_{-1}^{+1} C_{km}(\nu) C_{jm}(\nu)\, d\nu + \int_{-1}^{+1} S_{km}(\nu) S_{jm}(\nu)\, d\nu \tag{5.61}$$

Using (5.29) and (5.30) we can write this as

$$R_{m,kj} = \sum_{r_1=0}^{\frac{m}{2}} \sum_{q_1=0}^{\frac{k-m}{2}} \sum_{r_2=0}^{\frac{m}{2}} \sum_{q_2=0}^{\frac{j-m}{2}} \beta_{2r_1,q_1}^{km} \beta_{2r_2,q_2}^{jm} \int_{-1}^{+1} \nu^{2(r_1+r_2)} (1-\nu^2)^{n+\frac{k+j}{2}-r_1-r_2-q_1-q_2}\, d\nu$$
$$+ \sum_{r_1=0}^{\frac{m-1}{2}} \sum_{q_1=0}^{\frac{k-m}{2}} \sum_{r_2=0}^{\frac{m-1}{2}} \sum_{q_2=0}^{\frac{j-m}{2}} \beta_{2r_1+1,q_1}^{km} \beta_{2r_2+1,q_2}^{jm} \int_{-1}^{+1} \nu^{2(r_1+r_2)+2} (1-\nu^2)^{n+\frac{k+j}{2}-r_1-r_2-q_1-q_2-1}\, d\nu \tag{5.62}$$

By expressing these integrals as beta functions we obtain an analytic expression for the elements of $\mathbf{R}_m$:

$$\begin{aligned} & R_{m,kj} \\ &= \sum_{r_1=0}^{\frac{m}{2}} \sum_{q_1=0}^{\frac{k-m}{2}} \sum_{r_2=0}^{\frac{m}{2}} \sum_{q_2=0}^{\frac{j-m}{2}} \beta_{2r_1,q_1}^{km} \beta_{2r_2,q_2}^{jm} B(r_1+r_2+\frac{1}{2}, n+\frac{k+j}{2}-r_1-r_2-q_1-q_2+1) \\ &+ \sum_{r_1=0}^{\frac{m-1}{2}} \sum_{q_1=0}^{\frac{k-m}{2}} \sum_{r_2=0}^{\frac{m-1}{2}} \sum_{q_2=0}^{\frac{j-m}{2}} \beta_{2r_1+1,q_1}^{km} \beta_{2r_2+1,q_2}^{jm} B(r_1+r_2+\frac{3}{2}, n+\frac{k+j}{2}-r_1-r_2-q_1-q_2) \end{aligned} \tag{5.63}$$

The elements of $\mathbf{u}_m$ are given by

$$\begin{aligned} u_{m,k} &= \int_{-1}^{+1} \left(C_{km}(\nu) f_m^{(e)}(\nu) + S_{km}(\nu) g_m^{(o)}(\nu) \right) d\nu \\ &= \int_{-1}^{+1} \left(C_{km}(\nu) f_m(\nu) + S_{km}(\nu) g_m(\nu) \right) d\nu \end{aligned} \tag{5.64}$$

This last equality holds because $C_{km}(\nu)$ is an even function of ν and hence is orthogonal to the odd part of $f_m(\nu)$, while $S_{km}(\nu)$ is an odd function of ν and hence is orthogonal to the even part of $g_m(\nu)$. Likewise the elements of $\mathbf{v}$ are given by

$$v_{m,k} = \int_{-1}^{+1} \left(-C_{km}(\nu) g_m(\nu) + S_{km}(\nu) f_m(\nu) \right) d\nu \tag{5.65}$$

We must evaluate these integrals numerically since $f_m(\nu)$ and $g_m(\nu)$ are derived from discrete echo spectra.

The solutions to the normal equations (5.59) and (5.60) are

$$\hat{\mathbf{a}}_m = \tilde{\mathbf{R}}_m \mathbf{u}_m \tag{5.66}$$

$$\hat{\mathbf{b}}_m = \tilde{\mathbf{R}}_m \mathbf{v}_m \tag{5.67}$$

where $\tilde{\mathbf{R}}_m$ is the pseudo-inverse of $\mathbf{R}_m$ (Golub and Van Loan 1983). With the spherical harmonic coefficients thus solved for, we can now evaluate the sphere's radar reflectivity using (5.42). Whereas equations (5.59) and (5.60) are rigorously valid if the target's reflectivity distribution is completely described by equation (5.42), this will not be the case for an actual target; there will be higher-degree terms in any real reflectivity distribution. Therefore in practice we will not have equation (5.59), but rather

$$\mathbf{u}_m + \mathbf{e}_m = \mathbf{R}_m \mathbf{a}_m \tag{5.68}$$

where $\mathbf{e}_m$ is the contribution of all terms of degree higher than L. Because the L-degree model used to arrive at (5.59) doesn't "know" about higher degree terms, it "sees" $\mathbf{e}_m$ as systematic noise. The effects of this (and of statistical noise) on the image can be controlled somewhat if the singular value decomposition is used to form $\tilde{\mathbf{R}}_m$ with the singular values judiciously truncated (Press et al. 1986), as discussed below.

Suppose we are able to observe the sphere's phase-Doppler distribution for N different values of the subradar latitude, say $\delta^{(1)}, \delta^{(2)}, \ldots, \delta^{(N)}$. We can form (5.53) for each latitude, thereby generating a set of N equations

$$\begin{aligned} \mathbf{y}_m^{(1)} &= \mathbf{W}_m^{(1)} \mathbf{a}_m \\ \mathbf{y}_m^{(2)} &= \mathbf{W}_m^{(2)} \mathbf{a}_m \\ &\vdots \\ \mathbf{y}_m^{(N)} &= \mathbf{W}_m^{(N)} \mathbf{a}_m \end{aligned} \tag{5.69}$$

for the parameter vector $\mathbf{a}_m$. (This assumes that the reflectivity does not change between observations.) The least-squares solution to this set is the solution to

$$(\mathbf{u}_m^{(1)} + \mathbf{u}_m^{(2)} + \cdots + \mathbf{u}_m^{(N)}) = (\mathbf{R}_m^{(1)} + \mathbf{R}_m^{(2)} + \cdots + \mathbf{R}_m^{(N)}) \mathbf{a}_m \tag{5.70}$$

where

$$\mathbf{u}_m^{(i)} = \mathbf{W}_m^{(i)T}\mathbf{y}_m^{(i)} \tag{5.71}$$

Repeating this procedure with $\mathbf{z}_m$ and $\mathbf{v}_m$ allows us to solve for $\mathbf{b}_m$.

Summary of Inversion Process

Given the N phase-Doppler functions $\sigma^{(1)}(\nu;\psi), \sigma^{(2)}(\nu;\psi), \ldots, \sigma^{(N)}(\nu;\psi)$ measured at subradar latitudes $\delta^{(1)}, \delta^{(2)}, \ldots, \delta^{(N)}$, the sphere's radar brightness distribution $\rho(\theta,\phi)$ can be estimated as follows:

1. Express the Doppler spectra as Fourier series in rotational phase,

$$\sigma^{(s)}(\nu;\psi) = \sum_{m=0}^{L} f_m^{(s)}(\nu)\cos m\psi + g_m^{(s)}(\nu)\sin m\psi \tag{5.72}$$

   for each s, $0 \le s \le N$.

2. For each m, $0 \le m \le L$:

   (a) Use the functions $f_m^{(s)}(\nu)$ and $g_m^{(s)}(\nu)$ obtained above to calculate the vectors $\mathbf{u}_m^{(s)}$ and $\mathbf{v}_m^{(s)}$, as in equations (5.64) and (5.65), for each s. Form the vectors

$$\mathbf{u}_m = \mathbf{u}_m^{(1)} + \mathbf{u}_m^{(2)} + \cdots + \mathbf{u}_m^{(N)} \tag{5.73}$$

$$\mathbf{v}_m = \mathbf{v}_m^{(1)} + \mathbf{v}_m^{(2)} + \cdots + \mathbf{v}_m^{(N)} \tag{5.74}$$

   (b) For each subradar latitude, $\delta^{(s)}$, form the matrix $\mathbf{R}_m^{(s)}$ whose elements are given by (5.63); the dependence on δ enters through the coefficients β_{pq}^{jk}. Form the matrix

$$\mathbf{R}_m = \mathbf{R}_m^{(1)} + \mathbf{R}_m^{(2)} + \cdots + \mathbf{R}_m^{(N)} \tag{5.75}$$

   (c) Construct $\tilde{\mathbf{R}}_m$, the pseudo-inverse of $\mathbf{R}_m$, using the singular value decomposition. Then solve for the spherical harmonic coefficients $\mathbf{a}_m$ and $\mathbf{b}_m$ (in

a least-squares sense) via

$$\mathbf{a}_m = \tilde{\mathbf{R}}_m \mathbf{u}_m \tag{5.76}$$

$$\mathbf{b}_m = \tilde{\mathbf{R}}_m \mathbf{v}_m \tag{5.77}$$

3. Finally, calculate an estimate of the radar reflectivity distribution using

$$\rho(\theta, \phi) = \sum_{l=0}^{L} \sum_{m=0}^{l} (a_{lm} \cos m\phi + b_{lm} \sin m\phi) P_l^m(\cos \theta). \tag{5.78}$$

5.3 Simulations

How does the fidelity of a Doppler-radar image depend on such factors as subradar latitude coverage, the target's scattering law, our *a priori* knowledge of that law, and signal-to-noise ratio? This section is devoted to discussion of these issues and to simulations designed to explore the capabilities and limitations of our imaging system. (Note that the dynamic range of the black-and-white images which present the simulation results is limited. The interested reader can find color versions in [24]).

In conventional delay-Doppler mapping, two-dimensional resolution is provided by resolution of the radar echo in time-delay and Doppler for a single rotational phase. For all non-polar aspects, there are conjugate points on the sphere whose echoes have identical delay-Doppler coordinates, and this ambiguity normally is either resolved interferometrically or avoided by pointing the radar beam so it illuminates one hemisphere much more strongly than the other. However, in Doppler-radar imaging, the two dimensions of spatial resolution are extracted from the phase-Doppler distribution; the mapping's fidelity rests on the imaging system's ability to distinguish the different Doppler trajectories of the target's resolution cells. We remarked earlier that the NS-odd harmonics contribute to the echo spectra for $\delta \neq 0$, but not for $\delta = 0$. Consequently, our ability to image independently the northern and southern hemi-

spheres (i.e., to overcome the NS ambiguity) will be nil for $\delta = 0$ and generally will depend on the actual latitude coverage. Our simulations examine five single-latitude data sets ($\delta = -25°$, $-10°$, $0°$, $10°$, $25°$) as well as two dual-latitude data sets ($-10°$ and $10°$; $-25°$ and $25°$). These values were prompted by the ranges of δ observable for various planetary radar targets (Table 4.1).

The phase-Doppler function and the imaging system also depend on the scattering law exponent n. A uniformly bright target would have $n = 1$, while Lambert limb darkening corresponds to $n = 2$. It is now commonplace to transmit a circularly polarized signal and to use a two-channel receiver to collect echoes in the same circular polarization (the SC sense) as transmitted, as well as those in the opposite circular polarization (the OC sense). The OC polarization would contain all the echo power from a perfectly smooth spherical target; SC power arises if there is wavelength-scale, near-surface structure or multiple scattering. The terrestrial planets are extremely limb darkened ($n \gg 10$) in the OC polarization but have SC scattering laws characterized by values of n between 1 and 2. For the icy Galilean satellites, n is generally between 1 and 2 for both polarizations. For Io and the largest asteroids the relative weakness of SC echoes limits their usefulness for imaging, and the OC scattering laws are characterized by values of n between $\sim$2 to $\sim$8. Unfortunately, we expect images to degrade as n increases (i.e., as the scattering becomes less diffuse and more specular), because in this situation a surface feature's observable Doppler trajectory will shorten. Indeed, as n grows very large, only the region of the sphere near the subradar point will backscatter strongly, and locations much different from the subradar point will simply not be observable. Our simulations investigate the dependence of image fidelity on n and examine the nature of systematic error introduced if the value of n used in the inversion is different from the target's scattering law exponent. We also look at examples of a configuration in which the scattering law varies over the

target's surface.

Whereas most of our simulations are performed with noise-free data and are intended to probe the "intrinsic" limitations of the technique, all actual radar observations are corrupted by noise. The available signal-to-noise ratio (SNR) will depend on the target's distance and backscattering properties, the radar's sensitivity, and the integration time. Our final simulations use data corrupted by noise to provide insight into the SNRs required for our technique to work.

The first step in the inversion process is to express $\sigma(\nu;\psi)$ as a Fourier series in ψ, of order L. The Nyquist sampling period for the function $\cos L\psi$ is $\Delta\psi = \pi/L$ so we require at least $2\pi/\Delta\psi = 2L$ spectra to compute the Fourier series. Therefore the degree of our spherical harmonic series can be no larger than half the number of Doppler spectra available at each subradar latitude. The limitation this imposes on our ability to image a sphere is displayed in Figure 5.1. Here we show spherical harmonic expansions of various degrees, for each of the two model targets we use in our simulations. The left-hand images are maps, on a rectangular, linear, latitude-longitude grid, of a target consisting of seven point features whose (latitude, longitude) coordinates are (−50,−135), (−25,−90), (−75,−45), (0,0), (+75,+45), (+25,+90), (+50,+135). Note that in this type of projection, features become stretched out in longitude as they approach a pole; the features in the left-hand images all have the same size on the sphere's surface. The right-hand images are maps of a uniform sphere with six extended features of various sizes. Again the rectangular projection distorts true shapes; the features are all circular.

A spherical harmonic series of degree L has $(L+1)^2$ coefficients, which is equal to the maximum number of independent resolution cells we can obtain on the sphere's surface. We want as many resolution cells as possible, but the price we must pay for a large L is the requirement that we obtain at least $2L$ spectra, and, as we will

see below, that each spectrum resolves about L Doppler cells across the target. In our simulations the data consists of 30 echo spectra at each subradar latitude, at rotational phases 12° apart, and we use $L = 15$ in the inversion. (Note that there is no fundamental obstacle to obtaining spectra that provide arbitrarily thorough and uniform phase coverage.)

Throughout our analysis, we have assumed infinite resolution in Doppler frequency. In practice we work with discrete spectra whose SNR improves as the frequency resolution coarsens. We wish to use the coarsest possible spectral resolution that will accommodate an L degree series, and we can determine what that resolution should be from a simple degrees-of-freedom argument. With $2L$ spectra we need at least $L/2$ resolution cells per spectrum in order to provide the roughly L^2 constraints required to solve for all the coefficients. In our simulations we have conservatively chosen a Doppler resolution that gives us L samples per spectrum.

Impulse Response: Point-Like Features

For our first set of simulations we use the seven-point-feature target described above. Maps of this target are shown in Figure 5.2. The map on the left is simply the $L = 15$ spherical harmonic expansion of the seven point features. The map on the right is a NS-ambiguous version of the map on the left.

The simulations are organized into four figures of seven images each. Each figure has a different combination of the target's scattering law exponent and the value of n used in the inversion. Let us call these parameters n_{tar} and n_{inv} respectively. Note that $n_{inv} = n_{tar}$ in Figure 5.3 and Figure 5.4 and that $n_{inv} \neq n_{tar}$ in Figure 5.5 and Figure 5.6. In Figure 5.5, the inversion "assumes" that the target is less specular than it really is ($n_{inv} < n_{tar}$), while in Figure 5.6 the mismatch is reversed. The different images within each block show results for different subradar latitudes. Images labeled

$\pm 10°$ and $\pm 25°$ correspond to two-latitude data sets.

Because our imaging system is a linear one, these images of point features represent the system's impulse response. If the rotational phase coverage is uniform (as is assumed in all simulations in this chapter), the system is shift-invariant in longitude due to relation (4.23): a shift in the longitude coordinate ϕ results in the data set merely being shifted in rotational-phase ψ by an opposite amount and consequently the image is simply shifted in longitude. However, the impulse response can vary with latitude, and this is why we have placed point features at a wide range of latitudes.

Point Features: $n_{inv} = n_{tar} = 1$

Here (Figure 5.3) the target is uniformly bright ($n_{tar} = 1$) and the exponent used in the inversion is matched to the target's scattering law. For $\delta = 0°$ the image is completely NS ambiguous. When the subradar latitude track moves off the equator to $+10°$, the amplitude of the ambiguities drops off considerably. For $\delta = +25°$ the NS separation improves. The situations $-10°$ and $-25°$ are analogous. When two non-equatorial subradar tracks in opposite hemispheres are available, the potential of this technique becomes apparent. For $\delta = \pm 25°$, we obtain an essentially ideal image, with minor loss of amplitude for features near the equator. For $\delta = \pm 10°$ the result is almost as good, with only a very weak NS ambiguity for the features at latitudes of $\pm 25°$.

Point Features: $n_{inv} = n_{tar} = 3$

These images (Figure 5.4) demonstrate the difficulties encountered with increasing limb darkening. The features near the equator are generally elongated in latitude. The features in the polar regions are not imaged at all for $\delta = 0°$ and barely appear in the $+10°$ and $-10°$ images. However, for the $+25°$ and $-25°$ images the results

are similar to the $n_{tar} = n_{inv} = 1$ case. Clearly, as limb darkening (i.e., specularity) increases, imaging fidelity becomes more confined to the vicinity of the subradar track(s).

Point Features: $n_{inv} < n_{tar}$

Here (Figure 5.5) we give the target a scattering exponent $n_{tar} = 2$ but attempt to image it using $n_{inv} = 1$ in the inversion. The differences between this figure and Figure 5.3 are a small elongation in latitude due to increased specularity and a lowering of the amplitude of the polar features. The increased specularity results in less backscatter at high incidence angles from these features, which are always far from the subradar point. The inversion, "thinking" the target is less specular than it is, interprets polar features to be weaker than they really are.

Point Features: $n_{inv} > n_{tar}$

Here (Figure 5.6) the target is less specular ($n_{tar} = 2$) than assumed in the inversion ($n_{inv} = 3$). The only noteworthy difference between these images and those in Figure 5.4 is that here the amplitudes of the polar features are slightly increased relative to the other features. This is just the opposite of the effect seen in Figure 5.5 — now the polar features backscatter more strongly at high incidence angles than they would if they were as specular as the inversion assumes, so the inversion supposes they are brighter than they really are.

In performing the phase-Doppler inversions described in this section we used the singular value decomposition and determined the appropriate truncation level for the singular values (Press et al. 1986) as follows. For the cases $n_{inv} = n_{tar} = 1$ and $n_{inv} = n_{tar} = 3$, we formed images with a wide range of truncation levels and then chose the truncation that in each case produced the most accurate image. We used

these same respective truncations in the $(n_{inv}, n_{tar}) = (1,3)$ and $(n_{inv}, n_{tar}) = (1,3)$ cases, and also in the extended-feature simulations described below. This is a sensible approach to dealing with the singular-value-truncation problem: for a given imaging geometry and a given value of n_{inv}, choose a truncation level that optimizes the imaging system's impulse response.

From the results described above, we conclude that Doppler-radar imaging can isolate point-like features with little, or no, NS ambiguity. It is quite robust, in this regard, with respect to modest degrees of specularity and even to mismatch between the target's scattering law and the scattering law assumed in the inversion.

Extended Features

For our extended feature simulations, we placed six uniform, circular spots of various sizes at different places on an otherwise uniform sphere. These spots have a radar reflectivity 50% greater than that of the uniform background. Both unambiguous and ambiguous maps of this target are shown in Figure 5.7.

Extended Features: $n_{inv} = n_{tar}$

In Figure 5.8, with $n_{tar} = n_{inv} = 1$, the equatorial image is naturally NS ambiguous, but it captures fairly well the location and shape of the features in the ideal ambiguous image. Fidelity suffers most near the equator as expected. For the non-equatorial, single-subradar-latitude cases, the features in the fully observed hemisphere are generally well imaged. For the $-10°$ and $+10°$ cases, but not the $-25°$ and $+25°$ cases, there are small amounts of NS ambiguity. When two opposing subradar tracks are used the full target is well imaged with no ambiguity, although there is some blurring near the equator, especially in the $\pm 10°$ image.

When the scattering law becomes more specular (Figure 5.9) the results are essen-

tially the same as for the zero-limb-darkening case except for the tendency of image brightness to fall off away from the subradar track. Indeed, in simulations using $|\delta| \leq 10°$, polar features are not seen.

Extended Features: Non-Uniform n_{tar}

The spectra of specular targets tend to be more sharply peaked near $\nu = 0$ than is the case for diffuse targets. Therefore if one tries to fit spectra from a specular target using a diffuse model, the outcome will be more reflectivity in the "zero-Doppler" regions, i.e., polar regions. On the other hand, if the target is more diffuse than expected, there will seem to be an excess of power at large Doppler frequencies; the tendency then will be to enhance artificially the reflectivity of the region responsible for the largest Doppler frequencies, i.e., the equatorial region. This is precisely what we see in Figures 5.10 and 5.11. In Figure 5.10 the uniform part of the target has $n_{tar} = 1$ while the spot features are more specular, having $n_{tar} = 2$. When the inversion is done using $n_{inv} = 1$, the result, compared to Figure 5.8, is that the mapped reflectivity is forced towards the polar regions. In Figure 5.11 the spot features are more diffuse than expected; the uniform part of the target has $n_{tar} = 3$, the spots have $n_{tar} = 2$, and the inversions were done with $n = 3$. The result is that the mapped reflectivity is forced towards the equator.

Whereas it is desirable that the imaging system be matched to the target's scattering law, this issue is not terribly worrisome, for several reasons. First, the simulations indicate that sensitivity to scattering law mismatch is not severe, and that the degree of distortion introduced is least for targets with minimal limb darkening, i.e., for those situations best suited for Doppler-radar imaging in the first place because of minimal demands on latitude coverage. In practice we can treat n_{inv} as a free parameter in the least-squares calculation. We also can estimate the target's average n_{tar} directly

from the echo spectra and can investigate variations in the disc-averaged scattering law as a function of subradar location. Of course, with any such procedure, one risks misinterpretation of reflectivity variations as scattering-law variations. Conversely, in Doppler-radar imaging, scattering-law mismatch might cause variations in the local angular scattering law to show up as reflectivity variations. However, the primary objective of Doppler-radar imaging is delineation of regions whose radar (and hence surface) properties differ from those of the surroundings, and this objective seems unlikely to be compromised by modest mismatch between n_{inv} and n_{tar}. In any event, the nature and severity of imaging errors wrought by any conceivable sort of mismatch can be calibrated by suitable simulations.

Effect of Noise

A convenient measure of the overall strength of a set of echo spectra is the SNR of an optimally-filtered, weighted sum of all the spectra. We examined the effects of noise on Doppler-radar imaging by adding different realizations of Gaussian noise to the $+25°$ and $-25°$ spectra of the extended-feature target with $n_{tar} = 1$, and then performing a phase-Doppler inversion. We repeated this process for six different noise realizations at each of four values of the 30-spectrum SNR: 100, 250, 500, 1000.

Figure 5.12 shows examples of spectra corrupted at these noise levels. Each plot shows the noiseless spectrum (solid line) of the extended-feature target with $n_{tar} = 1$ taken at $\delta = 25°$, $\psi = 0°$, and a version corrupted by noise (dashed line) at the indicated 30-spectrum SNR. Note that the optimally-filtered, single-spectrum SNR is $\sim 30^{-1/2} = 0.18$ times the 30-spectrum SNR. In each case we assume optimal filtering; since the spectra in Figure 5.12 have $L = 15$ independent Doppler resolution cells, their unfiltered SNRs are $\sim (15 \cdot 30)^{-1/2} = 0.05$ times the corresponding optimally filtered, 30-spectrum SNRs.

Figures 5.13 and 5.14 show the simulation results. At an SNR of 100 none of the features are discernible. At an SNR of 250, the features begin to emerge from the noise but are significantly corrupted. When the SNR reaches 500, the fidelity of the images approaches a useful level. Finally, at an SNR of 1000, essentially no noise artifacts appear.

Let us describe the quality of the results at SNRs of 100, 250, 500, and 1000 as poor, fair, good, and excellent. Of course, in practice one might opt to sacrifice resolution in return for image quality. Our simulations use spherical harmonic series of degree $L = 15$ and having $(L+1)^2 = 256$ coefficients, so our images have 256 potential resolution cells on the target's surface. For any given level of image quality, L will be proportional to SNR. Thus for example, if we have (otherwise ideal) echo spectra providing an SNR of ~ 300, we could use $L = 4$ to construct an excellent image having about 25 cells. At the other extreme, with an SNR $\sim 100,000$ we could in theory use $L \sim 1000$ to obtain an excellent image resolving $\sim 10^6$ cells on the target, but inversions with L much larger than ~ 100 would stress existing computing capabilities. Therefore, even though SNRs $\sim 100,000$ are readily achievable for the inner planets, we do not foresee construction of Doppler-radar images resolving much more than $\sim 10,000$ cells (i.e., with pixel dimensions much less than 2°) in the near future.

5.4 Conclusion: Potential Applications

Doppler-radar imaging can furnish useful information about the surfaces of each of the targets in 4.1. Because of its relative simplicity in terms of data acquisition, reduction, and storage, it may prove to be an attractive alternative or supplement to more complicated, time-consuming, and computationally intensive techniques. The

quality and overall resolution of available images will improve with time as additional spectra are obtained, the gross SNR grows, and latitude coverage widens. It is beyond the scope of this chapter to develop detailed observational strategies, but we do offer a qualitative appraisal of imminent prospects for planetary Doppler-radar imaging of candidate targets.

Mars, Venus, and Mercury

SC maps at 3.5 and 13 cm can be constructed at resolutions on the order of 100 km for each of the inner planets with the existing Goldstone and Arecibo telescopes. In that polarization, brightness would be proportional to the severity of near-surface, wavelength-scale roughness and/or to dielectric constant. SC maps would also be valuable in refining physical interpretations of conventional radar maps, which use the echo's OC component (or its linearly polarized equivalent) and in which the brightness can also be modulated by large-scale slope statistics.

Aperture synthesis radar techniques, employing 3.5 cm transmission from Goldstone and reception at the Very Large Array [32], can yield global SC images at 3.5 cm but not at 13 cm. Doppler-radar imaging provides a way to make global SC maps at 13 cm, and that wavelength has important advantages for Venus (Magellan's radar operates at 13 cm) and Mars (13 cm-scale structure is more germane to lander site selection than 3.5 cm-scale structure).

It may also be possible to make maps using the diffuse component of the OC echoes of these bodies. In this case the presence of the characteristic quasi-specular spike near zero Doppler frequency will cause the image to have erroneously bright polar caps (these are the only regions that are always near the zero-Doppler contour), but regions away from the poles should be well imaged. Moreover, the technique presented in this chapter can be easily extended to a composite scattering law of the

form $\sigma_0(\gamma) = \rho_1 \cos^{n_1} \gamma + \rho_2 \cos^{n_2} \gamma$ with $n_2 \gg n_1$. The first term would account for the diffuse component, the second term would account for the quasi-specular component, and there would be separate spherical harmonic series for ρ_1 and ρ_2.

Io, Europa, Ganymede, and Callisto

The subearth latitude on Jupiter's moons stays within a few degrees of the equator, so all Doppler images will be NS ambiguous. Nevertheless, localization of reflectivity variations in longitude and absolute latitude would prove valuable in correlating radar anomalies with geologic terrain types in Voyager (and eventually Galileo) images. The icy satellites have extremely high radar reflectivities and $n_{tar} \sim 1.5$ in both the SC and OC polarizations, and the SNRs available with current radar telescopes are adequate to permit excellent images at $\sim 12°$ resolution (as in the SNR=1000 example in Figure 5.14) at 13 cm and $\sim 30°$ at 3.5 cm. Completion of proposed, large-scale upgrades in the Arecibo instrument would provide SNRs adequate to support Doppler-radar imaging at resolutions $\sim 1°$. Unfortunately, such fine resolution would require 360 spectra at rotational-phase intervals 1° apart. It would take hundreds of four-hour observing sessions (one per day) to construct this data set. Realistically, we can anticipate excellent, NS-ambiguous images of at least Callisto and Ganymede at 5°-to-10° resolution to be developed during the next decade. For Io, SNRs obtainable with current systems are too low for useful imaging, but construction of maps with resolutions $\sim 20°$ can be attempted with the upgraded Arecibo telescope.

Ceres, Pallas, and Vesta

These objects' pole directions are poorly known at present, but will be measurable to within a few degrees with the upgraded Arecibo telescope. Their OC echo spectra lack the strong, zero-Doppler spike observed for the inner planets, being characterized

instead by a $\cos^n \gamma$ law with $n \sim 5$. This is fortunate since their SC cross sections are negligible and so only OC maps can be made. The available information suggests that a very wide variety of subradar latitudes are observable, at least for Pallas. We expect that SNRs for OC echoes accessible from Arecibo will be adequate for imaging of all three asteroids at resolutions on the order of 20°. These objects rotate much more rapidly than the other targets in 4.1, so rotational-phase coverage is fairly easy to obtain. Consequently it will be possible to acquire in $\sim$ 10 observing sessions a single-latitude data set with SNR adequate to support Doppler imaging at $\sim$ 20° resolution.

In the case of OC echoes from a rocky surface the scattering law is primarily determined by large-scale surface slopes. It is probably not reasonable to assume a constant distribution of slopes over the entire surface of a large body and so OC Doppler-radar images would not provide a reliable estimate of surface reflectivity and/or small-scale roughness. However, such images would still serve to identify variations in surface properties, i.e., a combination of reflectivity, roughness, and surface slopes.

Titan

Titan's scattering properties are unknown. If Titan is as reflective as the rocky planets and has a reasonably broad OC scattering law ($\cos^n \gamma$ with $n \sim 5$ or less), then 60 dates of observations with the upgraded Arecibo could generate data with an SNR of 1000, providing an excellent image at $\sim$ 20° resolution.

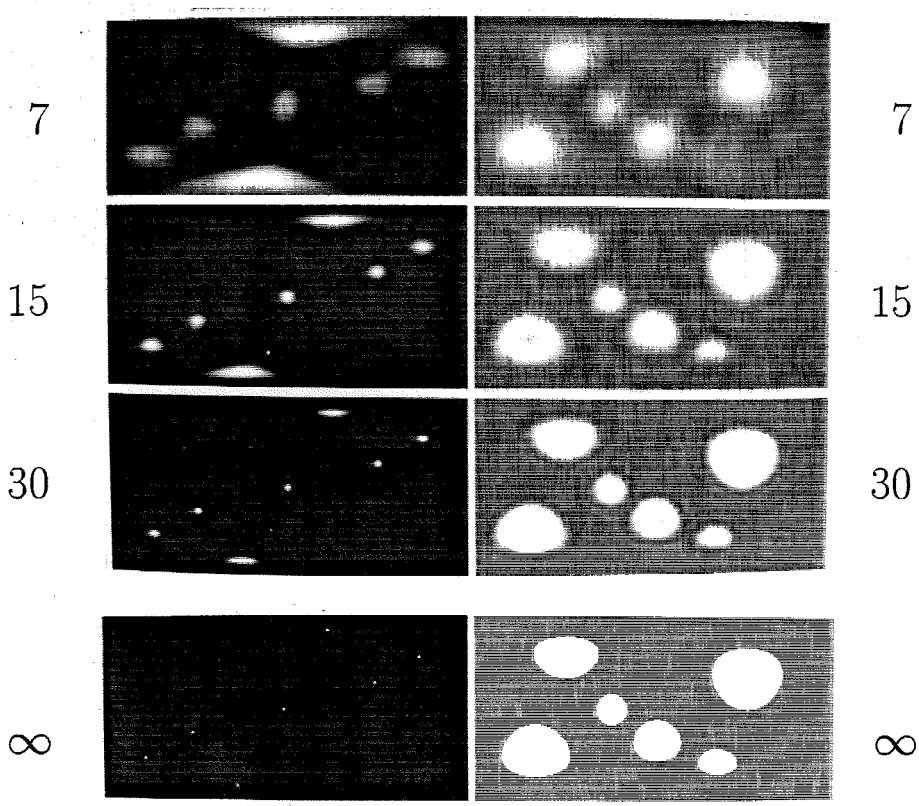

Figure 5.1: Finite spherical harmonic series representations of the two targets used in the simulations, $L = 7, 15, 30, \infty$.

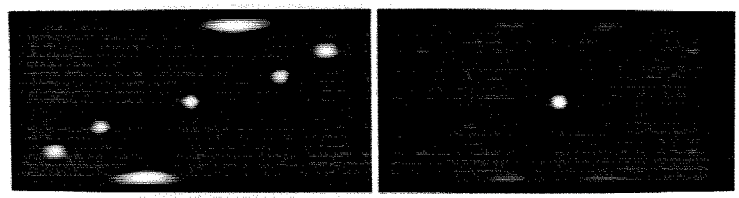

Figure 5.2: Ideal $L = 15$ images of simulated point-feature target, left image is unambiguous, right image is completely north-south ambiguous.

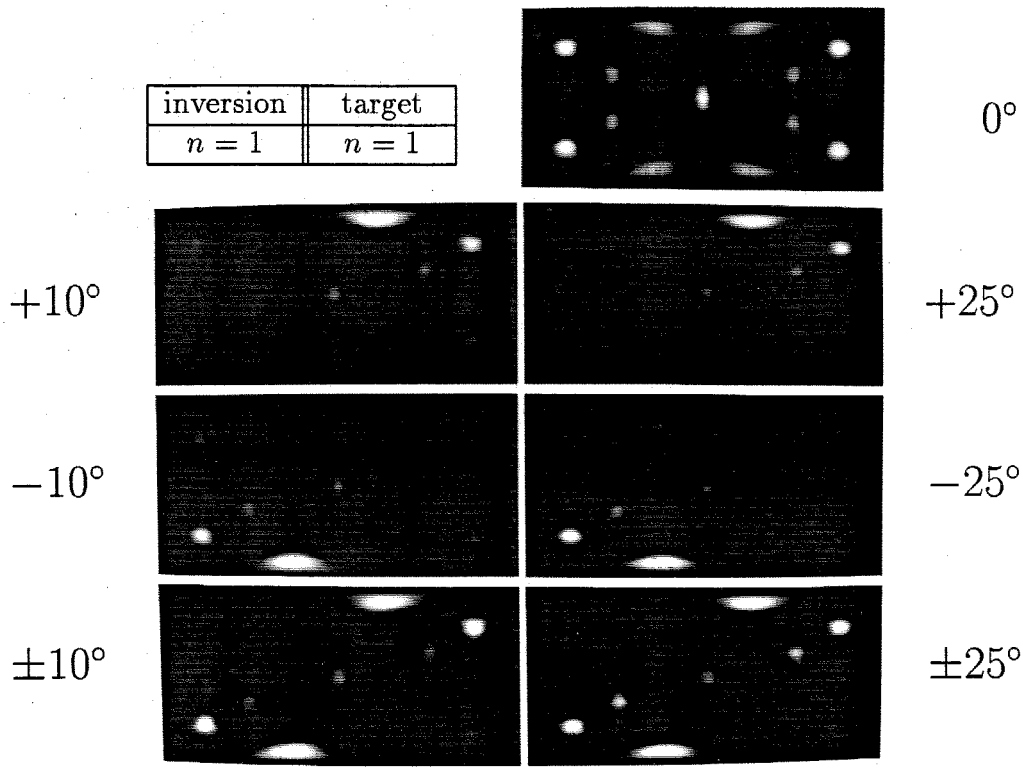

Figure 5.3: Images of point features with $n_{inv} = 1$, $n_{tar} = 1$.

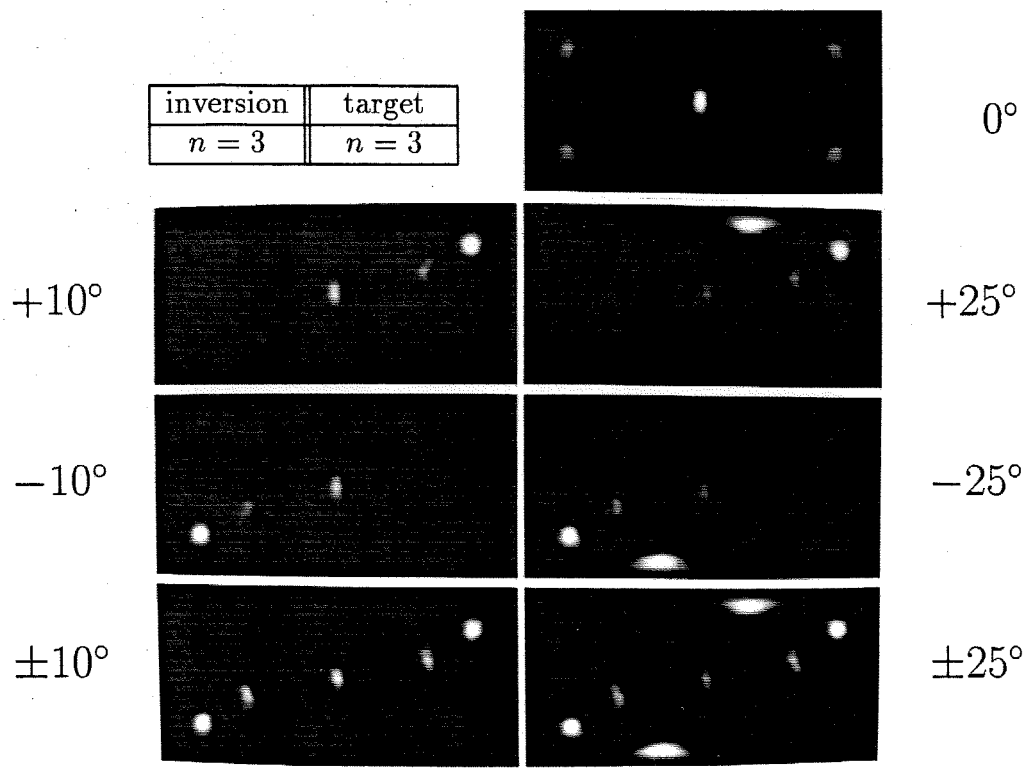

Figure 5.4: Images of point features with $n_{inv} = 3$, $n_{tar} = 3$.

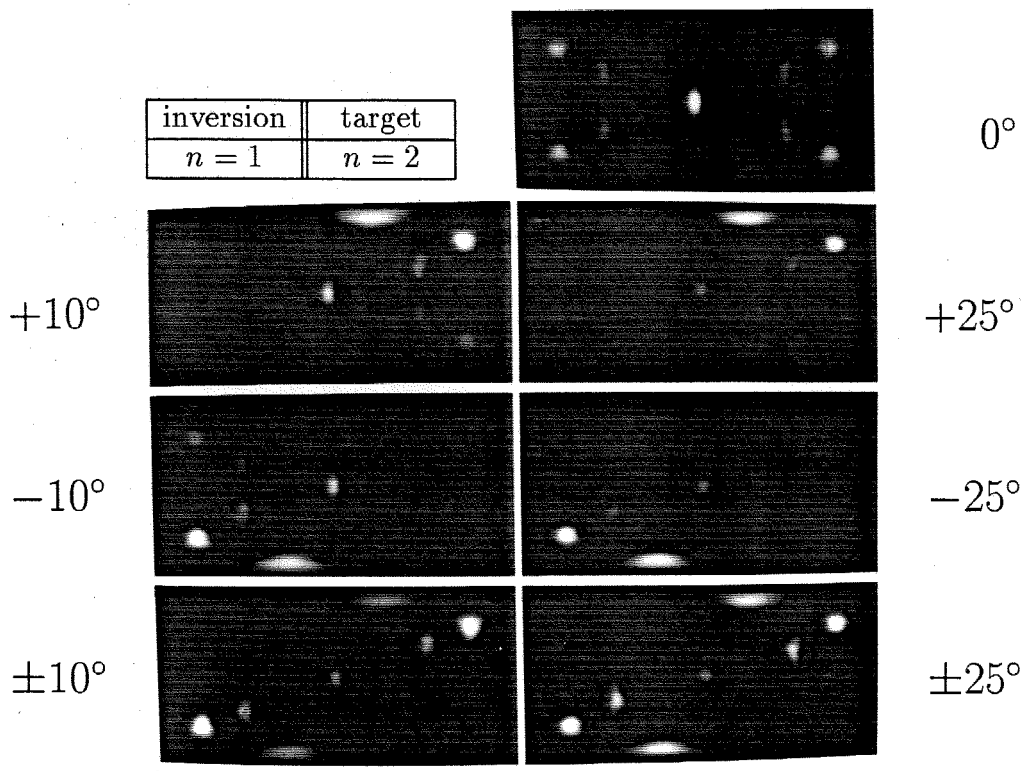

Figure 5.5: Images of point features with $n_{inv} = 1$, $n_{tar} = 2$.

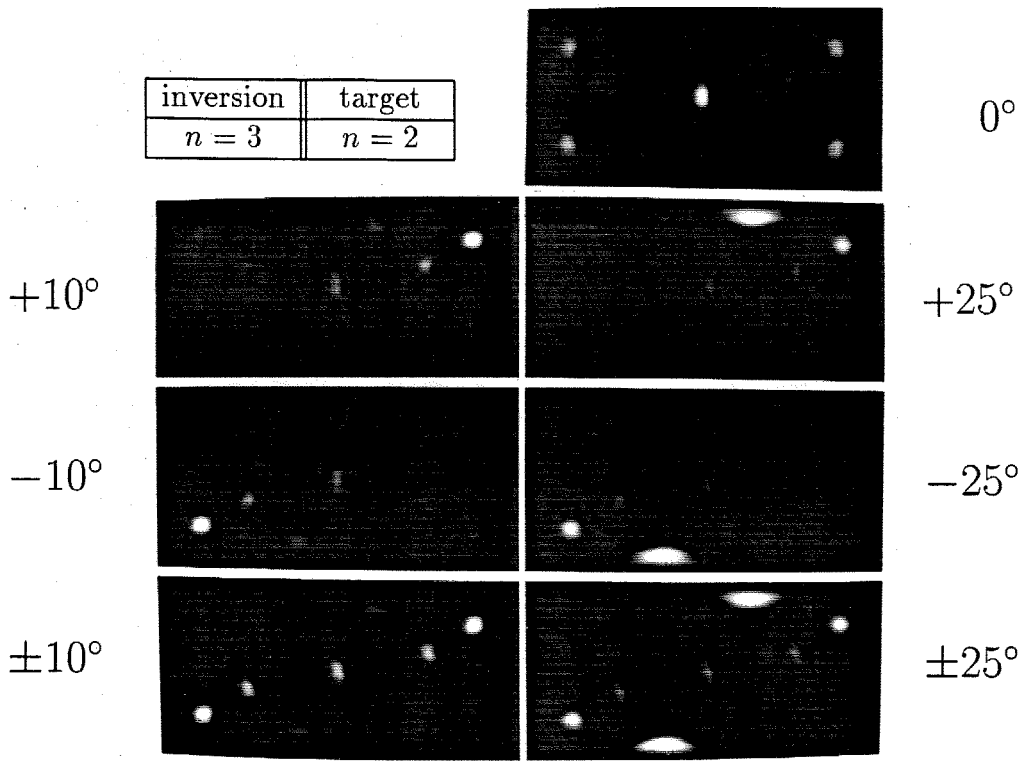

Figure 5.6: Images of point features with $n_{inv} = 3$, $n_{tar} = 2$.

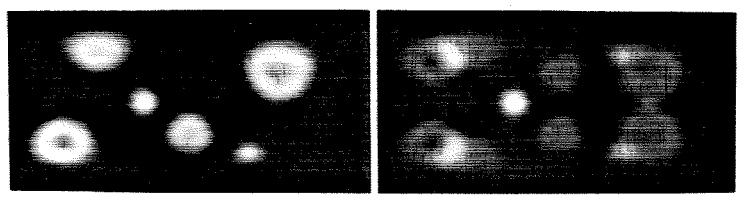

Figure 5.7: Ideal $L = 15$ images of simulated extended-feature target, left image is unambiguous, right image is completely north-south ambiguous.

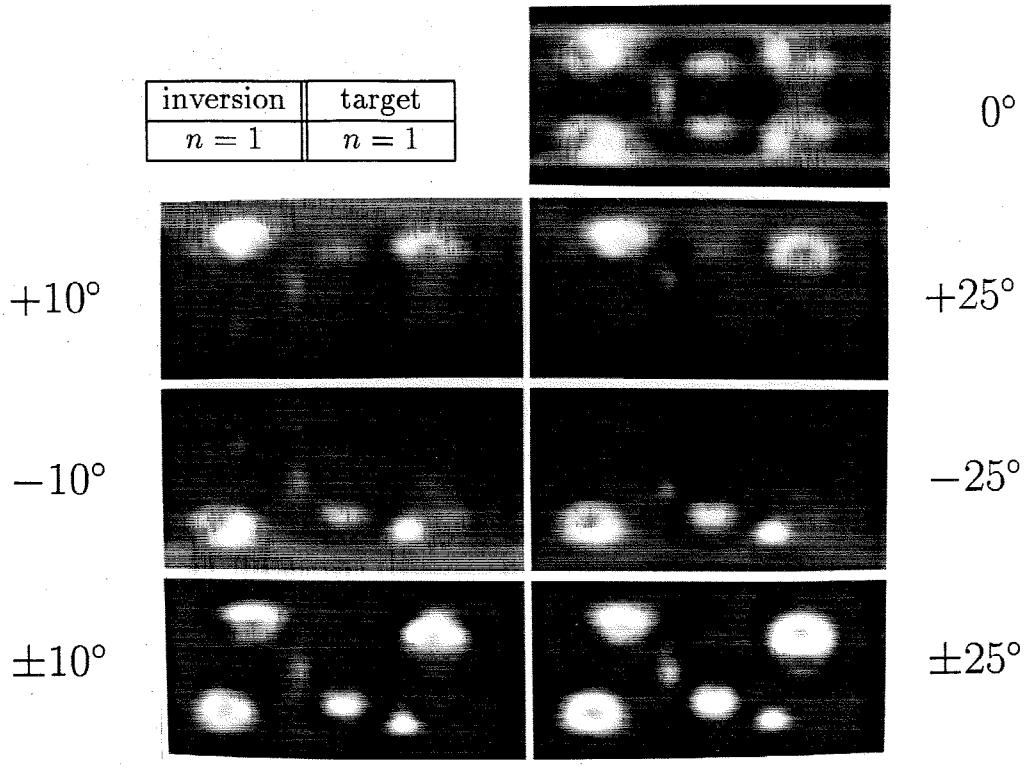

Figure 5.8: Images of extended features with $n_{inv} = 1$, $n_{tar} = 1$.

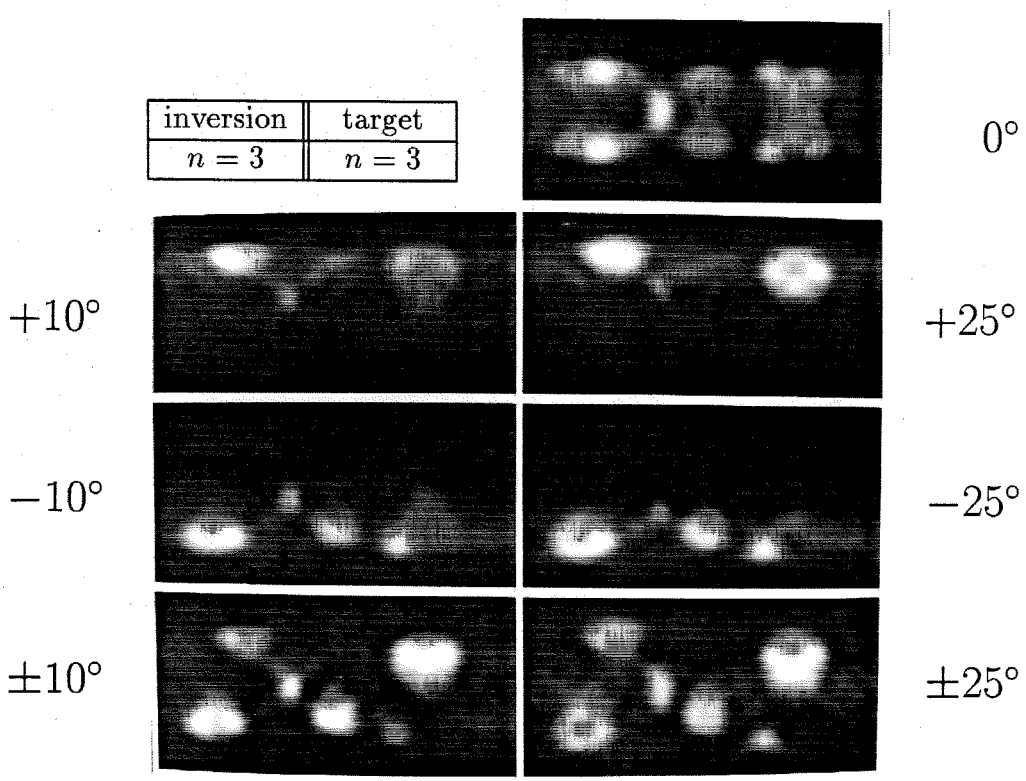

Figure 5.9: Images of extended features with $n_{inv} = 3$, $n_{tar} = 3$.

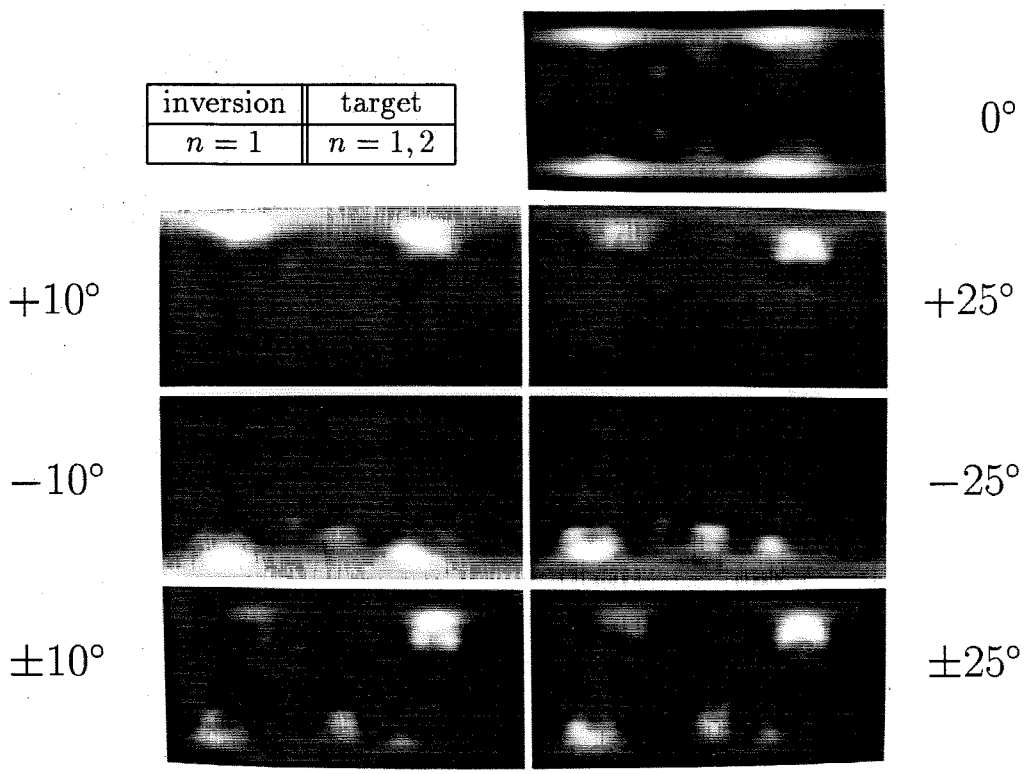

Figure 5.10: Images of extended features with $n_{inv} = 1$, $n_{tar} = 1$ for uniform background, $n_{tar} = 2$ within spots.

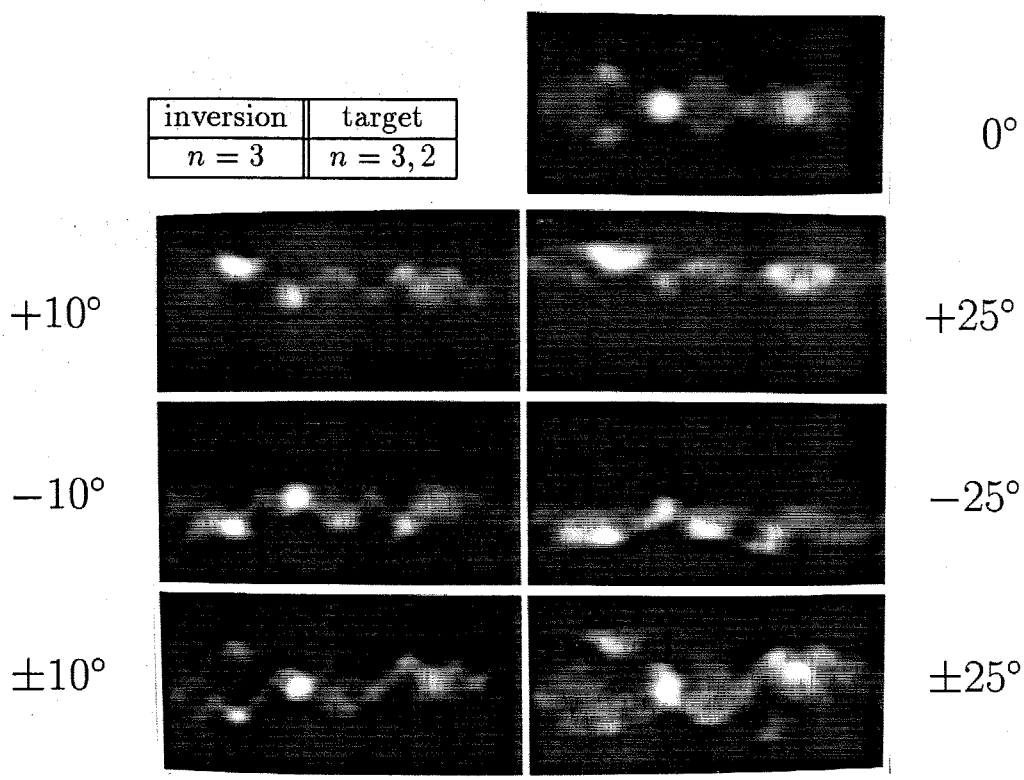

Figure 5.11: Images of extended features with $n_{inv} = 3$, $n_{tar} = 3$ for uniform background, $n_{tar} = 2$ within spots.

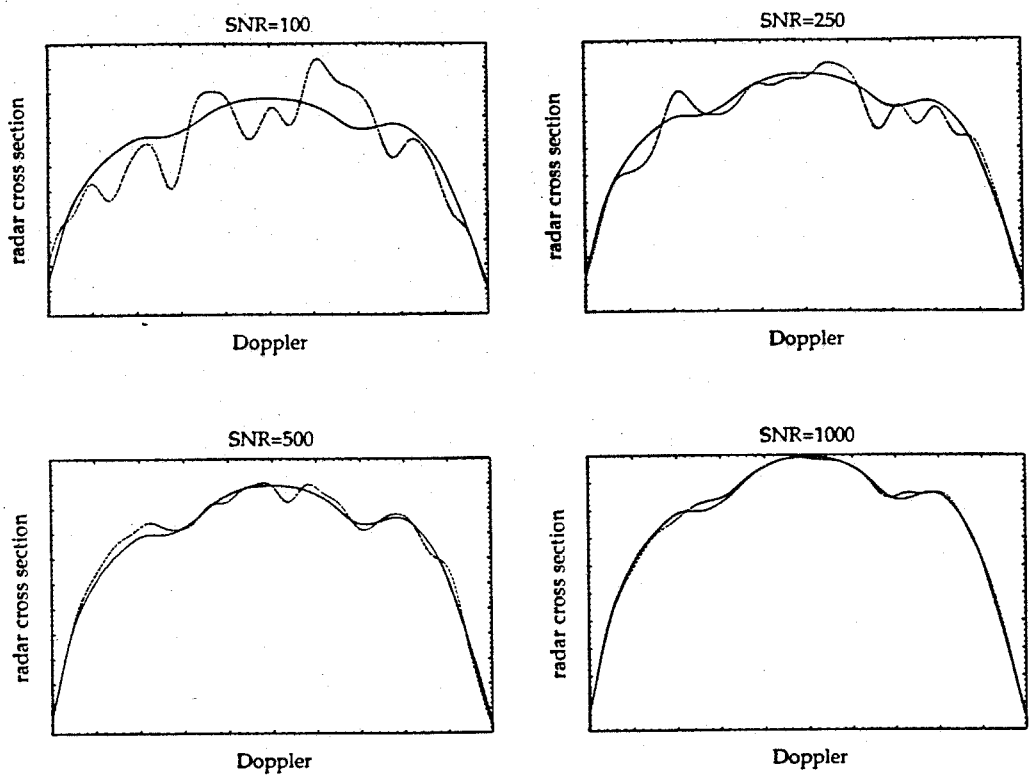

Figure 5.12: Examples of spectra corrupted by noise at SNR levels shown.

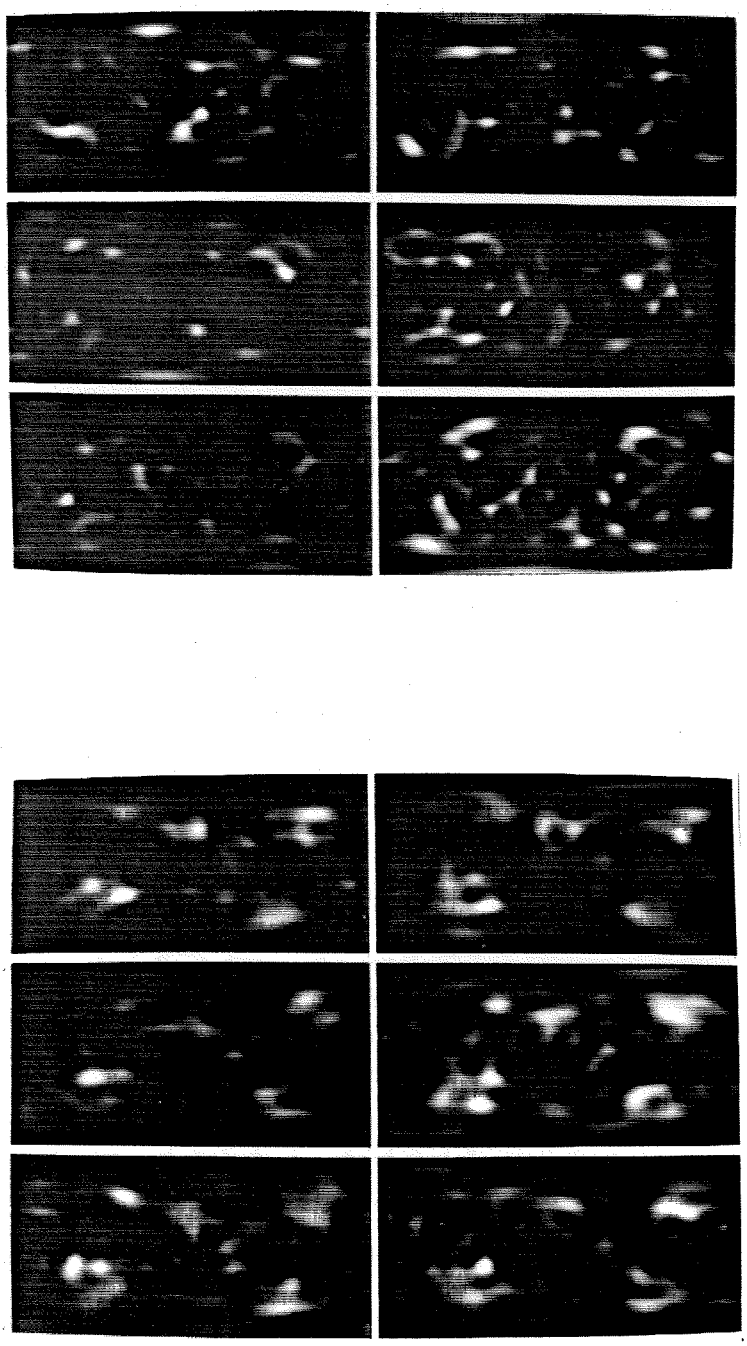

Figure 5.13: Extended-feature target imaged with SNRs of 100 (top) and 250 (bottom).

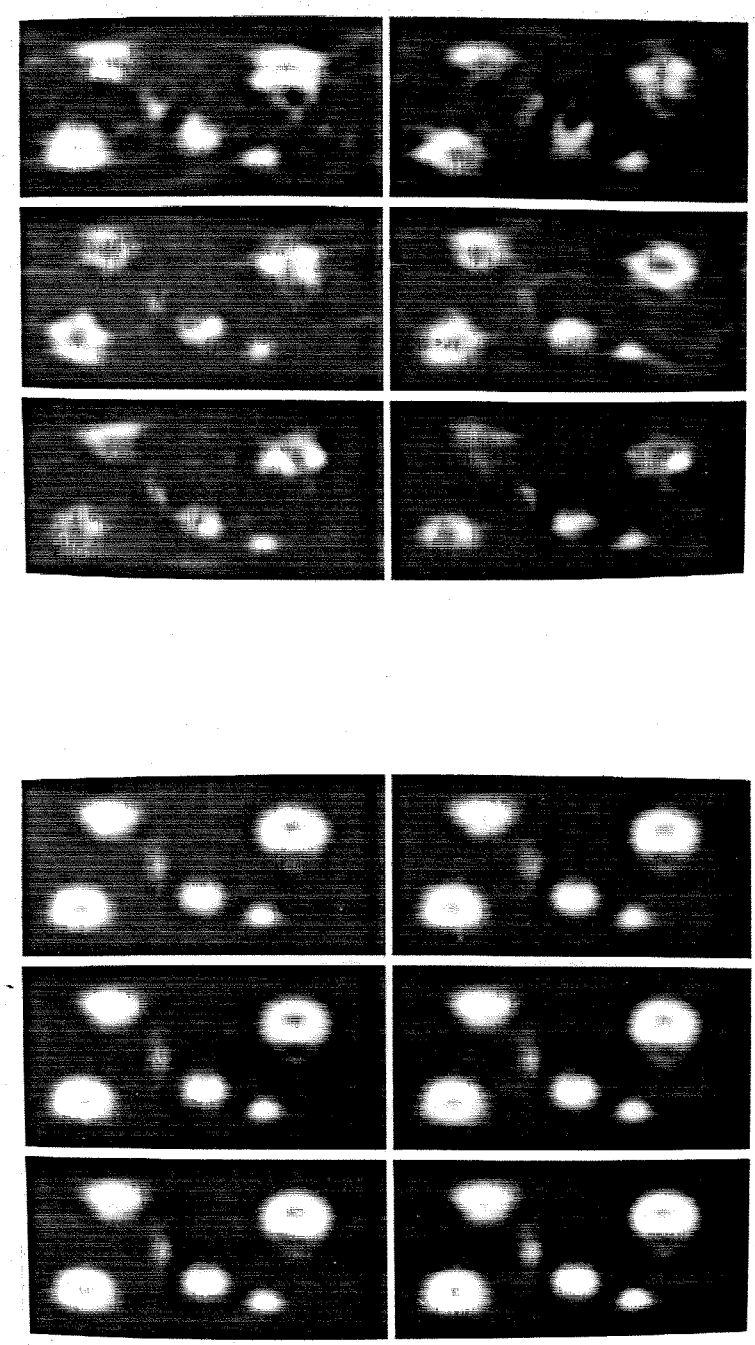

Figure 5.14: Extended-feature target imaged with SNRs of 500 (top) and 1000 (bottom).

Chapter 6

Applications of Doppler-Radar Imaging

In the previous chapter we developed a technique for modeling the distribution of radar reflectivity over the surface of a planetary body using a set of Doppler spectra. In this chapter we apply that technique to some of the existing Doppler-radar data sets. The results are radar images of Ganymede and Callisto (moons of Jupiter) in both SC and OC polarizations at 13 cm wavelength, and SC images of Mars at both 3.5 and 13 cm. The purpose of this chapter is to investigate the issues involved in applying the Doppler-radar imaging technique to real data sets rather than to analyze the resulting images from a planetary science perspective, however, we do briefly discuss the possible implications of these images in qualitative terms. The data sets were made available through collaborations with Dr. Steven Ostro of JPL (Ganymede and Callisto), Dr. Martin Slade of JPL (Mars 3.5 cm), and Dr. John Harmon of the Arecibo Observatory (Mars 13 cm).

Unfortunately, Ganymede and Callisto present the Earth with equatorial views

only, so the Doppler-radar images of these objects are necessarily north-south ambiguous. The Doppler spectral features are broad and weak, as in the "extended feature" simulations of the last chapter, and hence we expect, *a priori*, that the images will also suffer from the scattering law sensitivity problems we saw there. Moreover, the number of spectra currently available is relatively small, so the images have low resolution. Despite their very limited fidelity, these represent the only available radar images of these objects to date. Hopefully they can serve as motivation for, and help define the objectives of, more powerful radar imaging experiments on these objects in the future.

Mars offers the Earth subradar latitudes varying over approximately $\pm 25°$, and extensive 13 cm radar work has been done on Mars over the last decade, resulting in a large data set. A less extensive 3.5 cm data set was also obtained during the 1988 Mars opposition. Martian spectra have relatively high SNRs and strong features at all scales. Consequently, Mars is a prime candidate for Doppler-radar imaging. Recently 3.5 cm radar echoes of Mars were obtained utilizing transmission from the Goldstone radar and reception at the Very Large Array (VLA). Two-dimensional aperture synthesis techniques were applied to the echoes, producing high resolution images of the projected disk of Mars for a limited range of rotational phases [31]. These images represent a "gold standard" against which we can test the effectiveness of Doppler-radar imaging on a real target. Although the 3.5 cm Doppler-radar data set has only a single subradar latitude and poor rotational phase coverage over the region of Mars imaged by the VLA, we find that our 3.5 cm Doppler-radar images are in reasonable qualitative agreement with the VLA images. We then present 13 cm Doppler-radar images of Mars which are produced using a data set having both north and south subradar latitudes and fairly good rotational phase coverage, and we discuss the similarities and differences with the 3.5 cm images.

6.1 Ganymede

Ganymede is the largest of Jupiter's moons. With a diameter of 5,276 km it is the largest moon in the Solar System and larger than the planets Mercury and Pluto. The four largest moons of Jupiter: Io, Europa, Ganymede, and Callisto (in order of their distance from Jupiter), were the first satellites to be discovered revolving around another planet. They are collectively known as the "Galilean Satellites of Jupiter" after Galileo Galilei who discovered them on January 7, 1610. They are of considerable historical importance as their discovery debunked the belief, often put forward as an argument against the Copernican view of the Solar System, that only the Earth could be a "center of motion," as it showed conclusively that Jupiter was a "center of motion" for its moons. This was a key factor in the establishment of our modern view of the Solar System. Observations of the orbits of the new moons also provided an independent test of Kepler's laws of planetary motion, and they demonstrated the universality of the law of gravitation.

Modern interest in the Galilean Satellites stems from clues they may hold about the origin and evolution of Jupiter and the Solar System in general. Although we now know of sixteen Jovian moons, most of these are conjectured to be captured asteroids or comets due to their small sizes and generally eccentric and highly inclined orbits. The Galilean Satellites, on the other hand, are large and have nearly circular orbits in Jupiter's equatorial plane. They almost certainly were formed as part of the process by which Jupiter itself was formed, and their compositional and structural differences are probably indicative of the different conditions that existed at different distances from Jupiter during the formation of the Jovian system [1].

Most of our knowledge of Ganymede and the other Galilean Satellites comes from images sent back by the Voyager I and II spacecraft in 1979. Ganymede has no

detectable atmosphere. It is probably composed primarily of a rocky core and an ice and water mantle with a crust of ice and rock. In optical images the surface is characterized by light and dark patches. The dark patches have a higher density of impact craters which indicates that they are more ancient than the lighter regions that were probably resurfaced by some geological process. The most notable of these dark regions is Galileo Regio extending roughly from the equator to 50° north latitude and from 100° to 180° west longitude.

Twelve Doppler spectra in each polarization (OC and SC) are currently available for Ganymede. They were taken during the last three Jupiter oppositions using the 13 cm system of the Arecibo observatory. The subradar points are displayed in Figure 6.1. The spectra are plotted as the solid curves in Figures 6.4, 6.5, 6.7, and 6.8. The frequency resolution is $\delta\nu = 5.4$ Hz. Ganymede's rotation period is 7.155 days. Its Doppler bandwidth at Arecibo is therefore

$$\begin{aligned} B &= \frac{4\pi D}{\lambda P} \\ &= \frac{4\pi(5{,}276 \text{ km})}{(12.6 \text{ cm})(7.155 \text{ days})} \\ &= 851 \text{ Hz}, \end{aligned} \tag{6.1}$$

or 158 Doppler bins (rounded to the nearest integer).

In the analysis and simulations of the previous chapters we have assumed that the radar receiver is tuned to the Doppler frequency of the target's center of mass, resulting in a spectrum that is symmetrically positioned about $\nu = 0$. This can be accomplished, in practice, only to the extent that the radial velocity between Earth and target is known with sufficient accuracy. In the present case, to center the spectra to within one Doppler bin, we need to know the radial velocity to within

$$\delta v_r = \frac{\lambda}{2}\delta\nu = \frac{13 \text{ cm}}{2} 5.4 \text{ Hz} = 35 \text{ cm s}^{-1}. \tag{6.2}$$

This would require knowledge of both Jupiter's orbit around the Sun and Ganymede's orbit around Jupiter to an extremely high precision, much more than was available during the radar observations. Because of this we expect that spectra taken on different dates may be randomly shifted along the Doppler axis with respect to one another. Before we can apply the Doppler-radar imaging technique we need to estimate the Doppler centroid errors and compensate for them so that position on the Doppler axis corresponds precisely to position on the target, i.e., $\nu = -y_\tau$, as we assumed in the development of the technique in the previous chapter.

The method we used to estimate these errors was to align each spectrum with a rectangular template centered on $\nu = 0$ and having width equal to the Doppler bandwidth of the target. We shifted each spectrum along the Doppler axis so as to put as much spectral power as possible within the nominal bandwidth of the target. If the spectra were noise free this procedure would work perfectly as any misalignment would cause some of the spectral power to fall outside of the template. The presence of noise can lead to alignment errors if the portion of the target's echo that falls outside the template due to misalignment is more than compensated by noise power being shifted into the template.

It is interesting to note that byproducts of spectral alignment are estimates of Doppler centroid errors. These, in turn, put constraints on the errors in the orbit used to generate the predicted Doppler centroids. This information can be used with the technique of differential correction to refine knowledge of the orbit of Ganymede, something of interest due to the planned rendezvous of the Galileo spacecraft with the Jovian system in the near future.

Another problem that plagues real data is the difficulty in calibrating an astronomical radar system. A radar receiver measures received power, which the radar

equation tells us is

$$P_r = \frac{P_t G^2 \lambda^2}{(4\pi)^3 R^4} \sigma, \tag{6.3}$$

but we are interested in knowning the target's radar cross section σ. Obviously we can convert between the two only if we know the parameters P_t, G, and R with sufficient accuracy. Measuring the transmitted power P_t, and particularly the gain G, is a difficult task. Because of this, the spectra used in this chapter may suffer from relative calibration errors on the order of 10%. This will cause trouble for Doppler-radar imaging of Ganymede and Callisto since the features in their spectra are weak; the calibration "noise" may be greater than the spectral features. If the calibration errors are not compensated in some manner the least-squares inversion will tend to devote its degrees of freedom to "explaining" the calibration errors at the expense of the spectral features. Another way of looking at this is that improper calibration will create spurious "features" in the Doppler-radar image that will overpower the actual features of the target.

We want to "fine-tune" the calibration of each spectrum in a manner that as much as possible removes this problem without creating spurious features of its own. The most reasonable way to do this seems to be to add a preprocessing "calibration" step in which the spectra are scaled to fit as nearly as possible the spectrum of a uniform sphere:

$$\sigma(\nu) \propto (1 - \nu^2)^{n/2}, \tag{6.4}$$

with n the value of the scattering law exponent we are using in the imaging procedure. This creates a data set which, as much as is possible, is explained by a uniform spherical target. This minimizes the features we need to put in the target's image to explain the data; any features that do arise are absolutely required to explain the shape of the spectra.

With the spectra aligned and "calibrated", the next task at hand is to estimate the "best" global scattering law exponent n to use in the imaging process. With twelve spectra, that is, twelve different samples in rotational phase, we are justified in using up to a sixth-degree spherical harmonic model. Ideally we would perform sixth-degree inversions for a range of values of n, and one value of n would stand out as producing a much better fit to the spectra than the rest. Unfortunately the goodness of fit is quite insensitive to the value of n used in the model. This is shown in Figure 6.2 where the solid triangles denote the fitting error of the OC spectra and the open triangles denote the fitting error of the SC spectra, both for sixth-order models. The variations with n are very slight. The spectra do not uniquely constrain Ganymede's scattering law for a sixth-degree model.

Having failed to constrain n with a sixth-degree inversion, it seems reasonable to use as an estimate for n that value that produces the best fit to the spectra for a uniform sphere model, i.e., a spectrum of the form (6.4). The reasoning is the same as that used to correct for calibration errors; the resulting scattering law "explains" as much of the spectra as possible in terms of a uniformly bright target. Using this scattering law will minimize the surface inhomogeneities that the sixth-degree model needs to produce to fit the spectra. Fitting the spectrum of a uniform sphere to the Ganymede spectra for different values of n resulted in the errors plotted in Figure 6.2 as solid squares for SC spectra and open squares for OC spectra. There are clear minima in both cases at $n = 1.4$. Consequently, we have used this value of n in the sixth-degree inversions we describe below.

For a given n, the vertical distance between a solid symbol and the corresponding open symbol indicates the amount of spectral features explained by the sixth-degree model that are not explained by the uniform sphere model. For both the OC and SC spectra, this distance is a minimum at $n = 1.4$. Notice that there are more SC

features, and that the OC fits are consistently better. Both of these facts are probably due to Ganymede's polarization inversion, i.e., the fact that Ganymede is brighter in the SC polarization than in the OC polarization. Thus the SC SNRs are consistently higher. Consequently, more features will be above the noise in the SC spectra resulting in both more broad features that can be fit by a sixth-degree model and more narrow features that cannot be fit.

Applying the Doppler-radar imaging technique to the Ganymede spectra using $n = 1.4$ for both OC and SC polarizations produced the results shown in Figures 6.4 through 6.9. Figures 6.4 and 6.5 are plots of the observed SC spectra, the modeled SC spectra, and the residuals between the two. Each spectrum is labeled by rotational phase (first number above each plot), polarization (OC or SC), and the rms residual of the fit (last number above each plot).

The rms residual is the root-mean-square value of the residual curve (dashed line) measured in units of noise standard deviations, that is, in units of the rms value of the noise in that spectrum. Specifically,

$$\epsilon = \sqrt{\frac{1}{N_\nu} \sum_{n=1}^{N_\nu} \frac{(f_n - o_n)^2}{\sigma^2}}, \tag{6.5}$$

where ϵ is the spectrum's rms residual, N_ν is the number of Doppler bins, o_n and f_n are the observed and fitted values of the n^{th} bin, and σ is the rms noise. The summation factor is analogous to a χ^2 measure; however, since we are not independently fitting each spectrum, but are fitting all simultaneously, this will not necessarily obey χ^2 statistics. (The equivalent summation for *all* the spectra together will obey χ^2 statistics.) Nonetheless, we use this as a convenient measure of the goodness-of-fit of the individual spectra since it points out which ones have statistically significant features that have not been fit. Heuristically, we can say that if the fit was perfect,

i.e., the model exactly described the *noise-free* spectra, then

$$\sum_{n=1}^{N_\nu} \frac{(f_n - o_n)^2}{\sigma^2} \tag{6.6}$$

would be χ^2 distributed with N_ν degrees of freedom, and so, for even moderately large values of N_ν, quickly approach a Gaussian distribution with mean N_ν and standard deviation $\sqrt{2N_\nu}$ [42]. It would be very unlikely for this to exceed its mean by more than two standard deviations, that is, to be larger than $N_\nu + \sqrt{8N_\nu}$. Thus we would expect

$$\epsilon \leq \sqrt{1 + \sqrt{\frac{8}{N_\nu}}} \approx 1 + \sqrt{\frac{2}{N_\nu}}. \tag{6.7}$$

Hence for the Ganymede spectra a residual of more than about 1.1 probably indicates that statistically significant spectral features have not been fit.

Most of the spectra in Figures 6.4 and 6.5 appear to have significant unfit features. Those with the largest residuals are the $\psi = 141°$, $\psi = 257°$, and $\psi = 265°$ spectra. These turn out to be the spectra with the highest SNRs. The most notable of these unfit features is a fairly sharp peak about 1/4 of the way across the 141° spectrum which is too narrow for the sixth-degree model to fit completely. We do not see a corresponding residual in the 166° spectrum because its noise level is greater by about a factor of 2, and the feature has fallen below the noise. The presence of unfit features, and particularly the fact that more unfit features appear in the higher SNR spectra, indicate that many radar surface features remain to be uncovered by Doppler-radar imaging. We anticipate greatly improved images at finer resolutions and the revelationof henceforth undiscovered radar features when a significant number of spectra become available from the upgraded Arecibo telescope.

Figure 6.6 shows the north-south-ambiguous images that correspond to these spectral fits. The images have six shades of gray and are all to the same scale. Each is a view of Ganymede as it would look viewed from the Earth with "radar eyes." Fig-

ure 6.3 shows lines of constant latitude and longitude corresponding to these images. The most striking feature in this set of spectra is the depression that moves from left to right across the 90°, 116°, 141°, and 166° spectra. Being a broad feature, it has been well fit by the sixth-degree model. Looking at the 90°, 116°, 141°, and 166° images we see that this spectral depression is due to a dark region in the northern and/or southern hemisphere at approximately ±30° latitude, and centered at about 140° longitude, i.e., just passing the central meridian in the 141° image. This northern spot is in the center of Galileo Regio.

The images have lots of bright spots near the poles at latitudes ±60°. Voyager images show impact craters surrounded by bright ejecta in these regions. In particular, the bright spot in the 166° image near 50° S latitude and 210°W longitude corresponds to a large bright patch near the crater Isis.

The brightest feature in the SC images is an equatorial spot at about 160° longitude. This feature does not seem to correlate with any optical feature in the Voyager images. However, it seems to correspond to the source of the residual bump in the 141° spectrum, so we conjecture that it is a true radar-bright feature.

Figures 6.7 and 6.8 show the fits to the OC spectra. The sixth-degree spherical harmonic model has fit nearly all the statistically significant spectral features. As in the SC spectra, there is a depression that moves through the 90°, 116°, 141°, and 166° spectra, but it is not as pronounced as the the SC case. In the OC images (Figure 6.9), the Galileo Regio region does not appear as dark as it does in the SC images. The bright equatorial feature at 160° is present in these images as are the bright spots near 50° latitude and 210° longitude. The last four images show a very bright equatorial feature and a companion dark feature north and/or south of it. These do not correlate strongly with any optical features on Ganymede. They seem to be required to explain the slight skew of the last four spectra. Rotational-phase

coverage is sparser at these longitudes and hence this region is being imaged with poorer fidelity than the rest of the surface.

Figure 6.10 shows polarization ratio images of Ganymede. These were obtained by dividing, pixel by pixel, each of the SC images by the corresponding OC image. A high polarization ratio feature appears in the 317° and 350° images, but as mentioned earlier the rotational-phase coverage is not as complete in this region so we expect image fidelity to be correspondingly lower. The most pronounced polarization feature is the low polarization-ratio region corresponding to Galileo Regio and/or its southern ambiguity.

The fidelity of the images we have presented rests to a large degree on the validity of the scattering model we have used to form them. Recall that in all choices we had to make regarding recalibrating the data and choosing a scattering law, we made the choice that resulted in the data being fitted as closely as possible by a uniform sphere model. In this manner we sought to minimize the creation of spurious features and produce images with only those features absolutely needed to explain the spectra. However, the triangle markers in Figure 6.2 show that the spectra can be explained equally well with essentially any scattering law in a sixth-degree model, and it is quite possible that the criterion we have used to choose the scattering law for Doppler-radar imaging results in a bad choice. Figure 6.11 shows SC images of Ganymede at 141° rotational phase for $n = 1.0$ and $n = 2.0$. Notice that the $n = 1.0$ image results in very bright polar regions while the $n = 2.0$ image has a very bright equatorial region. These are the effects we discussed in section 5.3. Still it is quite possible that, for instance, Ganymede is largely characterized by $n = 1.0$ but that one or both polar regions are very radar bright, in which case the $n = 1.0$ would have better fidelity than the $n = 1.4$ image of Figure 6.6. The northern dark patch in the $n = 1.0$ image of Figure 6.11 certainly suggests the shape of Galileo Regio as it

appears in optical images more than the dark patch of the 141° image of Figure 6.6 does. Another possibility, of course, is that a uniform scattering law of the form $\cos^n \theta$ is not sufficient to model the true radar properties of Ganymede.

To the extent that these images are accurate what do they tell us? The principle result seems to be that Galileo Regio is relatively radar dark and that its polarization ratio is low. This is consistent with the hypothesis that Ganymede's surface in the Galileo Regio region has a much higher proportion of rocky material (hence its darker optical appearance), and that the exotic radar properties are suppressed by the presence of silicates.

6.2 Callisto

Callisto, like Ganymede has no detectable atmosphere. Unlike all other solid bodies in the Solar System it lacks any smooth plains regions, and the density of craters on Callisto's surface is quite uniform and is the highest yet observed for any body [1]. Evidently no geological processes have altered the surface of this 4,820 km object since early in the formation of the Solar System. The most striking features on Callisto are two huge impact structures. The largest, Valhalla, is about 3,000 km across, and is centered at about 15° north latitude and 55° west longitude. Asgard is about half the size of Valhalla, and is centered at approximately 30° north latitude and 140° west longitude.

Nineteen Doppler spectra in each polarization are currently available for Callisto. They were taken during the last three Jupiter oppositions using the 13 cm system of the Arecibo observatory. The subradar points are displayed in Figure 6.12 which shows that several of the spectra are very closely spaced in rotational phase. While there are nineteen spectra, there are *effectively* only about thirteen separate rotational

phase samples so we are justified in using no more than a sixth-degree model as we did for Ganymede. The spectra are plotted as the solid curves in Figures 6.14 – 6.16 (SC), and 6.18 – 6.19 (OC). The frequency resolution is $\delta\nu = 5.4$Hz. Callisto's rotation period is 16.69 days. Its Doppler bandwidth at 13 cm is therefore

$$B = \frac{4\pi(4{,}820 \text{ km})}{(12.6 \text{ cm})(16.69 \text{ days})} = 333 \text{ Hz} \tag{6.8}$$

or 62 Doppler bins (rounded to the nearest integer).

The same data processing steps were applied to the Callisto spectra that were applied to the Ganymede spectra. The fit errors for uniform sphere and sixth-degree spherical harmonic models are shown in Figure 6.13. As in the case of Ganymede, the scattering law exponent is not well constrained by a sixth-degree model, although the SC fit error does slightly increase with n. In fact the uniform sphere model is not as well constrained as it was for Ganymede. Nonetheless, minima occur at $n = 1.3$ for the SC spectra and at $n = 1.7$ for the OC spectra. The distance between the zeroth-degree and sixth-degree curves is greater in the SC case meaning there are more SC features than OC features, as was the case for Ganymede.

The resulting SC spectral fits are displayed in Figures 6.14, 6.15, and 6.16, and they are labeled by rotational phase, polarization, and rms residual (in units of standard deviations of the noise). There are fewer Doppler bins than for Ganymede, 62 instead of 158, so we can say that if the rms residual is more than about $1 + \sqrt{2/62}$, or 1.2, then there are statistically significant features that have not been fit. Several of the spectral fits have rms residuals larger than this. In some, like the 126° spectra, this seems to be due to relatively narrow spectral features of a few noise standard deviations in amplitude, but in others, like the 208°, 230°, and 237° spectra, the residuals slope upward to the right. This may indicate that the Doppler centroid error correction procedure failed to properly align these spectra.

The most interesting spectral features are in the 86°, 90°, 110°, and 126° spectra. The two bumps that move across these spectra have been fairly well captured by the sixth-degree model. When we examine the north-south ambiguous SC images (Figure 6.17), we see that the bump that is most prominent in the 90° spectrum has been attributed to a bright feature near Callisto's equator at about 65° longitude. This is the Valhalla region. The other spectral bump, the one that is most prominent in the 126° spectrum, is attributed to a bright region on Callisto centered on approximately 40° north and/or south latitude and 140° west longitude. The northern bright spot coincides with the Asgard region.

The OC spectral fits are shown in Figures 6.18, 6.19, and 6.20. The rms residuals are lower than for the SC spectra although the 208°, 230°, and 237° residuals display the same systematic increase to the right that they did for the SC spectra. The 86°, 90°, and 110° spectra do not have the double bump structure they did in the SC case. The OC images show the Valhalla region to be a bright OC feature but the Asgard region, while still discernible as a feature in the 90° and 110° images, is not as bright as in the SC images.

Figure 6.22 shows polarization ratio images for Callisto obtained by dividing the SC images by the OC images pixel by pixel. They are difficult to interpret since the different polarizations are characterized by different scattering laws. This shows up in the polarization images where it creates bright limbs due to the fact that the OC images are falling off faster with increasing angle of incidence.

The principal result from these images is that the large impact basins are the most radar bright regions on Callisto.

6.3 Mars

Mars is the closest superior planet (i.e., having an orbit outside the Earth's), and hence it has the fastest motion across the night sky of all naked-eye objects, except the Moon, close comets and meteors. Because of this and its brightness and distinctive red color, Mars has always been one of the most fascinating objects in the sky. Unlike Venus, which is perpetually cloud covered, the surface of Mars is readily visible through Earth-based telescopes. The presence of an atmosphere results in a dynamically varying landscape. In particular the existence of Martian seasons is readily discernible from Earth. Tremendous dust storms periodically alter the appearance of the planet. These effects led some early observers to postulate the presence of vegetation and even intelligent life on Mars. The Viking landers found no evidence of Martian life, and the general consensus is that there is none, but the possible past existence of free-flowing water on the surface of Mars continues to fuel speculation that life may have existed there at one time.

Mars is 6800 km in diameter. Its atmosphere is 95% carbon dioxide and is considerably thinner than the Earth's, the atmospheric pressure being only about 6 mb. A very interesting property of the Martian surface, first revealed in Mariner 9 images, is that it is divided by a great circle inclined roughly 35° to the equator into two hemispheres of very different geological makeup. The more southerly hemisphere is heavily cratered, hence more ancient, with an appearance similar to that of lunar highlands. The other hemisphere is dominated by smooth plains scarred by huge canyons and channels. Within this plains region lies Tharsis, a dome structure 10 km high and thousands of kilometers in extent. It is centered roughly on the equator at 100°W longitude. Near the center of Tharsis are three huge volcanos, the Tharsis Montes, about 800 km apart and arranged in a line oriented roughly 45° to the equa-

tor. About 1700 km northwest lies Olympus Mons, the largest volcano in the solar system, over 500 km in extent and 25 km high. Another 80° to the west, and about 25° North of the equator is Elysium, another region of volcanic activity, although not as dominating as Tharsis. The polar caps of Mars are composed primarily of condensed carbon dioxide and are large enough to be easily seen from Earth. Their sizes vary greatly with the Martian seasons, but they never disappear, even during the Martian summer when a relatively small residual cap remains.

As we mentioned previously, Mars spectra have been obtained with both the Goldstone (3.5 cm) and Arecibo (13 cm) instruments. Below we apply the Doppler-radar imaging technique to these data sets.

Goldstone

The Doppler centroid errors we worried about for Ganymede and Callisto are not a concern for Mars because its orbit is better known and its Doppler bandwidth is many times larger. The allows us to use much coarser Doppler resolution to obtain the same number of Doppler bins across the planet. thus it takes a much greater Doppler centroid error for a spectrum to be shifted by one Doppler bin. Although Martian spectra suffer the same calibration uncertainties as the Galilean Satellite spectra, we will not attempt to compensate for calibration errors before processing because Martian spectra have strong spectral features at all scales, and there are many more Martian spectra available. This should result in an averaging out of calibration errors as the inversion attempts to fit all the spectra simultaneously. However, when plotting the spectral fits, we have scaled the observed spectra to match the modeled spectra as closely as possible, a kind of post-processing calibration.

Fifty-nine Goldstone 3.5 cm SC Mars spectra were recorded during the last Mars opposition. The OC spectra of Mars, as for all rocky bodies, have both a sharp,

quasi-specular, polarized component and a broad, diffuse, depolarized component (Figure 4.9). The Doppler-radar imaging technique as developed in the previous chapter is not suited to the OC spectra as they cannot be well modeled by a single-n cosine scattering law, so we make use of only the SC spectra. The subradar points are shown in Figure 6.23. The corresponding spectra are plotted in Figures 6.24 through 6.31 and are labeled by subradar longitude (rotational phase) and subradar latitude. We see that the coverage is along a 25°S track which is well sampled between 27° and 86° longitudes and between 189° and 345° longitudes. There are two gaps in the coverage. The 103° gap between 86° and 189° arose because the Goldstone radar was involved in a Mars mapping experiment with the VLA which produced 3.5 cm images of this region of Mars.

We used a fifteenth-degree spherical harmonic series model to represent reflectivity variations over the Martian surface. This provides us with $(15+1)^2 = 256$ resolution cells. Since Mars has a diameter of 6,800 km, each of these resolution cells has an area of about 5.7×10^5 km^2 and has a linear extent of approximately 700 km. We processed the spectra using scattering law exponents of 1.0, 1.5, and 2.0. The fit errors were 10% smaller for the $n = 1.0$ case than for $n = 1.5$. The spectral fits using $n = 1.0$ are shown in Figures 6.24 through 6.31 in which the spectra are labeled by subradar latitude and subradar longitude. The SNRs of the spectra are very high and most of the residuals consist of actual Mars features that the fifteenth-degree model did not have enough resolution to fit. Images of Mars as both a rectangular latitude-vs-longitude map and as a spherical projection from subradar point (147°W, 25°S) are show in Figure 6.32, for both the $n = 1.0$ and $n = 1.5$ cases. One can see that the sensitivity of these images to n is much less than was the case for the Galilean Satellites.

Many of the spectra have a narrow peak in their center. There is a possibility

that this is due to cross talk between the receiver's OC channel and its SC channel as the OC spectra are characterized by large quasi-specular spikes near their centers (see Figure 4.9). It is very difficult to measure the isolation between the receiver channels, so it is difficult to make quantitative statements about the degree of cross talk. However, it has been observed that the positions of the SC and OC peaks do not always follow one another, and some of the SC spectra lack this peak. Both of these facts argue against a cross-talk explanation of the SC peak. Apparently it is a true feature. The fifteenth-degree model has fit this feature to within its limited spectral resolution, about twice the width of the feature as one can see in the spectra of Figure 6.24. The images of Figure 6.32 show that a very bright southern pole accounts for this peak. In fact, the south polar region is the brightness region of the 3.5 cm maps.

Another strong feature begins to appear on the left of the 48°, −25° spectrum and moves across subsequent spectra until it grows to a very large bump about 1/4 of the way across the 86°, −25° spectrum. Unfortunately the rotational phase coverage stops there and does not start again for another 103° so we do not get a good look at this feature as it crosses the disk of the planet. To the limited extent the spectra we do have allows us to image this feature, it appears in the 60° - 210° images as a patch centered near 30°S latitude and 130°W longitude. This is at the southern edge of Tharsis, on the southwest flank of Arsia Mons, the southernmost of the three Tharsis Montes.

The other particularly strong spectral feature is the bump that moves across the spectra, starting at about 212° rotational phase until about 246° of rotational phase. We can see the corresponding surface feature in the 150° - 240° images located about 25°N latitude and 200°W longitude. This is in Elysium, which is another volcanic region. This feature does not show up as brightly in the $n = 1.5$ images. Because

it is in the northern hemisphere, we expect the image of this region to be much more sensitive to scattering law as our subradar coverage is limited to the southern hemisphere.

We see that the strongest SC features on Mars are associated with the South Pole and with the volcanic regions. The brightness of the South Pole is particularly interesting as its icy nature implies a possible connection with the SC scattering processes on the Galilean Satellites. The presence of strong SC features, implying considerable wavelength-scale roughness, near the volcanic regions could be due to dense rock populations resulting from volcanic activity, or to the unique texture of lava flows [21]. Surprisingly, near the strong SC feature at the southwest flank of Arsia Mons is an equatorial region that is SC dark. This is particularly evident in the spherical projection images of Figure 6.32 where it appears as a black strip. This feature was first identified by Muhleman et al. in their VLA Mars images (Figure fig applicat vla images), and nicknamed "Stealth." There is evidence that this is a region of thick ash flows which, containing few wavelength-scale scattering centers such as rocks, would be expected to produce very little SC backscatter.

These 3.5 cm Doppler-radar images must be considered preliminary due to the lack of northern subradar latitude coverage, and to the presence of large longitude gaps. In particular, the large longitude gap corresponding to Tharsis seriously limits our ability to image this most interesting region. Nonetheless, it is reassuring that even under conditions that are much less than ideal, the main features of the images in Figure 6.32 are not terribly sensitive to n, and that the spherical projections compare reasonably well in qualitative terms with the 147° VLA image of Figure 6.33. As future 3.5 cm observations increase the subradar coverage, it will be very interesting to see how well Doppler-radar imaging can approach the VLA results. Of course for Mars this is of little more than academic interest since we already have the VLA

images. However, the VLA, which provides angular resolution limited by the spacing of its elements, will not be able to resolve many of the more distant targets of interest, such as the large, main-belt asteroids. Moreover, lacking 13 cm receive capability, it will not be in a position to exploit the imminent upgrades to the Arecibo instrument. It appears that, at present, Doppler-radar imaging is the only Earth-based technique with the demonstrated capability to resolve the surfaces of these objects. Therefore it will be important to exploit Mars as a "real-world" calibration test of the technique.

Arecibo

Mars has been observed with the Arecibo instrument for the last 25 years. However, it is only in the last decade that the system's sensitivity has been sufficient to allow high-quality SC spectra to be obtained. Observations during the 1980 and 1982 oppositions provided twenty-five spectra with subradar latitudes between 20°N and 25°N. The 1980 experiment concentrated on subradar longitudes in the eastern Tharsis region providing fifteen spectra between about 80°W and 125°W. The 1982 experiment provided ten spectra with a wide range of longitudes. These northern observations leave three approximately 70° gaps in the longitude coverage between 149°W and 222°W, between 262°W and 330°W, and between 330°W and 40°W. Observations during the 1988 opposition provided thirty-two spectra with southern latitude coverage between about 20°S and 25°S and at a wide range of longitudes. The subradar points for all spectra are show in Figure 6.34. The spectra themselves are show in Figures 6.35 through 6.42 and are labeled by subradar longitude and latitude.

The spectra were fit using a fifteen-degree model and scattering law exponents of $n = 1.0$, $n = 1.5$, $n = 2.0$, and $n = 2.5$. A value of $n = 2.0$ gave the best fit with an rms residual about 10% less than for $n = 1.5$, which gave the next-best fit. The $n = 2.0$ fits are show in Figures 6.35 through 6.42 as the dotted curves; the residuals

are shown as dashed curves. The fits are generally good except that the limited resolution possible with the fifteenth-degree model does not allow the fine details of the spectra to be accounted for. The worst fitting errors all occur in spectra having a subradar latitude of approximately $-20°$ (that is 20°S). These fits are seen to be consistently too low at the left of the spectra and too high at the right. John Harmon, who conducted these observations, has pointed out that even before seeing these results, he had suspected that these particular spectra were plagued by pointing errors, that is, during the transmit/receive cycles that produced these spectra the antenna beam was not centered on the target but rather was pointed slightly off to one side. This resulted in artificially attenuated radar echoes from the portions of Mars corresponding to the right sides of these spectra. It is reassuring that the inversion did *not* fit these pointing error artifacts as it provides an indication of the robustness of the technique.

The 13 cm Mars Doppler-radar images are shown in Figure 6.43 for $n = 2.0$ and $n = 1.5$. The layout is the same as that of the Goldstone images. As in the 3.5 cm images, the South Pole, the southwestern flank of Arsia Mons, and portions of Elysium are bright. The more extensive subradar coverage of the 13 cm images also reveals a bright region at the western flank of Olympus Mons and a bright North Pole, although not as bright as the South Pole. Again, the bright regions of Tharsis are accompanied by the very dark "Stealth" region.

6.4 Conclusion

We have demonstrated that it is possible to produce radar images of planetary bodies from their Doppler spectra. To date, none of the data sets have been collected with Doppler-radar imaging in mind, and subradar coverage is not ideal for any of

them. Even so, it has been possible to extract new and useful information from these data sets in the form of images, and it seems clear that as more and better data become available the quality of these images will increase. Hopefully in the future the subradar coverage requirements of Doppler-radar imaging will be a consideration in the scheduling of radar observations. The case of Mars is of particular importance as the VLA images provide "ground truth" against which to test the effectiveness of Doppler-radar imaging. If additional subradar coverage at 3.5 cm allows the technique to replicate the VLA results then we will be able to apply it with confidence in other cases. To begin with, we will be able to study the differences between the 13 cm and 3.5 cm Mars images to discern the wavelength dependence of the SC scattering mechanisms. Among the most exciting applications will be the imaging of the main-belt asteroids Ceres, Pallas, and Vesta, as well as all four Galilean satellites and Titan, when the Arecibo instrument is upgraded.

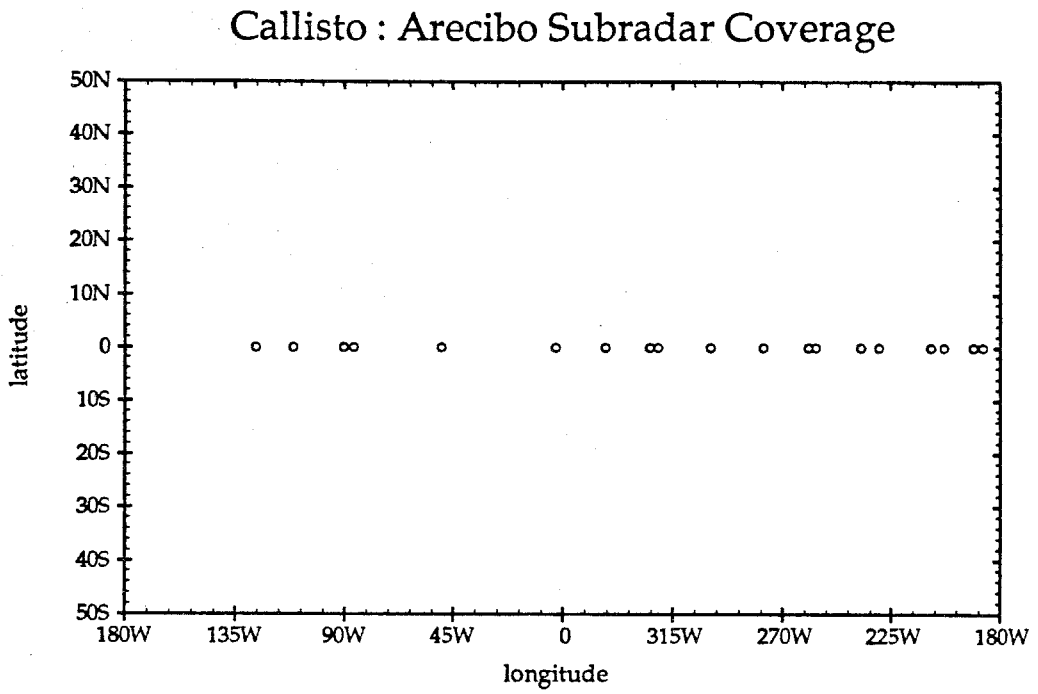

Figure 6.1: Subradar points on Ganymede at which Arecibo OC and SC Doppler spectra are currently available.

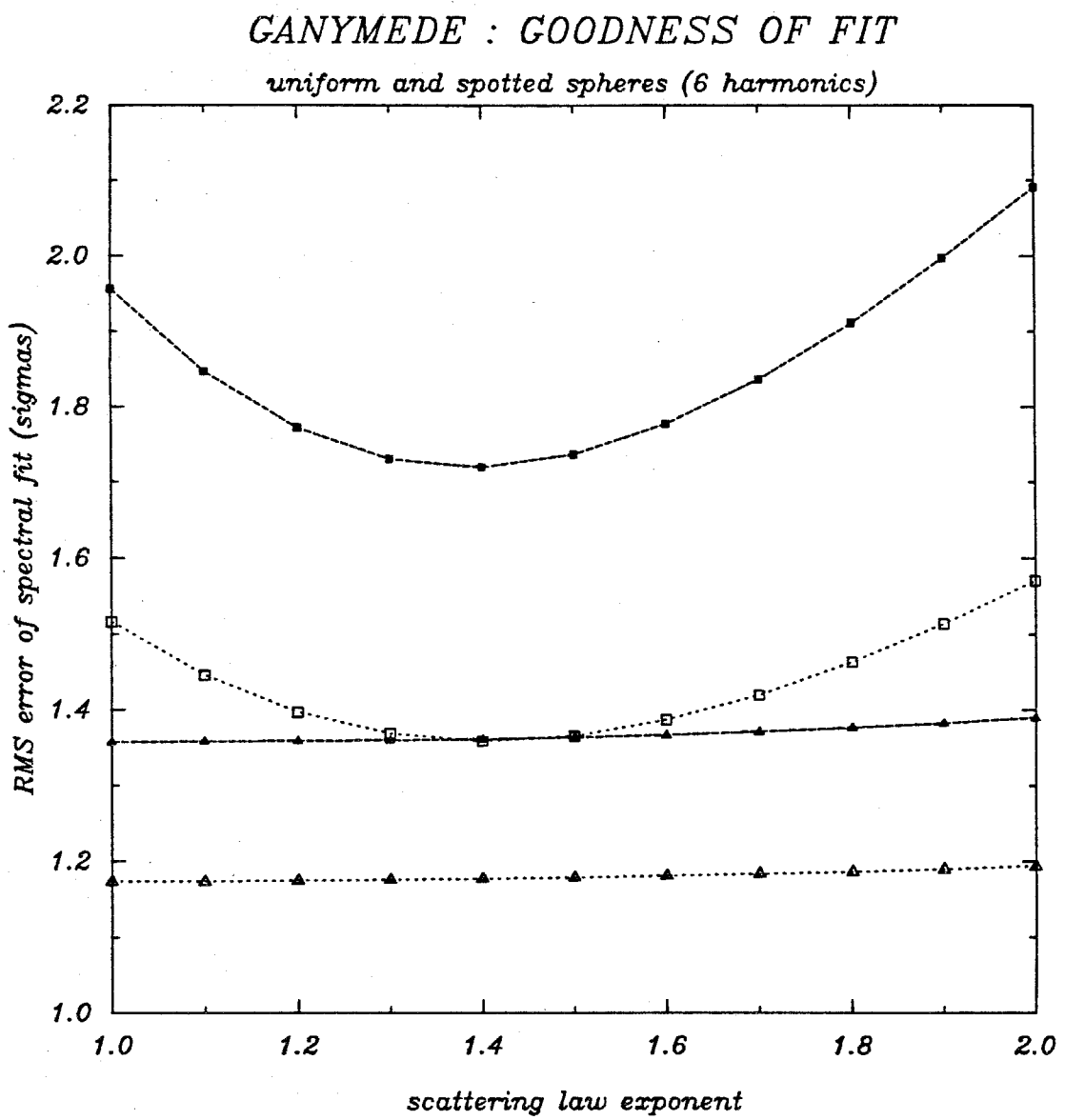

Figure 6.2: Errors in fits to Ganymede spectra. Open symbols are OC errors, solid symbols are SC errors. Squares correspond to uniform sphere models, triangles to sixth-degree models.

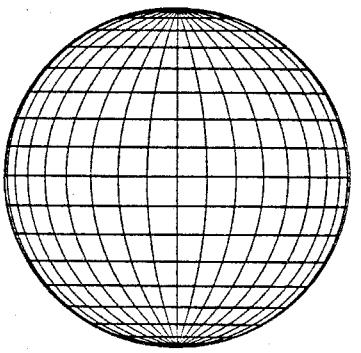

Figure 6.3: Lines of constant latitude (horizontal) and constant longitude (vertical and curved) corresponding to Galilean Satellite images. Spacing is 10° between each line.

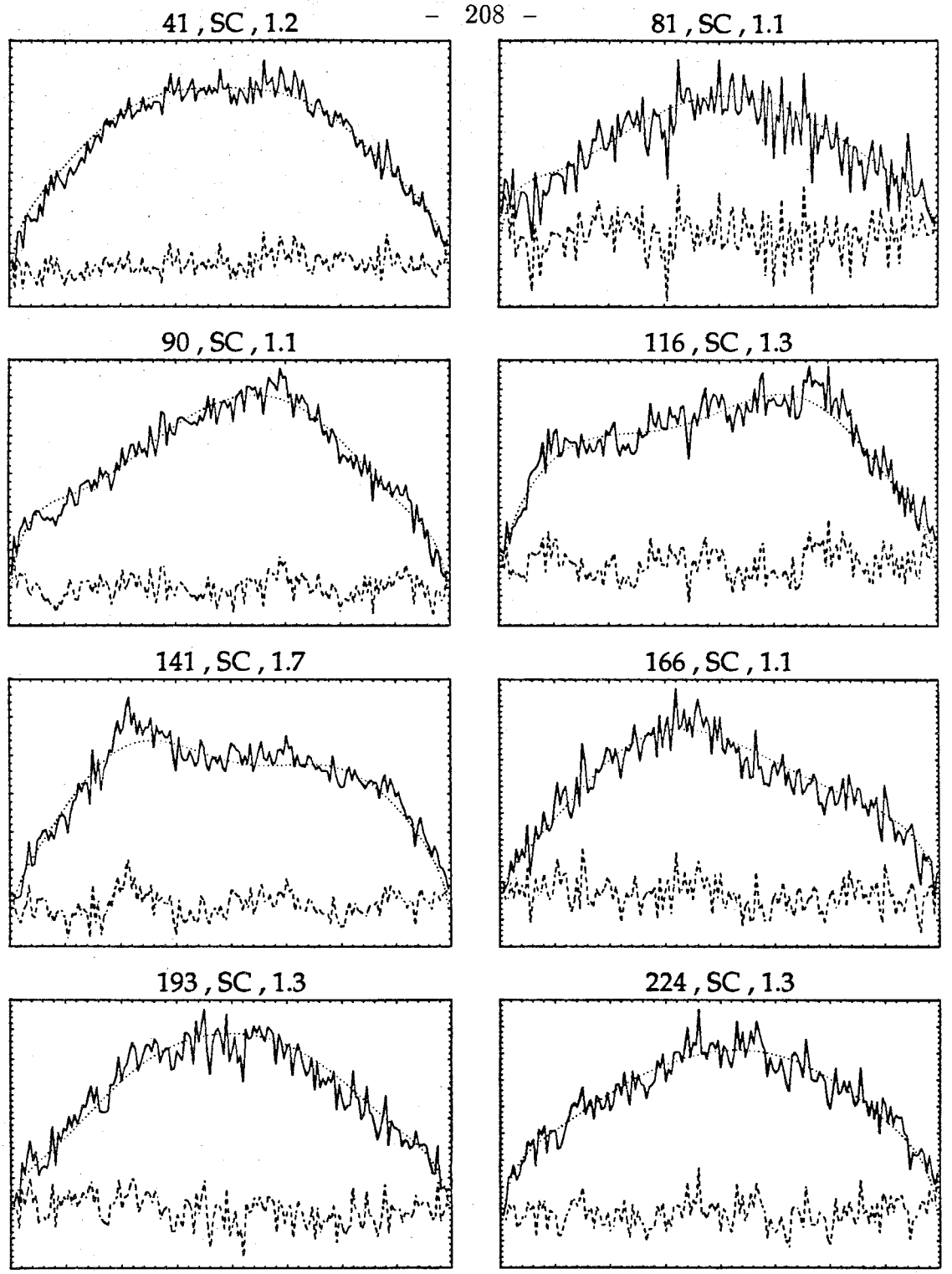

Figure 6.4: Ganymede SC spectra. Solid curves are observed spectra, dotted curves are modeled spectra, and dashed curves are residuals. Labels give rotational phase, polarization, and rms residual in units of noise standard deviations.

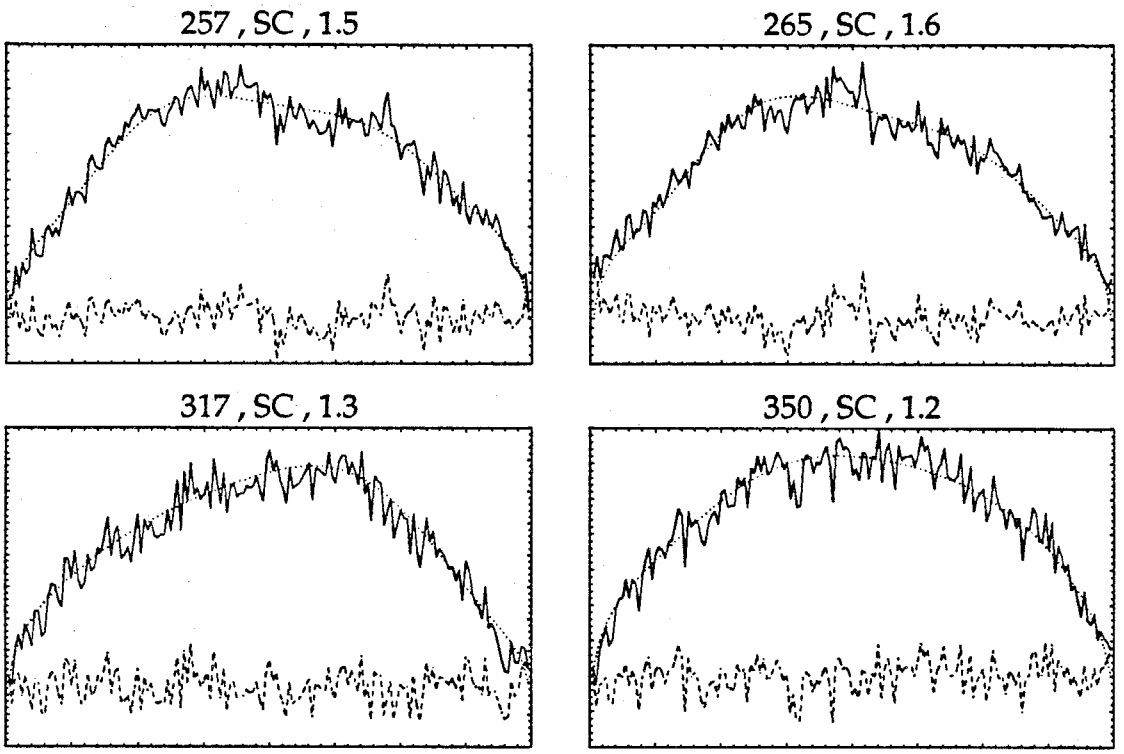

Figure 6.5: Ganymede SC spectra. Solid curves are observed spectra, dotted curves are modeled spectra, and dashed curves are residuals. Labels give rotational phase, polarization, and rms residual in units of noise standard deviations.

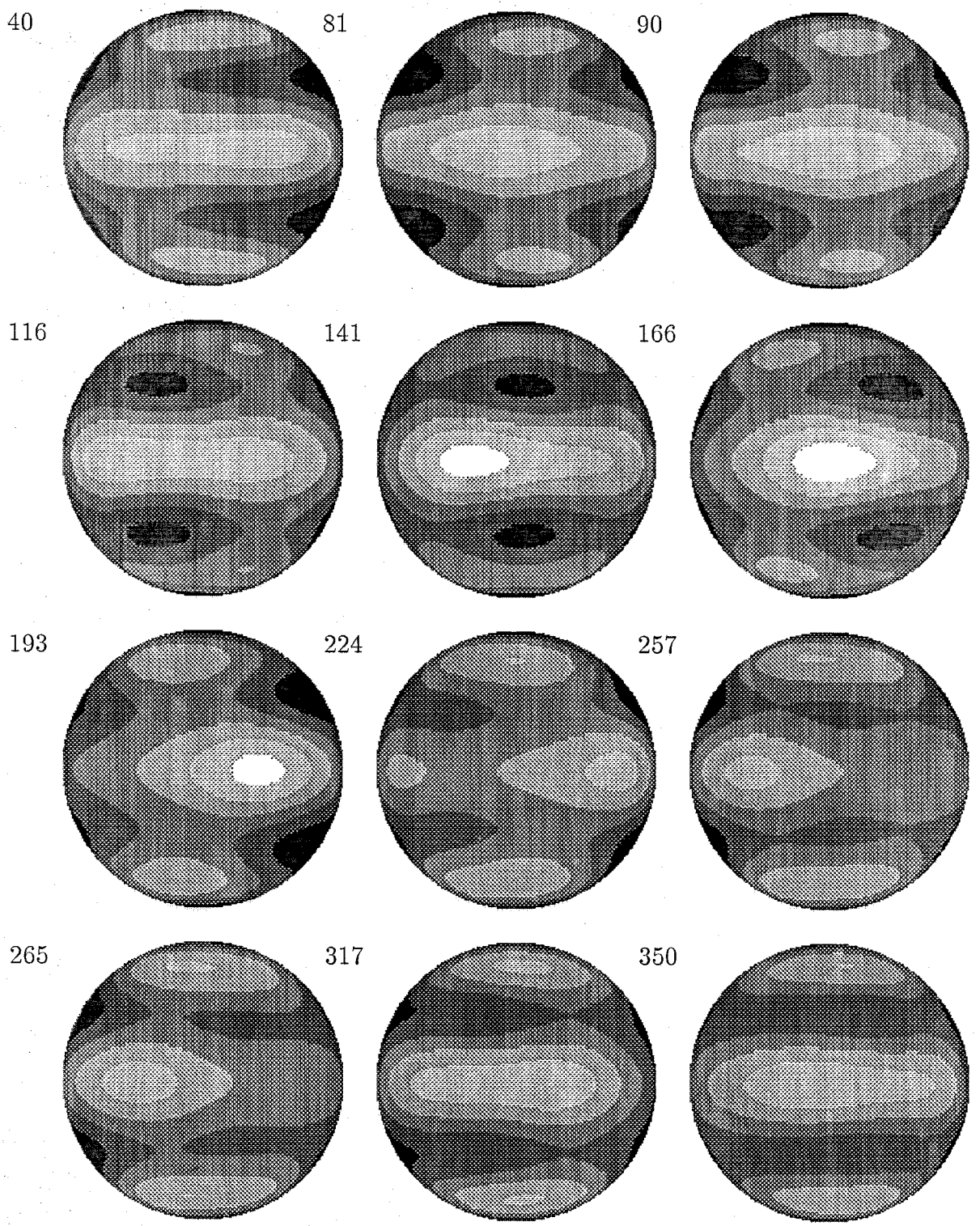

Figure 6.6: Ganymede SC images. Radar reflectivity of the target's projected disk on a linear scale quantized to six gray levels. Numbers above and to left are rotational phase of image.

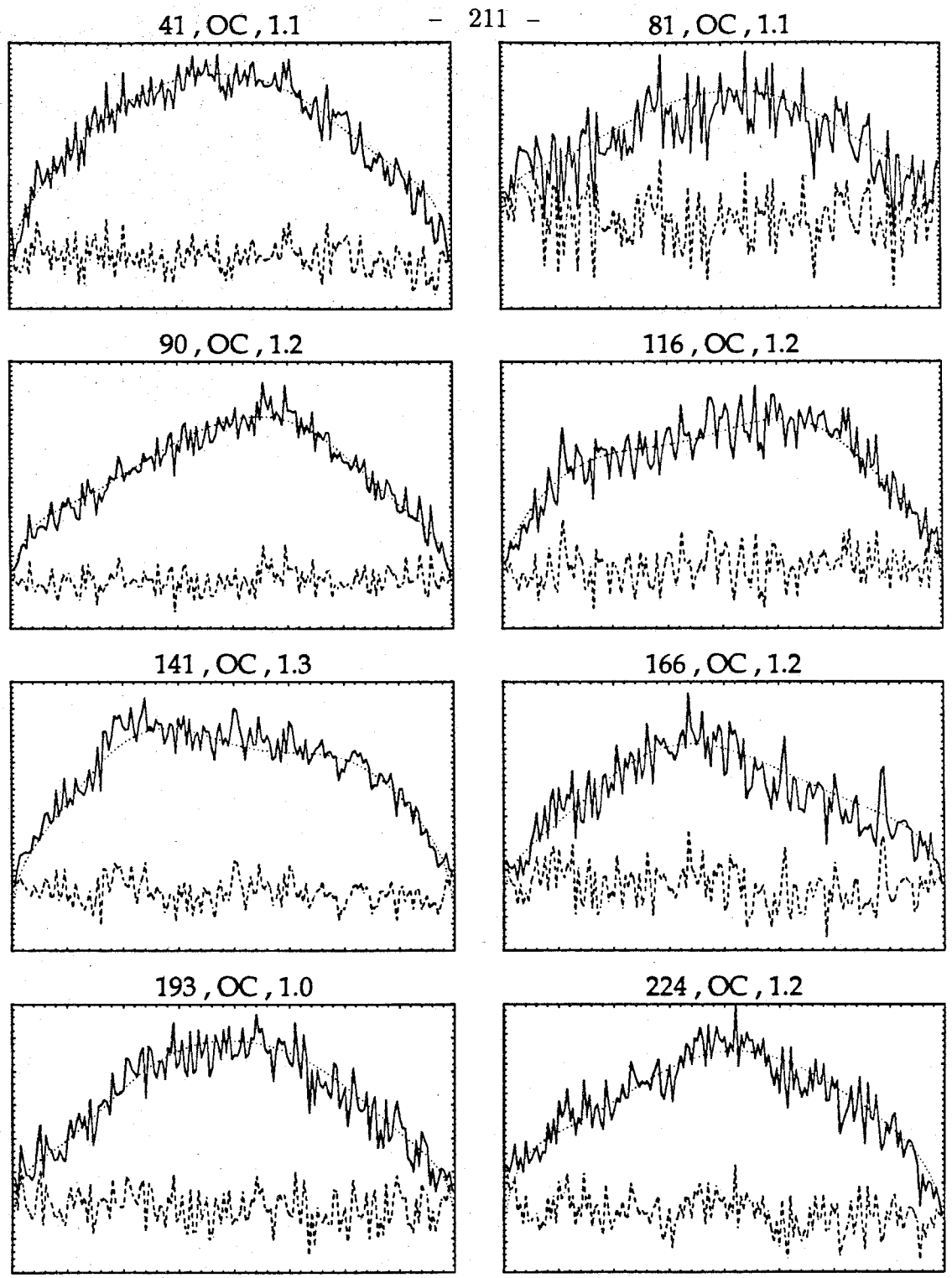

Figure 6.7: Ganymede OC spectra. Solid curves are observed spectra, dotted curves are modeled spectra, and dashed curves are residuals. Labels give rotational phase, polarization, and rms residual in units of noise standard deviations.

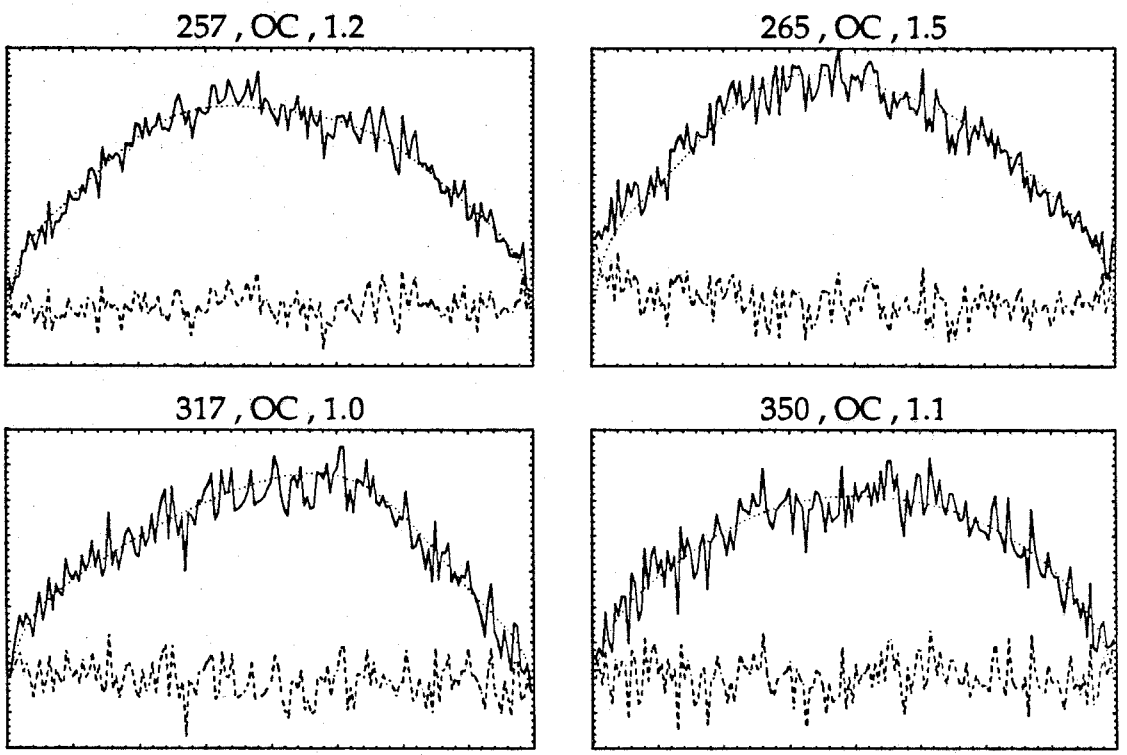

Figure 6.8: Ganymede OC spectra. Solid curves are observed spectra, dotted curves are modeled spectra, and dashed curves are residuals. Labels give rotational phase, polarization, and rms residual in units of noise standard deviations.

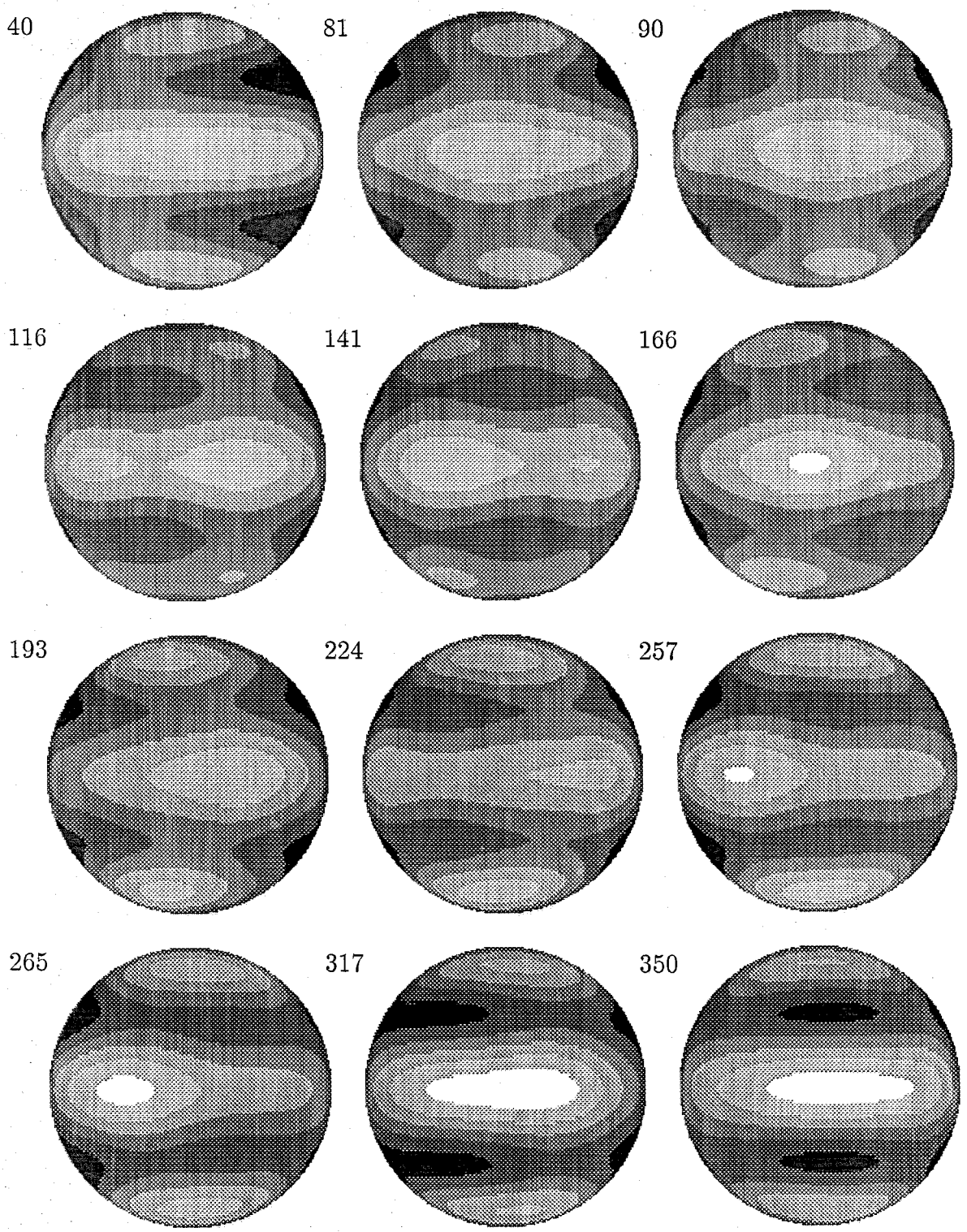

Figure 6.9: Ganymede OC images. Radar reflectivity of the target's projected disk on a linear scale quantized to six gray levels. Numbers above and to left are rotational phase of image.

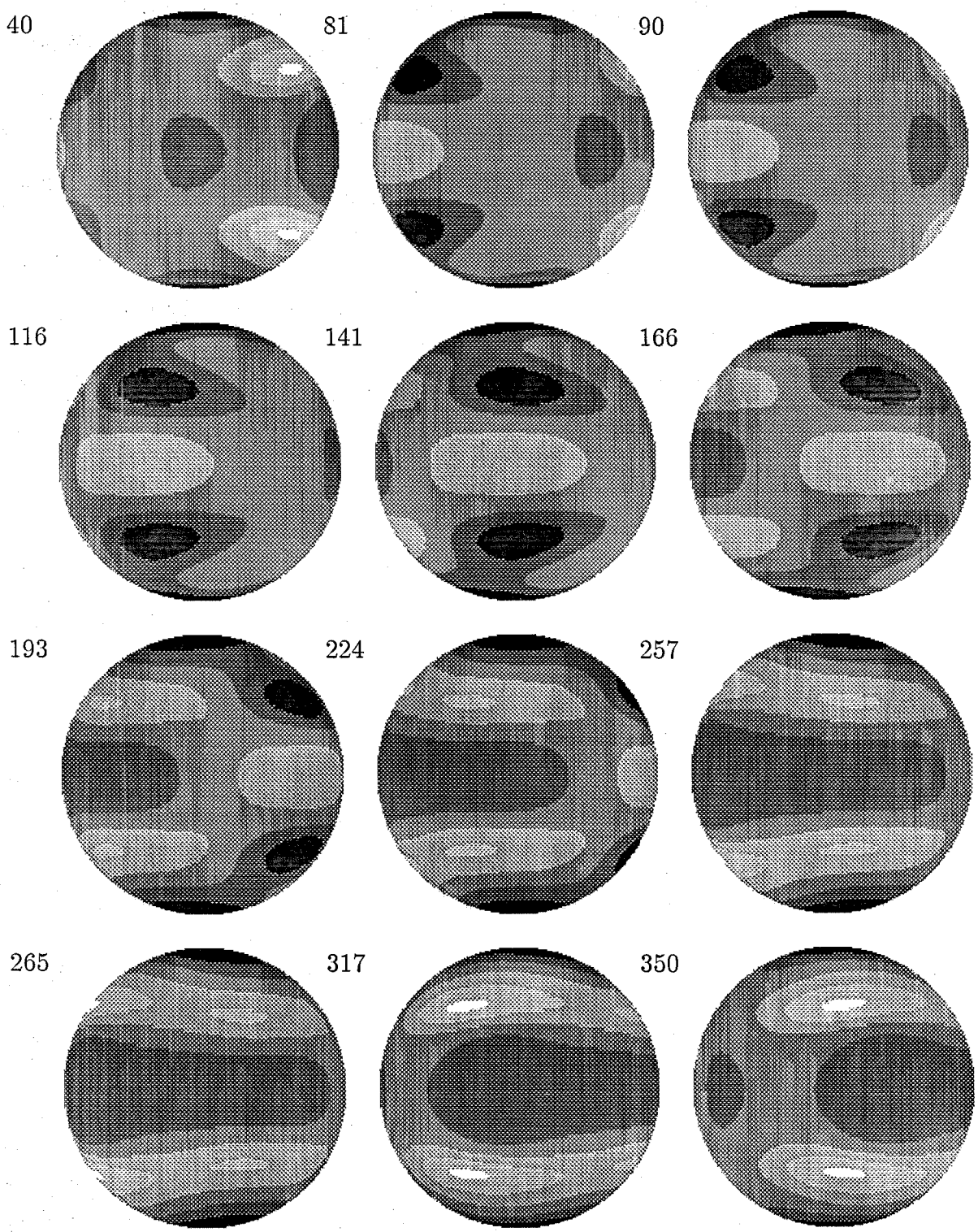

Figure 6.10: Ganymede polarization ratio images. Numbers above and to left are rotational phase of image.

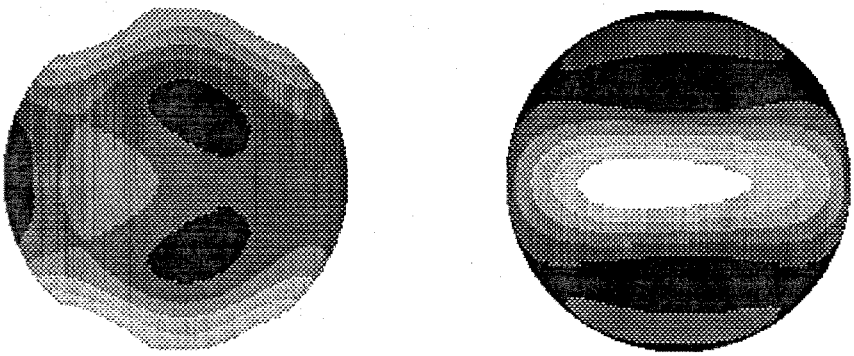

Figure 6.11: Sensitivity of Ganymede 141° SC image to scattering law exponent used in Doppler-radar imaging algorithm. Left image was made using $n = 1.0$, right image using $n = 2.0$.

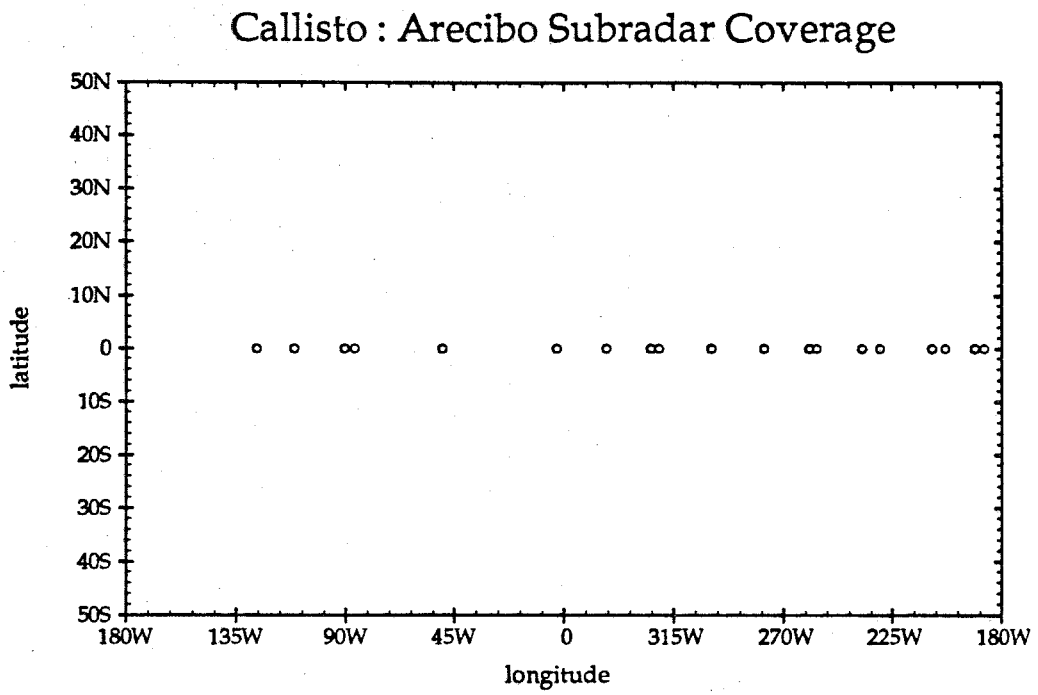

Figure 6.12: Subradar points on Callisto corresponding to Arecibo OC and SC Doppler spectra.

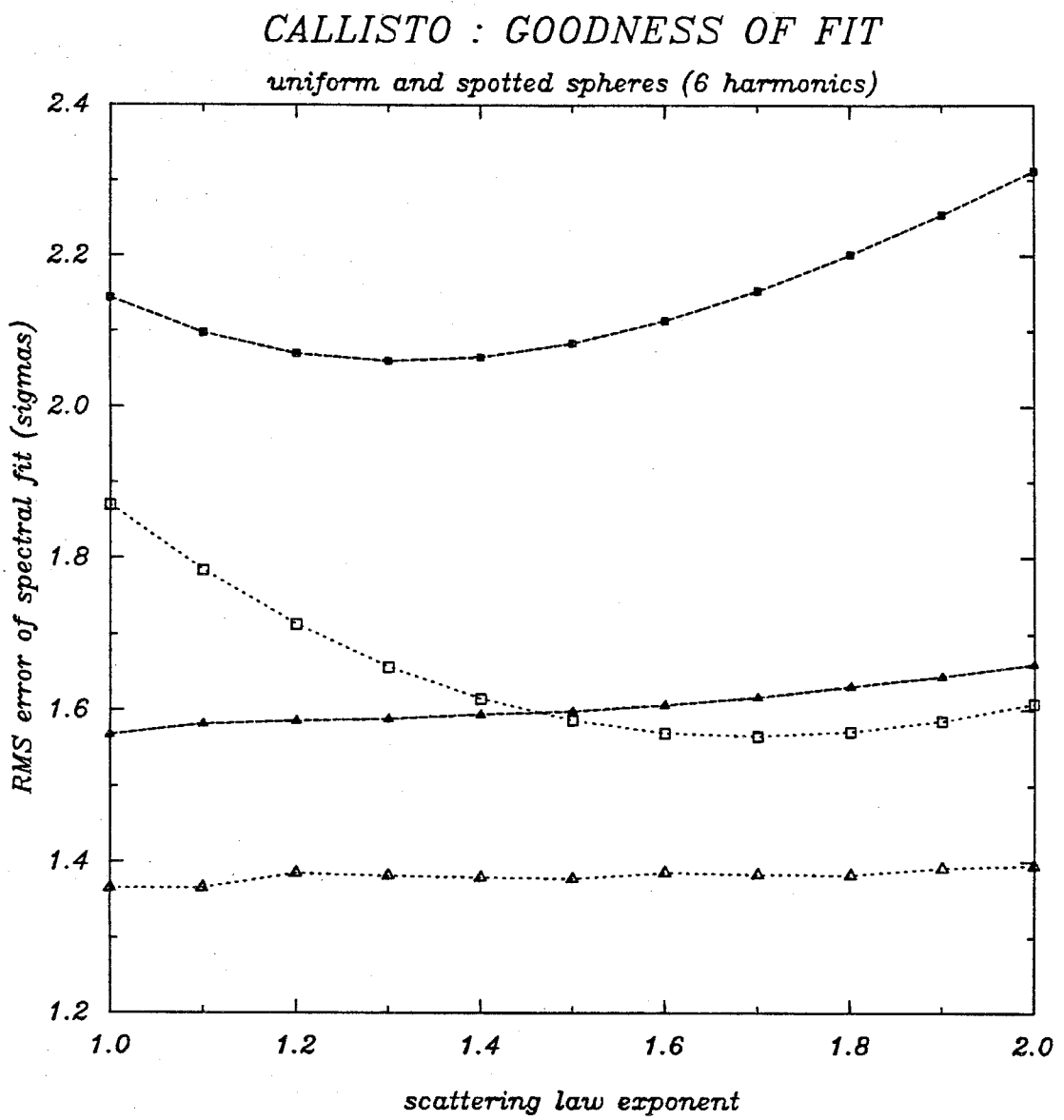

Figure 6.13: Errors in fits to Callisto spectra. Open symbols are OC errors, solid symbols are SC errors. Squares correspond to uniform sphere models, triangles to sixth-degree models.

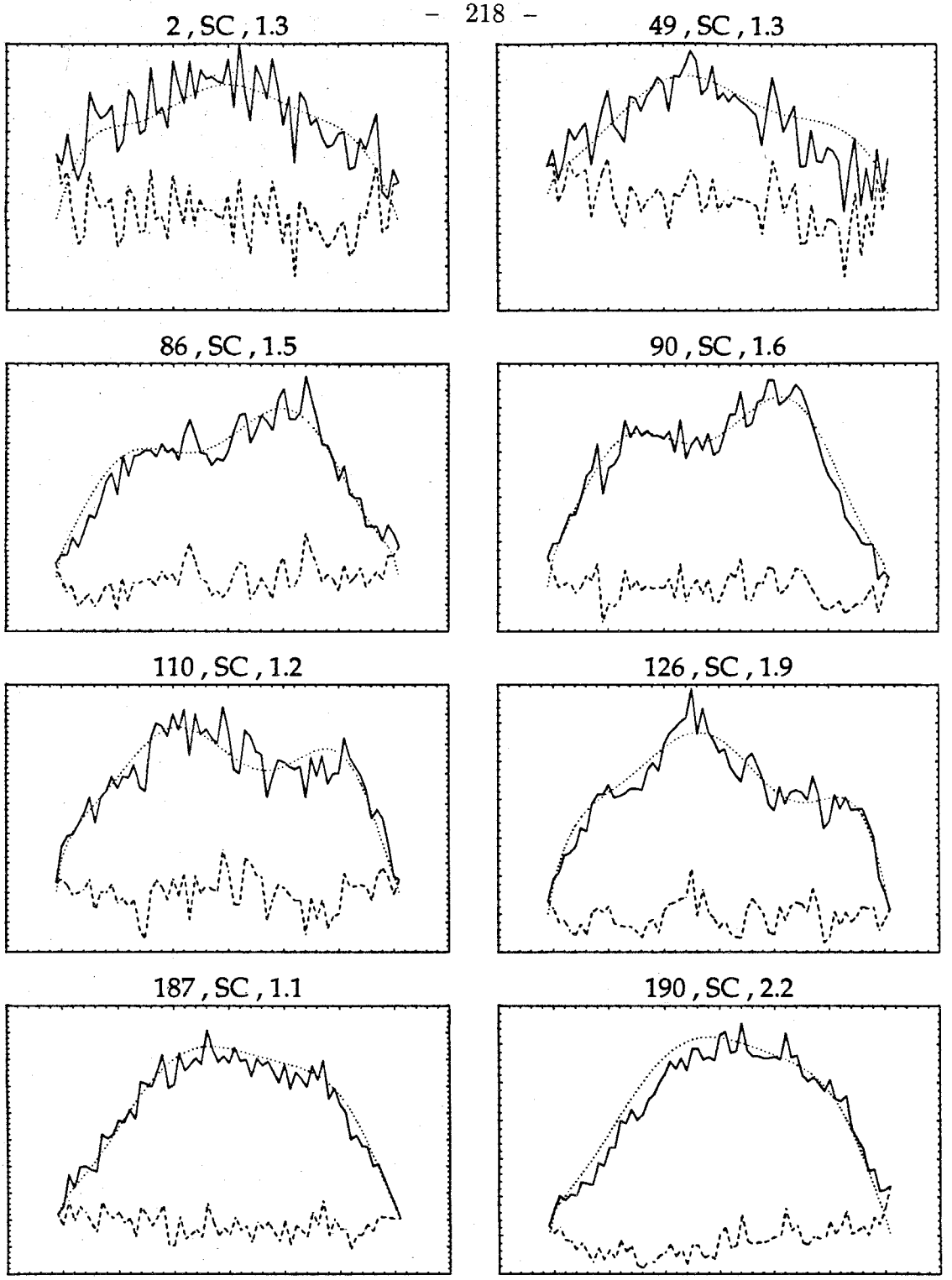

Figure 6.14: Callisto SC spectra. Solid curves are observed spectra, dotted curves are modeled spectra, and dashed curves are residuals. Labels give rotational phase, polarization, and rms residual in units of noise standard deviations.

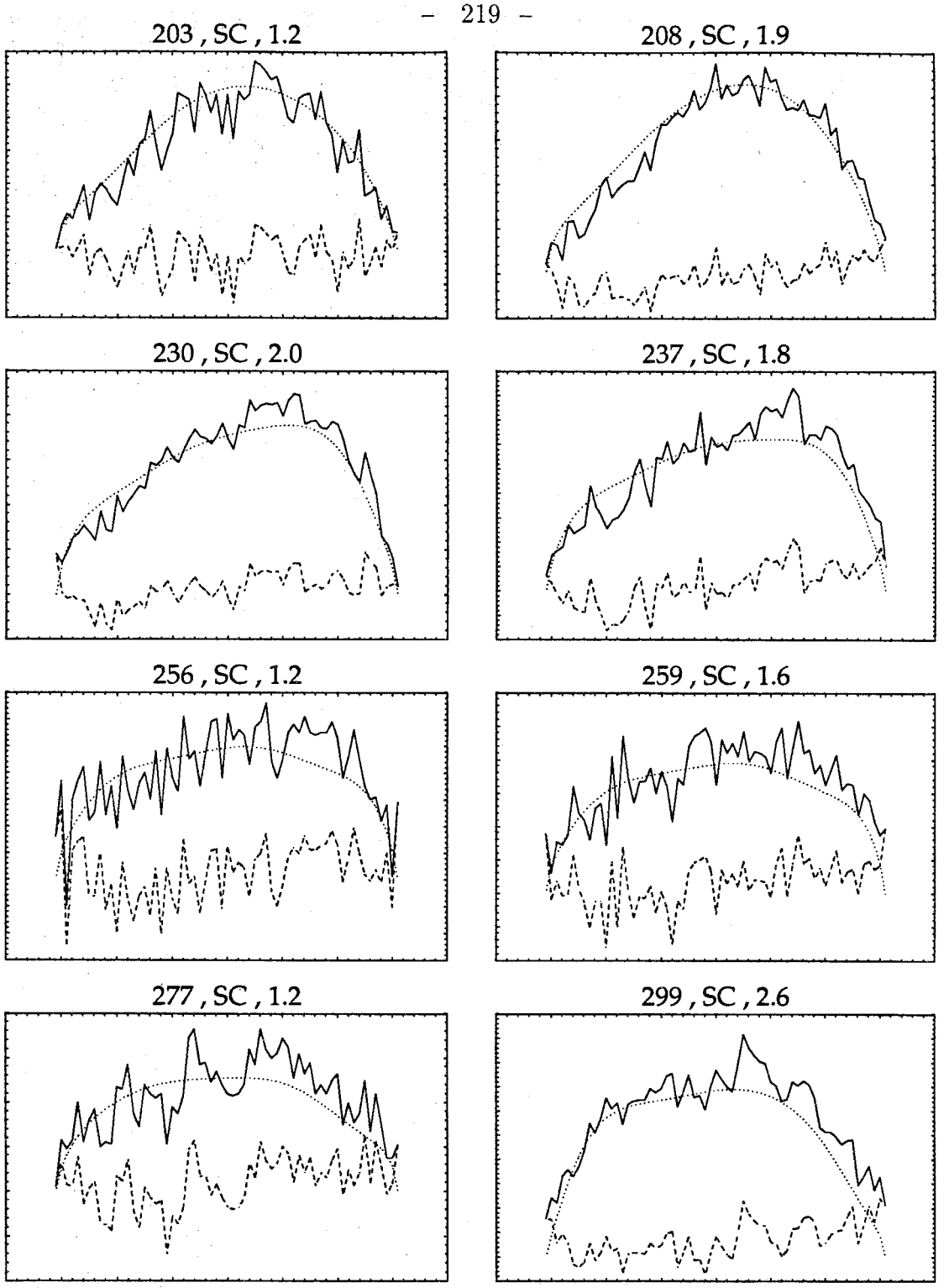

Figure 6.15: Callisto SC spectra. Solid curves are observed spectra, dotted curves are modeled spectra, and dashed curves are residuals. Labels give rotational phase, polarization, and rms residual in units of noise standard deviations.

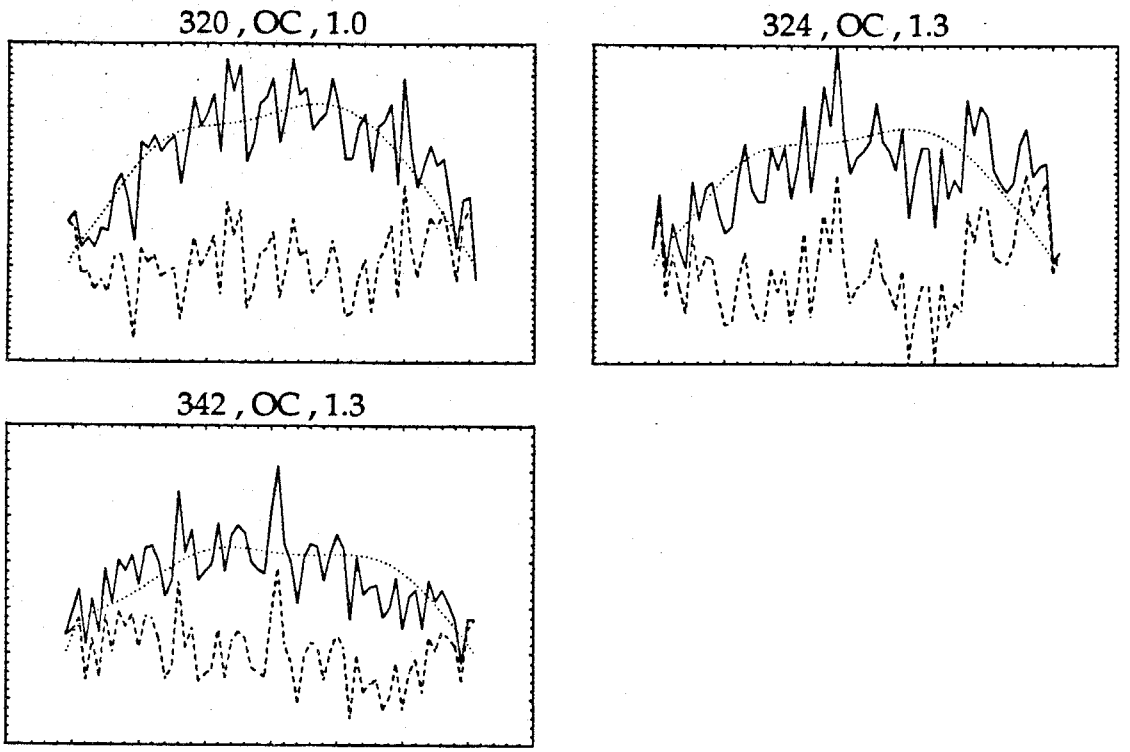

Figure 6.16: Callisto SC spectra. Solid curves are observed spectra, dotted curves are modeled spectra, and dashed curves are residuals. Labels give rotational phase, polarization, and rms residual in units of noise standard deviations.

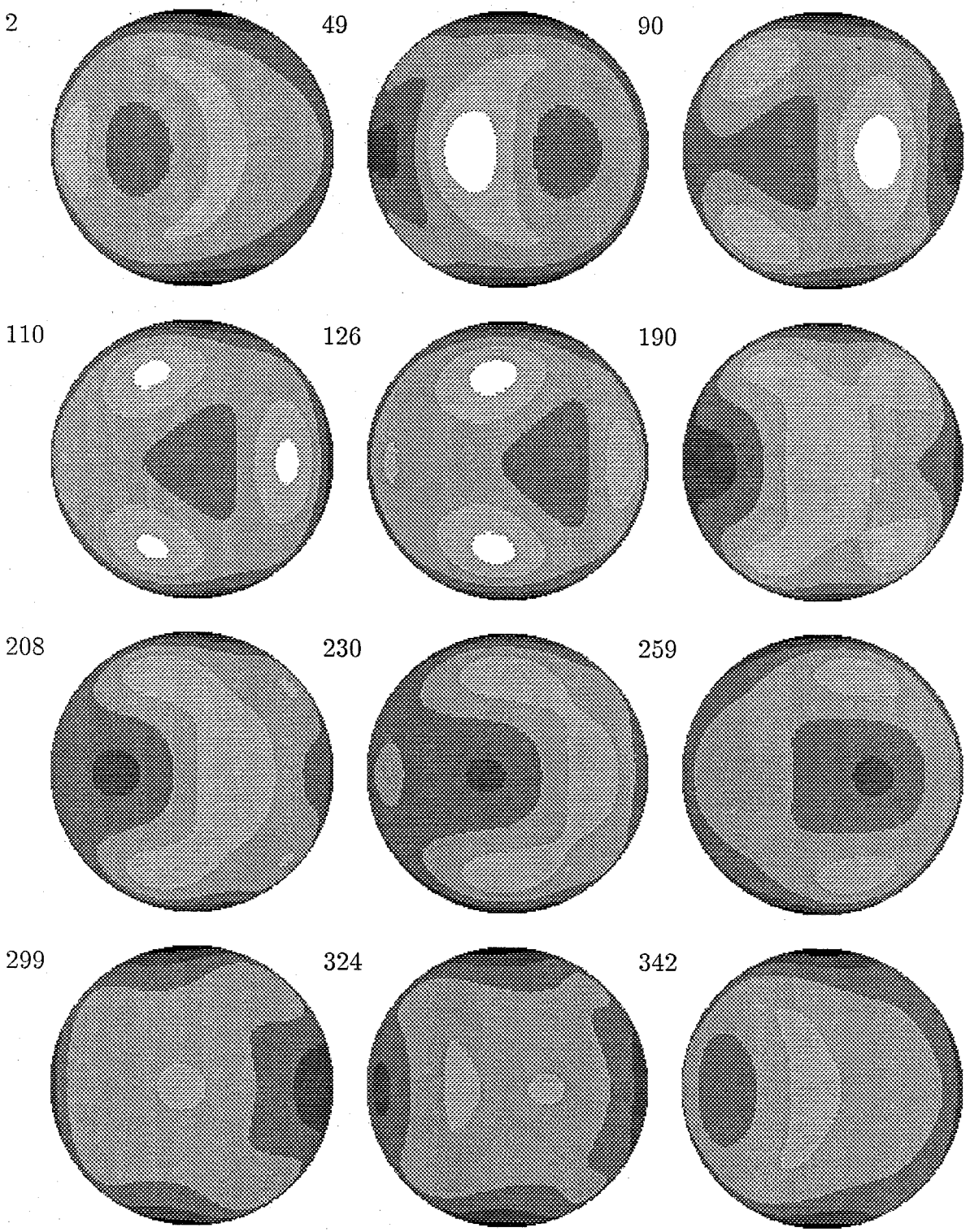

Figure 6.17: Callisto SC images. Radar reflectivity of the target's projected disk on a linear scale quantized to six gray levels. Numbers above and to left are rotational phase of image.

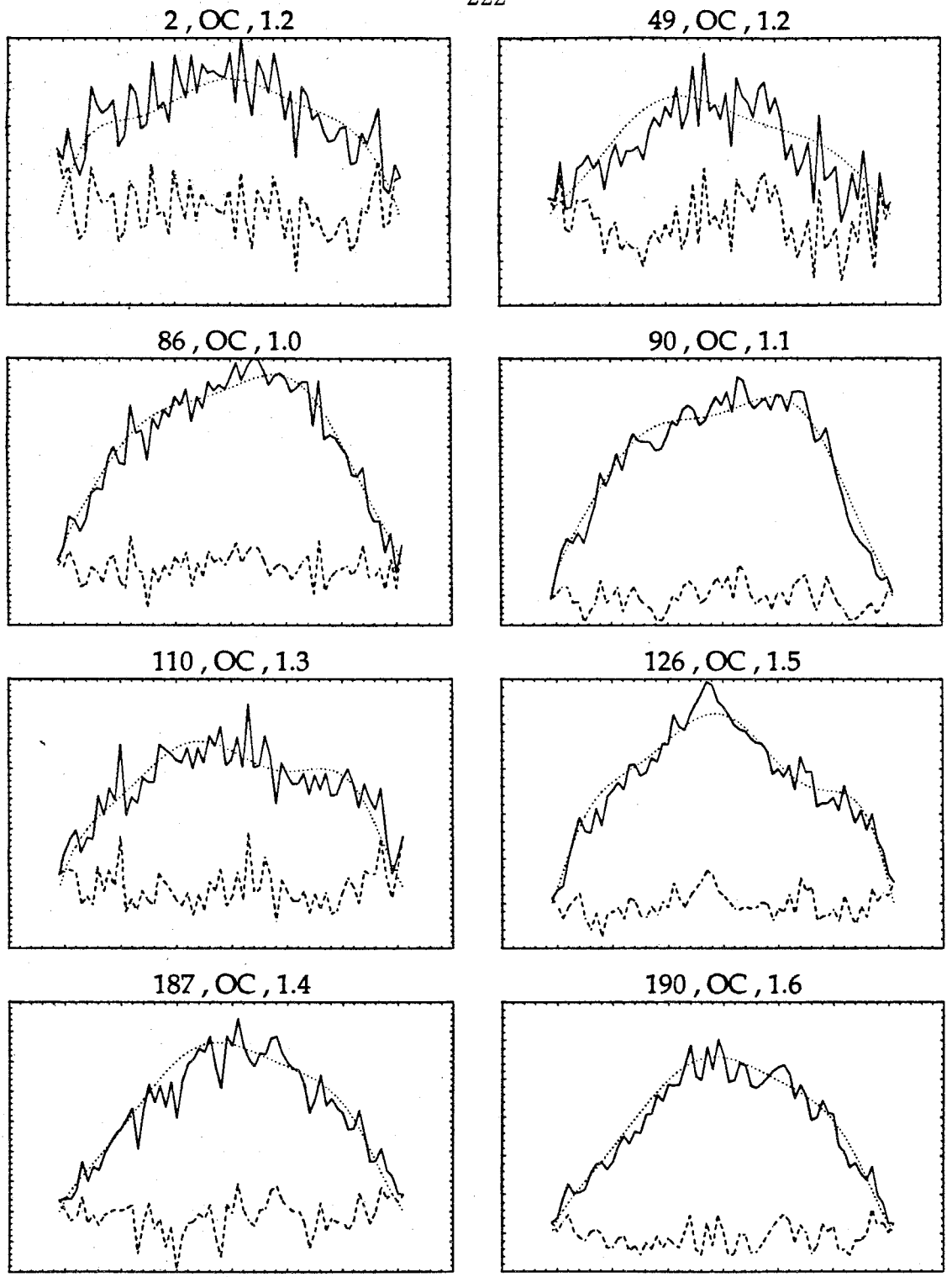

Figure 6.18: Callisto OC spectra. Solid curves are observed spectra, dotted curves are modeled spectra, and dashed curves are residuals. Labels give rotational phase, polarization, and rms residual in units of noise standard deviations.

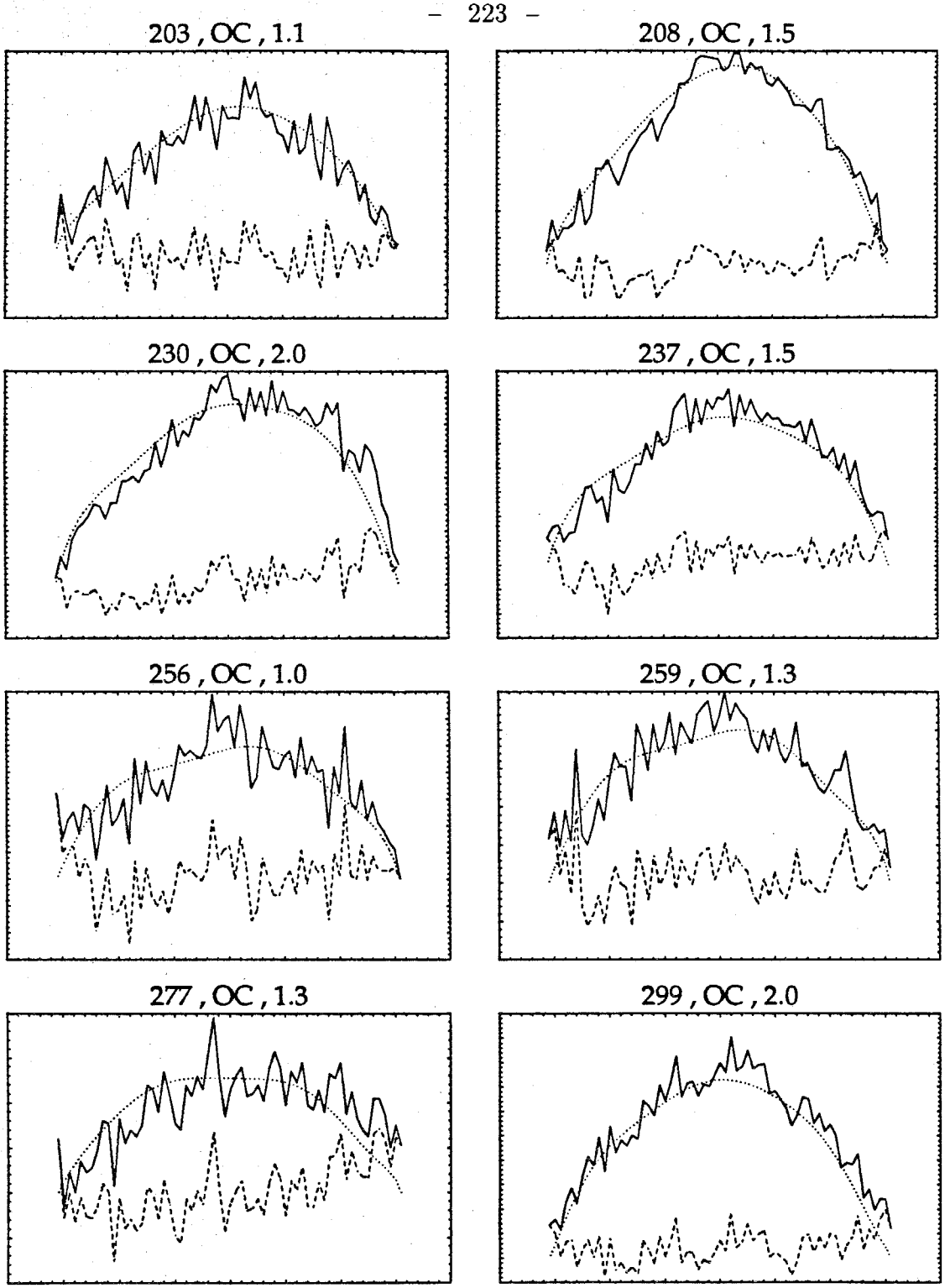

Figure 6.19: Callisto OC spectra. Solid curves are observed spectra, dotted curves are modeled spectra, and dashed curves are residuals. Labels give rotational phase, polarization, and rms residual in units of noise standard deviations.

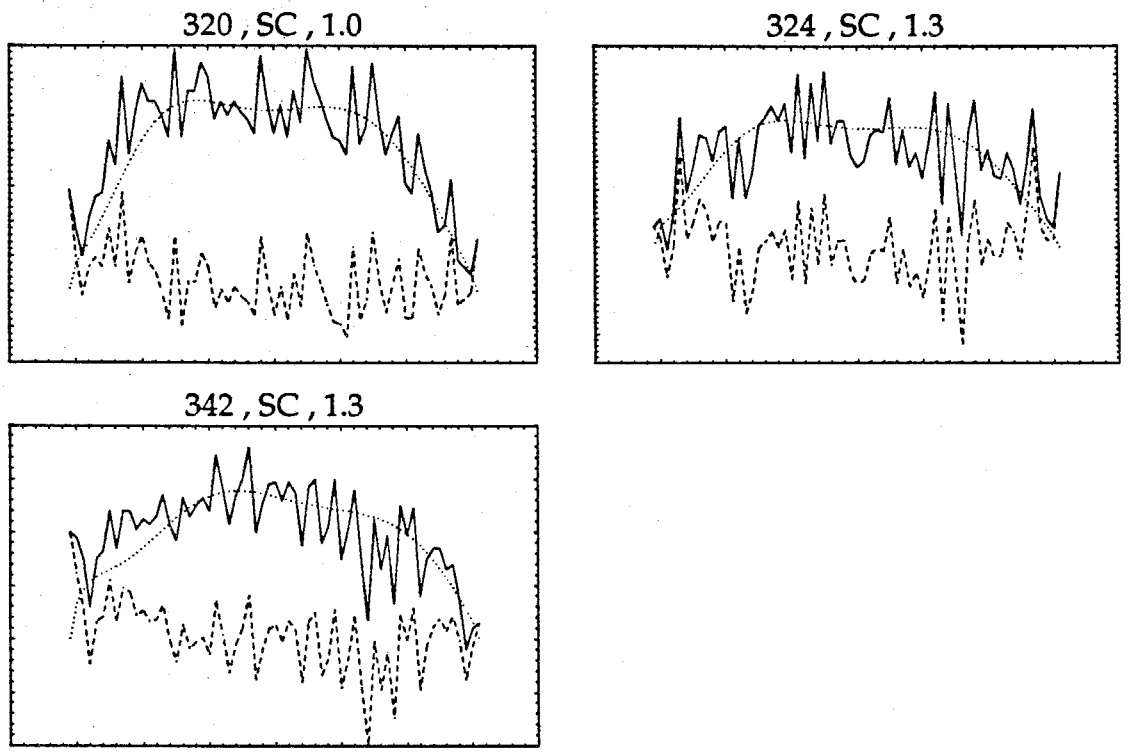

Figure 6.20: Callisto OC spectra. Solid curves are observed spectra, dotted curves are modeled spectra, and dashed curves are residuals. Labels give rotational phase, polarization, and rms residual in units of noise standard deviations.

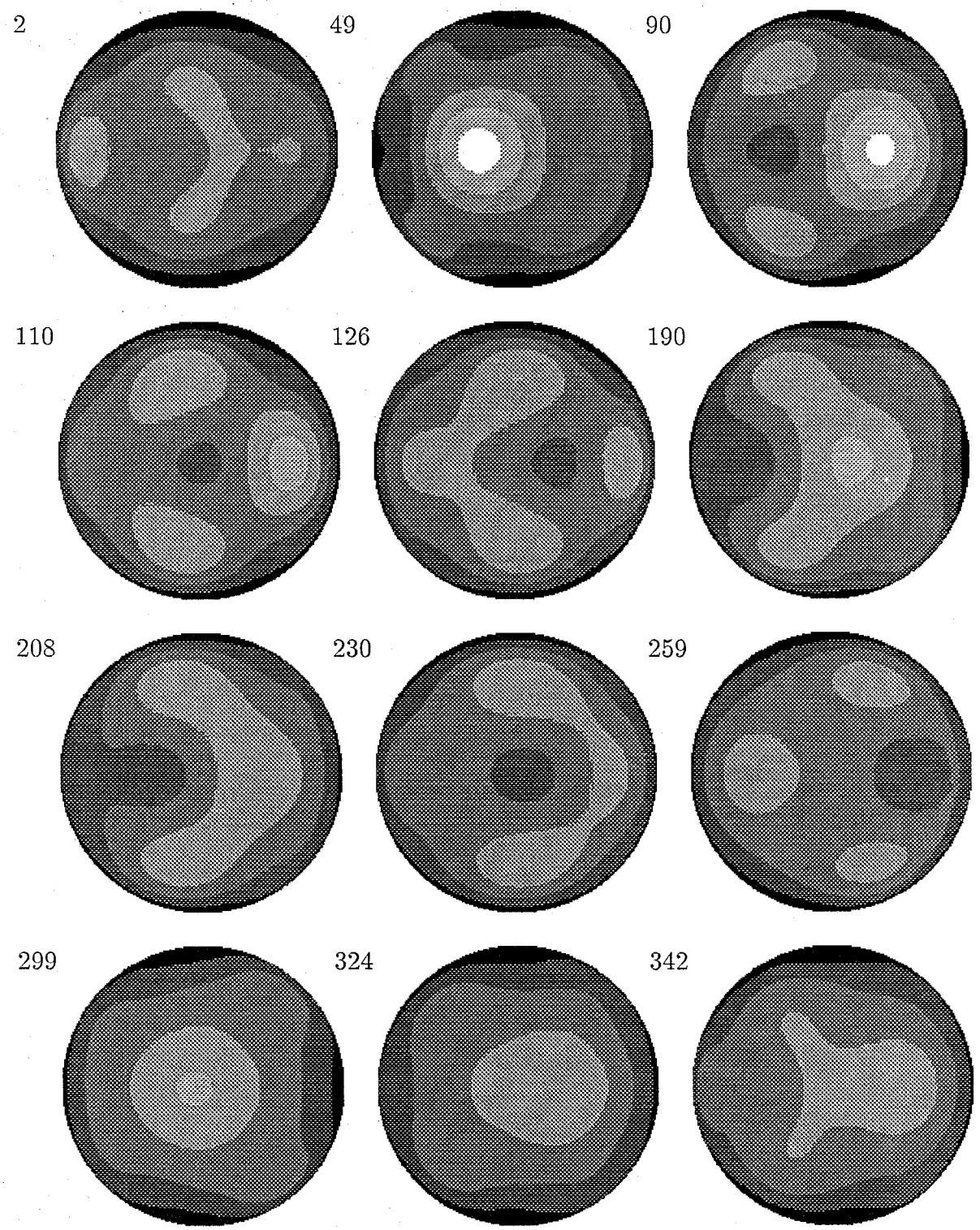

Figure 6.21: Callisto OC images. Radar reflectivity of the target's projected disk on a linear scale quantized to six gray levels. Numbers above and to left are rotational phase of image.

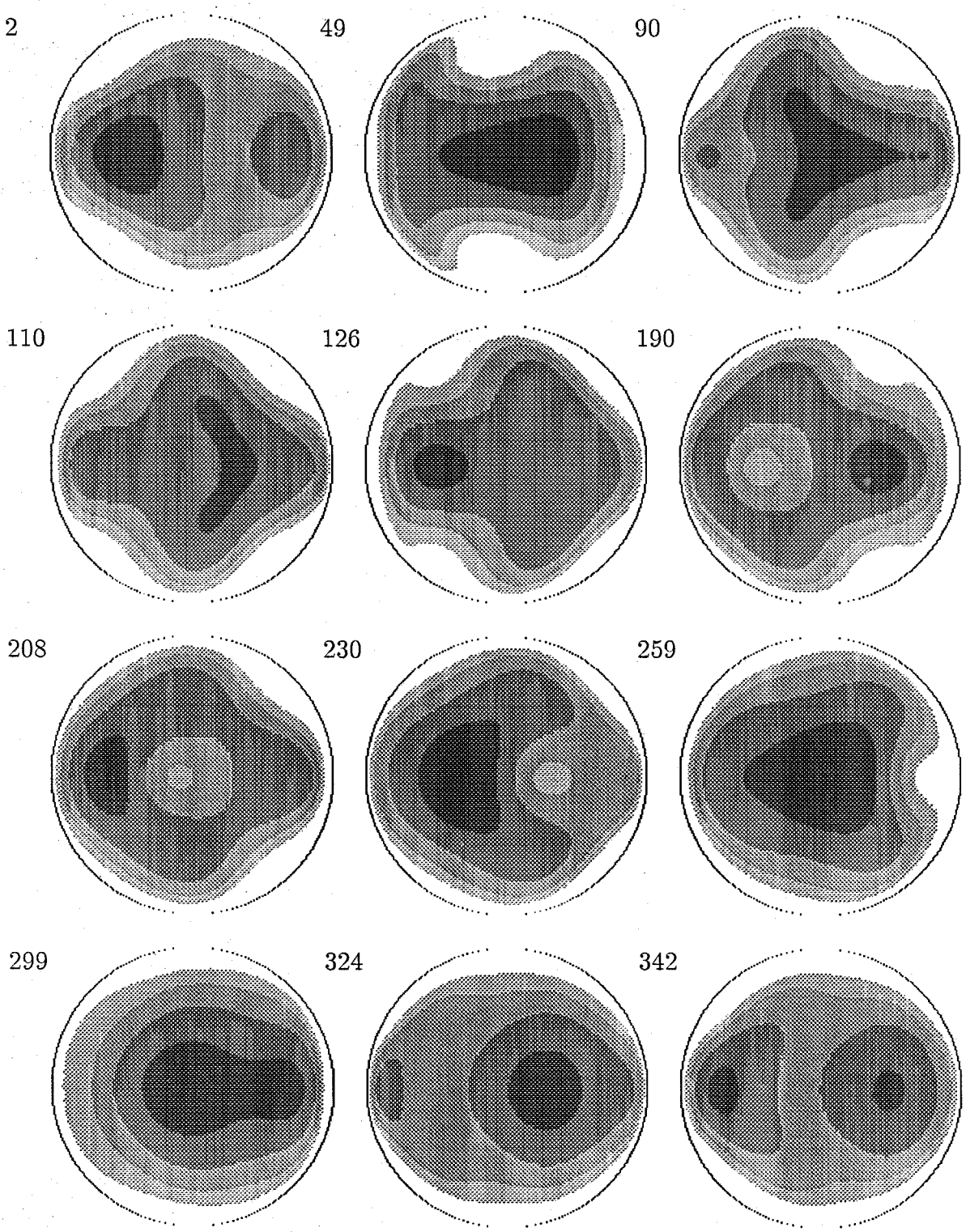

Figure 6.22: Callisto polarization ratio images. Numbers above and to left are rotational phase of image.

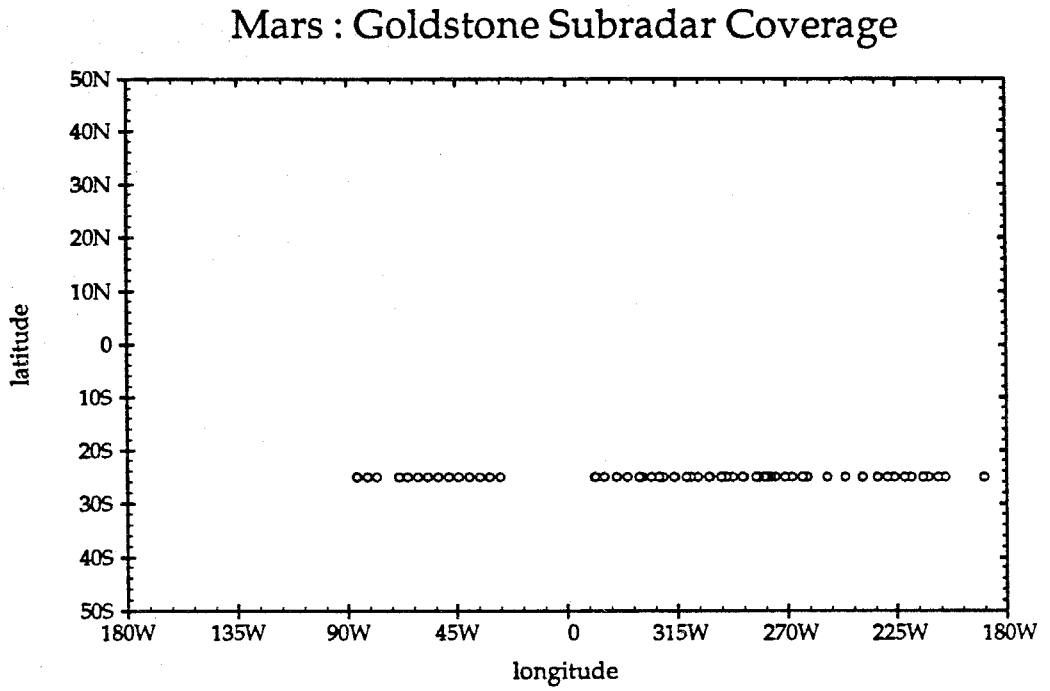

Figure 6.23: Goldstone subradar points on Mars.

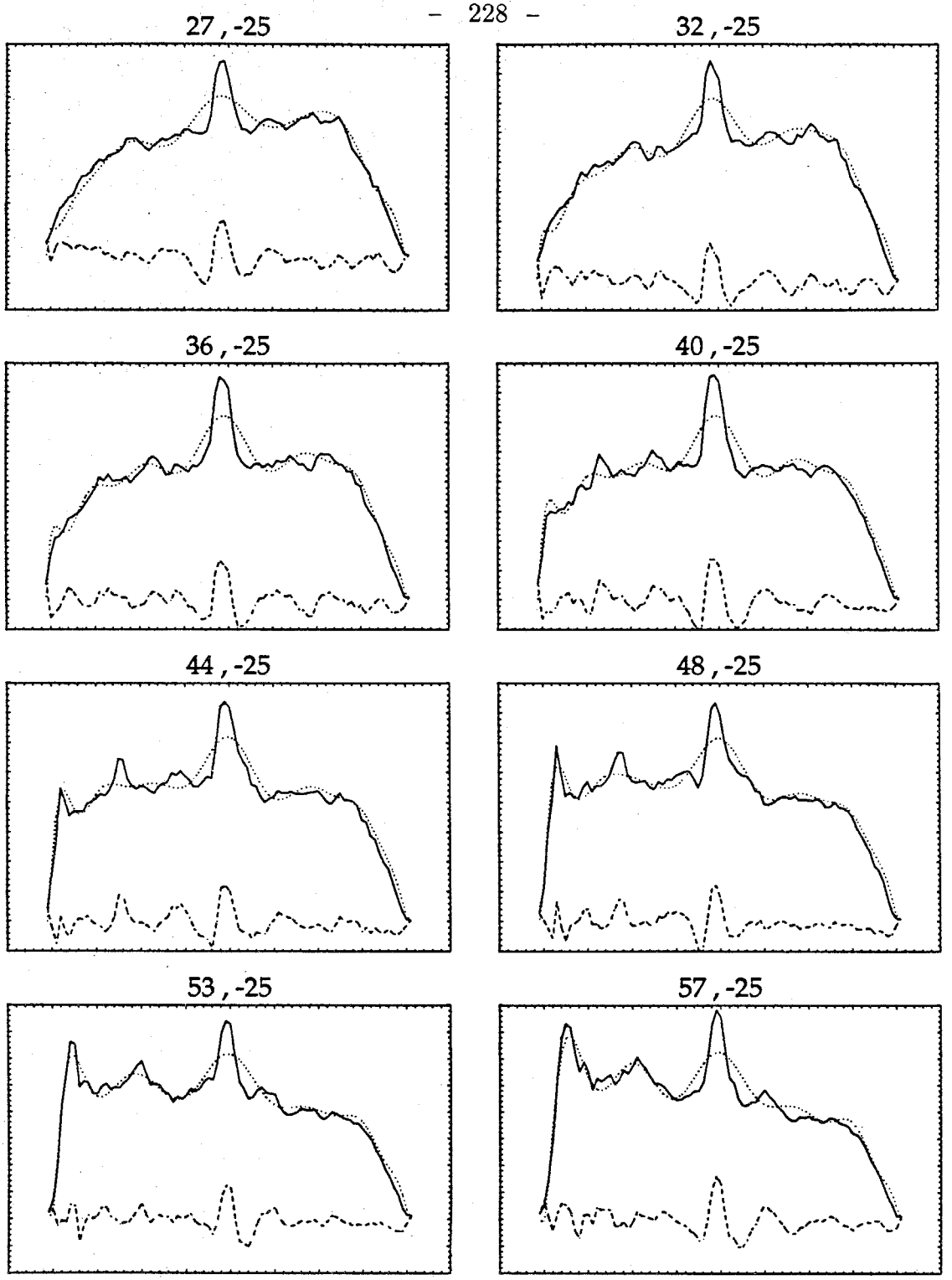

Figure 6.24: Mars Goldstone SC spectra labeled by subradar longitude (rotational phase) and subradar latitude. Solid curves are observed spectra, dotted curves are modeled spectra, and dashed curves are residuals.

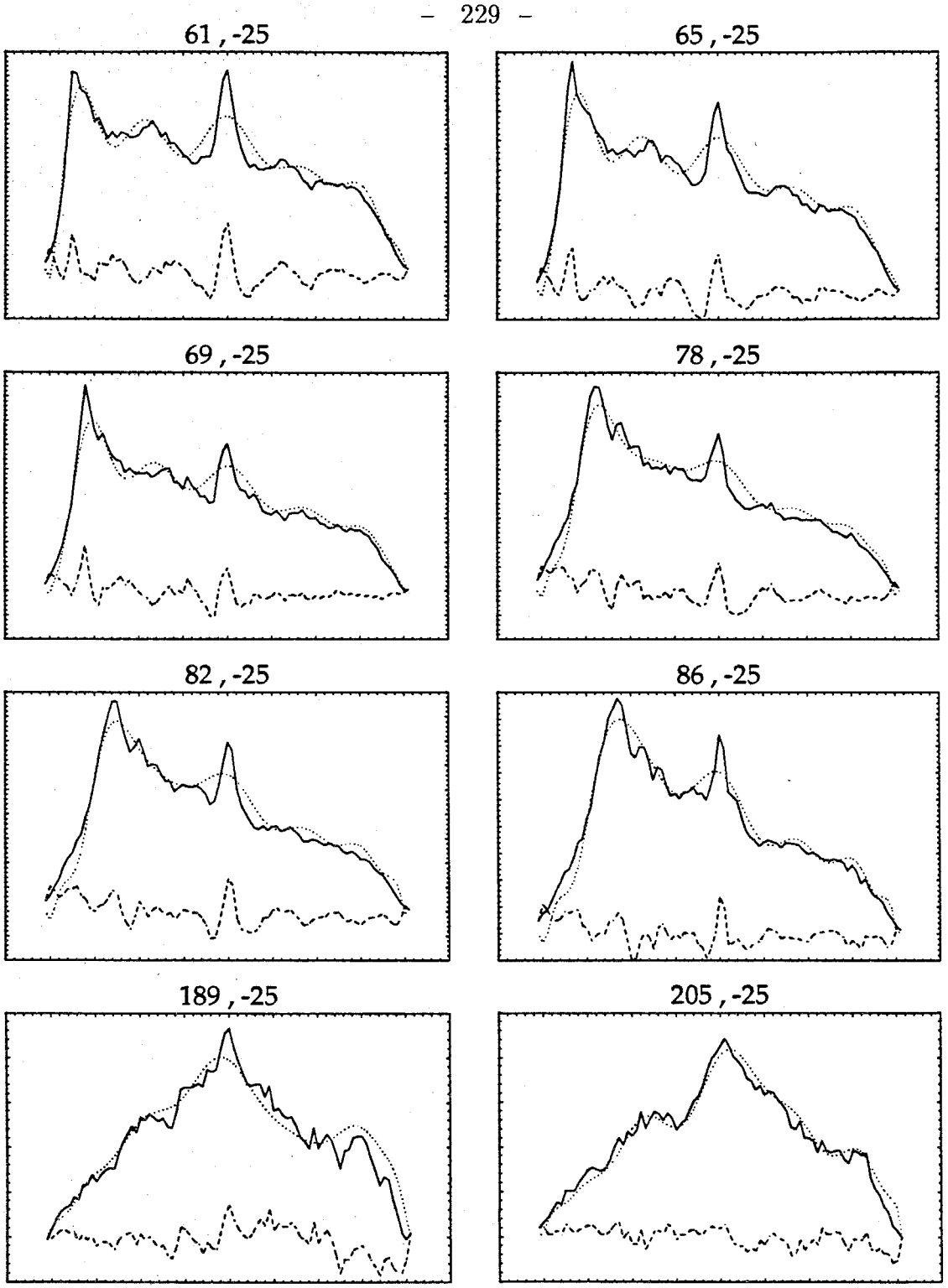

Figure 6.25: Mars Goldstone SC spectra labeled by subradar longitude (rotational phase) and subradar latitude. Solid curves are observed spectra, dotted curves are modeled spectra, and dashed curves are residuals.

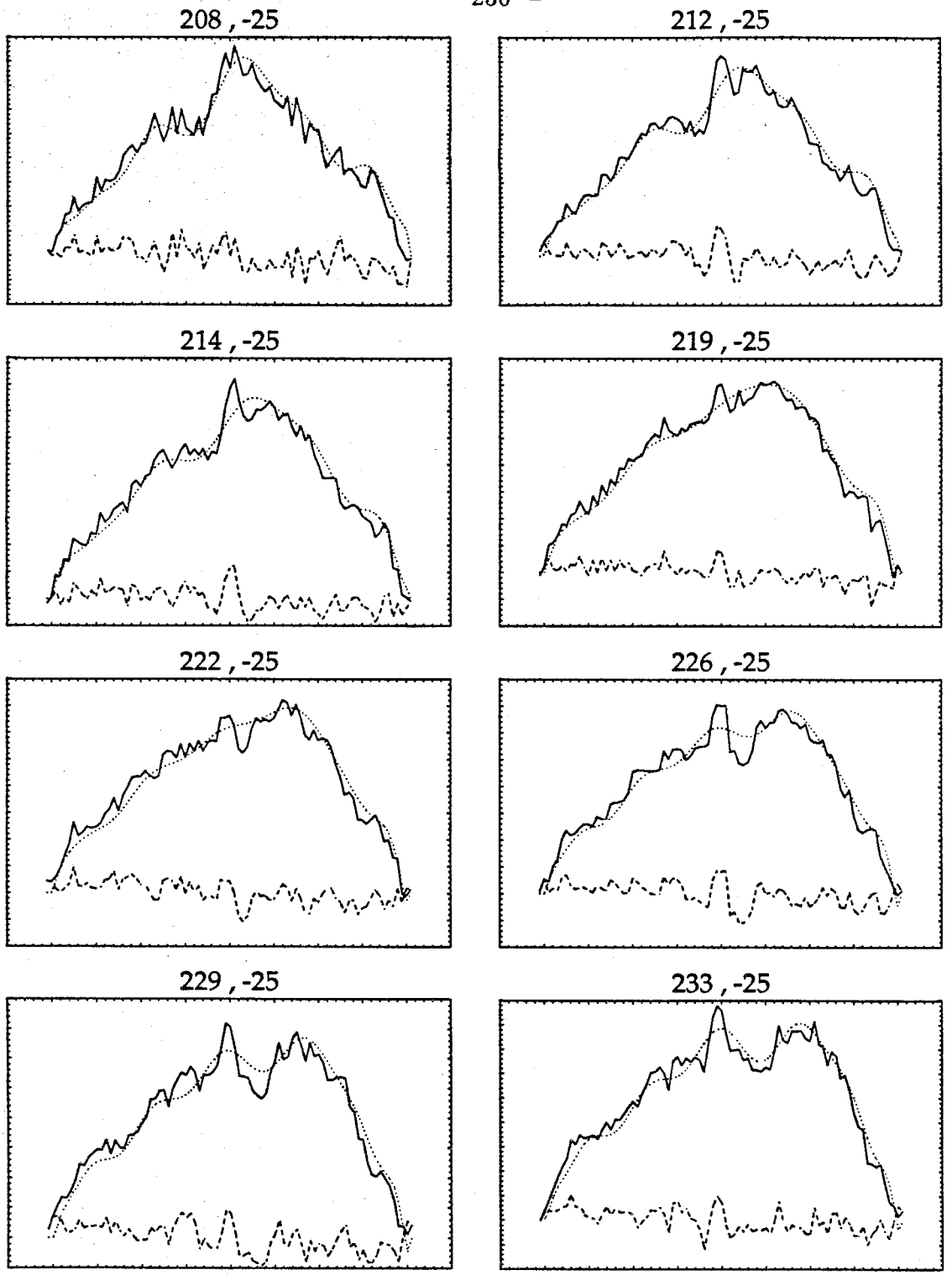

Figure 6.26: Mars Goldstone SC spectra labeled by subradar longitude (rotational phase) and subradar latitude. Solid curves are observed spectra, dotted curves are modeled spectra, and dashed curves are residuals.

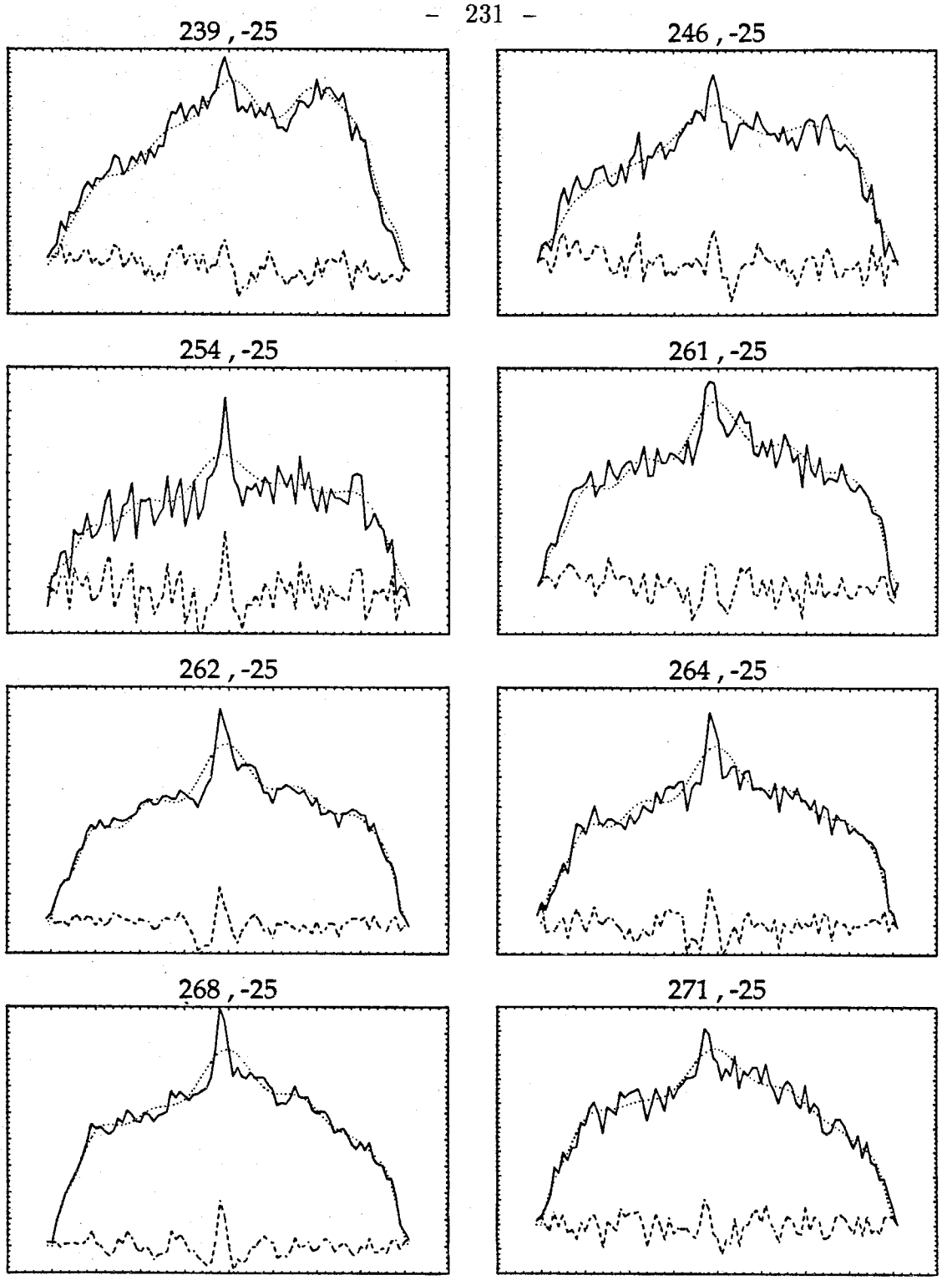

Figure 6.27: Mars Goldstone SC spectra labeled by subradar longitude (rotational phase) and subradar latitude. Solid curves are observed spectra, dotted curves are modeled spectra, and dashed curves are residuals.

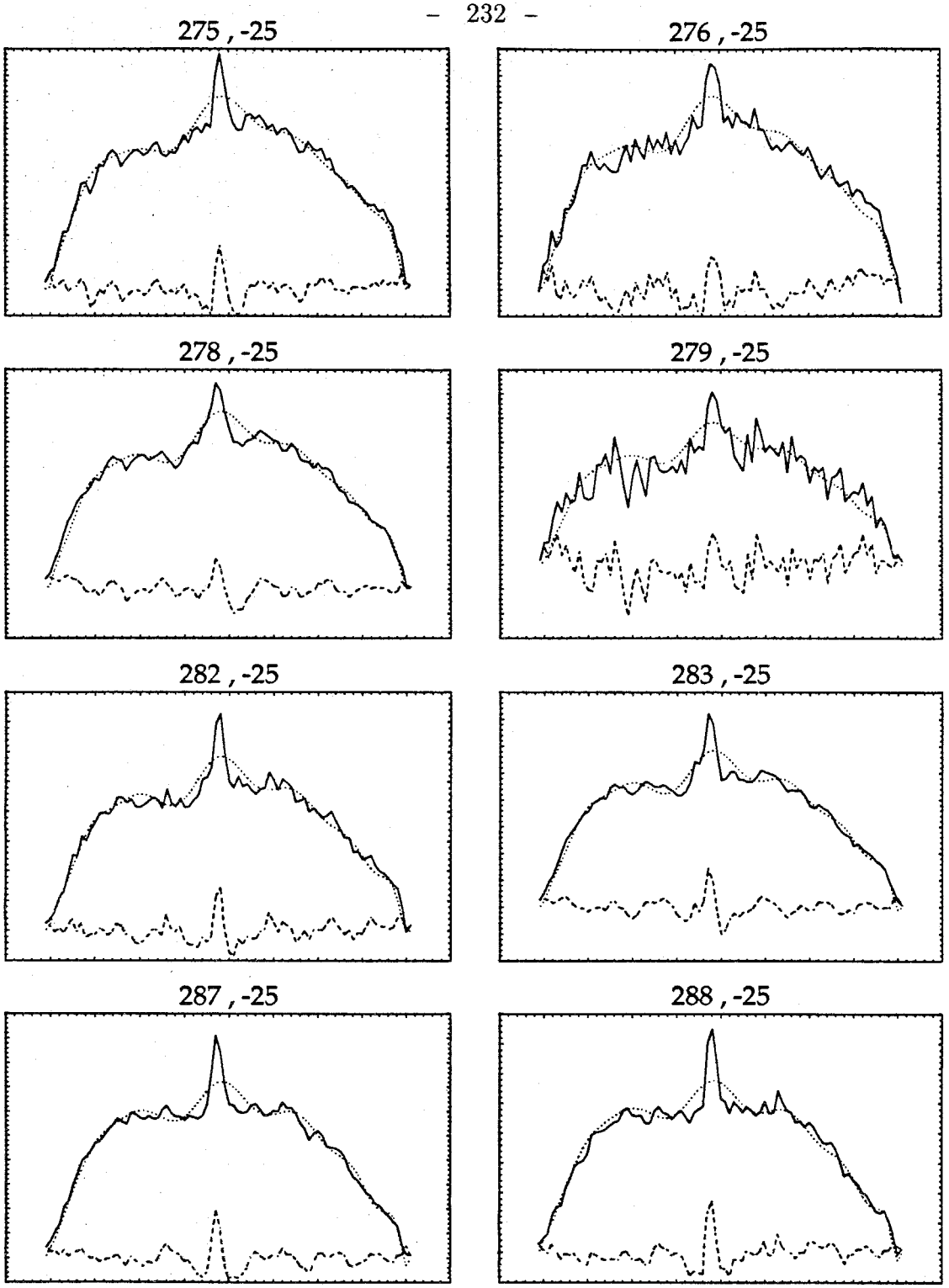

Figure 6.28: Mars Goldstone SC spectra labeled by subradar longitude (rotational phase) and subradar latitude. Solid curves are observed spectra, dotted curves are modeled spectra, and dashed curves are residuals.

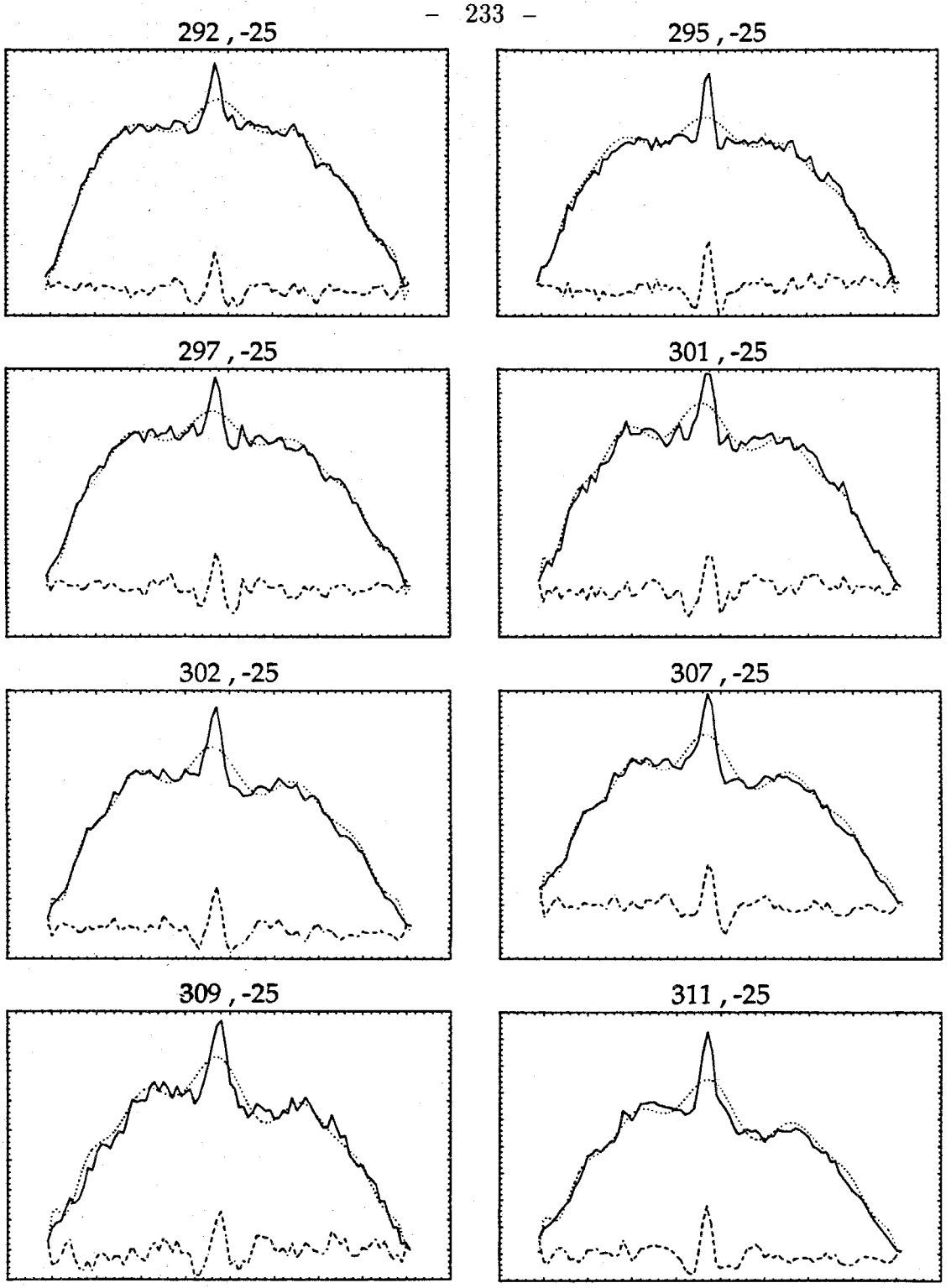

Figure 6.29: Mars Goldstone SC spectra labeled by subradar longitude (rotational phase) and subradar latitude. Solid curves are observed spectra, dotted curves are modeled spectra, and dashed curves are residuals.

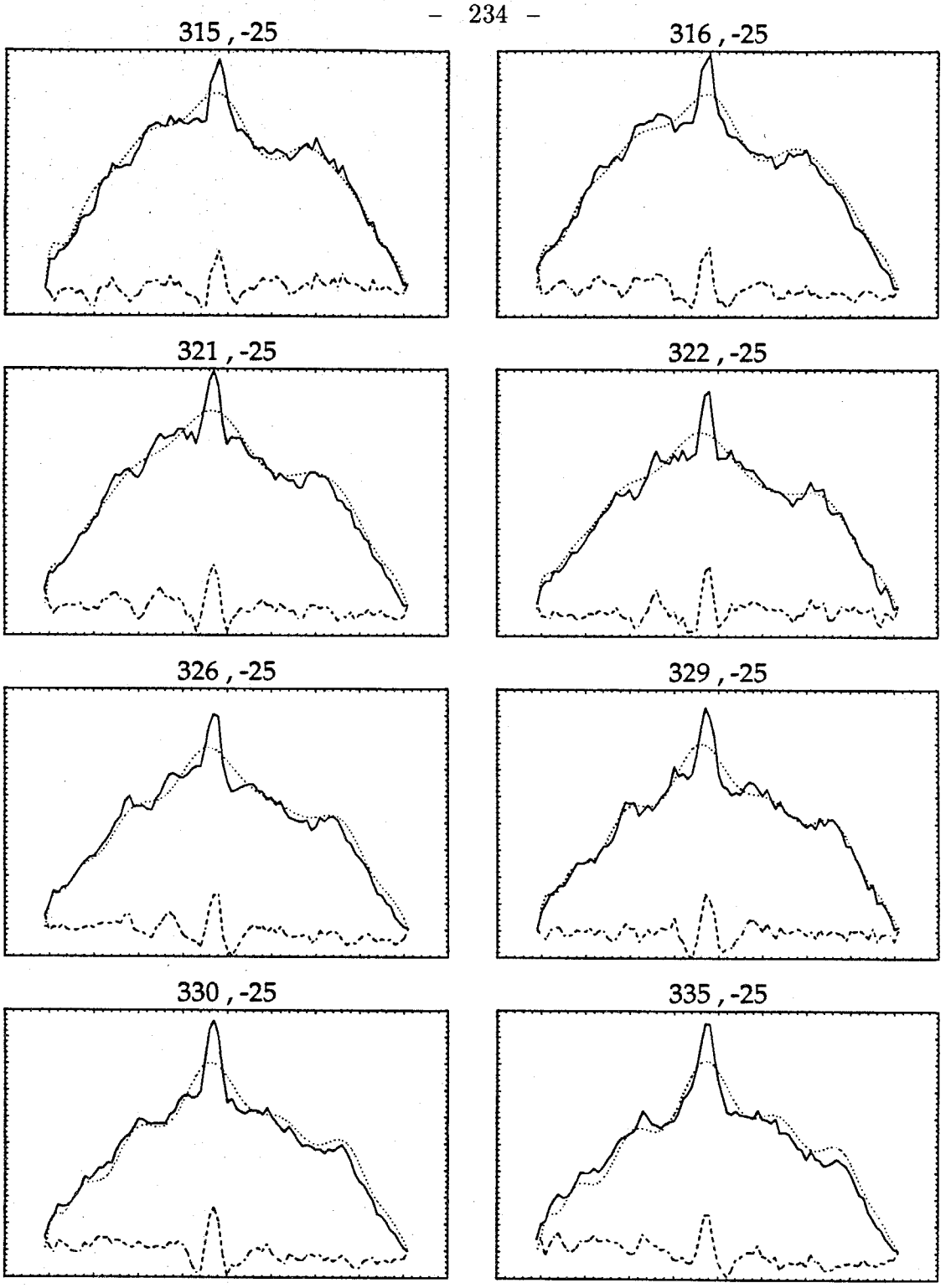

Figure 6.30: Mars Goldstone SC spectra labeled by subradar longitude (rotational phase) and subradar latitude. Solid curves are observed spectra, dotted curves are modeled spectra, and dashed curves are residuals.

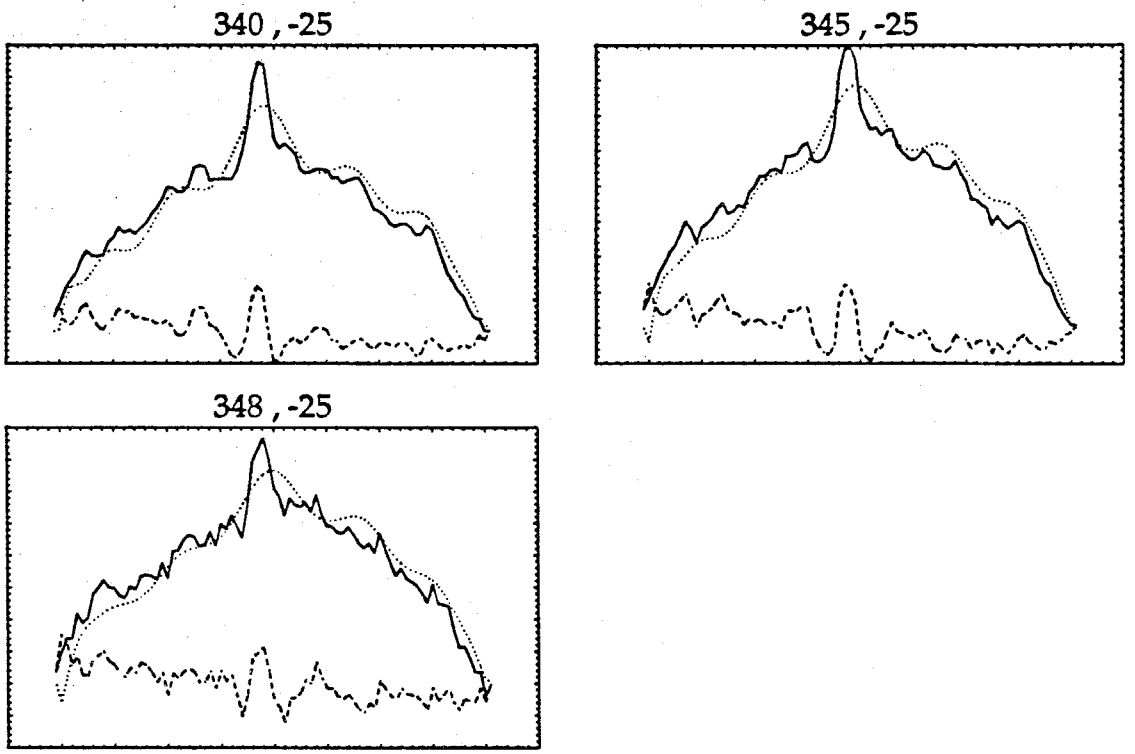

Figure 6.31: Mars Goldstone SC spectra labeled by subradar longitude (rotational phase) and subradar latitude. Solid curves are observed spectra, dotted curves are modeled spectra, and dashed curves are residuals.

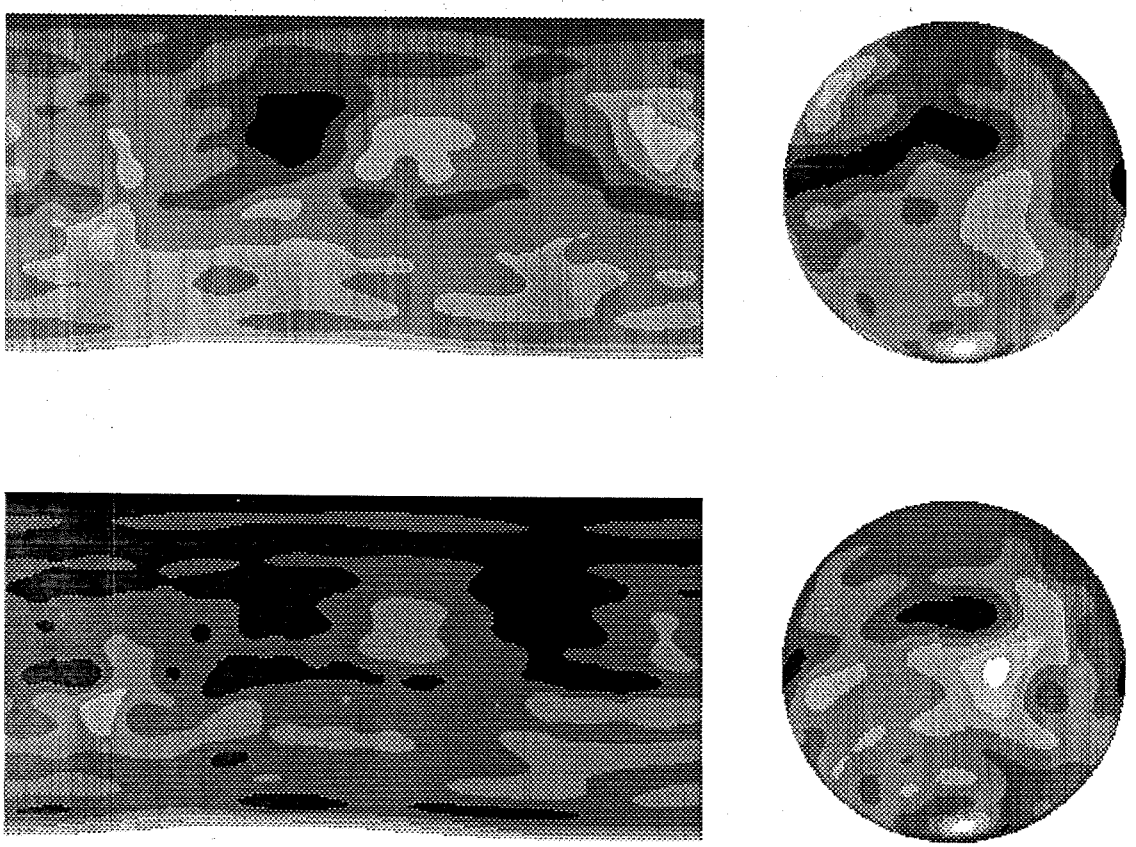

Figure 6.32: Mars 3.5 cm Doppler-radar images. Shown are both a rectangular latitude-vs-longitude map, with 0° longitude at the center, and a spherical projection with subradar point (147°W, 25°S). Top images correspond to $n = 1.0$, bottom images to $n = 1.5$. The spherical projection is shown for comparison with the corresponding VLA Mars image. (The interested reader will find color versions of these images in [21].)

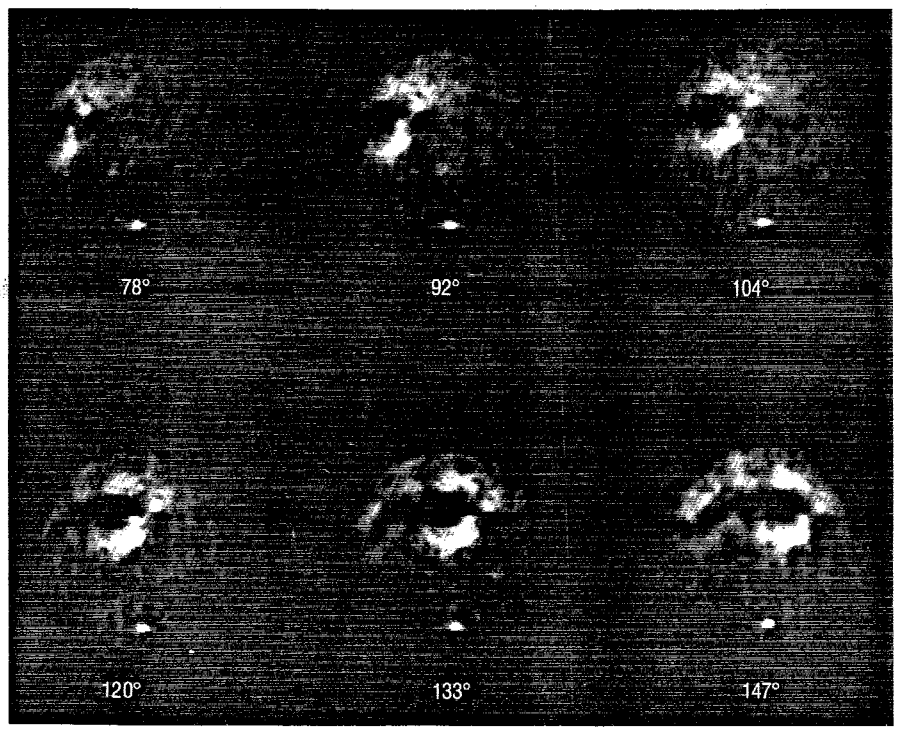

Figure 6.33: Goldstone-VLA 3.5 cm SC radar images of Mars (from [31]) at rotational phases shown. Subradar latitude is 25°S.

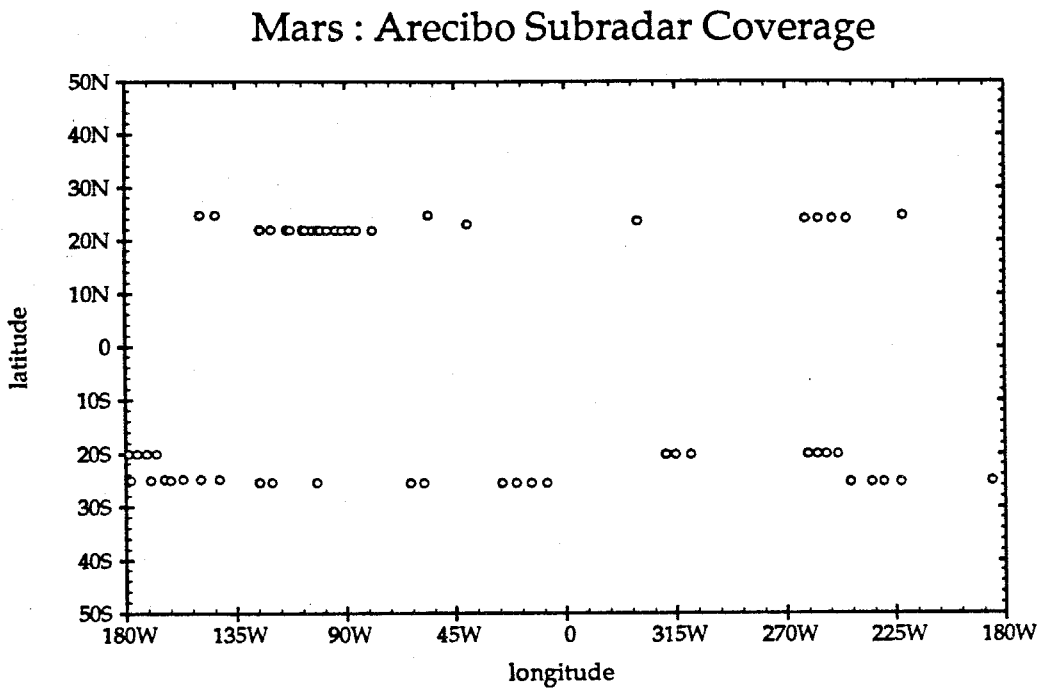

Figure 6.34: Arecibo subradar points on Mars.

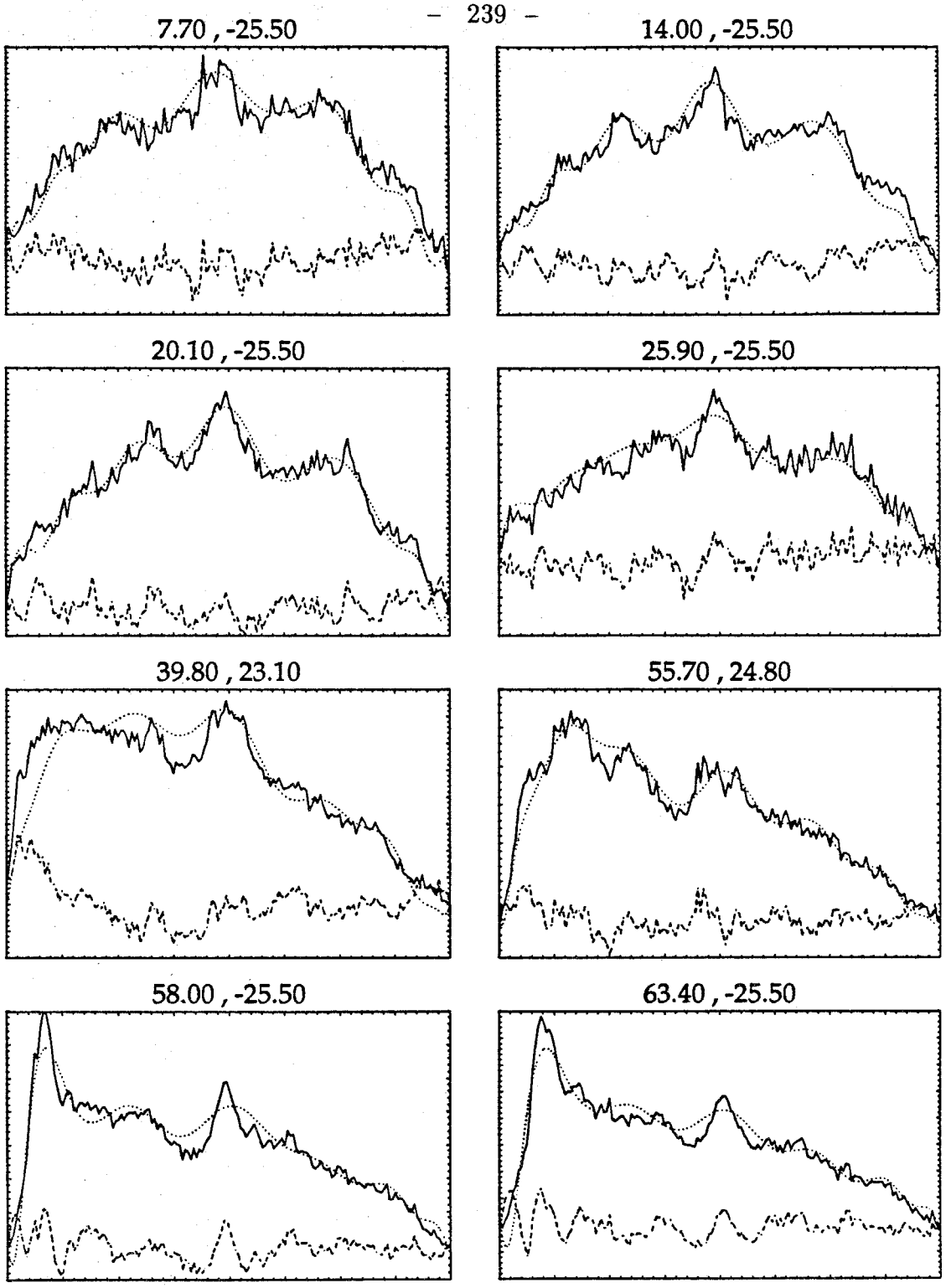

Figure 6.35: Mars Arecibo SC spectra labeled by subradar longitude (rotational phase) and subradar latitude. Solid curves are observed spectra, dotted curves are modeled spectra, and dashed curves are residuals.

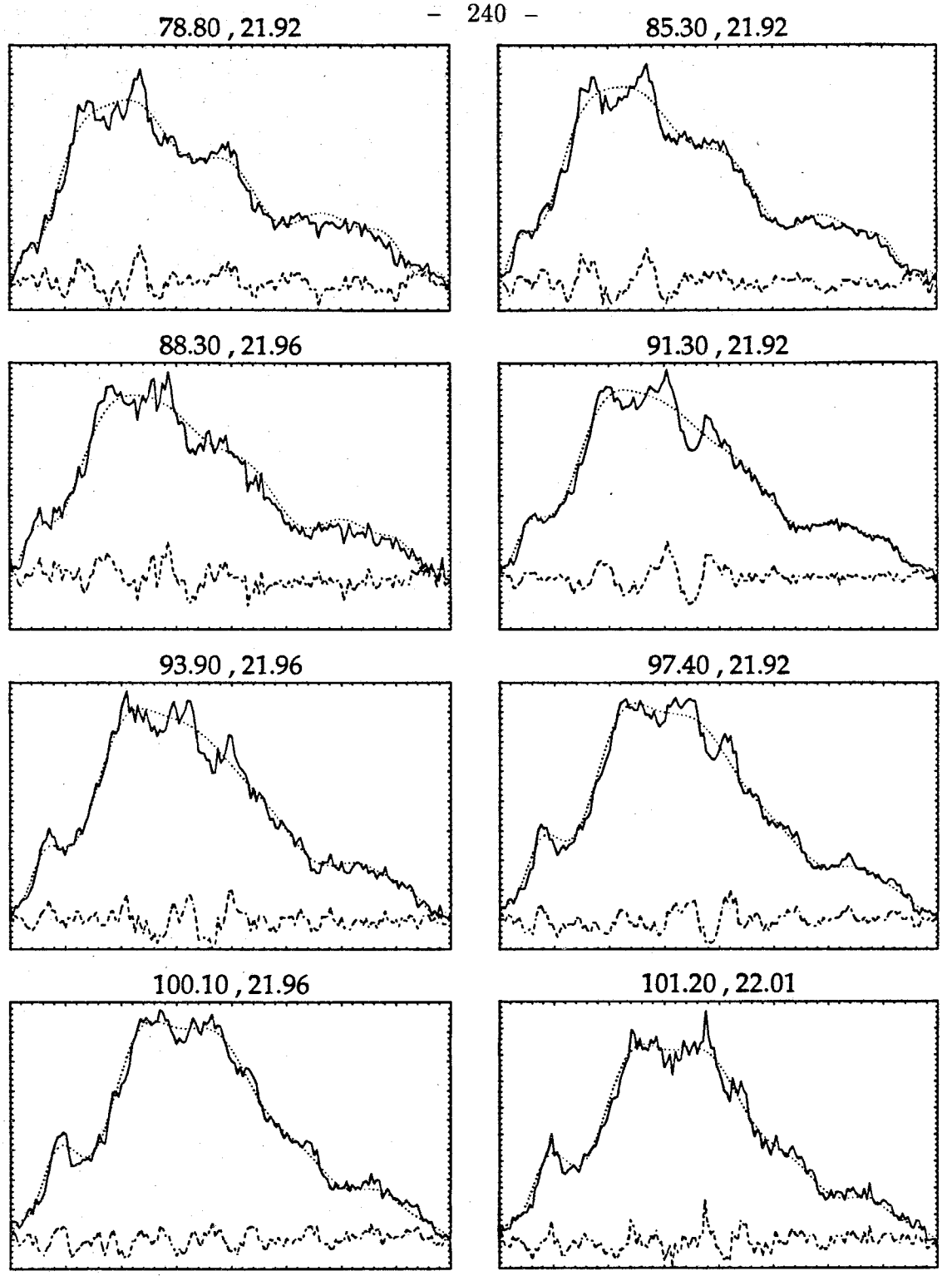

Figure 6.36: Mars Arecibo SC spectra labeled by subradar longitude (rotational phase) and subradar latitude. Solid curves are observed spectra, dotted curves are modeled spectra, and dashed curves are residuals.

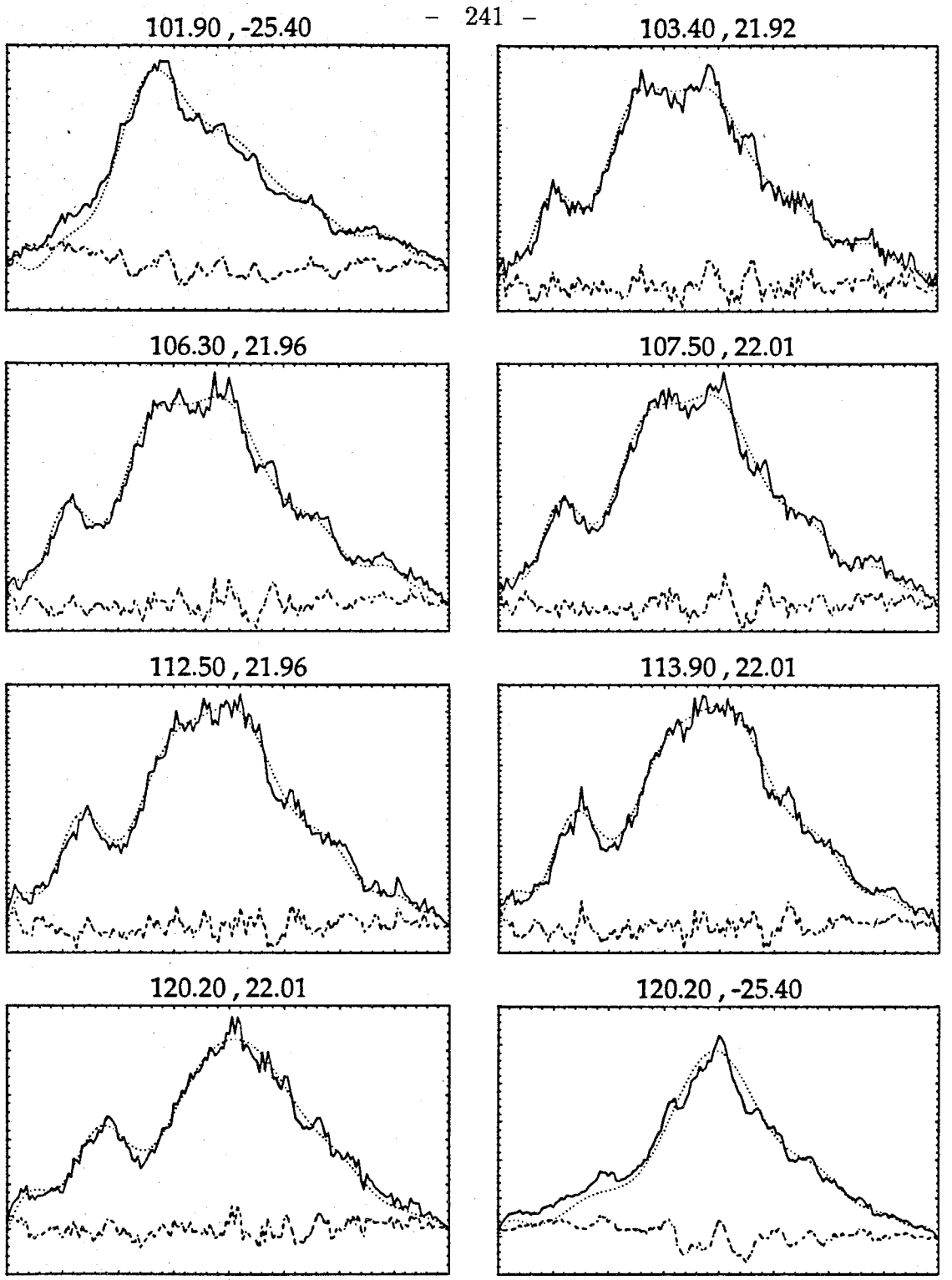

Figure 6.37: Mars Arecibo SC spectra labeled by subradar longitude (rotational phase) and subradar latitude. Solid curves are observed spectra, dotted curves are modeled spectra, and dashed curves are residuals.

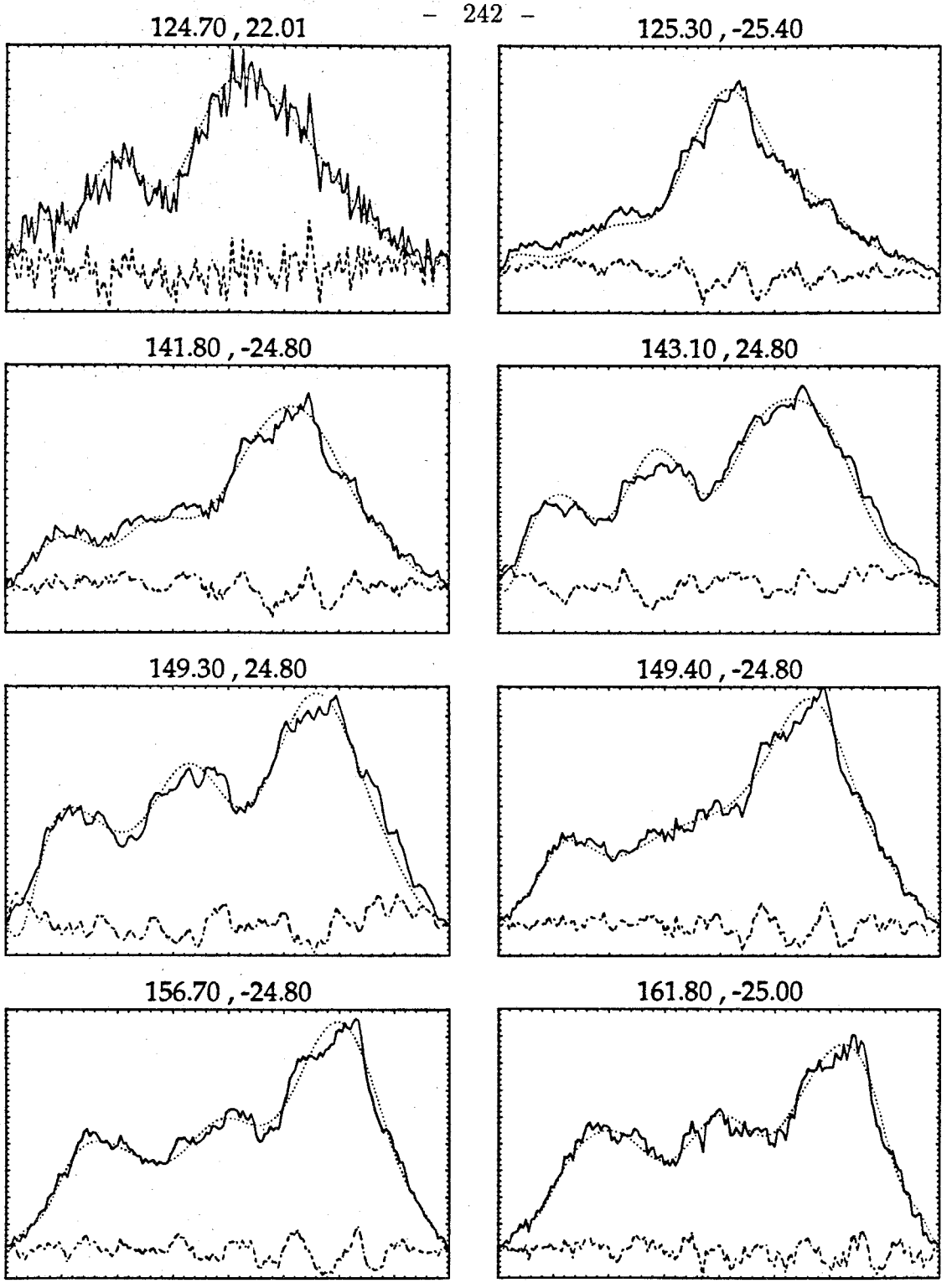

Figure 6.38: Mars Arecibo SC spectra labeled by subradar longitude (rotational phase) and subradar latitude. Solid curves are observed spectra, dotted curves are modeled spectra, and dashed curves are residuals.

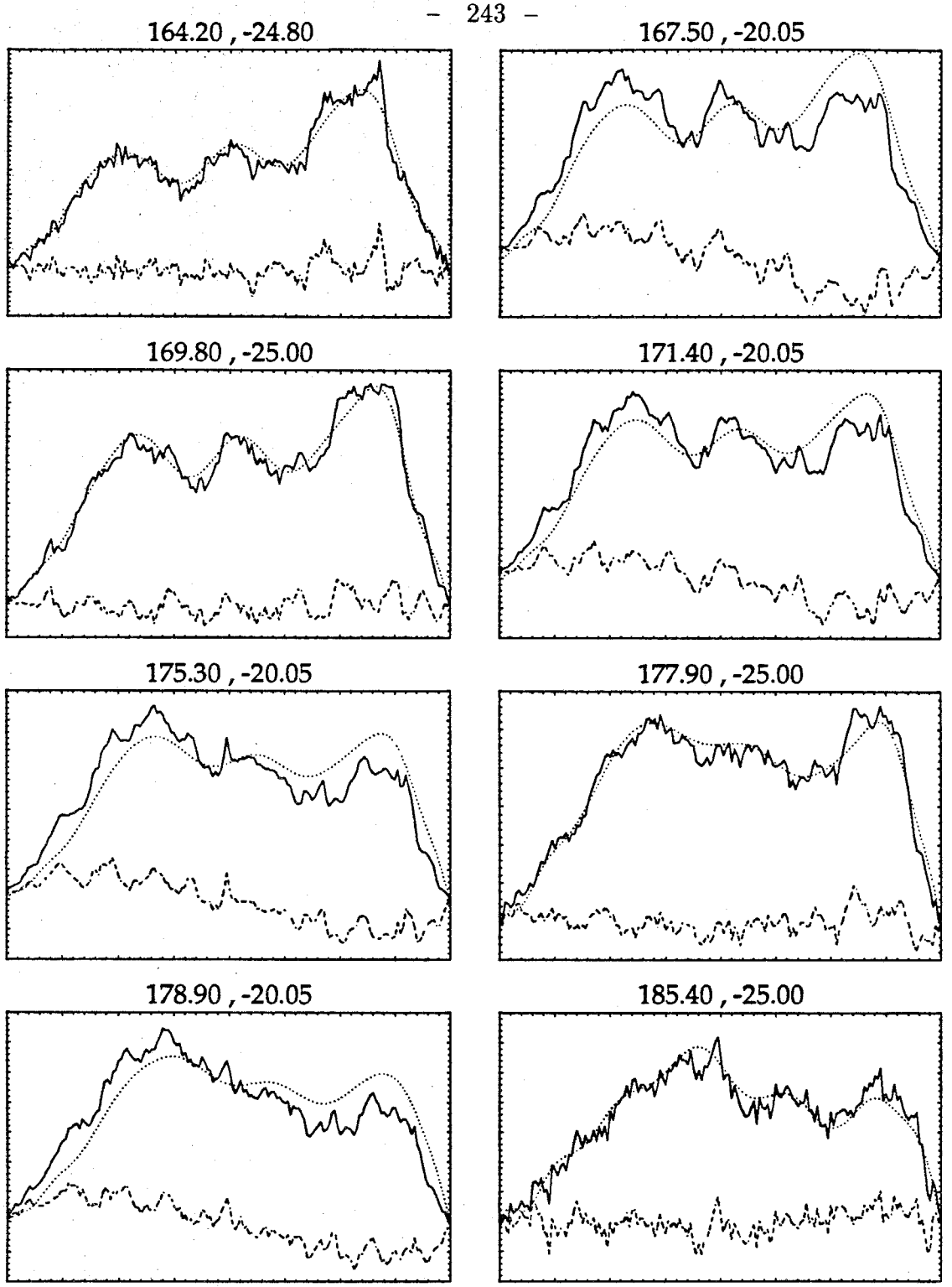

Figure 6.39: Mars Arecibo SC spectra labeled by subradar longitude (rotational phase) and subradar latitude. Solid curves are observed spectra, dotted curves are modeled spectra, and dashed curves are residuals.

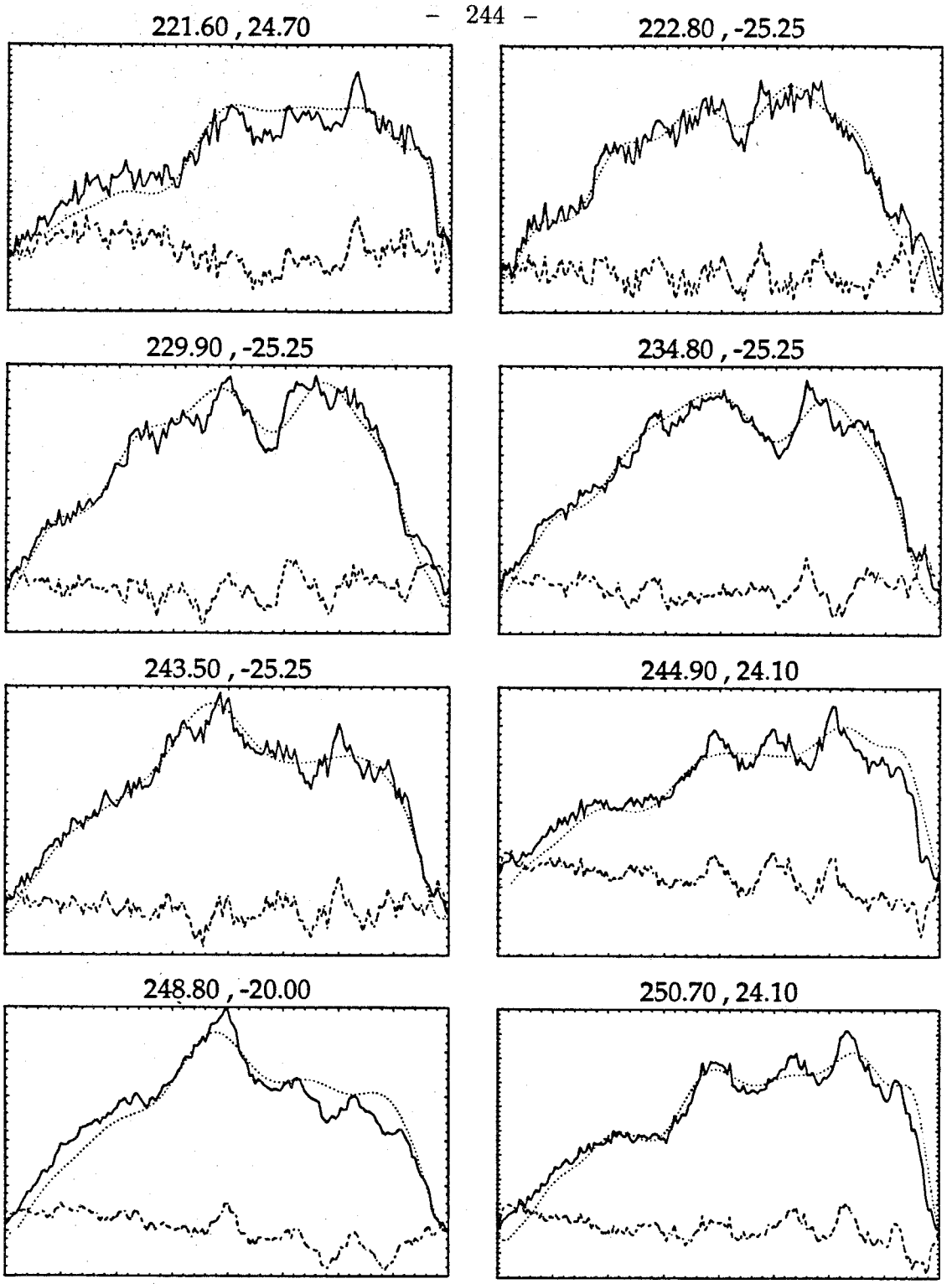

Figure 6.40: Mars Arecibo SC spectra labeled by subradar longitude (rotational phase) and subradar latitude. Solid curves are observed spectra, dotted curves are modeled spectra, and dashed curves are residuals.

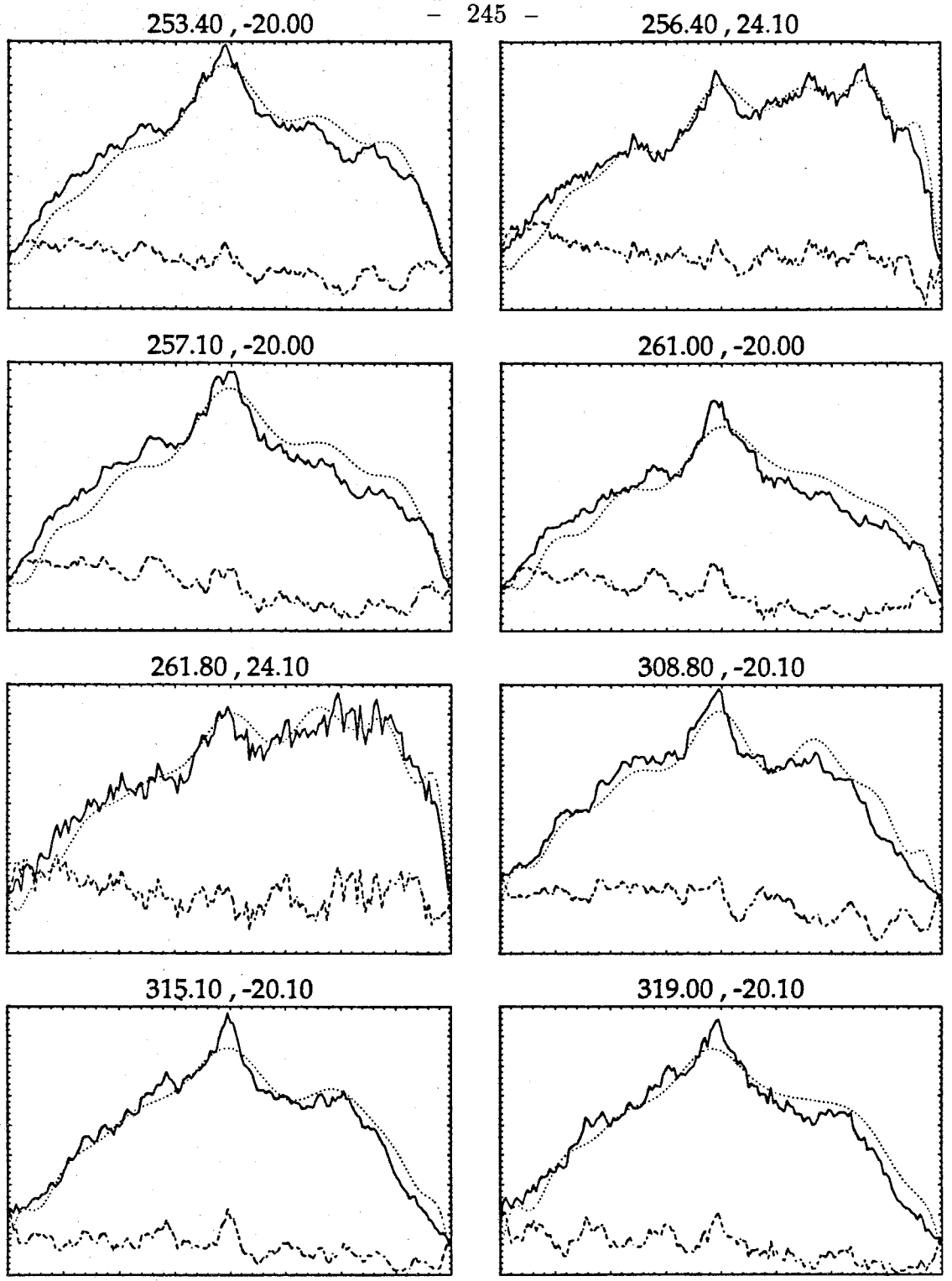

Figure 6.41: Mars Arecibo SC spectra labeled by subradar longitude (rotational phase) and subradar latitude. Solid curves are observed spectra, dotted curves are modeled spectra, and dashed curves are residuals.

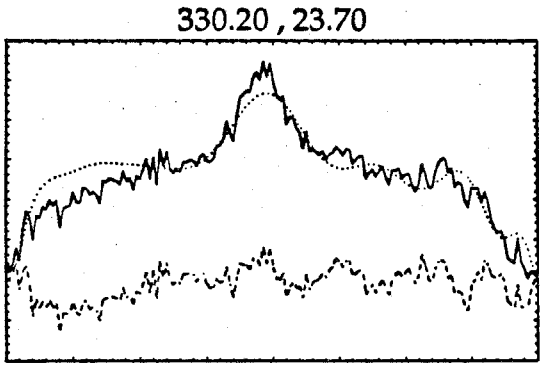

Figure 6.42: Mars Arecibo SC spectra labeled by subradar longitude (rotational phase) and subradar latitude. Solid curves are observed spectra, dotted curves are modeled spectra, and dashed curves are residuals.

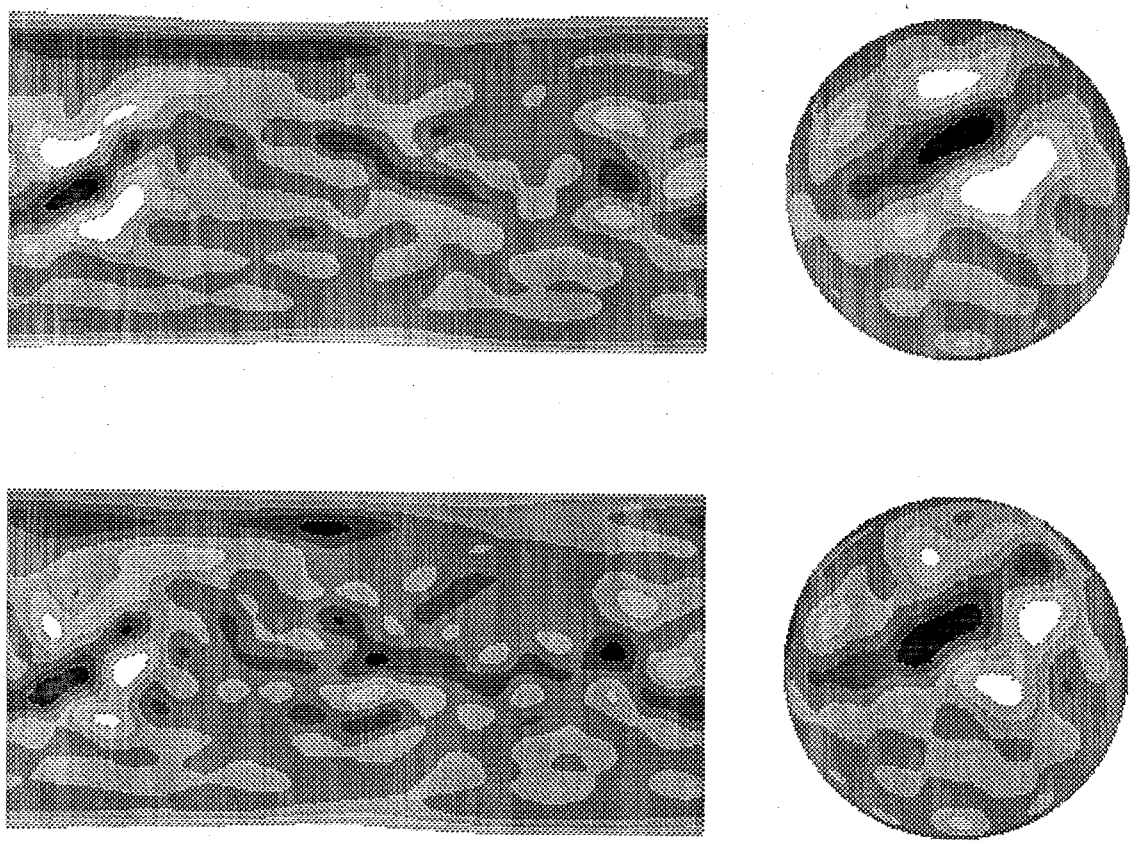

Figure 6.43: Mars 13 cm Doppler-radar images. Shown are both a rectangular latitude-vs-longitude map, with 0° longitude at the center, and a spherical projection with subradar point (147°W, 25°S). Top images correspond to $n = 1.0$, bottom images to $n = 1.5$. The spherical projection is shown for comparison with the corresponding VLA Mars image. (The interested reader will find color versions of these images in [21].)

References

[1] G. Briggs and F. Taylor. *The Cambridge Photographic Atlas of the Planets.* Cambridge University Press, New York, 1982.

[2] D. B. Campbell, R. F. Jurgens, R. B. Dyce, F. S. Harris, and G. H. Pettengill. Radar interferometric observations of Venus at 70-centimeter wavelength. *Science*, 170:1090–1092, 1970.

[3] C. C. Chen and H. C. Andrews. Target-motion-induced radar imaging. *IEEE Transactions on Aerospace and Electronic Systems*, 16:2–14, 1980.

[4] A. J. Deutsch. Harmonic analysis of rigidly rotating ap stars. *Astrophysical Journal*, 159:985–999, 1970.

[5] D. G. Dudley. Progress in identification of electromagnetic systems. *IEEE Antennas and Propagation Society Newsletter*, pages 5–11, August 1988.

[6] R. B. Dyce and G. H. Pettengill. Radar observations of Mars and Jupiter at 70 cm. *Astronomical Journal*, 72:771–777, 1967.

[7] P. H. Eichel, D. C. Ghiglia, and C. V. Jakowatz. Speckle processing method for synthetic-aperture-radar phase correction. *Optics Letters*, 14:1–3, 1989.

[8] C. Elachi. *Introduction to the Physics and Techniques of Remote Sensing.* John Wiley and Sons, New York, 1987.

[9] V. R. Eshleman. Mode decoupling during retrorefraction as an explanation for bizarre radar echoes from icy moons. *Nature*, 319:755–757, 1986.

[10] V. R. Eshleman. Radar glory from buried craters on icy moons. *Science*, 234:587–590, 1986.

[11] A. E. Falk. The line profiles of an oblique rotator. Master's thesis, University of Western Ontario, 1972.

[12] A. E. Falk and W. H. Wehlau. Harmonic analysis of the line profiles of an oblique rotator. *Astrophysical Journal*, 192:409–415, 1974.

[13] R. M. Goldstein. Preliminary Venus radar results. *Radio Science*, 69D:1623–1625, 1965.

[14] R. M. Goldstein. Radar observations of Mercury. *Astronomical Journal*, 76:1152–1154, 1972.

[15] R. M. Goldstein and R. R. Green. Ganymede: radar surface characteristics. *Science*, 207:179–180, 1980.

[16] R. M. Goldstein and H. C. Rumsey. A radar image of Venus. *Icarus*, 17:699–703, 1972.

[17] J. W. Goodman. *Introduction to Fourier Optics.* McGraw-Hill, San Francisco, 1968.

[18] T. Hagfors, T. Gold, and M. Ierkic. Refraction scattering as origin of the anomalous radar returns of Jupiter's satellites. *Nature*, 315:637–640, 1985.

[19] J. K. Harmon, D. B. Campbell, and S. J. Ostro. Dual-polarization radar observations of Mars: Tharsis and environs. *Icarus*, 52:171–187, 1982.

[20] J. K. Harmon and S. J. Ostro. Mars: Dual-polarization radar observations with extended coverage. *Icarus*, 62:110–128, 1985.

[21] J. K. Harmon, M. A. Slade, and R. S. Hudson. Mars radar scattering: Arecibo/Goldstone results at 12.6-cm and 3.5-cm wavelengths. *Icarus*, 1990. submitted.

[22] Thomas Heath. *Aristarchus of Samos, The Ancient Copernicus.* Dover Publications Inc., New York, 1981.

[23] E. W. Hobson. *Spherical and Ellipsoidal Harmonics.* Chelsea Publishing Company, New York, 1965.

[24] R. S. Hudson and S. J. Ostro. Doppler-radar imaging of spherical planetary surfaces. *Journal of Geophysical Research*, 95(B7):10947–10963, 1990.

[25] R. S. Hudson and D. Psaltis. Optical network that learns to perform motion compensation in radar imaging. *Proceedings of SPIE*, 882:154–161, 1988.

[26] R. G. Jurgens, R. M. Goldstein, H. R. Rumsey, and R. R. Green. Images of Venus by three-station radar interferometry — 1977 results. *Journal of Geophysical Research*, 85:8282–8294, 1980.

[27] E. M. Kennaugh. The k-pulse concept. *IEEE Transactions on Antennas and Propagation*, 29:327–331, 1981.

[28] E. F. Knott, J. F. Shaeffer, and M. T. Tuley. *Radar Cross Section.* Artech House, Dedham, MA, 1985.

[29] P. Magnusson, M. A. Barucci, J. D. Drummond, D. Lumme, S. J. Ostro, J. Surdej, R. C. Taylor, and V. Zappala. Determination of pole orientations and shapes of asteroids. In *Asteroids II.* University of Arizona Press, Tuscon, 1989.

[30] L. Marin. Natural-mode representation of transient scattered fields. *IEEE Transactions on Antennas and Propagation*, 21:809–818, 1973.

[31] D. O. Muhleman. Mars by radar. Astronomy, July 1989. page 12.

[32] D. O. Muhleman. Radar astronomy using the very large array. In *Reports of Planetary Astronomy — 1989, Nasa Technical Memorandum 4120*, page 97, 1989.

[33] S. J. Ostro. Radar properties of Europa, Ganymede, and Callisto. In D. Morrison, editor, *Satellites of Jupiter*. University of Arizona Press, 1982.

[34] S. J. Ostro. Planetary radar astronomy. *Encyclopedia of Physical Science and Technology*, 10:611–634, 1987.

[35] S. J. Ostro, D. B. Campbell, A. A. Hine, I. I. Shapiro, J. F. Chandler, C. L. Werner, and K. D. Rosema. Radar images of asteroid 1627 Ivar. *Astronomical Journal*, 99, 1990.

[36] S. J. Ostro, D. B. Campbell, and I. I. Shapiro. Mainbelt asteroids: Dual-polarization radar observations. *Science*, 229:442 – 446, 1985.

[37] S. J. Ostro, R. Connelly, and L. Belkora. Asteroid shapes from radar echo spectra: A new theoretical approach. *Icarus*, 73:15–24, 1988.

[38] S. J. Ostro and G. H. Pettengill. Icy craters on the Galilean satellites? *Icarus*, 34:268–279, 1978.

[39] S. J. Ostro, G. H. Pettengill, D. B. Campbell, and R. M. Goldstein. Delay-doppler radar observations of Saturn's rings. *Icarus*, 49:367–381, 1982.

[40] S. J. Ostro, K. D. Rosema, and R. F. Jurgens. The shape of Eros. *Icarus*, 84:334–351, 1990.

[41] S. J. Ostro and E. M. Shoemaker. The extraordinary radar echoes from Europa, Ganymede, and Callisto: A geological perspective. *Icarus*, 1990. to appear.

[42] A. Papoulis. *Probability, Random Variables and Stochastic Processes.* McGraw-Hill, New York, 1984.

[43] G. H. Pettengill. Radar astronomy. In *Radar Handbook.* McGraw-Hill, New York, 1970.

[44] W. H. Press, B. P. Flannery, S. A. Teukolsky, and W. T. Vetterling. *Numerical Recipes in C.* Cambridge University Press, Cambridge, 1988.

[45] S. Ramo, J. R. Whinnery, and T. Van Duzer. *Fields and Waves in Communication Electronics.* John Wiley and Sons, 1984.

[46] W. Rudin. *Real and Complex Analysis.* McGraw Hill, New York, 1987.

[47] H. N. Russell. On the light-variations of asteroids and satellites. *Astrophysical Journal*, 24:1–18, 1906.

[48] R. A. Simpson and G. L. Tyler. Radar scattering laws for the lunar surface. *IEEE Transactions on Antennas and Propagation*, 30:438–449, 1982.

[49] M. I. Skolnik. *Introduction to Radar Systems.* McGraw-Hill Book Company, New York, second edition, 1980.

[50] B. D. Steinberg. Microwave imaging of aircraft. *Proceedings of the IEEE*, 76:1578–1592, 1988.

[51] M. P. Sulzer. Recent incoherent scatter techniques. *Adv. Space Res.*, pages 153–162, 1989.

[52] T. W. Thompson. High-resolution lunar radar map at 70 cm wavelength. *Earth, Moon, and Planets*, 37:59–70, 1987.

[53] T. W. Thompson and H. J. Moore. A model for depolarized radar echos from Mars. *Proc. 19th Lunar Planet. Sci. Conf.*, 303:477–491, 1989.

[54] F. T. Ulaby, R. K. Moore, and A. K. Fung. *Microwave Remote Sensing.* Addison-Wesley, 1982.

[55] S. S. Vogt, G. D. Penrod, and A. P. Hatzes. Doppler images of rotating stars using maximum entropy image reconstruction. *Astrophysical Journal*, 321:496–515, 1987.

[56] D. R. Wehner. *High Resolution Radar.* Artech House, Norwood, MA, 1987.

[57] S. Werness, W. Carrara, L. Joyce, and D. Franczak. Moving target imaging algorithm for sar data. *IEEE Transactions on Aerospace and Electronic Systems*, 26:57–67, 1990.

[58] D. K. Yeomans, S. J. Ostro, and P. W. Chodas. Radar astrometry of near-earth asteroids. *Astronomical Journal*, 94:189–200, 1987.

[59] R. E. Ziemer and W. H. Tranter. *Principles of Communications.* Houghton Mifflin, Boston, 1985.

[60] S. Zohar and R. M. Goldstein. Surface features on Mercury. *Astronomical Journal*, pages 85–91, 1974.